CFD Analysis and Design of a Low-Twist, Hovering Rotor Equipped with Trailing-Edge Flaps

by

Adriano Gagliardi M.Eng

A thesis submitted in fulfilment
of the requirements for the degree
of Doctor of Philosophy

Department of Aerospace Engineering
Faculty of Engineering
University of Glasgow
August 2007

Abstract

This thesis reports the analysis and design of a hovering rotor equipped with both slotted and blended trailing-edge flaps. This was accomplished by combining a simple blade element method with 3D inviscid and RANS CFD that allowed for a robust sequence of design specification, analysis, and verification. Most modern helicopters have high levels of blade twist and various tip shape designs to help improve hover performance. However, such blade designs face problems due to compressibility effects on the advancing blade in forward flight. The twisted blade gives rise to negative incidence at the blade tip, which accelerates shock formation on the lower surface. The current work looks to evaluate the implementation of a low twist rotor for improved forward flight performance and recovering any potential losses in hover performance by deflecting fixed, trailing-edge flaps. The following paragraphs detail the process by which this was accomplished.

Initially, an extensive review of the current literature was conducted. This reviewed modern rotor blade performance, its limits, and the need for more advanced concepts. More specifically, the performance of a rotor in hover is considered with current methods for improving performance evaluated. With the consideration of flap technology, the various flap designs and methods for modelling flapped rotors are described. Finally, an extensive review of the experimental and computational work conducted so far in the field of flapped rotors is presented. This showed that of the experimental data available, the majority was concerned solely with active flap technology for forward flight including vibration reduction and Blade-Vortex Interaction noise mitigation. For CFD validation, only one report based on the HIMARCS I rotor was available which forms the basic design of this thesis. Of the computational data, no work is available for flapped rotor blades in hover. The CFD presented in this work is the first research attempt to investigate flapped rotors in hover.

The mathematical methods implemented in this work were then described. The initial stages were to be concerned with designing a rotor with trailing-edge flaps. Due to the complexity of CFD, another fast, accurate method was desired. The current work utilises a blade element method combined with momentum theory and 2D CFD aerodynamics to provide the basis for the design study. Following this, a description of the CFD solver used to verify the predicted design configurations is presented, along with explanations of the turbulence modelling, its hover formulation, and post-processing techniques.

Validation of the solver was then presented using both standard test cases and work based on the HIMARCS I rotor itself. Comparisons were presented against experimental rotors in hover and included data reported by NASA and ONERA. Further validation was obtained from comparisons against UH-60A rotor data. The validation was presented in two ways. Firstly, Cp distribution along the span of both experimental and computational results were compared and showed excellent agreement for the NASA (Caradonna and Tung), ONERA, and the UH-60A (Lorber *et al.*) test cases. Secondly, actual performance data in the form of thrust coefficients, torque coefficients, and figure of merit were presented for the HIMARCS I test case. Computational results included the effect of boundary walls on predicted loads. Predictions with both sets of wall distances fell within

experimental error, with excellent agreement obtained when walls were more than 4 rotor spans away.

With confidence in the methods, work then continued with the design study. This focused on evaluating the effect of various flap parameters including spanwise length, chordwise length, deflection angle and spanwise location on the performance of the standard HIMARCS I rotor blade. A slotted flap was chosen for this study since it was the original design presented in the HIMARCS I report. This design was located on the outboard portion of the HIMARCS I, which is of a different profile of the inboard section. Therefore, simple modification to the 2D inboard section geometry was conducted to allow for the evaluation of an inboard slotted flap design. The blade element method was combined with a look-up table of 2D aerodynamics generated using CFD. The BEM method allowed for fast and accurate assessment of the various flap configurations, with over 7000 different designs considered for inboard and outboard flap configurations. The BEM model indicated that up to 6° of blade twist could be recovered at high thrust settings by using a 32%c slotted flap of 24%R span, located at 36%R and deflected by 10°. Further performance improvements at medium thrust settings could be obtained with an outboard slotted flap located at 92%R, with spanwise length 8%R, chordwise length 32%c, and a deflection angle of 10°.

The optimum flapped rotor designs were then considered using 3D CFD. The effect of rotor twist was first evaluated with CFD and the obtained results agreed well with data available in the literature. The optimum slotted flap configurations were compared using inviscid CFD against the clean HIMARCS I rotor with 7° and 13° of twist. Results demonstrated that the low twist rotor with inboard slotted flap was able to match the hovering performance of a rotor with near twice the amount of twist. This was due to the inboard flap providing the larger inboard contribution to blade loading that is normally associated with increasing blade twist. This also resulted in reduced collective and coning angles by approximately 0.5^o-1° with losses recovered by flap deployment. An outboard slotted flap failed to provide any increase in performance, although it did reduce the control angles. The accuracy of the aerodynamics used in both the BEM and CFD methods was then compared by evaluating performance predictions in hover with the built-in inviscid trimmer available in the current solver. Results showed that there is benefit in trim settings that combine a low collective and low coning angle to achieve a specific thrust condition. With consideration of the complexity of a slotted flap design and its deployment mechanism with application to a rotor, a blended design was also implemented. By using the improved accuracy of the CFD trimmer, a blended flap configuration of the same dimensions as the slotted inboard flap was then evaluated. Results demonstrated the equivalent performance of a clean rotor with 10° of blade twist again with savings in trim angles of the order of 1°.

This work highlights the effectiveness of inboard flap deployment on hovering, low twist rotor blades for performance enhancement both in hover and forward flight. It offers a fast design method based on combining a blade element method with high fidelity 3D CFD, which offers a more robust scheme for rotor blade evolutionary design. The CFD calculations presented in this work are the only available in the open literature with respect to hovering flapped rotor blades.

Declaration

The author hereby declares that this dissertation is a record of the work carried out in the Department of Aerospace Engineering at the University of Glasgow during the period between January 2004 to August 2007. This dissertation is original unless otherwise indicated.

August 2007

Adriano Gagliardi

Acknowledgements

Contents

List of Figures

List of Tables

Nomenclature

Latin

a	Pitch axis location in semi-chords
a_{ij}	Acceleration tensor
a_s	Speed of sound [m/s]
A_N	Constants for approximating Wagner function
b	Aerofoil length in semi-chords [m]
b_n	Constants for approximating Wagner function
c	Blade chord [m]
c_f	Non-dimensional centre of pressure in chords
c_{nom}	Nominal blade chord [m]
C_d	Sectional drag coefficient
C_{d_0}	Zero-lift drag coefficient
C_D	Drag coefficient
C_l	Sectional lift coefficient
C_L	Lift coefficient
C_{L_α}	Lift-curve slope
C_m	Sectional $\frac{1}{4}$-chord moment coefficient
C_{m_α}	Moment-curve Slope
C_{m_0}	Zero-lift c/4 moment coefficient
C_M	Moment coefficient about the $\frac{1}{4}$-chord
C_N	Normal-force coefficient
C_Q	Torque coefficient $C_Q = \frac{Q}{0.5\rho\pi R^3(\Omega R)^2}$
C_T	Thrust coefficient $C_T = \frac{T}{0.5\rho\pi R^2(\Omega R)^2}$
$d_{outflow}$	Non-dimensional distance from the blade to the outflow boundary
dB	Decibels [db]
D	Drag force
e	Specific internal energy
E	Total energy
f_c	Flap effectiveness factor
ft	Feet
F	Flux vectors in x-direction
F	Froude-scaled experiment
F	Point of separation for Beddoes Model
FM	Figure of Merit, $FM = 0.707\frac{C_T^{1.5}}{C_Q}$
G	Flux vectors in y-direction
h	Height of gurney flap [m]
H	Flux vectors in z-direction
in	Inches

I_B	Blade flapping inertia in natural frequency mode
k	Reduced frequency, $k = \frac{\omega c}{U}$
k	Turbulent kinetic energy
k_n	Coefficients for modelling the behaviour of the centre of pressure
k_T	Heat transfer coefficient
K_α	Factor for circulatory component of normal force
K_N	Kirchoff approximation
L	Lift force
m	Meters
mm	Millimeters
M	Mach number, $M = \frac{U}{a_s}$
M_∞	Freestream Mach number
M	Moment force about the $\frac{1}{4}$-chord
M	Mach-scaled experiment
M_{tip}	Hover tip Mach number, $M_{tip} = \frac{\Omega R}{a}$
n_{trim}	Steps required for blade retrimming
NB	Number of rotor blades
p	Normalised Pressure
P	Pressure
Pr	Prandlt number
P_N	Critical pressure criterion
PD	Proportional-Differential controller
q	Heat flux vector
$\vec{r}$	Position vector of the cell
r/R	Normalised radial station
R	Blade span [m]
R	flux residual
R_{nom}	Nominal blade span [m]
$R_{outflow}$	Outflow radius
Re	Reynolds number, $Re = \frac{Uc}{\nu}$
Re_T	Turbulent viscosity ratio; turbulent Reynolds number, $Re_T = \mu_T/\mu$
s	Non-dimensional time in semi-chords corrected for compressibility effects, $s = S\beta^2$
S	Non-dimensional time in semi-chords, $S = \frac{2Ut}{c}$
S_n	Coefficients for describing pre- and post-stall moment behaviour
S	Mean strain rate tensor
t	Time [s]
T	Thrust
T	Fluid Temperature
T	Non-dimensional time in chords, $T = \frac{Ut}{c}$
T_I	Impulsive force time constant
T_{V_1}	Time for vortex convection from shedding to the trailing-edge
T_P	Pressure-lagged time constant
u	x-component of velocity vector
$\vec{u}_{ref}$	Mesh rotation velocity
$\vec{u}_h$	Velocity field in rotor-fixed frame of reference
u_i	Velocity vector
u_i'	Fluctuating component of velocity vector
U	Freestream velocity [m/s]
U_i	Mean component of velocity vector

v	y-component of velocity vector
V_r	Voltage [volts]
w	z-component of velocity vector
w	shed wake velocity
$\mathbf{w}$	Vector of conserved variables
wt	Weighting parameter for optimiser
W	Aircraft weight
x_i	Position vector
x/c	Non-dimensional blade station in chord-wise direction
X_n	Deficiency function for recursive formulation
Y_n	Deficiency function for recursive formulation
Z_n	Deficiency function for recursive formulation

Greek

α	Angle of attack [deg]
α	k-ω model closure coefficient
α_0	Zero-lift angle [deg]
α_s	Stall angle [deg]
α_P	Pressure-lagged angle of attack [deg]
β	Blade flapping angle in forward flight [deg]
β	Blade flapping higher harmonics [deg]
β	Prandtl-Glauert compressibility factor, $\beta = \sqrt{(1 - M^2)}$
β	k-ω model closure coefficient
β^*	k-ω model closure coefficient
β_0	Coning angle [deg]
δ	Flap deflection angle, +ive down [deg]
Δ	Incremental value
γ	Circulation
γ	Lock number
γ	Ratio of specific heats
λ_i	Non-dimensional inflow velocity
λ_2	Second eigenvalue of the roots of $\Omega_{ij}^2 + \mathbf{S_{ij}^2}$
θ	Rotor blade pitch angle [deg]
θ_0	Rotor blade collective pitch [deg]
θ_n	Higher harmonic cyclic pitch angles [deg]
θ_{nom}	Nominal blade twist [deg]
θ_{tpp}	Tip path plane angle [deg]
μ	Advance ratio, $\mu = \frac{U}{\Omega R}$
μ	Laminar kinematic viscosity; Laminar eddy viscosity
μ_T	Turbulent kinematic viscosity; turbulent eddy viscosity
ν	Kinematic viscosity (m^2/s or ft^2/s)
ν	Cell volume component
ρ	Density [kg/m^3]
σ	Rotor blade solidity [N/m]
σ	k-ω model closure coefficient
σ^*	k-ω model closure coefficient
χ	Propulsive force coefficient

τ	Shear stress
τ_{ji}	Viscous stress tensor
τ_{ij}^R	Reynolds stress tensor
ψ	Azimuth angle [deg]
ϕ	Wagner function
ω	Dissipation per unit turbulent kinetic energy
$\vec{\omega}$	Rotation rate
Ω	RPM [rev/s^2]
Ω	Mean rotation tensor
$\mathscr{V}_{i,j,k}$	Cell volume

Subscripts

$()_{1c}$	1st harmonic longitudinal cyclic
$()_{1s}$	1st harmonic lateral cyclic
$()_c$	Circulatory component
$()_C$	Chord force coefficient
$()_E$	Effective
$()_i$	Impulsive component
$()_m$	Mean
$()_{max}$	Maximum
$()_{min}$	Minimum
$()_q$	Pitch rate
$()_{qs}$	Quasi-steady
$()_s$	Stall angle
$()_s$	Shaft angle
$()_{tip}$	Tip value
$()_{tpp}$	Tip-path plane
$()_T$	Total
$()_\delta$	Flap angle

Superscripts

$(\dot{\ })$	Pitch rate
$(\ddot{\ })$	Pitch acceleration
$()'$	Time-averaged component
$()^C$	Circulatory component
$()^f$	Due to flap
$()^i$	Inviscid
$()^I$	Impulsive component
$()^v$	Viscous

Acronyms

ABC	Active Blade Control
AFC	Active Flap Control
ARES	Aeroelastic Rotor Experimental System
ATR	Advanced Technology Rotor
BEM	Blade Element Method
BVI	Blade-Vortex Interaction
CFD	Computational Fluid Dynamics
CHARM	Comprehensive Hierarchical Aeromechanics Rotorcraft Model
DSV	Dynamic Stall Vortex
FEV	Flap-Edge Vortex
GCL	Geometric Conservation Law
HIMARCS	High Maneuverability and Agility Rotor and Control System
HMB	Helicopter Multi-Block
IBC	Individual Blade Control
MAV	Micro-Air vehicle
MDART	McDonnell Douglas Advanced Bearingless Rotor
NS	Navier-Stokes
PZT	Piezoelectric materials
rev	Revolution
RANS	Reynolds-Averaged Navier-Stokes
RFA	Rational Function Approximation
ROM	Reduced-Order Model
TFI	Trans-Finite Interpolation
UMARC	University of Maryland Advanced Rotorcraft Code
WHL	Westland Helicopters Limited

Publications

Gagliardi, A., and Barakos, G.N., "Analysis and Design of a Flap-Equipped, Low-Twist Rotor for Hover", Journal of Aircraft. Accepted for publication.

Gagliardi, A., and Barakos, G.N., "Improving Hover Performance of Low-Twist Rotors Using Trailing-Edge Flaps - A Computational Study", Presented at the 32nd European Rotorcraft Forum, Maastricht, The Netherlands, September 2006.

Barakos, G.N., Badcock, K.J., and Gagliardi, A., "CFD Simulation of Flow Control Devices for Helicopter Rotors", Presented at the CEAS/KATnet Conference on Key Aerodynamic Technologies, Bremen, Germany, June 2005.

Gagliardi, A., Beedy, J., Steijl, R., Barakos, G., and Badcock, K.J., "Analysis of Flapped Rotors using CFD and Indicial Methods", Presented at the American Helicopter Society 61st Annual Forum, Texas, USA, June 2005.

Chapter 1

Introduction

1.1 Overview

In the design of a main rotor blade for both commercial and military helicopters, performance in hover and forward flight must be considered and balanced, accordingly [1]. The most common methods for evaluating rotor blade design centre on Reduced-Order Models (ROM) and experimental testing, followed by full flight tests. The latter two prove to be an expensive element in the design process and, more often than not, offer a narrow test matrix due to high operating costs. They also require specific equipment and test setups if any element of the flow is required to be captured such as Blade-Vortex Interaction (BVI) or the rotor in ground effect. Models, however, have the ability to evaluate a variety of flight conditions by utilising 2D aerodynamic data coupled with theoretical flight mechanics [2, 3, 4]. Compared to both experimental and flight testing, ROM's are a fast and cost-effective design tool. However, due to the complexity of the aerodynamic and aeroelastic problems encountered on the rotor blade, the accuracy of the modelling can still be considered insufficient and experimental testing is still required for validation. Moreover, data visualisation for both models and experiments are limited. The former since sectional blade loads are calculated and offer little scope for presentation of results, and the latter since they are dependent on various techniques like Particle Image Velocimetry with expensive setup costs to try and visually capture features of the flow. Therefore, an evident gap exists in the design chain for an accurate method that will be able to verify model predictions, whilst offering greater insight into the flow physics surrounding the rotor. In turn, this could help reduce the amount of experimental testing required for validation and cut costs associated with model manufacturing and wind tunnel time, thus promoting a compact, cost-effective design process for future rotorcraft development.

An appropriate candidate would be Computational Fluid Dynamics (CFD) based on high-fidelity Reynolds-Averaged Navier-Stokes (RANS) solvers. Research using RANS has been proven to offer accurate aerodynamic loads predictions and detailed flowfield visualisations, with the list of publications too long for reference here. Initially, CFD development for rotors was limited to inviscid Euler calculations [5]. However, due to the increased complexity of the rotor flow environment, including rotating-blade motion, blade-vortex and -wake interactions, localised blade stall, and vibratory loadings to name but a few, to be able to fully capture these effects using CFD required viscous calculations. Fortunately, technological advances in computing power and CFD algorithms make the daily use of RANS CFD in the design and development process more feasible and, as numerical algorithms have evolved, so has the accuracy with which rotor flows can be predicted.

Although combined design methods offer potential, current helicopter performance is gradually approaching the stage where the rotor blades themselves are the bottleneck in the design [1, 6]. A modern rotor blade can incorporate up to three or more blade section profiles, non-linear blade twist, blade taper, and a variety of tip shapes; such designs are generally optimised for specific flight conditions and suffer high manufacturing costs. For example, helicopters are unique in that, unlike other aircraft, they have the ability to hover. In designing a rotor for hover or axial flight, implementing high levels of blade twist can increase the rotor's performance. Also, applying blade taper and anhedral to the blade tip can help reduce induced drag and increase thrust. However, problems can be encountered in forward flight when shocks can begin to form at the advancing blade tip. At this point, such designs can exacerbate shock strengths, which increase control loads and limit maximum forward flight speeds. The inherent difficulty in the rotor blade design problem is now obvious. Clearly, a variable blade design for each flight condition would be the best solution. Improving the effectiveness of prediction methods and increasing rotor blade performance feature highly in the US Army's vision for helicopter aeromechanics [6] (see Table 1.1). Coupling CFD and ROM's have shown to give excellent benefits in the accuracy of rotor performance prediction [7, 8], and there has been various research into flow control devices such as air-jet vortex generators [9]. A design that is able to tailor a rotor for specific flight regimes was the Controllable Twist Rotor (CTR) implemented on Kaman aircraft [10], which has been further developed to the Multicyclic Controllable Twist Rotor (MCTR) [11]. A 25%R span servo-flap was placed at 75%R on a rotor blade with low-torsional stiffness. Torsional bending of the blade was induced via the external moments produced by the servo-flap, thus allowing for active control of the blade twist in flight. More recently, NASA have been developing the Active Twist Rotor (ATR) [12, 13], which aims to resolve issues with blade loadings, vibrations, and Blade-Vortex Interactions. It's achieved

by implementing hundreds of piezoelectric actuators underneath the blade's skin, both in the span-wise and chordwise directions. By passing a variable current through the actuators, bending can be induced in each individual actuator, thus allowing for blade deformation to suit the present flight condition.

Aeromechanics	Improvement (%)		
	By 2000	By 2005	By 2010
Reduce vibratory loads	20.0	40.0	60.0
Reduce vehicle adverse aerodynamic forces	5.0	12.0	20.0
Increase maximum blade loading	8.0	16.0	24.0
Increase helo/rotor aerodynamic efficiency	3.0	6.0	10.0
Increase prop/rotor aerodynamic efficiency	1.5	3.0	4.5
Increase rotor inherent lag damping	33.0	66.0	100.0
Aeromechanics prediction effectiveness	65.0	75.0	85.0

Table 1.1: US Army's objectives set out for improvements in the rotorcraft field up to the year 2010 [6].

1.2 Hover

It is common knowledge that fixed wing aircraft are more efficient flying vehicles than helicopters, as are gyrocopters at low advance ratios. However, these aircraft lack the ability to hover [1]. This allows a helicopter to perform essential tasks such as sea rescue, people transport, sky crane functions, and close troop support extremely efficiently. Therefore, the hovering performance of a new rotor has to be carefully considered. The hover efficiency of a rotor is judged in terms of the Figure of Merit (FM), which is the ratio of ideal power over actual power:

$$FM = \frac{IdealPower}{ActualPower} = \frac{C_T^{1.5}/\sqrt{2}}{C_Q} \tag{1.1}$$

The ideal power assumes all thrust is produced with no rotor power requirements [1]. The actual power takes into account effects that contribute to increased rotor power requirements such as pressure drag and induced drag. The higher the FM, the better the hovering efficiency of a rotor. The main detrimental factor in a helicopter's hovering performance is heavy loadings at the blade tip due to the varying dynamic head and, consequently, strong tip vortices and high induced drag. A few methods are generally used to help improve hovering efficiency. Blade taper, swept tips, and varying tip angles can all have beneficial effects. An interesting design study by Le Pape and Beau-mier [14] using CFD looked to optimise a rotor for hover using such design constraints. The final design included a parabolic, swept tip with anhedral deflection angle. However, the most common

method is by implementing twist along the span of the rotor as on a propeller, making it possible to distribute the loading on the blade more evenly (see Figure 1.1). This results in a rotor blade which requires less loading at the tip to achieve similar performance as a blade with less twist and, therefore, induced power is reduced due to a weaker tip vortex. By reducing the induced power, it can be seen from Equation 1.1 that an increase in FM can be obtained.

ROOT   TIP ROOT   TIP

(a)   (b)
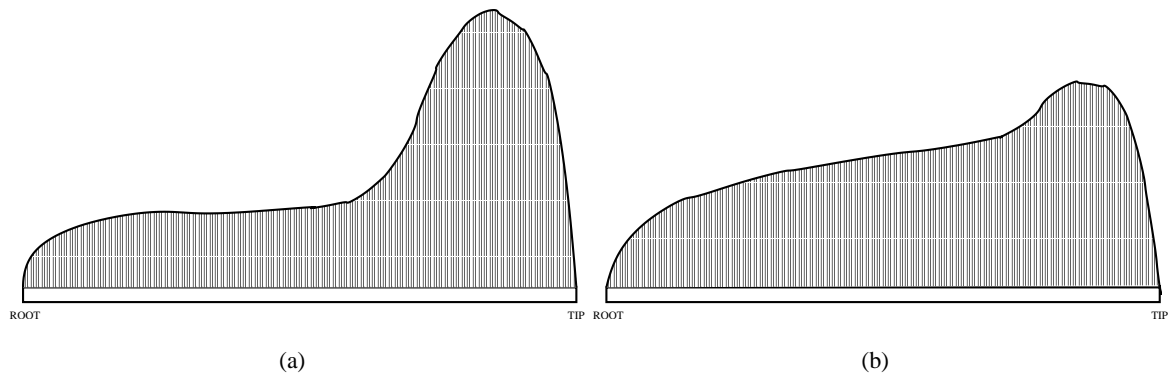
Figure 1.1: Schematic of the lift distribution over twisted blades at the same C_T. (a) Low twist. (b) High twist.

The amount of twist implemented on rotor blades varies greatly depending on the aircraft's primary design purpose. A compromise normally has to be reached between hover performance and the limits of the flight envelope for forward flight. For large helicopters that are used primarily for large cargo transport or sea and rescue missions where they will have to operate in hover for long periods of time, highly twisted blades are used to ensure optimum efficiency. On the other hand, light 2- or 3-bladed helicopters that are designed for scouting or transporting a few people generally have very low levels of blade twist, since they will operate in forward flight more than in hover. This can be explained with respect to the transonic effects experienced on the rotor blade of a helicopter in forward flight. In forward flight, the advancing blade produces tremendous amounts of lift and can approach near sonic speeds at the blade tip. However, it is beneficial for limiting induced power and noise if the strength of shocks is kept to a minimum. Therefore, designers will target a local angle of attack at the blade tip near the zero-lift angle. Unfortunately, large amounts of blade twist can make this very difficult to achieve. The consequence of which is a negative effective angle at the blade tip and the formation of shocks over the lower surface of the rotor. This has the effect of reducing thrust, increasing control loads, and reducing the working life of rotor blades [15]. An example of the effect blade twist has on the hover and forward flight performance of a helicopter rotor can be clearly seen in Figure 1.2, with the highly twisted blade losing what advantage it had in hover over

the low twist blade when entering forward flight.

(a)   (b)
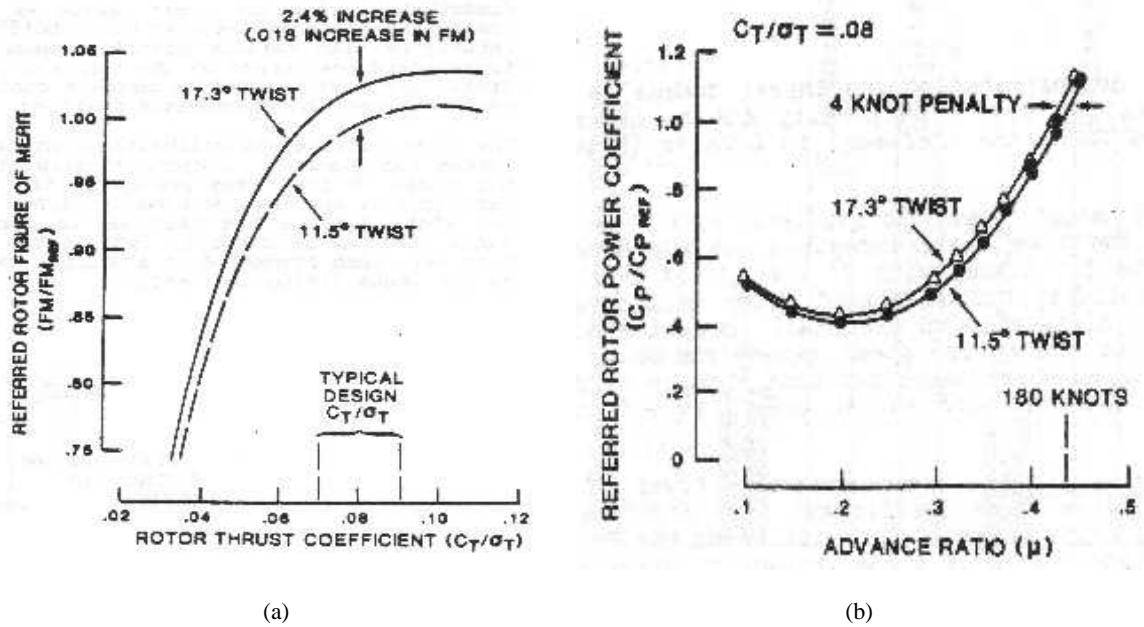
Figure 1.2: Performance data for two identical rotors with varied blade twist. (a) Hover. (b) Forward flight. Taken from Ref. [15].

In view of the above, being able to achieve good hover performance with as little blade twist as possible would seem ideal. This was exactly what Noonan *et al.* [16] investigated by considering a rotor equipped with high-lift devices for hover and forward flight improvement. The high-lift devices, common on fixed-wing aircraft, included a 3° slotted flap and two leading-edge slat designs located at the blade tip region. When deployed, they would be fixed in hover with very low actuation power requirements. Some benefits were evident with the -6° leading-edge slat design, but the results for the slotted flap, however, were inconclusive [16]. Therefore, it is still to be seen whether there is a future in this concept. The idea of using fixed flaps was given further consideration in experiments and computations by Wachspress and Quackenbush [17]. They demonstrated that fixed, inboard flaps were capable of reducing Blade-Vortex Interaction (BVI) noise in low-speed, axial descent. They noted a shift in circulation to the inboard portion of the blade, greater wake mixing and, consequently, a weaker tip vortex. Although both computations and experiments offered similar results in noise reduction levels, it should be noted that the method for modelling the flap and the physics associated with the design used in the experiment are fundamentally different, but this will be discussed in more detail later.

5

1.3   History of Active Flap Control

Interest in Active Flap Control (AFC) technology has been on-going since the early 1990's. Although the majority of research in AFC has been limited to whirl towers, wind-tunnel testing, and computational evaluation, some flight tests have been conducted by Eurocopter [18] showing good results in reducing vibrations and pilot control loads. The concept of using flow control devices on rotorcraft, however, is not a new one. Pescara [19] in 1923 patented a method of using ailerons to induce blade twist and hence control local blade pitch angles. A schematic of the design can be seen in Figure 1.3. Vertical motion was obtained by increasing or decreasing thrust by deflecting the flap, with horizontal motion obtained by unbalancing the lift produced on the advancing and retreating sides by variable blade warping.
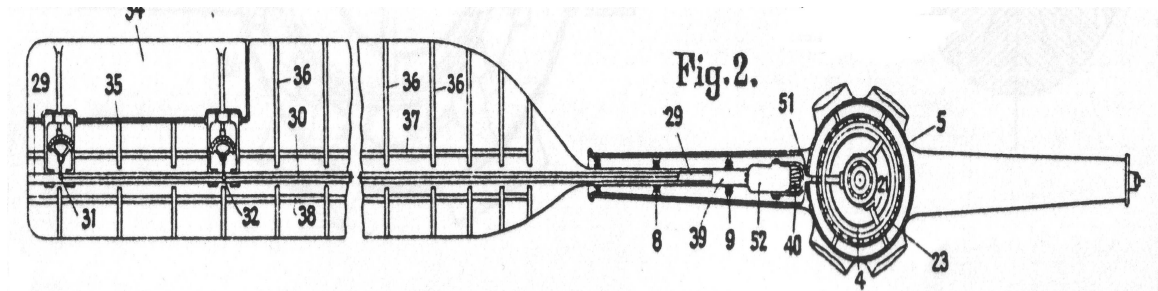
Figure 1.3: An early rotor blade, or screw propeller, by Pescara [19] with an integrated, trailing-edge flap (34) for blade pitch and cyclic control.

He was followed by D'Ascanio in 1934 [20] who patented a 2-bladed, co-axial rotor helicopter that used servo-tabs on the blades to control the amount of blade lift they produced (see Figure 1.4). Blade control was obtained by varying the tabs separately for horizontal flight and in unison for vertical flight to increase or decrease the thrust produced by the rotor disc. Both ideas were prevalent in a time when the modern Sikorsky swashplate design was still to be accepted as the standard for blade collective and cyclic pitch control.

The Kaman Corporation produce helicopters that use servo-flaps at the 3/4 blade chord to induce blade twist that alters the local blade pitch by means of 1/rev inputs from the swashplate, an idea that Kaman himself had patented back in 1948 [21]. The early design involved inter-meshing rotor blades with a flap device located at the blade 3/4-chord. The flap device was attached to the blade by an arm (see Figure 1.5(a), item 29). By applying collective and cyclic inputs to the blade root and the flap, the distribution of lift along the blade could be optimised by introducing torsional moments to induce blade twist, which in turn varied the effective angle of attack [10] along the blade span. A

similar idea to that of Pescara [19]. A modern application of this concept can be seen on the Kaman K-MAX heavy lift helicopter, which uses servo-flaps for rotor control (see Figure 1.5(b)) and has many improvements over the original design. The development of the Multicyclic Control Twist Rotor (MCTR) has additional benefits due to higher harmonic inputs to reduce vibration levels, as reported by Wei and Weisbrich [11].
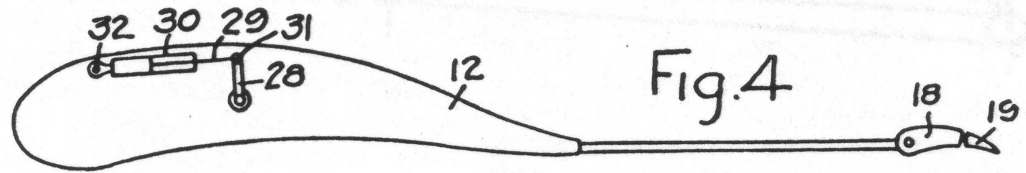
Figure 1.4: Schematic of the blade section and the 2-piece, servo-tab used for thrust variation on D'Ascanio's 1934 co-axial helicopter. Taken from Ref. [20].

The advantage of AFC over other existing or aspiring active control technologies is the variety of problems to which it can be applied. So far it has been shown to be effective in reducing noise due to blade-vortex interaction [22], where the flap can either (1) displace the blade position relative to the approaching vortex so as to avoid it by either increasing or decreasing the local aerodynamic lift and moments, (2) by canceling out the impulsive aerodynamic response induced by BVI using active flap inputs, or (3) allow for a spanwise shift in circulation that reduces trailed vortex strength, as well as (4) allowing for increased wake mixing and vortex dissipation. The mitigation of rotor hub vibration levels and pilot control loads [23] has also been shown to be possible. In this case, the main vibratory hub loads present in the rotor environment, namely the (N-1)/rev, N/rev, and (N+1)/rev vibrations, are countered by applying equal and opposite aerodynamic loads via a trailing-edge flap to cancel out the baseline blade loads. The most demonstrated application, however, is reserved for blade pitch control [10, 11, 24], which as explained earlier induces blade twist (or warping) to effectively alter the local blade pitch angle and lift.

There is also the benefit that, by utilising the progresses in piezoelectric materials [25, 26, 27], AFC actuators can now be located on the rotor blade itself offering reduced complexity and high efficiencies in terms of flap power consumption and blade/hub maintenance. Interestingly, there is very little work in the open literature evaluating both fixed and actuated trailing-edge flaps for improved aerodynamic performance, including the associated benefits in increased payloads, forward

flight speeds, and reduced control loads. As described before, blade twist is beneficial in hover, but retards blade tip efficiency in forward flight. To avoid this, low twist rotors could be utilised with fixed flaps to recover hover performance.
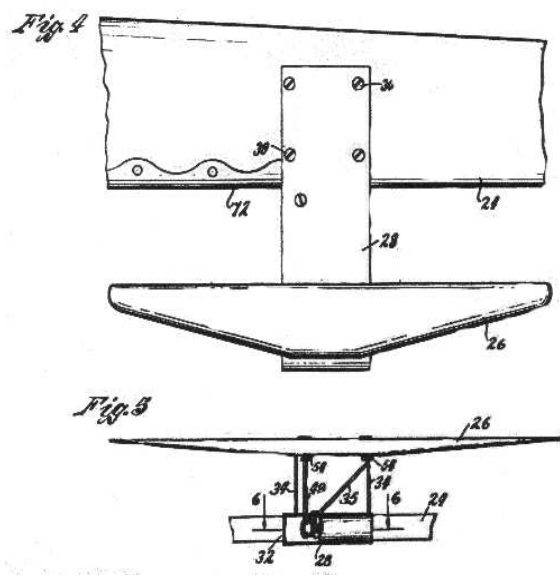
(a)   (b)

Figure 1.5: The progression of blade control on the Kaman helicopters. (a) The design from the initial patent in 1948. (b) The modern day MCTR. Figure (a) is taken from Ref. [21].

1.4 Flap Designs

There is an important choice to be made when selecting which flap design to use for rotorcraft applications. The most common types of flap are considered below, each of which could offer benefits in improving rotorcraft performance. These are integrated, slotted, split, Gurney, and servo flaps.

Integrated or plain flaps (see Figure 1.6(a)) are widely used in fixed-wing aircraft for lift generation and as ailerons for flight control. For rotor blades, they are compact enough to be located within the blade planform. When they are deflected, effective camber is introduced and local suction peaks at the hinge point give either lift or downforce. Unfortunately, due to their location at the rear of the aerofoil, sharp adverse pressure gradients are obtained over the flap and cause the aerofoil to stall earlier the more flap deflection that is applied. They are well-suited to dealing with harmonic problems such as blade vibrations and BVI encountered in forward flight due to the low power requirements required to oscillate the flap. For lift enhancement, they are not as effective as other designs, but the combination of simplicity and low drag makes them feasible. For this reason,

the majority of modern research on flapped rotors has concentrated on integrated flap technology. This design would also lend itself well to problems in hover and retreating blade stall.

Slotted flaps (see Figure 1.6(b)) can also be found on the wings of aircraft and have many advantages over the standard integrated design. The inclusion of the flap gap between the main element and the flap gives both the main element and the flap separate boundary layers. This allows for higher angles of attack before flow separation occurs compared with the plain flap with increases in maximum lift and the static stall angle. Boundary layer mixing also occurs between both elements and has two effects, (1) due to the low pressure on the upper surface of the flap, the pressure gradients on the main element are improved since (2) the adverse pressure gradient is transfered from the main element to the flap, hence causing the boundary layer on the flap to separate earlier than expected [28]. Therefore, the flap gap is a very important design criterion. For rotorcraft applications, the flap gap could cause problems at high inflow velocities since shocks could form in the gap on the advancing blade. This would reduce its effectiveness, increase blade vibrations, and reduce the integrity of the flap actuation mechanism. However, it would make no sense to implement a slotted flap for vibration and noise mitigation, as it is a design that is aimed at pure aerodynamic performance improvement and not torsional moment control. That is why it is especially suited to a steady-state environment such as a helicopter in hover, where it could prove to be extremely beneficial.

Servo-flaps (see Figure 1.6(c)) are less common on fixed-wing aircraft, but are capable of producing large aerodynamic pitching moments due to the large offset from the rotor blade's elastic axis. When deflected, pitching moments induced by the flap can cause the blade to elastically distort in torsion as used in Kaman rotorcraft. There are issues with this design, however, as the flap gap and actuation mechanism can increase drag significantly. Although it has proven to be a good solution for the Kaman KMAX and the Super Seasprite, it is interesting that the design hasn't been implemented by other rotorcraft companies.

The split flap (see Figure 1.6(d)) was widely used in early aircraft (pre-1940's aircraft) since it was a simple design that could produce a lot of lift. It was invented in 1920 by Wright and Jacobs [29] and is essentially a thin plate that is hinged on the main section and, when deflected, rotates downwards like a normal flap, although in this case the main section does not alter geometry. The disadvantage of the design is the high drag caused by the bluff body flow behind the flap. This makes it ideal for landing and slowing down whilst taxiing, but poor for enhancing perfor-

mance on rotors. There could also be potential problems with the instabilities in the bluff body flow behind the flap and their influence on the flexible rotor blade's bending loads.

The Gurney flap (see Figure 1.6(e)) was invented by Dan Gurney in 1971 during testing for his racing team, AAR, to increase downforce, although it was never patentable as Edward Zaparka had been credited with a similar device in 1934. Liebeck [30] was the first to describe the flow physics behind the design. The Gurney flap has the effect of creating two counter-rotating vortices behind it, which delays the Kutta condition at the trailing-edge and produces increased lift due to an increase in effective camber and hence circulation. It is the simplest of all the flap designs and it can provide significant increases in L/D, although its size is limited to the height of the boundary layer for maximum efficiency. It has gained some interest in rotorcraft performance enhancement, especially in conjunction with leading-edge droop, but its high drag is a limiting factor.

1.5 Flap Modelling

An important element of design using numerical methods is to assure that you are capturing all the relevant physics properly. Both 2D and 3D RANS CFD have been shown in the past 20 years to be adequate in predicting performance parameters of aerofoils with flaps, although there have been consistent problems with drag prediction, stall angles, and correct boundary layer mixing (see Appendix B). However, before RANS CFD was available to the aerodynamicist, models were developed based on potential theory that offered excellent accuracy for attached flow. They included boundary layer lag effects to increase the fidelity of the method and offered viable drag models, which contributed greatly to early fixed-wing aerodynamics. Other models have also been developed based on various techniques such as lifting-line theory, Rational Function Approximations (RFA), and indicial methods, although they weren't without their drawbacks.

Table 1.2 presents a short description of these methods. They encompass both time-domain and frequency-domain models in incompressible and compressible flow, for fixed and time-varying freestream velocities. Some require simple superposition on the aerofoil loads to obtain the total loads, whereas others contain an entire aerodynamic model for aerofoil and flap motion.
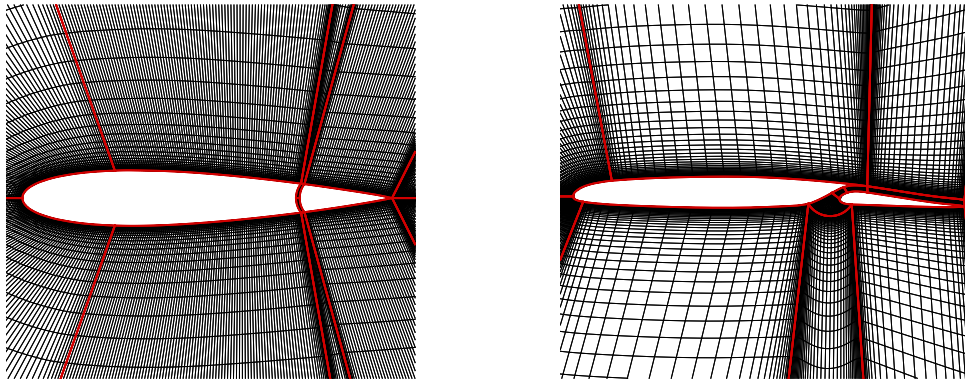
(a)   (b)
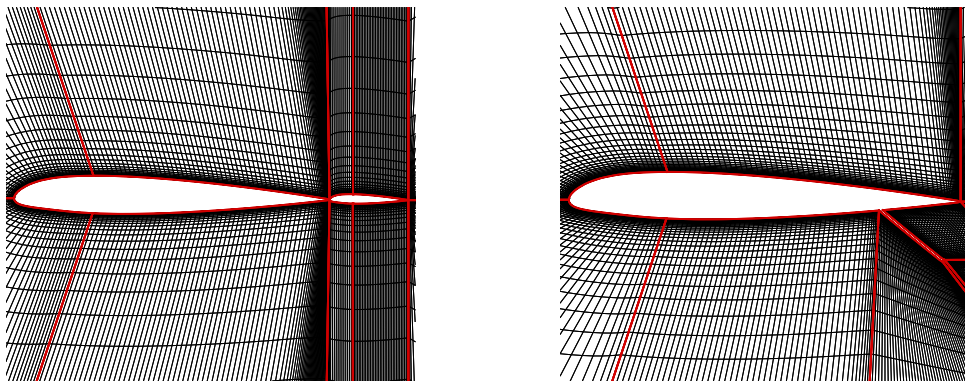
(c)   (d)
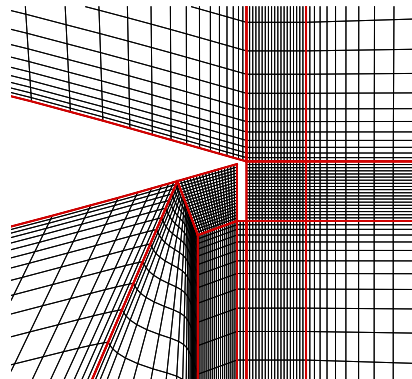
(e)

Figure 1.6: Flap designs for rotorcraft application. (a) NACA 0015 with a 25%c plain flap. (b) RC(6)-08 blade section with a 32%c slotted flap. (c) NACA 23012 aerofoil with a 25%c servo-flap without a flap gap. (d) NACA 23012 with a deflected, 25%c split flap. (e) Close-up of a NACA 0012 with a micro Gurney flap.

Flap Modelling							
		Corrected Loads				*Comp./*		
Ref	*Year*	C_L	C_M	C_D	C_H	*Incomp.*	*Motion*	*Method*
[31]	1935	Y	Y	Y	Y	Incomp.	Harm.	Potential Theory
[32]	1940	Y	Y	N	Y	Incomp.	Harm.	Potential Theory
[33]	1957	Y	N	N	N	Incomp.	Arbt.	Lifting-Line Theory
[34]	1977	Y	Y	Y	Y	Comp.	Arbt.	RFA
[35]	1994	Y	Y	Y	Y	Comp.	Arbt.	Potential Theory
[36]	1995	Y	Y	N	Y	Incomp.	Arbt.	Lifting-Line Theory
[37]	1996	Y	Y	Y	Y	Comp.	Arbt.	Indicial Methods
[38]	1997	Y	Y	Y	Y	Comp.	Arbt.	RFA
[39]	1999	Y	Y	N	Y	Comp.	Arbt.	2D CFD Modified,
								Lifting-Line Theory
[40]	2001	Y	Y	N	N	Incomp.	Arbt.	Lifting-Line Theory

Table 1.2: Various work on flap modelling using various approaches.

One of the pioneers in this field was Theodore Theodorsen [31] who looked to model wing flutter using incompressible, potential theory in the frequency domain as early as 1935. Essentially, this was an extension of thin aerofoil theory to take into account six degrees of freedom in the aerofoil motion (pitch, plunge, trailing-edge flap) and modelled the lift, drag, c/4-moment, and hinge moment. The model considered both circulatory and impulsive loadings with apparent mass effects to treat the boundary layer lag due to the shed wake. These viscous wake effects were accounted for by the Theodorsen function, C(k), which is applied as a correction to the circulatory equations. It can be known exactly in terms of Bessel functions and is dependent on the reduced frequency of oscillation. Its inclusion is critical to the theory, as it has a significant effect on the magnitude and phasing of the circulatory loads. Similar work was completed around the same time by Kussner [32] and modifications to the theory have been made to account for time-varying freestream velocity [35], arbitrary flap motion [41], and for rotorcraft application [42]. However, the theory breaks down when compressibility effects begin to influence the flow at high subsonic-transonic conditions where the phasing is calculated incorrectly. Also, as will become apparent with all the models discussed here, the model is valid only for conditions below stall.

Narkiewicz *et al.* [36] extended unsteady thin aerofoil theory to account for arbitrary motion of an integrated, trailing-edge flap. The flap was simply modelled as a variation in the camber of the aerofoil with a difference in velocity potential on the upper and lower surfaces along with the Kutta condition applied at the trailing-edge. The unsteady, integrated loads were then obtained in terms of the velocities induced by the aerofoil, flap, and the wake motion. The effects of the shed wake, hence the apparent mass effects, were accounted for in the circulatory lift by a best-fit

approximation to the Theodorsen function. Limitations to this method include the assumption of a thin aerofoil, small flap deflections, inviscid flow, and therefore no viscous drag or separation model.

Hariharan and Leishman [37, 43] used indicial methods to develop a subsonic, compressible flap model that offered exact and approximate responses to the arbitrary motion of an integrated flap. The unsteady lift, drag, c/4-moment, and hinge moment were calculated with boundary layer lag included via indicial response methods, similar to the method pioneered by Beddoes [44]. The initial airloadings were computed directly from piston theory and are relevant only to the instant in time when the perturbation is applied. These amount to the impulsive components of the indicial response. The impulsive loadings after the initial perturbation were then approximated using exponential decays based on indicial response functions, with the rate of decay dominated by non-circulatory time constants. Similarly, linearised, subsonic theory was used to obtain the final, circulatory loadings for the flap motion when the perturbation had settled to a quasi-steady value. An approximation to the Wagner function was used to model the shed wake effects [37]. Exact values for both the circulatory and impulsive loads were also demonstrated for very small time increments. Flap effectiveness parameters were introduced for the lift, c/4-moment, and the hinge moment to account for flap gap effects. Finally, a model for the unsteady drag for both aerofoil and flap motion was given. The drag due to aerofoil/flap motion is dependent on the total lift and the effective angle of attack of the main aerofoil and is theoretically equivalent to the model first proposed by Theodorsen [31].

Hassan [39] evaluated the aerodynamics of a standard NACA 0015 with a 25% chord integrated, trailing-edge flap. Quasi-steady, 2D Navier-Stokes CFD calculations were used with variations in freestream velocity, aerofoil angle of attack, and flap deflection angles considered and 2D aerodynamic look-up tables were generated. Using this data, simple modifications were also made to thin aerofoil theory to take into account flap deflections and effectiveness.

Chan and Brocklehurst [40] investigated the application of a trailing-edge flap for performance enhancement via 2/rev actuation. They used basic thin aerofoil theory to calculate changes in the lift coefficient, the zero-lift moment, and the zero-lift angle and superimposed them on to the baseline values present in the an in-house code for rotor analysis. A correction, f_c, was also applied to modify the loads for flap effectiveness. As with Ref. [36], this approach is only valid for thin aerofoils in inviscid, incompressible flow. No drag correction is implemented and the flow is assumed to be fully attached. An extension of this theory to account for wing taper and sweep can be found

in Lowry and Polhamus [33].

1.6 Flapped Rotor Studies Using ROM's

Reduced-order models are used extensively in rotorcraft design and development due to the fast turnover times and sufficient accuracy in performance prediction, while validation via standard wind tunnel tests is still required. Issues with the reliability of these codes includes the accurate aerodynamic and aeroelastic modelling of the rotor blades, and the lack of sufficient experimental data for validation purposes. The first issue, flap modelling, was discussed in the previous section and there are many methods reported in the literature. The second problem proves important since the majority of research into AFC has targeted blade-hub vibrations, with interest in BVI a close second. The following section describes some of the more important studies into AFC using reduced-order models obtained from an extensive literature survey. A concise list of these studies can be found in Table 1.3.

1.6.1 Early Work with ROM's

The first vibration reduction study can be found in Milgram *et al.* [45] and Milgram [46] who looked to validate the use of the UMARC (University of Maryland Advanced Rotorcraft Code) code for vibration studies involving AFC. The UMARC code discretises the blade into 1-D beam elements each with 15 degrees-of-freedom (4 in-plane, 4 out-plane, 4 axial deflections, and 3 for torsion), with the unsteady aerodynamics modelled using Beddoes indicial method [44] and the flap modelled using the Hariharan and Leishman model [37, 43].

To represent the finite control system stiffness, the blade root was assumed to be restrained by a torsional spring, k_1, through which control inputs were applied. The aeroelastic equations of motion were solved using a modal reduction with eight modes under investigation - rigid blade flapping and lag modes, the first three elastic flapping modes, the first two elastic in-plane modes, and the first torsional mode. A more in-depth look into the model can be found in Ref. [46]. The CAMRAD/JA model [64] was also used and results compared with the UMARC code. Experimental data for validation was obtained from the McDonnell Douglas Active Flap Rotor (AFR) wind tunnel test at NASA Langley [22], which included vibratory load data from open-loop experiments and will be discussed later. A summary of the structural properties of the rotor is available in all three papers.

As in the experiment, the model had a plain trailing edge flap of 25% chord located between 79%

ROM Simulation				
Ref	*Year*	*Code*	*Flaps*	*Compared Data*
[47]	1996	CAMRAD/JA	1	BVI noise control
[45]	1998	UMARC, CAMRAD/JA	1	Vibration and control loads mitigation
[48]	1998	BEM	1-2	BVI noise mitigation
[49]	1998	RFA	1-2	Vibratory loads reduction
[50]	2001	CAMRAD/JA, CAMRAD II	1	Flap optimisation for vibratory and control load mitigation
[40]	2001	CFRM	1	Performance enhancement using thin-aerofoil theory and an integrated flap
[51]	2002	RFA	1-2	Dynamic stall induced vibratory loads reduction
[52]	2003	-	1	Flap configuration for blade pitch control
[53]	2004	UMARC	1	Flap configuration for blade collective and cyclic pitch control
[17]	2004	CHARM, WOPWOP	1	BVI noise mitigation
[54]	2004	-	1-4	Hybrid optimisation study for vibration reduction
[55]	2004	-	2-4	Multiple flap configurations for vibratory load mitigation
[56]	2005	BEM	1	Study of fixed flaps for hover performance improvement
[57]	2005	ROTOR	-	Performance enhancement using miniature gurney flaps
[58]	2005	RFA	2	Simultaneous vibration and noise reduction using flaps
[59]	2006	-	1-4	Blade loads control
[60]	2006	CAMRAD II	1	Parametric study of flap geometry and location for vibration reduction
[61]	2006	RFA	2	Vibration reduction and performance enhancement in fast forward flight
[62]	2006	BEM	1	Fixed flap optimisation study for hover performance improvement
[63]	2006	R150	1-2	Vibration reduction on the WHL Lynx

Table 1.3: Reduced-order model investigations into flapped rotor aeromechanics.

and 97% of the blade radius. Validation looked at the baseline rotor and the 5/rev flap excitations with $\pm 4^o$ of flap deflection. Results yielded good correlation between the predicted trim controls for the baseline rotor in forward flight and experimental data, although lateral cyclic pitch was under predicted in both models. Blade moments for the baseline rotor were reasonably well predicted with some minor discrepancies. As reported for the trailing-edge flap configuration, fair predictions for flatwise bending and torsional moments were obtained, while in-plane bending moment predictions were poor. The results generally showed to be sensitive to assumptions made regarding the blade

flap and lag hinge stiffness, as well as flap aerodynamic effectiveness. A comprehensive sensitivity study can be found in Ref. [46].

Baeder and Sim [48] used a combination of CFD and indicial methods to investigate the alleviation of Blade-Vortex Interaction noise by using rotor blades with AFC. The indicial method was based on the Beddoes model [65]. The isolated vortex was modelled using a compressible, stationary gust function with the Sculley and Kaufman algebraic core model [42] providing the vortex tangential velocity. The near wake was modelled using a Weissinger L-type model and the wake age was monitored up to 50° of azimuthal time. 3D Euler CFD runs were computed using a field velocity approach to describe the vortex velocity field. Surface pressure distributions in the wake were taken from CFD and used as input into the aeroacoustic code to provide predictions away from the blade. The experimental setup from the non-lifting rotor in Kitapliglu and Caradonna [66] was used as the baseline geometry and for validation.

Single and dual flaps were examined for both parallel and oblique BVI noise reduction. The dual configuration consisted of two flaps of with a chord length of 20%c, spanwise length of 15%R, and located at 75%R. The single flap consisted of a combination of the dual flaps into a single, actuated flap. Both the low aspect ratio blade from the experiment and a high aspect ratio blade equivalent to an untwisted, UH-1H rotor were examined. Good to excellent agreement in the lift variation around the azimuth was obtained between the unsteady aerodynamic model, CFD, and experiment. The actuation schedules were seen to be heavily dependent on blade aspect ratio and the inclination of the vortex at the point of intersection. However, reductions in noise between 7 db and 10 db for oblique and parallel BVI were obtained using the dual-flap configuration.

Straub and Charles [50] looked to evaluate the effectiveness of the CAMRD/JA and CAMRAD II codes in predicting vibratory load reductions via AFC. An optimisation study was also completed by Milgram [46]. The numerical predictions were once again validated against data from the McDonnell Douglas Advanced Bearingless Rotor (MDART) test. Both models predicted the flap bending moment and torsional moment fairly well, although the chordwise bending moment was overpredicted. A flap configuration study was conducted with results showing that spanwise location, aerodynamic balance, mass balance, and blade dynamics (fundamental torsion and the higher bending modes) are important factors. Interestingly, excitation frequencies for the flap hinge moments were seen to peak where the frequencies were close to the flap bending modes, and flap effectiveness increased when actuated at frequencies near the first torsional mode. The optimum

flap location was finally chosen to be at located at 83%R, with the flap chord and span 25% and 18%, respectively. Both the codes were then compared for a variety of dynamic inputs and loadings and showed good agreement.

Chan and Brocklehurst [40] used the Westland Helicopters Ltd. aeromechanic code, CFRM, to evaluate the potential for performance enhancement in rotorcraft with integrated flaps. The flap was modelled quite simply using thin aerofoil theory to account for changes in the lift coefficient and the zero-moment coefficient. Performance improvements were achieved although drag due to flap deflection was not included in the model.

Taking a different approach, Celi [52] offered an analytical study of the dynamics and reconfiguration requirements of a 4-bladed rotor helicopter where the main pitch links had been severed, and trailing-edge flaps were used to control blade pitch. The application of the flap managed to suppress the first and second harmonic hub loads by more than three orders of magnitude. The dynamic pitch response of the flap acted in such a way that it was seen to match the expected pitch inputs from the pitch links. The flap acted by generating a rigid-body pitching moment of the free-floating blade that matched, at every azimuth, the angles that would have been generated by the swashplate. The steady-state flapping motion of the re-configured blade was nearly identical to that of the undamaged blade. The results showed that trailing-edge flaps could be used as emergency control surfaces following a failure of the flight control system.

Depailler and Friedmann [51] looked to reduce blade vibrations due to dynamic stall by using actively-controlled, single and dual servo-flaps. The unsteady aerodynamic model for both the main blade airloads and for the flap were calculated via a Rational Function Approximation of aerodynamic loads [34, 38], with the ONERA dynamic stall model implemented for separated flow. To account for drag due to flap deflection, a very simple approximation to experimental data published in Ref. [67] was implemented and is defined as:

$$C_d = 0.01 + 0.001225|\delta| \tag{1.2}$$

This was implemented in the attached flow model. No correlation between the flap aerodynamics and the dynamic stall model was made. The control algorithm was based on the performance minimisation function equivalent to that in Myrtle and Friedmann [49]. The single flap configuration had a spanwise length of 12%R, chord length of 25%c, and was located at 75%R. The dual flap

configuration consisted of the single flap split in two. Mid-range advance ratios were tested with flap deflection angles configured by the control algorithm, with a limiter set at $\pm 4^o$ to mimick the control authority imposed by mechanical restrictions. The model predicted between 60%-85% reduction in hub vibration levels. The limiter reduced actuation power requirements by 40% and had a small effect on predictive loads. As described earlier, it is thought that the vibration reduction achieved was due to the blade avoiding retreating blade stall, although the lack of a comprehensive flap model in the study may have had an effect.

1.6.2   Recent Efforts

More recently, the UMARC code was used to evaluate the performance and actuation requirements for an ultralight helicopter with flaps for primary control, similar to the method used on Kaman rotorcraft. The work by Shen *et al.* [53] later evolved to include vibration reduction schemes [68, 69].

The model used a 2-bladed, teetering rotor flying at a cruise speed of 16 knots. The blade torsional frequency for the baseline and flapped rotor was 2.2/rev with the rotors rotating at 525 RPM. The flap was located at 82%R and had a chord of 25%c and span of 18%R. A list of the modal frequencies is available in the report [53]. The parasite drag of the swashplateless configuration was taken as 15% less than baseline and the weight of the model was reduced by 3%. Results were compared at advance ratios of 0 (hover) to 0.17. They demonstrated that the trailing-edge flap collective and cyclic angles were below 4° for all advance ratios. Pitch angles for both configurations were similar, although the swashplateless configuration showed less collective blade pitch in forward flight due to the additional lift generated by the deflected flap. In high speed forward flight, the swashplateless rotor consumed less power than the baseline rotor and the same or slightly less in hover and low speed flight. Less forward tilting of the main hub was predicted in forward flight also.

The blade pitch index angle was found to be a key parameter. To obtain the desired blade pitch angle and avoid having to deflect a flap upwards to obtain the nose-up moment and, in the process, negative lift, a preset blade pitch angle is used (the blade pitch index angle or pre-collective angle) that is set higher than the desired pitch angle. Once the rotor is accelerated to operational speed, the nose-down moment generated by deflecting the flap downwards will bring the preset blade pitch angle down to the desired pitch angle for the blade. The optimal pitch index angle, which varies with advance ratio, reduced both the cyclic and mean component of the flap angles and minimised actuation power. Intuitively for such a design, an increase in blade root stiffness resulted in greater

actuation power requirements, with low blade torsional stiffness increasing flap effectiveness. Locating the flap at the blade tip region where high dynamic pressure exists also helped improve results.

A rare study on the use of fixed flaps to decrease the effect of BVI and reduce noise levels in low-speed descent was considered by Wachspress and Quackenbush [17]. To investigate the problem, the reduced-order model, CHARM, which utilised an advanced vortex roll-up model, was coupled with the WOPWOP acoustic prediction code to study various flap deployments, with the final design being validated using wind tunnel tests.

The numerical study considered varied deployments of a series of 5%R span split flaps along the inboard section of a rotor to determine optimum locations for noise reduction. The rotor blade geometry was taken from the AH-1G OLS and had a blade chord of 4.09 inches and a span of 3.142 feet. The blade had a total geometric twist of 7.5^o from 25%R to the tip, with 1.2^o of tip sweep. Steady flap angles of 5°, 10°, 15°, and 20° were tested for three different flap deployment strategies. The first two flap configurations extended up to 70%R with the third extending to 54%R only. Testing was performed at an advance ratio, $\mu = 0.164$ and thrust coefficient, $C_T = 0.0054$ over shaft angles from -3° to 6°. The computational results predicted the flap devices were pushing the interacting vortex downward and away from the blade. A possible explanation for this is that, since the inboard section of the rotor is loaded more than the baseline rotor, the blade tip will see a smaller local angle of attack and hence shed a weaker tip vortex. Experiments were then run in the NASA Ames Wind Tunnel to validate the predicted data. Predicted values for noise reduction were in the region of 6-12 dB, whereas experimental tests showed a drop in peak BVI noise of 7 dB. The experiment showed that increased wake turblence encouraged by the deployment of the flaps had the effect of increasing wake-vortex mixing, hence reducing the vortex strength. However, there is a notable discrepency in how both the numerical and experimental procedures were conducted. The aerodynamics modelled in CHARM were that of a split flap - a design common in early propellor-based aircraft due to its simplicity and ease of deployment. However, this design is very inefficient as it produces a bluff body flow behind the flap. In the experiment, for reasons of structural integrity, it was decided to fill the space normally resident behind a deployed split flap. The physics of the flap then change since the new device begins to operate like a Gurney flap, with the phenomenon of two counter-rotating vortices forming at the trailing-edge directly behind the flap. No remarks were made on this matter in the report, but it would be interesting to know what effect it would of had on the performance of the noise reduction mechanism.

1.6.3 Optimisation and Gurney Flaps

Further vibration control studies were conducted by Viswamurthy and Ganguli [55], who looked into reducing vibratory loads by means of multiple trailing-edge flaps on rotor blades. Three cases were considered in total - a single flap of 20% span and one-fifth chord, centered about the 90% span position - two flaps of 10% span each and one-fifth chord with each centered at 95% and 85% span respectively, and four flaps of 5% span each and one-fifth chord, with each flap being centered at 97.5%, 92.5%, 87.5%, and 82.5% span respectively. There is a brief summary of the aeroelastic model used including the calculation of the governing equations of motion, finite element discretisations, normal mode transformation, blade/hub loads, and the coupled trim. A description of the trailing-edge flap actuation control law was also given, which allowed for flap deflections at the 3/rev, 4/rev, and 5/rev harmonics. The authors aimed to achieve optimal vibration reduction of the 4/rev hub loads and at the same time limiting the flap deflection to $\pm 6^o$. The blade was split into sections using basic 2D blade element theory. The flaps were to be located at the outer span of the blade ($R > 80\%$). For each flap to be modelled, a section was used where the aerodynamic properties were altered to account for the flap properties. Results showed that compared to the baseline case, the maximum vibration reduction obtainable was 72% at the Pareto optimal control point. Also, results showed that multiple flaps require much smaller deflection angles and, therefore, less actuation power compared to single flap configurations for the same level of vibration mitigation (in accordance with Depailler and Friedmann [51]). Further, it was shown that locating more than four flaps at the blade tip region was unlikely to yield better performance.

Maughmer *et al.* [57] looked to utilise miniature, deployable Gurney flaps, or MiTE's (Miniature Trailing-Edge Effectors), on rotors to improve performance. They are placed inboard and deployed both in hover and on the retreating-side of the disc in forward flight.

The investigation was conducted using an indicial code, ROTOR, which is based on the Beddoes indicial method [44]. The effect of the Gurney flaps were included by modifying the Hariharan-Leishman integrated flap model [70]. CFD was used to take into account apparent mass effects due to deploying a Gurney flap by modifying the functions used by Beddoes to approximate the Wagner function. An indicial response function is also generated to account for the height of the MiTE's when the circulatory lift and moment are calculated. The effects of blade stall with respect to lift

are included by utilising the Kirchoff/Helmholtz relationship detailed in Ref. [71]. No corrections for the centre of pressure or the drag is considered. Increases in flight speed of 20% and rotor thrust in hover of 10% were predicted. The MiTE's were indicated to delay retreating-blade stall, but no further explanation was offered.

Both Patt *et al.* [58] and Liu *et al.* [61] investigated the application of an inboard and outboard flap to reduce blade vibrations, BVI noise, and rotor power required using the same RFA model as proposed by Myrtle and Friedmann [38], which was also used in Ref. [51]. Patt *et al.* predicted that both noise and vibrations could be reduced effectively by the dual flap configuration with reductions in noise and vibration achieved. Liu *et al.* predicted that at high advance ratios, power reductions in the range of 4%-6.37% and vibration reductions of 50% were achievable simultaneously by means of both Higher Harmonic Control (HHC) algorithms and, to a lesser extent, non-linear optimisers. Similar vibration reduction improvements using dual-flap configurations were also conducted by Jones and Newman [63] using WHL's R150 coupled with the Hariharan and Leishman indicial flap model [72] on the Lynx helicopter.

1.7 Flapped Rotor Studies Using CFD

As shown previously, the use of reduced-order models in evaluating flapped rotors is fairly common. Research has looked at vibration reduction and BVI noise mitigation fairly extensively. Some work has also looked at enhancing the aerodynamic performance of the rotor. The weakness in most of such methods lies in their dependence on 2D look-up tables for their aerodynamics. Although this data has mostly been based on experimental results, it has been shown that CFD-computed data could also be used to good effect [7, 48], especially for flight conditions where no experimental data exists for certain aerofoils. The advantage of CFD over such models is its ability to accurately predict both blade loads and the flow around the rotor with no other input other than the blade geometry, although at considerable computational expense. Table 1.4 provides a concise list of CFD simulations of rotor blades with trailing-edge flaps.

Standish and Van Dam [73] used 2D CFD to demonstrate the feasibility of using micro-tabs on the lower surface of an aerofoil, in a similar fashion to a Gurney flap, as a means of active load control over the rotor surface as well as increased aerodynamic performance at both subsonic and transonic flow conditions. The solver used was ARC2D which solves the compressible, two-dimensional, RANS equations in strong conservation form. The governing equations are central-differenced in

Simulation					
Ref	*Year*	*Type*	*Code*	*Flaps*	*Compared Data*
[73]	2004	2D NS	ARC2D	1	Active load control via Gurney flaps
[74]	2004	2D NS	FLUENT	1	Performance enhancement
[75]	2004	2D VPM	-	1	Turbine blade load control
[76]	2005	2D NS	-	1	Gurney flap combined with leading-edge droop for dynamic stall control
[56]	2005	2D NS	HMB	1	Dynamic stall control using a NACA 0012 with 25% chord integrated flap
[57]	2005	2D NS	-	-	Modification of Hariharan-Leishman model to account for Gurney flaps
[77]	2005	3D Euler	-	1	BVI noise reduction using an integrated flap
[62]	2006	3D Euler, 3D NS	HMB	1	Evaluation of fixed, slotted flaps for blade twist reduction and hover performance enhancement

Table 1.4: CFD investigations into flapped rotor aeromechanics.

standard second-order form and solved using the implicit Beam-Warming approximate factorisation scheme. The Spalart-Allmaras turbulence model was used for all calculations. Primary to running the tests, the solver was validated against experimental results from the NASA Ames Research Center and showed considerable agreement that warranted the continuation of the analysis.

For subsonic conditions (Re = 1,000,000 and M = 0.2), the University of Glasgow's GU 25-5(11)8 aerofoil section was used. For transonic conditions (Re = 9,940,000 and M = 0.8), the SC1095 aerofoil section was used. Transition was specified at 45.5%c for the GU 25-5(11)8 section. All calculations on the SC1905 aerofoils were performed fully turbulent. All tabs had a fixed thickness of 0.2%c, tab height of 1%c and were placed at 85%c, 90%c, 95%c, and 100%c. Results showed that the deployment of tabs on the lower surface in the vicinity of the trailing-edge is an effective means of lift enhancement. Increases in L/D were also predicted at moderate-to-high lift coefficients for both subsonic and transonic flight conditions. The optimal location of the tab was found to be at the trailing-edge, essentially operating as a Gurney flap. However, the trailing-edge of standard rotor blades do not have enough space to house a deployable tab, hence the optimal flap position would be as far aft as possible where rotor blade volume allowed for housing of the tab. Similar research relating to the application of Gurney flaps on rotary-wing, Micro-Air Vehicles (MAV) can be found in work by Nelson and Koratkar [74]. This is also a precourser to more recent work by Maughmer *et al.* [57] on MiTE's for performance enhancement.

Basualdo [75] considered an integrated, trailing-edge flap to alleviate vibratory loads on wind tur-bines. He used an incompressible, irrotational panel method where the velocities over the aerofoil were computed using Laplace's equation with the Kutta condition applied at the trailing-edge. Once the velocities were known, the pressure distribution over the aerofoil could be obtained using the Bernoulli equation. Unsteady effects were added by considering a varying wind velocity (tip speed was constant), the unsteady Bernoulli equation, and modelling of the wake via Euler integration. A simple structural model was included to account for flapwise and edgewise bending. A PD (pro-portional and differential) controller was implemented to control flap deflections. Although firm values for vibration mitigation were not given, the work clearly lays out the problems associated with vibrations on rotor blades and the potential of an active flap to alleviate them.

Another implementation of a Gurney flap for rotors has been considered by Joo *et al.* [76] who looked at combining them with fixed nose droop to alleviate dynamic stall using 2D RANS CFD. The employed CFD method solves the Navier-Stokes equations using Roe's method for spatial dis-cretisation, with MUSCL interpolation and the Van Albada limiter providing high order accuracy.

The Gurney flap and fixed-nose droop combination was optimised for various tests cases using the following objective function:

$$wt\sqrt{(\frac{C_{l_{max}}}{C_{l_{max-Base}}} - 1)^2 + (\frac{C_{m_{min-Dn}}}{C_{m_{min-Dn-Base}}} - 1)^2} - (1-wt)(C_{m_{\alpha-min-Base}} - C_{m_{\alpha-min}}) \qquad (1.3)$$

(a)   (b)
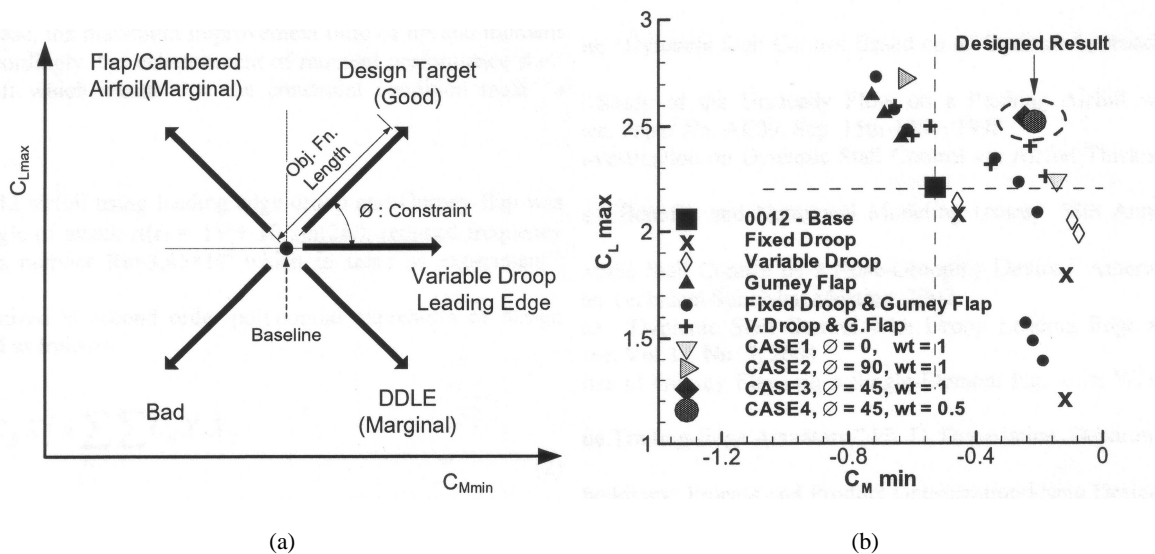
Figure 1.7: Optimising for dynamic stall control. (a) Bousman's Dynamic Stall Function. (b) Optimised result. Taken from Ref. [76].

where wt is a weighting term and looks to achieve the design target as detailed by Bousman's Dynamic Stall Function (see Figure 1.7(a)). The tests cases considered were (1) improving the pitching moments, (2) maximising lift production, (3) improving both of the previous cases simultaneously and, finally, (4) improving both the lift and pitching moments due to dynamic stall and minimizing detrimental effects due to nose droop. The optimum design case was shown to decrease the maximum nose-down pitching moment by 57%, the negative damping area was reduced by 84%, and the lift coefficient was increased by 14%. This was achieved using a fixed nose droop of 21° hinged at 31.25%c with a Gurney flap of length 1.3%c.

There has been almost no research in the open literature with regards to 3D Euler or Navier-Stokes CFD calculations with respect to AFC technology. Yang *et al.* [77] performed 3D Euler calculations for an active flap study into BVI noise reduction. The rotor geometry was based on the AH1-OLS, which had a tip Mach number of 0.664 and zero twist. An overlapped grid system was used for simplicity to combine three separate grids. The first, the rotor blade grid, contained 271,825 points. The second, the inner background grid, contained 14,400,000 points to contain the vorticity and the entire helicopter geometry (rotor, fuselage, tail rotor). The spacing in this grid was equivalent to 5% of the blade chord, which limits the number of cells that can be concentrated in the vortex core. The third and final grid, the outer background grid, consisted of 321,293 points for a total grid size of approximately 15,000,000 points. The rotor grid was allowed to articulate in pitch, flapping, and lead-lag. Calculations were run with a freestream velocity of 20.1 m/s, a rotor rpm of 600 (approximate $M_T = 0.19$), and zero degrees of cyclic pitch and shaft tilt angles. A single integrated, trailing-edge flap with spanwise length, 18%R, and chordwise length, 25%c, was located at 89% of the blade span, and was actuated twice per revolution with an amplitude of 6°. Each rotor revolution was divided into 4800 incremental steps, which is effectively 0.075^o per unsteady step. Results showed that the flap was most effective the closer it was to the blade tip and any interactions between the tip and flap-edge vortices were negligible in terms of increased BVI noise.

1.8 Rotor Experiments for CFD Validation

Tables 1.5 and 1.6 list all documented 2D and full-rotor experimental testing conducted on rotor blades with trailing-edge flaps. This includes testing for vibration mitigation, BVI noise reduction, and performance enhancement. For each reference, the rotor and flap configurations are given as well as a brief description of the experiment. Experimental data is crucial when dealing with reduced-order models and CFD as they allow for the validation of computational predictions. Al-

though there is a wide amount of data available for 2D and 3D validation of clean rotors, there is very little concerning scaled or full-scale flapped rotors. Of the data that is published, the only suitable work for 3D CFD validation for performance enhancement is that of Noonan *et al.* [16], which will be discussed thoroughly later.

1.8.1 2D Experiments

Table 1.5 lists the most recent 2D experimental tests undertaken with respect to aerofoil/blade sections with flaps. A brief review of these experiments follow. The majority of the experiments on ABC technology that have been conducted to date have involved mainly plain flaps, slotted flaps, and servo-flaps. However, as described by Kentfield [78], the Gurney flap is an option for increasing the aerodynamic performance of the rotor blade as well. To obtain a gauge of Gurney flap performance potential, Gai and Palfrey [79] conducted experiments on a NACA 0012 aerofoil using both solid and serrated Gurney flaps (both fixed). The Gurney flap heights were 5% of chord with the depth of the serrated Gurney 2.5% of chord. Tests were run at Reynolds numbers of 1.56×10^5 and 2.16×10^5 with fixed transition. Results show that compared to the baseline values, $C_{l_{max}}$ increased by 80% and 65%, α_s decreased to 8° (from 10°), and α_0 decreased to -6° and -4.5^o (from 0°) for the solid and serrated flaps, respectively. Serrated Gurney flaps also produced slightly less drag than the solid Gurneys. Both flaps gave higher C_l at lower α than baseline and at a slightly lower lift-to-drag ratio, L/D. Results also showed a large change in C_l for small change in L/D and a significant nose down pitching moment was evident. However, it should be noted that from Ref. [30], the height of a Gurney flap should be no larger than the boundary layer, which could be why these tests had a small effect on L/D.

Similarly, Chandrasekhara *et al.* [80] looked at using Gurney flaps to improve dynamic stall performance by combining it with a Variable Droop Leading-Edge (VDLE). The concept considers VDLE for inhibiting the shedding of the dynamic stall vortex. Reducing the sharp pressure gradients and suction at the leading-edge by redistributing lift across the rest of the aerofoil means that a higher α is achievable before stall occurs. However, with the reduction in drag and nose-down pitching moment, there is an associated loss in lift also. To recover the loss in lift, a Gurney flap was implemeneted.

The experiments were carried out in the NASA Ames Compressible Dynamic Stall Facility in a 10 x 14 foot squared wind tunnel that allows for speeds of up to Mach = 0.5. The assembled VDLE

aerofoil can be found in Figure 1.8(a). Three Gurney flap heights were considered namely 0.85%, 1.35%, and 2.4% of the blade chord. The VDLE was hinged at the centre of rotation, c/4, with angles of 0°-20° considered. Further details of the experiment can be found in Table 1.5. Results demonstrated that the combination can be sucessful in reducing drag and nose-down pitching moments, but still be effective in producing lift. The optimum configuration at the stated flow conditions was the 1%c Gurney flap with the VDLE. At low angles of attack, lift was improved with $C_{l_{max}}$ preserved, but with a 55% reduction in C_d and a 38% reduction in nose-down pitching moment.
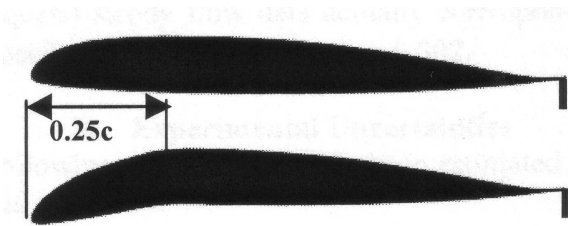
(a)

Figure 1.8: VDLE and Gurney flap combination for dynamic stall alleviation. (a) The VDLE aerofoil. Taken from Ref. [80]. (Poor quality original.)

Although Gurney flaps do offer potential, the current work looks to consider only integrated and slotted flaps since without VDLE the moment penalty is too high. Hassan *et al.* [81] experimentally tested plain flaps for overhand effects. This involved examining the effect flap overhang had on the sectional performance of a rotor blade in both subsonic and transonic conditions. This is a culmination of previous research by Hassan and Straub [83] and Hassan *et al.* [84].

Wind tunnel testing was conducted on HH-06 and HH-10 aerofoils. The HH-06 was designed for the tip region of a rotor and has a trailing-edge tab of 10%c set at 0°. The HH-10 was designed for the main portion of a rotor blade and has a trailing-edge tab of 4%c set at -1°. Both sections were considered with an integrated, trailing-edge flap of 25% chord with the flap overhang. This was the distance from the flap pitch axis and flap leading-edge and it was varyied from 30% to 45%. Pressure taps were located along the sections to evaluate the integrated loads, with the total lift, drag, c/4 moment, and the lift and moment about the flap pitch axis recorded for Mach and Reynolds numbers ranging from 0.2 to 0.95 and 4 million to 9 million, respectively. Sectional angles of attack were varied from -4° to 14° and the trailing-edge flaps were fixed at deflection angles between -8° and 8°. The authors concluded that flap overhang increased the hinge moments created by the flap, which can lead to increased actuation power requirements. However, it had little effect on the lift-curve slope and lift of the blade sections. Thicker flap thickness ratios were capable of reducing hinge

2D Flapped Blade Data									
Ref	*Year*	*Section Profile*	*Mach*	*Re*	*k*	*α* (^{o})	*Model Span* (inches)	*Model Chord* (inches)	*Flap Chord/ Height* (%c)	*Other*
						Description of Experiment			
[79]	2003	0012	0.03-0.15	1.56-2.16x10^5	0	-6°-10°	17.91	5.12	5%	Serrated Gurney
Normal and serrated Gurney flaps are considered for aerodynamic performance enhancement.										
[80]	2004	VR-12	0.2-0.4	0.7-1.6x10^6	0-0.1	10°±10°	10	6	0.85%-2.4%	Droop: 0°-20° at c/4
Evaluation of leading-edge droop and Gurney flap combination for dynamic stall alleviation.										
[81]	2005	HH-06/10	0.3-0.8	2.7-5.7x10^6	0	0°-14°	13	8	25%	Overhang: 30%-40%
Investigation into flap overhang aerodynamics with integrated, trailing-edge flaps.										
[82]	2006	0015	0.03	1.65x10^5	0.233	15°±10°	15	10	25%	δ: ±7.5^o,±15°
Investigation into upward and downward flap deflections to reduce negative dynamic stall moments.										

Table 1.5: 2D experiments for flapped rotor sections available in open literature.

moments and improving lift capability at high angles of attack. Shock waves were seen to appear
at the overhang at transonic speeds downstream from the main shocks, which resulted in increased
wave drag. Finally, the pitching moment uniformity was seen to have a nonlinear variation with flap
overhang percentage.

The most recent 2D experimental tests on flapped aerofoils was by Gerontakos and Lee [82], who
looked to alleviate the nose-down pitching moments associated with dynamic stall by pulsing an
integrated, trailing-edge flap up or down. Similar work can be found in Ref. [56]. A NACA 0015
was fitted with a 25%c flap and various flap deflection profiles were considered. See Table 1.5 for
further details on the experimental setup. They reported that upward flap deflections were capable
of reducing the nose-down pitching moments associated with dynamic stall, by introducing a low
pressure region on the lower surface of the aerofoil, near the region of the flap hinge. An increase in
flap deflection angle was shown to improve results. The performance of the downward flap deflec-
tion was shown to have no effect on performance, although the pitching angles remained the same.
As described in Ref. [56], for a downward flap deflection to be beneficial, it must be combined
with a lower mean pitching angle. They concluded that the flap should be actuated between the stall
angle and the maximum angle of attack during pitch-up, with a duration of half the cycle time and
flap deflection magnitude of greater than 60% of the maximum angle of attack.

1.8.2   3D Rotor Experiments

Table 1.6 lists the most recent full-scale 3D rotor tests with AFC technology. A short review of
these experiments follow. The first published data on a flapped rotor blade was conducted by Lem-
nios and Howes [10] for the Controllable Twist Rotor (CTR) designed by the Kaman Aerospace
Corporation. Improvements to this design were made with the Multicyclic Controllable Twist Rotor
(MCTR) [11], which included higher harmonic deflections for reduced vibratory and control loads.
The concept requires a torsionally soft blade that allows for blade warping via external moments.
Primary pitch control was supplied by a standard pitch-horn at the root. External moments were
then introduced by a servo-flap that, by introducing blade torsion and hence changing the effective
α along the blade, altered the lift distribution. By changing the blade twist, the local inflow velocity
could be optimised and as a result improved rotor performance could be obtained. The servo-flap
was summarised as inducing 0.5^o of change in the local angle of attack per 1° of flap deflection. The
experiment looked to validate the concept using a conventional blade, namely the H-34, for which
experimental results were already available. The original blade, the H-43, was increased in length

by 3 feet (28 feet in total), and a standard servo-flap was placed outboards. No geometry was given for the servo-flap. Testing was conducted at a tip Mach number of 0.524 at advance ratios of 0.23, 0.345, 0.382, and limited results at 0.45. Longitudinal and lateral cyclic flapping was kept to zero. The proof-of-concept test demonstrated that rotor stall could be avoided at all test conditions. This allowed for up to 20% higher blade loadings before retreating-blade stall was encountered. Some whirl-tower test data was published with negative flap deflections (flap up) of -4° and -8° used with a linear decrease in hover performance exhibited.

Results of a wind tunnel investigation on the effect AFC has on BVI noise, vibration reduction, and rotor performance improvement were presented by Dawson *et al.* [22]. The three objectives of the investigation were, firstly, to perform an aeroacoustic investigation into BVI noise reduction. Secondly, to investigate the performance characteristics of an active flap rotor with a 2/rev flap deflection. Finally, to test for vibration reduction with N/rev flap deflections. A 1/7th-scale, two-bladed BELL AH-1G OLS model rotor system was used. The NACA 0015 section was chosen with blade dimensions R = 72.75 in, c = 5.25 in, with 9° of blade twist. The hover tip Mach number was 0.619. There was one flap per blade and each had a spanwise length of 17.9%R, chordwise length of 25%c, and was located at 79.4%R. Previous analysis by CAMRAD/JA [85] detailed that 2/rev flap deflections would have the best effect on rotor performance and 3, 4, and 5/rev harmonic flap deflections would have the best effect on reducing vibratory loads. All actuation schedules were open-loop with no feedback control.

Cams were manufactured for each objective. For BVI noise reduction testing, the flap deflection magnitudes were 12.5^o, 17.5^o, and 20°. For performance improvement, the flap deflection magnitudes were 3° and 6°. Finally, for vibration reduction, the flap deflection magnitudes were 2° for the 3/rev harmonic and 4° for the 5/rev harmonic. Strain gauges were mounted at r/R = 0.32 and 0.70 to measure flapwise bending, chordwise bending, and torsional moments. Pressure transducers were placed at x/c = 0.03 and r/R = 0.752, 0.821, 0.911, and 0.970. The baseline test matrix for the acoustic data was obtained by a shaft sweep from $\alpha = 0^\circ$ to 10° to locate the point of maximum BVI noise. C_T / σ and M_T were kept constant and rotor and tunnel conditions remained generally stable. Tests conditions were listed in the report and included testing over a range of μ, C_T / σ, and χ, with phase adjustments for forward flight.

The results of the tests showed reductions in the 4/rev, 5/rev, and 8/rev vibratory loadings with up to 76% reduction at $\mu = 0.30$ and $C_T = 0.0653$. CAMRAD/JA predicted that performance im-

							Full-Scale Flapped Rotor Data						
Ref	*Year*	*Rotor*	*Scaling* (M=Mach, F=Froude)	*Blade Radius* (feet)	*Blade Chord* (inches)	*Blade Twist* (deg.)	σ	M_T	*Flap Span* (%R)	*Flap Chord* (%c)	*Flap Location* (%R)	*Flap Frequency* (per rev.)	*Flap Angle* (deg.)
						Description of Experiment							
[10, 11]	1977	H-34	M	28	16.4	6.6^o	0.062	0.524	-	-	-	Various	$\pm 6^o$
Wind-tunnel tests of the Kaman Controllable Twist Rotor at NASA Ames.													
[22, 86]	1995	0015	M	6	5.25	9°	0.0919	0.619	17.9%	25%	88.35%	2,3,5	$\pm 2^o$-20°
Proof-of-concept tests for a rotor with a plain flap oscillating at higher harmonics to reduce vibrations, BVI noise, and improve performance.													
[87, 88]	1997	V-22	F	7.6	5.01	0°	-	0.27-0.33	45.4%	11%	-	3	$\pm 3^o$
Active flaperons on a scaled V-22 rotorhead for vibration reduction.													
[89, 90]	1998	0012	M	3.75	3.4	0°	0.048	0.267	12%	10%	75%	1-5	$\pm 5^o$
Vibration reduction tests using a plain flap oscillating at higher harmonics in hover and forward flight.													
[16]	2001	HIMARCS I	M	4.7	4.5	8°	0.101	0.627	15%	-	90%	-	3°
Application of high-lift devices on rotors to reduce induced power in hover and forward flight.													
[23, 91, 92]	2002	0012	F/M	5	3	0°	0.1273	0.45	8%	20%	75%	1-5	$\pm 2^o$-4.5^o
Vibration reduction proof-of-concept tests of a rotor with a plain flap in forward flight.													

Table 1.6: Experiments for full-scale flapped rotors available in open literature.

Full-Scale Flapped Rotor Data														

Ref	$Year$	$Rotor$	$Scaling$ (M=Mach, F=Froude)	$Blade$ $Radius$ (feet)	$Blade$ $Chord$ (inches)	$Blade$ $Twist$ (deg.)	σ	M_T	$Flap$ $Span$ (%R)	$Flap$ $Chord$ (%c)	$Flap$ $Location$ (%R)	$Flap$ $Frequency$ (per rev.)	$Flap$ $Angle$ (deg.)
						Description of Experiment							
[26, 93]	2002	EC145 rotor	-	18.04	12.8	12°	-	-	5.33%	15%	69%-85%	1-5	$\pm10^o$
Wind-tunnel and whirl tower testing of the OA rotor with active flaps for vibration reduction.													
[17]	2004	AH1-OLS	M	3.14	4.09	7.55^o	-	0.51	0%-70%	25%	89%	Fixed	5°-20°
Experiments conducted to reduce BVI noise in low-speed descent by using inboard, split flaps. See Section 1.6.													
[94]	2004	0012	M	3.28	4.724	-	-	0.188	18%	20%	89%	2	$\pm3.8^o$
Application of an active tab to BVI noise reduction in low speed flight.													
[95]	2006	ABC Blade	M	6.89	5.512	-	-	0.527	10%	15%	69%-90%	2-5	$\pm2.3^o$
Wind-tunnel tests of the ONERA ABC blade with active flaps for BVI noise and vibration mitigation.													
[18]	2006	EC145 rotor	-	18.04	12.8	12°	-	-	5.33%	15%	72%-83%	3-5	$\pm10^o$
First flight test results of AFC for vibration reduction on a BK117 with EC145 main rotor.													

Table 1.7: Experiments for full-scale flapped rotors available in open literature (continued).

provement was achievable via 2/rev flap deflection at high thrust ($C_T = 0.009$, $\mu = 0.25$) and high speed ($C_T = 0.008$, $\mu = 0.4$). Unfortunately, the performance evaluation in the experimental investigation proved inconclusive, as the improvements were predicted to be smaller than the resolution of the rotor balance. Aerodynamic and acoustic data supported the data trend of tip vortex mitigation due to flap deflection. BVI noise reduction via flap deflection was seen to be dependant on the peak deflection angle and the azimuthal shift in its actuation schedule, and was often accompanied by an increase in low frequency harmonic noise and high frequency broadband noise. Further analysis of the results can be found in Ref. [86].

The use of AFC technology was also considered for the V-22 rotor blades. Settle and Nixon [87, 88] wind tunnel tested the Multipoint Adaptive Vibration Suppression System (MAVSS) that would be used to control flaperons at the trailing-edge of the V-22 rotors. Testing was conducted using a Froude-scaled rotor at conditions listed in Table 1.6. Both open-loop and closed-loop 3/rev flap oscillations were tested at cruise speeds with flap authority of $\pm 3^o$. The optimiser was able to identify the vibrations and trim the flap to reduce them by a factor of 5. Better performance was possible when optimising for a single control point, rather than attempting to reduce vibrations using multiple higher harmonics.

Fulton and Ormiston [89] also looked at reducing blade vibratory loads in both hover and forward flight using a single, active flap per blade. The experimental setup included a 7.5 foot diameter, untwisted, 2-bladed, hingeless rotor with a tip speed of 298 ft/sec (approximately M = 0.267). The blade section profile was the NACA 0012 from root to tip. One flap was located on each blade with spanwise length of 12%R, chordwise length of 10%c, and located at 75%R. The actuation mechanism was a biomorph, bender beam cantilevered at the rear of each blade spar [90]. Vibration reduction at advance ratios from 0.1 to 0.3 at rotor speeds of 450 RPM and 760 RPM was investigated. Only the mitigation of vibrations from single, flap harmonics was attempted.

The tests demonstrated that vibration reductions of the 3/rev, 4/rev, and 5/rev harmonics were indeed possible via active flaps. However, in certain cases, higher harmonic vibratory loadings than that of the flap frequency, infact, increased. Results did suggest, however, that flap actuations at multiple higher harmonics would be effective at tackling multiple, harmonic blade vibrations. Also, due to the open loop control system, vibration reduction was not as effective as one would expect with a closed loop system since there is no optimisation, hence no assurance that the flap is always improving on the baseline loads and not, infact, deteriorating performance. Interestingly, there was

some evidence to indicate that elevon reversal was occurring at high advance ratios, which has been an issue for more recent tests by ONERA [95].

Koratkar and Chopra [23] is a highly detailed paper that builds-on previous work done by the authors on flapped rotor wind tunnel testing [91, 92]. The smart rotor model consisted of a NACA 0012 blade section with a trailing-edge flap of spanwise length of 8%R, chordwise length of 20%c, and located at 75%R. Tests were run at 1800 RPM with a tip Mach number of 0.45. The 8-layered, tapered piezoelectric bender from previous work was used to deflect the flap once again (see Figure 1.9). The actuator was designed for soft in-torsion to optimise the control authority of the flap. Vibration reduction capability is known to depend mainly on the 3/rev, 4/rev, and 5/rev excitation frequencies when a four-bladed rotor is considered. To maximise vibration suppression, therefore, the blade first torsional and flap-wise bending moments were placed close to the rotor 3/rev and 5/rev harmonics. Open-loop, closed-loop, and neural-network controlled tests were performed.
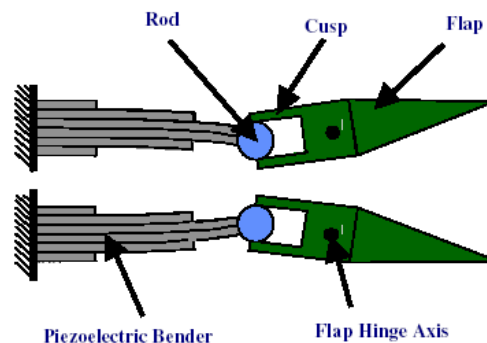
Figure 1.9: Diagram of the flap to actuator connection. Taken from Ref. [23].

Initial tests confirmed that advance ratio and collective pitch have little effect on actuator performance. Excellent suppression (over 89%) was demonstrated for the 4/rev vibratory rolling and pitching momenta at various advance ratios and collective pitches. Also, the blade root, flat-wise bending moment was seen to reduce by 80% at 3/rev and 40% at 5/rev, with the trailing-edge flaps deflecting by 4.5^o and 2° in each case.

As part of the ADASYS research project, Enenkl *et al.* undertook flight testing of a main rotor with trailing-edge flaps based on previous IBC testing [26]. A review of the development of the full-scale rotor based on the previous system is offered in [93]. The report states that for BVI noise suppression and stall delay on the retreating blade a 2/rev flap input is required, whereas vibration reduction of four-bladed rotors is dealt with by 3, 4, and 5/rev excitations. The baseline rotor has in-

board tapering and features a swept-back parabolic tip. The flap system consists of three, 0.3m flaps located side-by-side at radial stations from 3.8m to 4.7m, with flap chordwise length of 15%c and total spanwise length of 16%R. Optimum response of the flap is noted to occur when the blade torsional frequency is near the envisaged harmonics [91]. For this reason, the blade torsion frequency was lowered from 4.9/rev to 3.4/rev. The performance improvement was confirmed by analytical predictions obtained via the CAMRAD II simplified aeroelastic model. As well as ground testing to validate the performance of the PZT actuator system, whirl tower testing of a 2-bladed configuration of the ATR rotor with ABC technology was conducted. The tests were completed at a nominal rotor speed of 450 RPM and collective pitch settings of up to 8°. Dynamic tests consisted of the flaps being run at various amplitudes with frequencies of up to the 6/rev harmonic.

Noboru *et al.* [94] took a novel approach to using active flaps by having a slim deployable tab at the trailing-edge of the rotor that, when desired, could be slid out and actuated. The design has advantages over the standard plain flap design such as its ability to be located in the blade planform and low power requirements. However, the design is disadvantaged since the lifting area of the tab is half that of a normal plain flap. A rectangular blade that consisted solely of NACA 0012 sections was tested with the deployable active tab located at 80%-98%R, oscillating at 2/rev with a amplitude of 3.8^o. The maximum noise reduction capability of the design was around 2 decibels, which is small compared to similar predictions [47, 58] and wind-tunnel tests [95].

More recently, Crozier *et al.* [95] conducted wind-tunnel experiments of a model rotor with active flaps for vibration reduction. The work formed part of a collaboration project between ONERA, Eurocopter, DLR, and Eurocopter Deutschland into AFC technology. The model rotor had three small flaps of 7%R each located outboard from 69%-90%R. Initial test results identified a problem with elevon reversal when the flap was operated at high advance ratios. However, reducing the tip speed and maximum advance ratio eliminated this effect, although the maximum flap deflection angle was limited to $\pm2.3^o$. Using a 4/rev flap actuation of magnitude 1.8^o, BVI noise was reduced by 1.2 dB. Increasing the flap magnitude to 2.2^o more than doubled the noise reduction effectiveness (-2.7 dB). The primary purpose of the experiments, however, were to test for vibration reduction effectiveness. Tests looked to reduce the 4/rev vertical shear force by using 1/rev to 5/rev open-loop flap inputs. These results showed that reductions in vibrations of up to 9% could be achieved depending on the actuation and azimuthal angle. Interestingly, however, similar increases in vibrations were also evident at other azimuthal angles. By applying an optimiser to the 4/rev component, overall reductions in the 4/rev vertical shear force of around 20% were achieved within 5 rotations.

Finally, Roth *et al.* [18] presented results for full-scale, in-flight AFC technology testing on a BK117 for vibration reduction, which follows on from work by Enenkl *et al.* [26]. Diagrams of both the ADASYS blade during whirl tower testing and full-scale flight tests can be found in Figure 1.10. Open loop investigations gave similar results to those reported in Ref. [95, 22] with effectiveness dependent on the azimuthal position. Closed-loop tests were much more promising with the 4/rev rolling moment, pitching moment, and vertical hub forces all showing reductions of up to 80% with the flap plus controller turned on at 100% rotor speed and 100 knots flight speed. Similar reductions were achieved with the 4/rev gearbox vibrations, cabin vibrations, and at slow climb/descent. Although the flight tests were short, the actual reductions in vibration levels were noticeable by the pilot and welcomed. However, considering the elevon reversal issues suffered by previous wind-tunnel tests [95, 89], it would be interesting to see how this project will develop when higher advance ratios are attempted.

1.8.3   The HIMARCS I Experiment

Noonan *et al.* [16] undertook a series of experiments at the NASA Langley Research Center to evaluate the aerodynamic effects of leading and trailing-edge devices on the HIMARCS (High Maneuverability and Rotor Control System) I rotor blade. The report considered slotted devices to increase both the lift and stall boundaries of current rotor blades for performance enhancement in both hover and forward flight.

Figure 1.11 details the blade geometry, twist distribution, as well as the ARES experimental test bed. As can be seen from Figure 1.11(a), the baseline HIMARCS I rotor consisted of two main blade sections: the RC(4)-10 from blade root to 80% span, transition between 80%-85% span, and the RC(6)-08 from 85% to the blade tip. See Noonan [96, 97] for more detail on the development of the RC(4) and RC(6) series blade sections. A total of 7° of linear twist from root to tip can be seen in Figure 1.11(b). Four configurations were tested including a -6° slat, -10° slat, 3° slotted, trailing-edge flap, and the baseline rotor with all high-lift sections being located at the blade tip ($85\% < R < 100\%$). An example of the full blade with the 3° slotted flap can be found in Figure 1.11(c). Data was obtained in hover and forward flight at advance ratios from 0.15 to 0.45. The hover tip Mach number was 0.627. Tunnel wall effects were assumed to be negligible, although as can be seen from Figures 1.11(d) and 1.11(e), the wall distances are quite close for hover testing. Lift, drag, and torque coefficients were recorded from an average of 5000 data samples taken at

a rate of 1000 samples/sec with a filter cut-off at 200Hz. Pitch-link loads were normalised to the largest pitch-link oscillatory load measured, and all 4/rev loads and moments were normalised to the 4P fixed-system force or moment generated by all tests.

Results showed that the slat configuration in forward flight provided benefits at advance ratios of 0.25 and over and for higher lift coefficients ($C_T > 0.007$), whereas the baseline model was more beneficial at lower C_T (< 0.007) and advance ratios. The leading-edge slat performance benefit could possibly be attributed to the nose-up moment induced in forward flight, which effectively reduces the amount of blade twist. The performance at higher blade loadings is also probably due to the higher collective at the tip, since the slat has the effect of delaying stall. The trailing-edge flap configuration was very close to the baseline results with the 10° slat giving the lowest values of them all. With regards to loads, the flap configuration showed the greatest suppression of pitch-link and 4/rev loads, with the baseline rotor suffering the greatest loadings of all the configurations. However, it is to be seen whether such a small flap deflection could ever offer performance benefits in hover and forward flight, as sought by the authors.

(a)   (b)

Figure 1.10: Flight tests of AFC for vibration reduction. (a) Whirl tower equipped with AFC blade. (b) BK117 in-flight with AFC blades. Taken from Ref. [18].
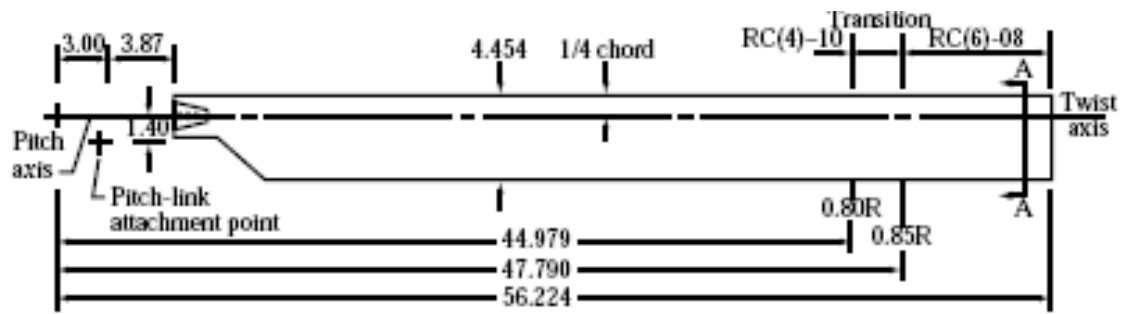
(a)
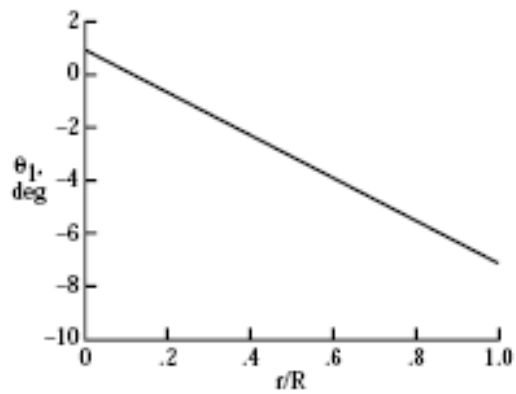
(b)

(c)
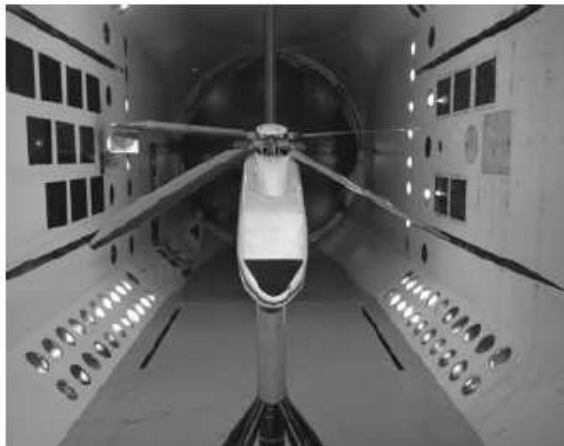
(d)
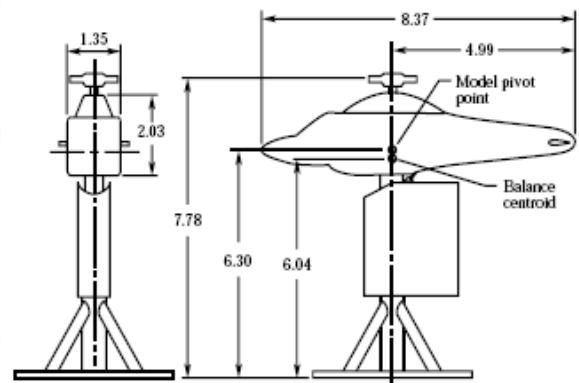
(e)

Figure 1.11: The HIMARCS I rotor experiment. (a) HIMARCS I geometry. (b) Twist profile. (c) Slotted flap viewed from below. (d) ARES test bed. (e) Schematic of the ARES test bed. Taken from Ref. [16].

37

1.9 Thesis Objectives

To date, research into flapped rotors has been undertaken to a large extent with reduced-order models. These have allowed issues involved with vibration levels and BVI noise to be evaluated with flapped rotors, although the accuracy of the methods is still not reliable. CFD offers increased accuracy and detailed flow physics due to its predictive nature. The coupling of CFD and models has been shown to be effective for improving rotor performance and vibration prediction [7, 8], and it has also been utilised for flapped rotors [48, 56, 57, 62] with good effect. However, there is a severe lack of 3D CFD data on flapped rotors.

The majority of flapped rotor research has looked at obtaining the 'jet-smooth ride' for rotorcraft by attempting to reduce hub vibrations and BVI noise. No 3D viscous CFD on flapped rotors has to date been published. However, these problems require large grids, high computational power requirements, and special mesh treatment such as overset grids [94]. Full-scale rotor experiments have also concentrated on vibration and BVI noise reduction. However, Noonan *et al.* [16] took a different perspective. They considered the application of high-lift devices on low-twist rotors for hover performance improvement. Although some improvements were evident from the leading-edge slat devices, the trailing-edge flap design actually performed worse than the clean blade. Therefore, the primary aim of this research looks to:

1) Consider the application of trailing-edge flaps on low-twist rotors for hover performance improvement. Blade twist improves hover performance by allowing the lift to be distributed move evenly along the blade span. The subsequent reduced tip loading reduces induced power requirements and improves rotor performance. However, large amounts of twist at the blade tip can deteriorate performance on the advancing blade in forward flight due to local compressibility effects.

2) Combine a reduced order aeromechanical model for rotorcraft analysis with 2D CFD to evaluate the flapped rotor concept. The combination of both methods will allow for a comprehensive analysis of a hovering rotor's performance with slotted, trailing-edge flaps. Optimum designs can then be identified from a parametric study and evaluated further.

3) Verify the results of 2) by evaluating the optimum designs using 3D Euler and RANS hover calculations. The CFD can then be fully exploited to evaluate the performance of the hovering flapped rotors using flowfield data and confirm the validity of the concept.

The secondary aim of this research is to:

1) Evaluate the predicted trim settings of the model by comparing to 3D CFD trim predictions. This particular solver has a built-in hover trim functionality that will automatically alter the trim settings to obtain a specified thrust setting. Both methods are compared by using similar trim algorithms to generate required blade collective and coning angles for hover. For the 3D CFD, these initial calculations are performed using solely 3D Euler CFD to reduce computational times. The trim settings predicted using both methods are then implemented using 3D RANS CFD and comparisons are made to evaluate the effectiveness of the reduced-order model.

2) Blended flaps are then considered using trim settings predicted by the 3D inviscid CFD trimmer using fine grids. The blended flap is a simpler design and allows for a multiblock topology consistent for both clean and flapped rotors.

1.10 Thesis Outline

Chapter 1 provides an introduction to the area of research. An extensive literature survey is presented, covering flapped rotor research with reduced-order models including modelling the flap, 2D and 3D CFD, and both scaled and full scale experimental work. Chapter 2 details the mathematical models used in the thesis. These include blade-element theory, helicopter aeromechanical modelling, CFD methodology, and post-processing techniques. Chapter 3 offers validation for the 3D hover CFD used in this work, including lifting and non-lifting rotors, rotors with complex planforms, and the HIMARCS I rotor. Chapter 4 presents results from a comprehensive parametric study using a combined 2D CFD and blade element method. The study looks at enhancing the performance of the HIMARCS I rotor by evaluating the effects of deploying various slotted flap configurations on the blade. Chapter 5 consists of 3D hover results that verify the designs selected in the previous chapter. Also, the accuracy of the reduced order model's aerodynamics are considered along with the design time, by comparing against similar 3D inviscid calculations using a built-in CFD trim routine. Chapter 6 presents the main conclusions of the work including potential branches of research for the future. The bibliography follows Chapter 6. Appendix A presents x-y plots of the aerodynamic parameters used in this work. Appendix B presents the results of the parametric study conducted using the blade element method.

Chapter 2

Mathematical Modelling

The following chapter provides the mathematical theory upon which the methods used in this research are based on. This includes the elaboration of the blade-element method, the 3D CFD solver, the helicopter rotor trimming algorithms, and the post-processing techniques. The two methods used for all the calculations in this research are described below. They are a blade element method that is used to approximate the blade loadings experienced on a helicopter in hover, and CFD which is used to verify both the blade loadings and the optimisations performed using the reduced-order model.

2.1   Blade Element Method

The reduced-order model utilised in this research is based on the blade element method [1], which is widely used in the modelling of wings and rotors and is the same model used in the work by Beedy [98]. It allows for the simplification of the 3D rotor problem to reduce computational times by relying on 2D sectional aerodynamic look-up tables. Time-dependency via indicial methods [65] and 3D wake effects can introduce further accuracy by accounting for boundary layer lag and tip vortex convection. Finally, the modelling of separated flow and compressibility can be introduced by implementing models such as the Leishman-Beddoes dynamic stall model [71].

The blade element method described hereon is used for the calculation of rotor loads whilst in hover. Hover, for reasons of simplicity, can be considered a steady-state problem where the inflow velocity along a blade at a single time step remains constant around the rotor disc. In reality, helicopters have to deal with gusts, side-winds and the blade loads may be required to vary by re-trimming the blades, but this is outwith the scope of the current research. For the present method, the rotor blade model is considered 2D having both a spanwise and chordwise length. It is then discretised

into N number of 1D sections along the blade span. Each 1D section requires both geometric and aerodynamic data to be supplied as input. Aerodynamic data is provided at Mach numbers ranging from 0.3 to 0.9 and include sectional zero-lift angles, stall angles, lift-curve slopes, as well as pre- and post-stall behaviour with a total of 19 parameters required. The necessary geometric data includes information regarding the radial variation of chord, twist, and sweep. For each time step, the local loading is calculated at each radial element for a given azimuth, followed by integration and progressive stepping through the azimuth range.

2.1.1 Attached Flow Model

The attached flow model used in this work is based on indicial methods developed by Tom Beddoes [65]. Although this work concentrates on an idealised hover (steady-state), it is necessary to include the formulation of the indicial method since the blade load predictions are still calculated via these attached and separated flow models. Since hover is a steady-state case, the initial and final indices are one time step away. The replacement of the indicial outcome with a simple look-up of the stall angle calculated out of CFD computations has no difference to one step of the indicial algorithm, which was used since it was already implemented. The Beddoes model for attached flow implements time-lag effects for pitching aerofoils by introducing an effective angle of attack that is less than the actual angle of attack. The effective angle of attack or α_E is obtained by introducing a lift decay function that is based on an exponential approximation to Wagner's function [99]. The Prandtl-Glauert factor ($\beta^2 = 1 - M^2$) is also introduced to account for compressibility effects [100]. With the aerofoil angle of attack now modified for boundary layer lag and compressibility, the effective angle of attack can then be used to calculate C_l using the lift-curve slope of the aerofoil.

The first step is to obtain the equation to calculate the lift of a blade section due to circulatory effects. Assuming the blade is pitching upwards, for an increase in circulation due to a step increase in angle of attack there is an equal amount of circulation shed into the wake. This is given by $w = U sin\alpha \doteq U\alpha$, where w is the shed velocity of the wake, U is the freestream velocity, and α is the aerofoil angle of attack.

Assuming that there is a finite velocity at the trailing edge, the circulatory lift is given by:

$$L(S) = 2\pi b \rho U w \phi_C(S) \tag{2.1}$$

$$= 2\pi \frac{c}{2} \rho U U \alpha \phi_C(S)$$

$$= 2\pi \alpha \left(\frac{1}{2} c \rho U^2 \right) \phi_C(S) \tag{2.2}$$

where α is the blade section angle of attack, c is the blade chord, ρ is the fluid density, U is the freestream velocity, and $\phi_C(S)$ is Wagner's function. S is the time non-dimensionalised by the freestream velocity and the blade semi-chord:

$$S = \frac{2Ut}{c} \tag{2.3}$$

Now, by simply dividing through Equation 2.1 by the middle terms we can obtain the non-dimensional lift coefficient, $C_l^C(S)$:

$$C_l^C(S) = \left(\frac{L}{\frac{1}{2} \rho c U^2} \right) = 2\pi \alpha \phi_C(S) \tag{2.4}$$

The Wagner function is approximated here by means of exponential functions modified using pre-determined constants. For lift, the approximation to Wagner's function is defined as:

$$\phi_C(S) = 1 - \sum_{i=1}^{n} A_i^{-b_i S} \tag{2.5}$$

The coefficients A_i and b_i can be obtained from Table 2.1.

Ref	A_1	A_2	A_3	b_1	b_2	b_3
[101]	0.165	0.335	-	0.0455	0.3	-
[102]	0.3	0.7	-	0.14	0.53	-
[65]	0.165	0.335	0.5	0.0455	0.3	0.8/M
[41]	0.2048	0.2952	1	0.0557	0.333	0.5

Table 2.1: Constants for approximating Wagner's function.

The constants, A_n, define Wagner's function for application to the lift coefficient and the constants, b_n, define Wagner's function for application to the pitching moments. Compressibility effects are included by means of applying the Prandtl-Glauert [100] transformation approach to the non-dimensional time in Equation 2.3:

$$s = S\beta^2 = S(1 - M^2) \tag{2.6}$$

Using the above modified Wagner function, the lift due to harmonic variations in the incidence of the aerofoil section can be calculated. Using Equation 2.4, the introduction of an arbitrary, Mach number dependent, lift-curve slope, $C_{l_\alpha}(M)$, and the effective angle of attack, $\alpha_E(s)$, can be determined:

$$C_l^C(s) = 2\pi\alpha\phi_C(s) = C_{l_\alpha}(M)\alpha_E(s) \tag{2.7}$$

where $\alpha_E(s)$ is given in time as exponential lift decrements:

$$\alpha_E(s) = \alpha_{n=0} + \sum_1^n \left(\Delta\alpha_n - X_n - Y_n - Z_n\right) \tag{2.8}$$

where the deficiency functions are defined as:

$$X_n = X_{n-1}e^{-b_1\beta^2\Delta s} + A_1\Delta\alpha_n e^{-b_1\beta^2\Delta s/2} \tag{2.9}$$

$$Y_n = Y_{n-1}e^{-b_2\beta^2\Delta s} + A_2\Delta\alpha_n e^{-b_2\beta^2\Delta s/2} \tag{2.10}$$

$$Z_n = Z_{n-1}e^{-b_3\beta^2\Delta s} + A_3\Delta\alpha_n e^{-b_3\beta^2\Delta s/2} \tag{2.11}$$

Equation 2.7 now allows for the lift-curve slope of any section at any Mach number, taken from experiment or CFD, to be introduced for greater accuracy in the spanwise blade loadings. The non-circulatory normal force can also be calculated and is given by:

$$C_{l_n}^I(s) = \frac{4K_\alpha T_I}{M}\left(\frac{\Delta\alpha_n}{\Delta t} - D_n\right) \tag{2.12}$$

where D_n is the deficiency function given by:

$$D_n = D_{n-1}e^{\frac{-\Delta t}{K_\alpha T_I}} + \left(\frac{\Delta\alpha_n - \Delta\alpha_{n-1}}{\Delta t}\right)e^{\frac{-\Delta t}{2K_\alpha T_I}} \tag{2.13}$$

This accounts for time history effects on the airloads due to the accumulation of wave-like pressure disturbances [71]. The non-circulatory time constant, T_I, is given by $T_I = c/a$, where a is the speed of sound. The factor, K_α, is defined as:

$$K_\alpha = \frac{0.75}{(1-M) + \pi\beta^2M^2(A_1b_1 + A_2b_2)} \tag{2.14}$$

Therefore, the total lift in attached flow is given by the sum of both the circulatory and impulsive terms:

$$C_{l_n}(s) = C_{l_n}^C(s) + C_{l_n}^I(s) \tag{2.15}$$

It is now possible to calculate the lift produced by the blade section in real time. A similar process for the calculation of the pitch-rate and moment terms can be found in Ref. [103]. The unsteady pressure drag is calculated by resolving the normal lifting force and the chord force through the pitch angle and is defined as:

$$C_{D_n}(s) = C_{l_n}(s)\sin\alpha - C_{C_n}(s)\cos\alpha \tag{2.16}$$

where $C_{C_n}(s)$ is the chord force coefficient obtainable from:

$$C_{C_n}(s) = C_{l_n}(s)\tan\alpha_E \tag{2.17}$$

This model applies only to attached flow regions of the aerofoil. For helicopter operations near the edge of the flight envelope, the rotor encounters regions of separated flow. Hence, it is necessary to incorporate the effects of separation using a different model.

2.1.2 Separated Flow Model

A model for trailing-edge stall based on the Kirchoff approximation is implemented, since in hover this is the most likely blade stall scenario to occur. Trailing edge separation is the gradual separation of the boundary layer from the surface of the aerofoil from the trailing edge. This form of separation has a gradual effect on the lift and pitching moment. Trailing edge separation also causes a loss of circulation which introduces non-linearities into the lift and pitching moments, and delays the onset of critical conditions at high incidences.

To account for the above, a critical pressure rise criterion is implemented to relate the normal lifting force coefficient on the blade section to the change in pressure on the surface. This takes into account any phase lag in leading-edge pressure. With a defined pressure criterion for separation due to the onset of static stall, dynamic stall, or shock formation, its occurrence with respect to the normal force can be computed using the following relationship:

$$P_n = P_{n-1}e^{\frac{-\Delta t}{T_P}} + (C_{l_n}^C(S) - C_{l_{n-1}}^C(S))e^{\frac{-\Delta t}{2T_P}} \tag{2.18}$$

where P is the increment in pressure due to a step change in angle of attack and T_P is the pressure rise time constant. The new normal force with the phase lag effects taken into account can then be computed from:

$$C_{l_n}^{C'}(s) = C_{l_n}^{C}(s) - P_n \qquad (2.19)$$

The model requires the relative blade angle of attack at this normal force, which can be obtained from the simple lifting-line relationship:

$$\alpha_P = C_{l_N}(s)/C_{l_\alpha}(M) \qquad (2.20)$$

The aforementioned equations are used solely for the purpose of approximating the movement of the trailing-edge separation points before and after stall in this model. As described later in Table 2.2, data on the forward movement of the trailing-edge separation point, F, is obtained from computations or experiments and stored in variables S1 (pre-stall) and S2 (post-stall). Therefore, the separation point, F, can be approximated by using the following relationships:

$$F = 1.0 - 0.4e^{((\alpha_P - \alpha_1)/S_1)}, (\alpha_P < \alpha_1) F = 0.02 + 0.58e^{((\alpha_1 - \alpha_P)/S_2)}, (\alpha_1 < \alpha_P) \qquad (2.21)$$

where α_1 is the static-stall angle. Time-history effects in the separation parameter also have to be considered and this is achieved using a similar method to before with:

$$F_n = F_{n-1}e^{\frac{-\Delta s}{T_F}} + (F - F_{n-1})e^{\frac{-\Delta s}{2T_F}} \qquad (2.22)$$

where:

$$F_{new} = F - F_n \qquad (2.23)$$

The corrected trailing-edge separation point, F_{new}, has now been obtained. To account for the effect of trailing-edge separation on the lifting loads of the blade section, the Kirchoff relationship is implemented:

$$K_{N_n} = \frac{1}{4}\left(1 + \sqrt{F_{new}}\right)^2 \qquad (2.24)$$

To obtain the final normal lifting force on the blade section with static stall accounted for, the normal force must be multiplied by the Kirchoff factor:

$$C_{l_{N_{sep}}}(s) = K_{N_n}C_{l_N}(s) \qquad (2.25)$$

Now, the effect of trailing-edge separation on the lifting force of the blade section is approximated by $C_{l_{N_{sep}}}$. The theory can be expanded to account for leading-edge separation, but that is outwith the scope of this thesis. The implementation of trailing-edge separation's effect on the pitching moment

can be found in Ref. [103]. The pressure drag is calculated using Equation 2.16 using the updated value for the normal circulatory force.

2.1.3 Inflow Model

A linear inflow model is implemented in the current work, which assumes a constant induced velocity across the rotor disk. It is obtained from Glauert's Propeller Theory [104] and is defined as:

$$\lambda = \frac{U \sin \theta_{tpp} + u_i}{\Omega R} = \mu \theta_{tpp} + \lambda_i \tag{2.26}$$

where λ is the non-dimensional inflow factor, $U \sin \theta_{tpp}$ is the inflow velocity due to the rotor disk tilt, u_i is the induced velocity, and ΩR is the angular velocity of the blade tip. Since this work considers hover solely, $\mu = 0$. It remains to solve for the non-dimensional inflow velocity, λ_i, which is a non-linear equation solved via a Newton-Raphson scheme, defined as:

$$\lambda_i = -\frac{C_T}{2} \frac{1}{\sqrt{\mu^2 + (\mu \sin \theta_{tpp} + \lambda_i)^2}} \tag{2.27}$$

where C_T is the thrust coefficient. In hover, $\mu = 0$, so the above equation can be reduced to:

$$\lambda_i = -\frac{C_T}{2\lambda_i} \tag{2.28}$$

which becomes:

$$\lambda_i = -\sqrt{\frac{C_T}{2}} \tag{2.29}$$

2.1.4 Trim Routine

The helicopter trim routine calculates the orientation and position of the rotor blades by means of changes to the collective and coning for a prescribed rotor thrust. This controls the helicopter's aerial alignment in hover and forward flight. The current model uses a standard trim routine with slight modifications. Figure 2.1 details the reference axis considered here.
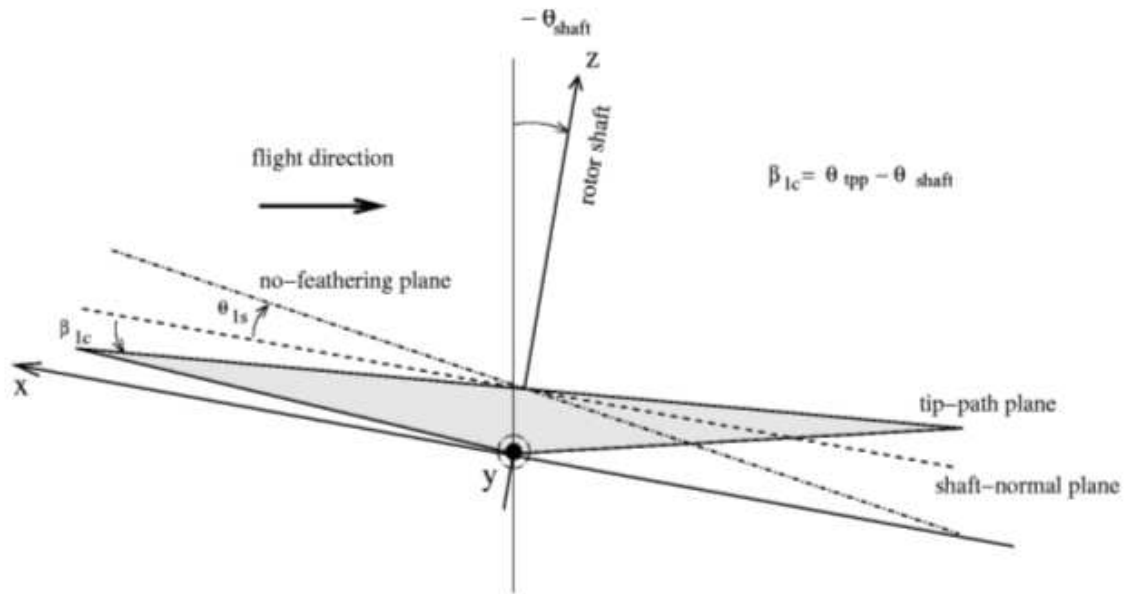
Figure 2.1: Reference axis for rotor trim routine in current model.

The model calculates the rotor trim collective and cyclic angles in the body reference axis. The trim collective defines the blade pitch angle and controls the amount of thrust the rotor produces. It is constant in hover (θ_0 = constant) where there are no cyclic inputs, hence only the blade collective pitch is considered in the model. Therefore, from classical theory [1] the collective pitch for a rotor in hover can be calculated from:

$$\theta_0 = \frac{6C_T}{\sigma C_{L_\alpha}} - \frac{3\lambda}{2} - \frac{3\theta_{nom}}{4} \tag{2.30}$$

where C_{L_α} is the lift-curve slope factor, λ is the inflow factor, and θ_{nom} is the linear blade twist. Normally, the first two terms would only be considered and, for a twisted blade, the above equation would give the collective pitch at 0.75R. The addition of the final term in Equation 2.30 assures that the collective pitch, θ_0, is determined at the location of zero twist (approximately 0.11R for the HIMARCS I blade). Blade flapping is also considered in the rotor trim, atlhough in hover only the coning angle is present, β_0, since the lift across the rotor disk is balanced (zero flapping). So, with the centrifugal moments balanced, the blade coning angle will only change due to the aerodynamic moments at the hinge because of changes in the blade lift. Therefore, in hover the coning angle, β_0, is calculated from:

$$\beta_0 = \frac{\gamma}{8}\left(\theta_0 - \frac{3\theta_{nom}}{4} - \frac{4\lambda}{3}\right) \tag{2.31}$$

where θ_{nom} is the linear blade twist, λ is the inflow factor, and μ is the advance ratio. The lead term takes the blade inertia into account. Again, the inclusion of the 2nd term within the parenthesis

assures the collective pitch angle used in the calculation is related to 3/4R.

Integrated into the model is an automated trimming method that calculates the required collective pitch, θ_0, and coning angle, β_0, for a specified thrust coefficient, C_T. An initial estimation is made for the trim conditions via Equations 2.30 and 2.31. If the calculated thrust at these trim conditions does not balance the specified weight of the helicopter at that C_T, then the rotor blades are required to be re-trimmed. At each time step where the hover condition is not met, then the following method is applied:

$$\Delta\theta_{0_{i+1}} = \Delta\theta_{0_i} + \frac{(\Delta\theta_{0_i} - \Delta\theta_{0_{i-1}})}{(C_{T_i} - C_{T_{i-1}})}.(W/NB - T) \tag{2.32}$$

where $\Delta\theta_0$ is the increment in collective pitch to trim to a target C_T, NB is the number of blades, W is the target weight of the helicopter, and T is the resultant thrust from collective input, θ_{0_i}. The step change in collective pitch, $\Delta\theta_{0_{i+1}}$, is added to θ_0 and a new coning angle is calculated, $\beta_{0_{i+1}}$. This process continues until the calculated thrust from the trimmed rotors matches the target weight of the helicopter.

2.1.5 Prescribed Wake

The loads experienced by the rotor blades are not only due to the local flow conditions, but also affected by the wake produced by the preceding blades. The effect of the wake is to alter the local incidence experienced by the blades. This alteration is often rapid when vortices shed by the previous blade, interact with the reference blade. To include the effects of the wake in the rotor code, the method of wake prediction must be compatible with the indicial model for unsteady aerodynamic loading response already outlined in the previous sections. The influence of time varying shed wake is included implicitly in the model outlined previously, but the effects of tip vortices needs to be included explicitly and this is where the wake model is used. The standard approach is to keep track of all the individual vortex elements along with the geometry of the wake and sum the individual contributions from each element. Unfortunately, this method may be too lengthy and can increase computational time. To avoid this problem, an approximation is made. Firstly, the model is divided into two sections, the near wake model and the far wake model.

In the near wake model a detailed computation of the of the effect of the vortical filament on the blade is carried out. Away from the blade, the far wake model is used which is more efficient [44]. Beyond the first quadrant, the vortex is assumed to be rolled up, and hence can be treated as a single

tip vortex. The approach taken by Beddoes for resolving the wake influences, while maintaining the simplicity and efficiency of the model, uses a prescribed "free wake" method to calculate the mutual distortion and induced velocities of the trailing and shed elements of the wake. The distortion of the wake is achieved by using a prescribed downwash field which is time averaged. Using this distorted wake, the local induced velocity on the blades can be evaluated by dividing the vortex trails into a series of elements, and applying the Biot Savart Law. To avoid the excessive computational costs of evaluating every element of the vortex trail for several turns of the rotor, an approximate method is used. This identifies the most critical points of the wake and positions large vortex elements there. It then approximates the influence of the remaining wake points by using a vortex ring element.

2.1.6 Aerodynamic Parameters

As mentioned previously, up to 19 aerodynamic parameters are required as input to the blade element method for rotor predictions. A brief description of each of the most important parameters and how they are extracted from experimental or numerical data follows. In the current work, these parameters are extracted from 2D quasi-steady ramping CFD computations and are are presented in Table 2.2:

Parameter	Description	Extraction
Attached Flow		
C_{L_α}	Lift-curve slope	Linear fit to lift-curve data.
α_0	Zero-lift angle	Angle where the lift-curve cuts the x-axis.
α_1	Static stall angle	Angle where the separation parameter, f = 0.6.
C_{m_0}	Zero-lift moment	$\frac{c}{4}$-moment coefficient at α_0.
C_{d_0}	Zero-lift drag	Pressure drag coefficient at α_0.
Separated Flow - Pitching Moment		
$S1, S2$	Pre-stall factor, Post-stall factor	This is the separation parameter, f, before ($S1$) and after ($S2$) stall. Taken from the point of initial trailing-edge separation in 2D data.
k_0	Aero offset from c/4	Extracted from $\frac{c}{4}$-moment curve data.
k_1	COP change due to separated flow	Calculated from α_0, α_1, and the pre- and post-stall factors, $S1$ and $S2$.
k_2	Moment break shape at stall	Extracted from $\frac{c}{4}$-moment curve data.
m		Values assumed from 0.5 to 2.

Table 2.2: Description of aerodynamic input parameters for the blade element method.

2.2 Computational Fluid Dynamics

2.2.1 Navier-Stokes Equations

The CFD solver used in this research is based on the Reynolds-averaged Navier-Stokes equations, which describe the motion of a fluid within a specified domain in space and time. In partial differential form, they are given as:

(1) Conservation of Mass:

$$\rho \frac{\partial u_i}{\partial x_i} = 0 \tag{2.33}$$

where u_i is the velocity vector and x_i is the position vector.

(2) Conservation of Momentum:

$$\rho \frac{\rho \partial u_i}{\partial t} + \rho u_j \frac{\partial u_i}{\partial x_j} = -\frac{\partial p}{\partial x_i} + \frac{\partial \tau_{ji}}{\partial x_j} \tag{2.34}$$

where u_i is the velocity vector, x_i is the position vector, ρ is density, p is pressure, t is time, and τ_{ji} is the viscous stress tensor. The first two (convective) terms, $\rho \frac{\partial u_i}{\partial t}$ and $\rho u_j \frac{\partial u_i}{\partial x_j}$, describe the rate of change of momentum in the fluid and the fluid flux across the domain, respectively. The final (diffusive) terms, $-\frac{\partial p}{\partial x_i}$ and $\frac{\partial \tau_{ji}}{\partial x_j}$, describe the change in pressure and the viscous stresses through the domain, respectively. The Boussinesq approximation states that the viscous stress tensor, τ_{ji}, is directly proportional to the strain-rate tensor:

$$\tau_{ji} = 2\mu s_{ij} \tag{2.35}$$

where μ is the laminar kinematic viscosity and s_{ij} is the strain-rate tensor:

$$s_{ij} = \frac{1}{2} \left(\frac{\partial u_i}{\partial x_j} + \frac{\partial u_j}{\partial x_i} \right) \tag{2.36}$$

(3) The Energy Equation:

$$\rho \frac{\partial E}{\partial t} + \rho u_i \frac{\partial E}{\partial x_j} = -u_i \frac{\partial p}{\partial x_i} + u_i \frac{\partial \tau_{ij}}{\partial x_j} - \frac{\partial q_i}{\partial x_j} \tag{2.37}$$

where E is the total energy of the fluid, q is the heat flux vector, and all other terms are described as with Equation 2.34. The first two (convective) terms, $\rho \frac{\partial E}{\partial t}$ and $\rho u_i \frac{\partial E}{\partial x_j}$, describe the rate of change of energy and the flux of energy in the domain, respectively. The final two (diffusive) terms, $-u_i \frac{\partial p}{\partial x_i}$ and $u_i \frac{\partial \tau_{ij}}{\partial x_j} - \frac{\partial q_i}{\partial x_j}$, describe the change in pressure, viscous stresses and heat flux in the domain, respectively. The total energy of the fluid, E, is defined as:

$$E = \rho \left(e + \frac{1}{2} u_i u_i \right) \tag{2.38}$$

where e is the specific internal energy. The heat flux vector, q_i, is defined as:

$$q_i = -k_T \frac{\partial T}{\partial x_i} \tag{2.39}$$

where T is the fluid temperature and k_T is the heat transfer coefficient, which is defined as:

$$k_T = \frac{\mu}{(\gamma - 1) M_\infty^2 Pr} \tag{2.40}$$

where γ ratio of specific heats, M_∞ is the freestream Mach number, and Pr is the Prandlt number.

2.2.2 Reynolds Averaging

Rather than solve the Navier-Stokes (NS) equations directly, which requires a huge amount of computational resources, it is more common to take the time-average of the equations. This is achieved by splitting the variable in question into a mean part and a fluctuating part. For example, the velocity vector, u_i, becomes:

$$u_i = U_i + u_i' \tag{2.41}$$

where U_i is the mean component of velocity, and u_i' is the fluctuating part. This can be carried out for all the variables in the NS equations, as follows:

$$u_j = U_j + u_j', \quad p = P + p', \quad s_{ij} = S_{ij} + s_{ij}' \tag{2.42}$$

with the third term emanating from the relationship between the viscous stress tensor, τ_{ji}, and the strain-rate tensor, s_{ij}, stated in Equation 2.35. Thus, with the time averaging rules applied we have:

$$\rho \frac{\partial U_i}{\partial t} + \rho \frac{\partial}{\partial x_j} (U_i U_j + \overline{u_i' u_j'}) = -\frac{\partial P}{\partial x_i} + \frac{\partial}{\partial x_j} (2\mu S_{ij}) \tag{2.43}$$

where the instantaneous values have been replaced with the mean, time-averaged values and the viscous stress tensor, τ_{ji}, is replaced according to Equation 2.35. This can be re-arranged to the following format:

$$\rho \frac{\partial U_i}{\partial t} + \rho U_j \frac{\partial U_i}{\partial x_j} = -\frac{\partial p}{\partial x_i} + \frac{\partial}{\partial x_j} (2\mu S_{ij} - \rho \overline{u_i' u_j'}) \tag{2.44}$$

which is known as the Reynolds-Averaged Navier-Stokes equation. The term, $-\rho\overline{u_i'u_j'}$, is known as the Reynolds stress tensor and is more commonly written as:

$$\tau_{ij}^R = -\overline{u_i'u_j'} \tag{2.45}$$

where τ_{ij}^R is the specific Reynolds stress tensor. This adds further unknowns to the problem. For closure, a method to treat τ_{ij}^R is required, which can be handled using the Boussinesq approximation, so:

$$\tau_{ij}^R = -\overline{u_i'u_j'} = 2\mu_T s_{ij} \tag{2.46}$$

where μ_T is the turbulent eddy viscosity. To calculate μ_T, a variety of turbulence models based on the turbulence kinetic energy and its rate of dissipation have been developed. In the current work, a two-equation turbulence kinetic energy model is applied, the Wilcox k-ω model.

2.2.3 Wilcox k-ω Model

The Wilcox k-ω model was developed by David C. Wilcox [105] and offers good validation with experiments for both wall-bounded and free-shear flows. Although other turbulence models were available, the Wilcox k-ω model was the only one used to promote both consistency and reliability in the computed results. It offered a good balance of results accuracy and efficiency in computation of the eddy viscosity compared to other models, especially in the case of hovering rotors [106].

The principle of the model is to calculate the turbulent eddy viscosity, μ_T, based on the following equation:

$$\mu_T = \rho k/\omega \tag{2.47}$$

where ρ is the gas/fluid density, k is the specific turbulent kinetic energy, and ω is the specific rate of dissipation of k. The latter two are calculated from the following transport equations:

(1) Turbulent Kinetic Energy:

$$\underbrace{\rho\frac{\partial k}{\partial t}}_{Unsteady} + \underbrace{\rho U_j\frac{\partial k}{\partial x_j}}_{Convection} = \underbrace{\rho\tau_{ij}\frac{\partial U_i}{\partial x_j}}_{Production} - \underbrace{\rho\beta^* k\omega}_{Dissipation} + \underbrace{\frac{\partial}{\partial x_j}\left[(\mu + \sigma^*\mu_T)\frac{\partial k}{\partial x_j}\right]}_{Diffusion} \tag{2.48}$$

where the two terms on the left-hand side, the unsteady and the convection term, describe the evolution of k for a fluid particle. The production term specifies the rate at which the kinetic energy is transferred to turbulence. Dissipation accounts for the rate at which turbulent kinetic energy is

converted into internal thermal energy. The final terms describe the diffusion of turbulence due to molecular transport. We have a similar transport equation for ω:

(2) Specific Rate of Dissipation:

$$\underbrace{\rho\frac{\partial \omega}{\partial t}}_{Unsteady} + \underbrace{\rho U_j\frac{\partial \omega}{\partial x_j}}_{Convection} = \underbrace{\rho\alpha\frac{\omega}{k}\tau_{ij}\frac{\partial U_i}{\partial x_j}}_{Production} - \underbrace{\rho\beta\omega^2}_{Dissipation} + \underbrace{\frac{\partial}{\partial x_j}\left[(\mu+\sigma\mu_T)\frac{\partial \omega}{\partial x_j}\right]}_{Diffusion} \tag{2.49}$$

Finally, we have the closure coefficients that are constants used to alter the model's output and can be fine-tuned for specific flows. The current model uses the constants defined in Table 2.3.

α	β	β^*	σ	σ^*
5/9	3/40	9/100	1/2	1/2

Table 2.3: Closure coefficients for the Wilcox k-ω model. Taken from Ref. [105].

2.2.4 HMB Solver

All CFD computations were performed using the Helicopter Multi-Block (HMB) flow solver [107] developed at the University of Glasgow. The solver has been successfully applied to a variety of problems including rotorcraft in hover and forward flight [106], dynamic stall [108], and BVI [109]. HMB solves the 2D and 3D URANS equations on multiblock structured grids in serial or parallel mode. The governing equations are discretised using a cell-centred finite volume method. The convective terms are discretised using either Osher's or Roe's scheme. MUSCL interpolation is used to provide formally third order accuracy in the calculation of the fluxes. The Van Albada limiter is used to avoid spurious oscillations in flow properties across shocks by reducing the accuracy of the numerical scheme to first order. The time-marching of the solution is based on an implicit, dual time stepping method. The final algebraic system of equations is solved using a Conjugate Gradient method, in conjunction with Block Incomplete Lower Upper factorisation. A number of one and two equation turbulence models are available, as well as Large Eddy Simulation and Detached Eddy Simulation. The conservation laws can be converted into vector form to simplify their use in the computational method. The Navier-Stokes equations now take the form:

$$\frac{\partial \mathbf{w}}{\partial t} + \frac{\partial\left(\mathbf{F}^i + \mathbf{F}^v\right)}{\partial x} + \frac{\partial\left(\mathbf{G}^i + \mathbf{G}^v\right)}{\partial y} + \frac{\partial\left(\mathbf{H}^i + \mathbf{H}^v\right)}{\partial z} = 0 \tag{2.50}$$

where $\mathbf{w}$ is the vector of conserved variables, defined by:

$$\mathbf{w} = (\rho, \rho u, \rho v, \rho w, E)^T. \tag{2.51}$$

53

The superscripts i and v in Equation 2.50 denote the inviscid and viscous components of the flux vectors, $\mathbf{F}$, $\mathbf{G}$ and $\mathbf{H}$, respectively. The inviscid flux components are given by:

$$
\begin{aligned}
\mathbf{F}^i &= \left(\rho u, \rho u^2 + p, \rho uv, \rho uw, u\left(\rho E + p\right)\right)^T, \\
\mathbf{G}^i &= \left(\rho v, \rho uv, \rho v^2 + p, \rho vw, v\left(\rho E + p\right)\right)^T, \\
\mathbf{H}^i &= \left(\rho w, \rho uw, \rho vw, \rho w^2 + p, w\left(\rho E + p\right)\right)^T.
\end{aligned}
\tag{2.52}
$$

The viscous flux vectors contain terms for the heat flux and viscous forces exerted on the body are:

$$
\begin{aligned}
\mathbf{F}^v &= \frac{1}{\text{Re}}\left(0, \tau_{xx}, \tau_{xy}, \tau_{xz}, u\tau_{xx} + v\tau_{xy} + w\tau_{xz} + q_x\right)^T, \\
\mathbf{G}^v &= \frac{1}{\text{Re}}\left(0, \tau_{xy}, \tau_{yy}, \tau_{yz}, u\tau_{xy} + v\tau_{yy} + w\tau_{yz} + q_y\right)^T, \\
\mathbf{H}^v &= \frac{1}{\text{Re}}\left(0, \tau_{xz}, \tau_{yz}, \tau_{zz}, u\tau_{xz} + v\tau_{yz} + w\tau_{zz} + q_z\right)^T.
\end{aligned}
\tag{2.53}
$$

The terms τ_{ij} in Equation 2.53 represent the viscous stress tensor components while q_i denotes the heat flux vector. These equations can be transformed into the averaged equations simply by substituting $\left(\tau_{ij} + \tau_{ij}^R\right)$ for τ_{ij} and $\left(q_i + q_i^R\right)$ for q_i and taking the flow variables as averaged quantities. All quantities are non-dimensionalised using the relations:

$$
\begin{aligned}
x &= \frac{x^*}{L^*}, \quad y = \frac{y^*}{L^*}, \quad z = \frac{z^*}{L^*}, \quad t = \frac{t^*}{L^*/U_\infty^*}, \\
\rho &= \frac{\rho^*}{\rho_\infty^*}, \quad u = \frac{u^*}{U_\infty^*}, \quad v = \frac{v^*}{U_\infty^*}, \quad w = \frac{w^*}{U_\infty^*}, \\
p &= \frac{p^*}{\rho_\infty^* U_\infty^{*2}}, \quad T = \frac{T^*}{T_\infty^*}, \quad e = \frac{e^*}{U_\infty^{*2}} \quad \mu = \frac{\mu^*}{\mu_\infty^*}
\end{aligned}
\tag{2.54}
$$

where the superscript * denotes the dimensional variables. For this investigation, the non-dimensional characteristic length, L^*, is taken to be the root chord of the rotor.

Steady State Solver

The HMB flow solver uses a cell-centred finite volume approach to discretise the governing equations described above. According to this method, the spatial discretisation of the RANS equations for each cell results in the equation:

$$
\frac{\partial}{\partial t}\left(\mathbf{w}_{i,j,k}\mathscr{V}_{i,j,k}\right) + \mathbf{R}_{i,j,k}\left(\mathbf{w}_{i,j,k}\right) = 0.
\tag{2.55}
$$

where $\mathscr{V}_{i,j,k}$ denotes the cell volume and $\mathbf{R}_{i,j,k}$ represents the flux residual. The convective fluxes are discretised using Osher's upwind scheme [110]. The central differencing spatial discretisation

method is approximate to solve the viscous terms. For the time-accurate simulations presented in this research, temporal integration is performed using an implicit, dual-time stepping method. The updated mean flow solution is calculated by solving the steady-state problem:

$$\mathbf{R}_{i,j,k}^{*} = \frac{3\mathscr{V}_{i,j,k}^{n+1}\mathbf{w}_{i,j,k}^{n+1} - 4\mathscr{V}_{i,j,k}^{n}\mathbf{w}_{i,j,k}^{n} + \mathscr{V}_{i,j,k}^{n-1}\mathbf{w}_{i,j,k}^{n-1}}{2\Delta t} + \mathbf{R}_{i,j,k}\left(\mathbf{w}_{i,j,k}^{n+1}\right) = 0 \tag{2.56}$$

where the terms $\mathscr{V}^{n+1}$, $\mathscr{V}^{n}$, and $\mathscr{V}^{n-1}$ represent the cell volumes at different time steps. Equation 2.56 represents a nonlinear system of equations. This system can be solved by introducing an iteration through pseudo-time, τ, to the steady state, as given by:

$$\underbrace{\mathscr{V}_{i,j,k}^{n+1}\frac{\mathbf{w}_{i,j,k}^{n+1,m+1} - \mathbf{w}_{i,j,k}^{n+1,m}}{\mathscr{V}_{i,j,k}^{n+1}\Delta\tau}}_{A} + \frac{3\mathscr{V}_{i,j,k}^{n+1}\mathbf{w}_{i,j,k}^{n+1,m} - 4\mathscr{V}_{i,j,k}^{n}\mathbf{w}_{i,j,k}^{n} + \mathscr{V}_{i,j,k}^{n-1}\mathbf{w}_{i,j,k}^{n-1}}{2\mathscr{V}_{i,j,k}^{n+1}\Delta t} + \frac{\mathbf{R}_{i,j,k}\left(\mathbf{w}_{i,j,k}^{n+1,m}\right)}{\mathscr{V}_{i,j,k}^{n+1}} = 0$$

$$\tag{2.57}$$

where the pseudo-time iteration at real time step n+1 is denoted by $\mathbf{w}_{i,j,k}^{n+1,m}$ and the cell volumes remain constant during these iterations. The unknown, $\mathbf{w}_{i,j,k}^{n+1,m+1}$, is obtained when term A converges to a specified tolerance (three orders of magnitude for the current work). The flux residual, $\mathbf{R}_{i,j,k}^{n+1}$, is linearised in time using an implicit scheme:

$$\mathbf{R}_{i,j,k}\left(\mathbf{w}^{n+1}\right) \approx \mathbf{R}_{i,j,k}\left(\mathbf{w}_{i,j,k}^{n}\right) + \frac{\partial\mathbf{R}_{i,j,k}^{n}}{\partial\mathbf{w}_{i,j,k}^{n}}\left(\mathbf{w}_{i,j,k}^{n+1} - \mathbf{w}_{i,j,k}^{n}\right) \tag{2.58}$$

An iterative Generalised Conjugate Gradient method is used to solve the equations efficiently in terms of time and memory requirements. This is used in conjunction with a Block Incomplete Lower-Upper (BILU) factorisation method used as a pre-conditioner to solve the system of equations. Message Parallel Interface (MPI) is used for the communication between the processors in parallel and was available in the code and is common in almost all research and commercial codes. All computations undertaken have been performed on the Beowulf Pentium 4 120-processor workstation cluster of the CFD Laboratory at the University of Glasgow.

2.2.5 Hover Formulation

A brief account of the hover formulation is given here, although both the hover and forward-flight formulation of the HMB solver is provided in detail in Ref. [106].

Rotational Forces

Assuming that the wake shed from the rotor is steady, the flow around a hovering rotor can be treated as a steady-state problem. Moreover, if steady-state is assumed, domain periodicity in the azimuthal

direction can be assumed to reduce computational times. Hence, with periodic boundaries, an n-bladed rotor can be approximated using a 1/n domain segment, reducing necessary grid sizes by up to 75% and eradicating the need for the unsteady solver.

For a rotor hovering in the x-y plane at a constant rotation rate, ω, the rotation vector about the z-axis could be:

$$\vec{\omega} = (0,0,\omega)^T \tag{2.59}$$

A non-inertial frame of reference is used to account for the rotor rotation. Both the centripetal and Coriolis acceleration terms in the momentum equations are accounted for using a combination of a mesh velocity in the formulation of the Navier-Stokes equations and a source term for the momentum equations. The mesh velocity introduced is essentially the mesh rotation velocity:

$$\vec{u}_{ref} = \omega x \vec{r} \tag{2.60}$$

where $\vec{r}$ is the position vector of the cell. In addition to the mesh velocity, a source term for the momentum equations is introduced:

$$\vec{S} = [0, -\rho \omega x \vec{u}_h, 0]^T \tag{2.61}$$

where $\vec{u}_h$ is the velocity field in the present rotor-fixed frame of reference.

Boundary Conditions

Two types of farfield boundary conditions are used. The first is based on imposing free-stream/linear extrapolation at the farfield of the computational domain. Extrapolation is used in the vertical direction on the inflow and outflow boundaries. The second approach is a potential sink/Froude boundary condition and is designed to suppress re-circulation. A potential sink is placed at the rotor origin and, based on actuator-disk theory, a constant axial (outflow) velocity is prescribed on a circular part of the outflow boundary face. The magnitude of the velocity is determined by:

$$\frac{R_{outflow}}{R} = 0.78 + 0.22e^{-d_{outflow}/R} \tag{2.62}$$

where R is the rotor span, $R_{outflow}$ is the outflow radius of the wake, and $d_{outflow}$ is the non-dimensional distance of the rotor to the outflow boundary. The strength of the sink is chosen to balance the mass flow into and out of the computational domain. Freestream boundaries are used at the farfield.

Hover Trimming

To accompany the hover formulation of the code, a trimmer based on blade-element theory is built-in to the code. An initial trim state is computed using the blade-element theory (see Section 2.1), and the blocks around the blade in the domain are deformed using a blade deformation algorithm such as TFI (Trans-Finite Interpolation). TFI is a technique used to rearrange the computational grid after specified boundaries have been altered. Geometric laws are then applied to the grid to propagate the changes to the deformed boundaries. For further information on these algorithms, see Ref. [106]. The solution is then allowed to reach an acceptable level of convergence. At this point, further re-trimming is conducted, but this time the blade loads computed by the CFD solver are used. Both the collective pitch and coning angle are updated every n_{retrim} number of steps via a Newton-Raphson approach similar to the one described in Section 2.1.4. The solution is then allowed to converge again, before re-trimming takes place. This continues until an acceptable level of convergence in the trimming angles is achieved.

As stated previously, for a hovering rotor ($\mu = 0$) only the collective pitch and the coning angle are unknowns. The trimming procedure goes as follows:

1) At start-up, an initial estimate of the trim state is computed using the following equation for the collective pitch:

$$\theta_0 = \frac{6}{\sigma a} C_T + \frac{3}{2} \sqrt{\frac{C_T}{2}} \tag{2.63}$$

where σ is the rotor solidity. In this case, inflow factor, λ_i, can be obtained directly from the equation:

$$\lambda_i = -\sqrt{\frac{C_T}{2}} = -\frac{\sigma a}{16} \left[\sqrt{1 + \frac{64}{3\sigma a}\theta_0} - 1 \right] \tag{2.64}$$

For a twisted rotor blade, this gives the collective pitch at 0.75R since it lacks the correction available in Equation 2.30. For the coning angle, β_0, we have:

$$\beta_0 = \frac{\gamma}{8} \left[\theta_0 + \frac{4}{3}\lambda \right] \tag{2.65}$$

where the Lock number γ is obtained iteratively via estimations to θ_0 and λ_i.

2) The mesh is subsequently deformed to account for the new rotor blade incidence and position.

3) A steady flow simulation is performed until a prescribed level of convergence is reached.

4) After n_{retrim} steps, a re-trimming is performed. The collective is updated using the following relation:

$$\Delta\theta_0 = \frac{C_{T,target} - C_T}{dC_T/d\theta_0} \tag{2.66}$$

where:

$$\frac{dC_T}{d\theta_0} = \frac{\sigma a}{6}\left[1 - \frac{1}{\sqrt{1 + (64/3\sigma a)\theta_0}}\right] \tag{2.67}$$

The coning angle is then re-calculated using Equation 2.65.

5) Steps 3-4 are repeated until an acceptable level of convergence is reached.

2.3 Post-processing

2.3.1 Iso-surfaces of λ_2

To improve the quality of the flowfield visualisations, the parameter λ_2 was used to clearly capture the vortical structures in the near wake of the rotors [111]. By taking the gradient of the incompressible Navier-Stokes equations, it is possible to locate pressure minima in the domain due only to vortical motion. Expressing this in terms of the pressure Hessian we have:

$$-\frac{1}{\rho}p_{ij} = a_{ij} + \frac{1}{\rho}\mu u_{i,jkk} \tag{2.68}$$

where ρ is fluid density, p_{ij} is the pressure, a_{ij} is the acceleration tensor, μ is the laminar kinematic viscosity, and $u_{i,jkk}$ is the velocity. From term a_{ij}, the acceleration tensor, the antisymmetric part which describes inviscid vorticity transport is assumed to be satisfied and the second term on the right-hand side of Equation 2.68 is ignored, including any unsteady terms. Equation 2.68 then simplifies to:

$$-\frac{1}{\rho}p_{ij} = \Omega_{ij}^2 + S_{ij}^2 \tag{2.69}$$

where Ω is the mean rotation tensor and S is the mean strain rate tensor, defined by:

$$\Omega_{ij} = \frac{1}{2}\left(\frac{\partial U_i}{\partial x_j} - \frac{\partial U_j}{\partial x_i}\right) \tag{2.70}$$

$$S_{ij} = \frac{1}{2} \left(\frac{\partial U_i}{\partial x_j} + \frac{\partial U_j}{\partial x_i} \right) \tag{2.71}$$

Taking the second derivative of Equation 2.69 to find the local maxima or minima, the low pressure found in vortex cores could be obtained when the second largest eigenvalue, λ_2, is less than zero. This function is made available as an add-on to Tecplot, with a full derivation available from the work in Ref. [111].

2.3.2   Iso-surfaces of Re$_T$

The turbulent Reynolds number, or Re$_T$, is the ratio of turbulent kinematic eddy viscosity, μ_T, to the laminar kinematic viscosity, μ:

$$Re_T = \frac{\mu_T}{\mu} \tag{2.72}$$

Since μ depends on viscosity, contours of Re$_T$ will also show the wake including tip vortex and shed wake vorticity. With respect to interpreting the ratio, the greater the value the more turbulence that is predicted.

Chapter 3

CFD Validation

3.1 Introduction

Although the use of CFD in modern engineering is more common than ever, it is still important that we conduct proper validation of the numerical method against experiments. For hovering rotors, this is generally conducted with comparisons of the blade pressure coefficient, Cp, the pressure or vorticity in vortex cores, and/or visualisations of the flowfield itself such as the downwash. However, in most cases validating the CFD solver is limited to the experimental data available in the open literature for the specific field of engineering being investigated. The current work looks at applying trailing-edge flaps on rotor blades in hover for performance enhancement - a new design concept first considered by Noonan *et al.* [16] and taken to new levels here. The downside of attempting to research such a design concept using CFD is that very little experimental data is available for validation. Of that which exists, the HIMARCS I report itself [16] offers some data for 3D rotor validation. For hover, the only data available is the C_T, C_Q, and Figure of Merit, FM, with no blade Cp data or flowfield visualisations presented in the report. Therefore, to affirm the validity of the HMB solver for conducting 3D hovering rotor calculations, results for hovering rotors for well-known validation test cases are presented here. Table 3.1 lists all the validation test cases considered in the following sections, including the HIMARCS I experiment. Results presented in Ref. [106] demonstrated that both full-size grids and those with periodic boundaries were similar, so periodic boundaries are used with confidence in this work.

The sections that follow present the validation results for four separate test cases relating to 3D hovering rotors with periodic boundaries. As listed in Table 3.1, they are the (1) Caradonna and Tung, (2) ONERA 7A/7AD1, (3) UH-60A, and (4) HIMARCS I test cases. This selection of test cases

Case	Profiles	AR	Twist	$\theta_{0.7}$	M_T	Re	Grids	Model
Caradonna	NACA	6.0	0°	0°,	0.520,	2.3×10^6,	1.1M,	Inv.
& Tung	0012			8°	0.439	1.9×10^6	2.0M	
ONERA 7A	OA209,	15.0	NL	7.5^o	0.6612	2.1×10^6	0.6M	Inv.
	OA213							
ONERA 7AD1	OA209,	15.0	NL	7.5^o	0.6612	2.1×10^6	0.6M,	Inv.
	OA213						1.3M	
UH-60A	SC1095,	15.404	18^{o*}	10.45^o,	0.626	-	1M,2M,	Inv.
	SC1095R8			11.47^o			3M	
HIMARCS I	RC(6)-08,	12.623	7°	Varied	0.627	168,590	2.7M	Inv.,
	RC(4)-10							k-ω

NL = Nonlinear blade twist. See Figure 3.2 for more details.
* = Nonlinear blade twist. Equivalent value given.

Table 3.1: CFD Validation details.

covers a range of tip Mach numbers, blade sections, twist profiles, and other geometric designs. Each section provides a short lead-in to the test case and a presentation of the results. Test cases 1 to 3 are standard within the validation database of the HMB solver, whereas test case 4 is original to this work.

3.2 Caradonna and Tung Test Case

The first set of comparisons between CFD and experiment are based on tests conducted by Caradonna & Tung [112]. They considered a simple 2-bladed, untwisted, low-aspect ratio rotor blade in hover. The same NACA 0012 section profile was used for the entire blade with no sweep or taper being applied. Further details of the geometry can be found in Table 3.1 and Figure 3.1. Tip Mach numbers from 0.23 to 0.9 were considered at collective pitch angles of 0° to 12°, and Cp data was recorded at blade stations r/R = 0.5, 0.68, 0.8, 0.89, and 0.96. The CFD used a medium-coarse grid of 1.1 million points for the inviscid case and 2 million points for the viscous case, since a finer first wall spacing was required to properly capture the boundary layer.

Results are presented in Figure 3.2 for Cp distributions at r/R = 0.8 and 0.96. Firstly, the non-lifting case is considered with the blade at a collective pitch of 0° in Figures 3.2(a) and 3.2(b). No blade coning is applied. Excellent agreement with experiment is demonstrated for the inviscid calculations. For the lifting case where $\theta = 8^o$ in Figures 3.2(c)-(d), excellent agreement is again predicted for both the upper and lower surfaces at both outboard locations.

NACA0012   NACA0012

Caradonna & Tung rotor blade: $\Lambda = 6.0$
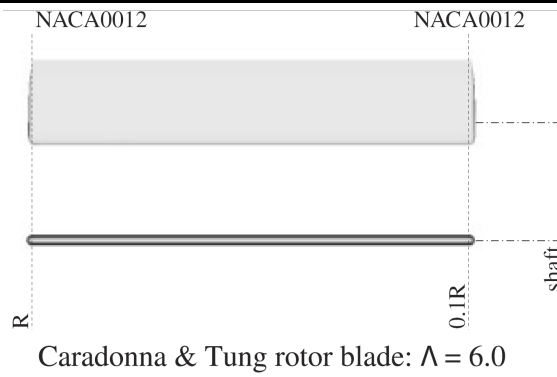
Figure 3.1: Caradonna & Tung's rotor. Taken from Ref. [106].

(a)

(b)

(c)

(d)
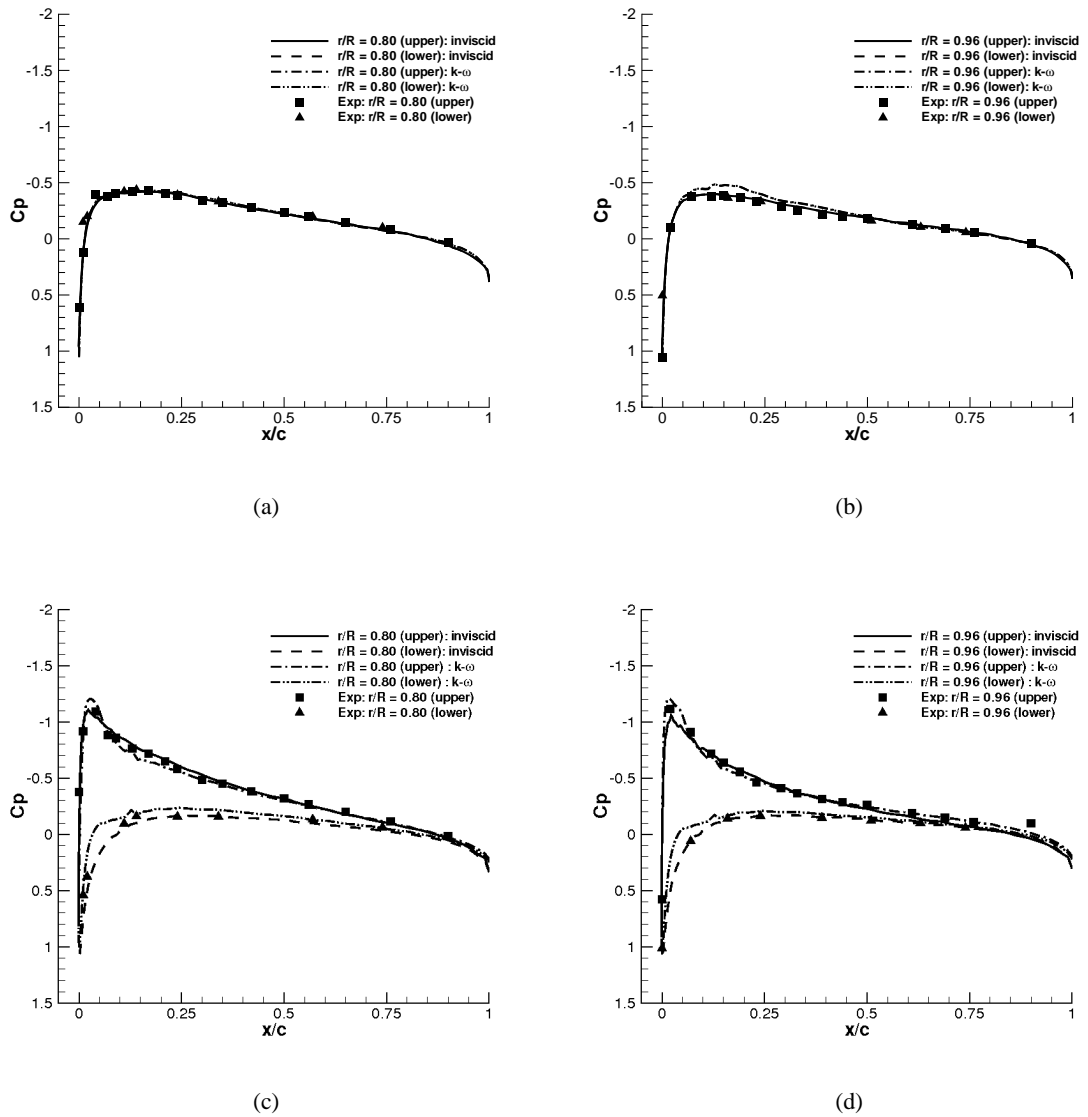
Figure 3.2: Comparisons of Cp for Caradonna and Tung. $\theta = 0^o$: (a) r/R = 0.8. (b) r/R = 0.96. $\theta = 8^o$: (c) r/R = 0.8. (d) r/R = 0.96 [106]. ($M_T = 0.52$ (a-b), 0.439 (c-d))

3.3 ONERA 7A/7AD1 Test Cases

The 7A and 7AD1 rotors were designed and tested by ONERA as part of the HELISHAPE project [113]. The tests on the 7A rotor were conducted for a 4-bladed, high-aspect ratio, rectangular plan-form with nonlinear twist. The blade section profiles used were the OA213 and OA209. The 7AD1 rotor differs from the 7A type by the inclusion of a swept, parabolic tip with anhedral. Details of the blade geometry and twist can be found in Table 3.1 and Figure 3.3, respectively.

Results are presented here at a high tip Mach number of 0.6612 with coarse and medium grids of 0.6 and 2 million grid points, respectively. All cases were run inviscid at a collective pitch setting of 7.5^o. Comparisons of the pressure coefficient, Cp, are compared at r/R = 0.826 and 0.987 for the ONERA 7A rotor (in Figure 3.4(a-b)) and at r/R = 0.915 and 0.975 for the ONERA 7AD1 rotor (in Figure 3.4(c-d)). As can be seen, there is excellent agreement at all locations for both the rectangular 7A blade and the 7AD1 rotor with the complex blade tip.

(a)

(b)
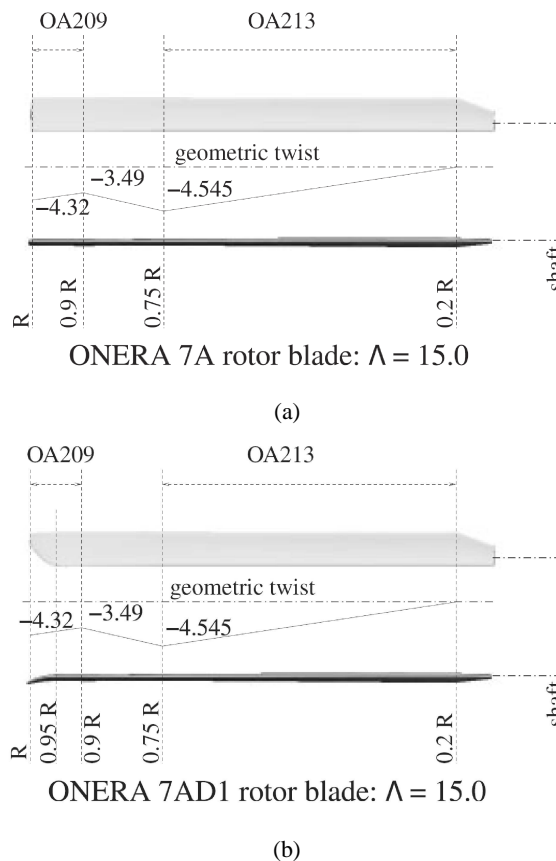
Figure 3.3: ONERA rotor geometry. (a) 7A. (b) 7AD1. Taken from Ref. [106].
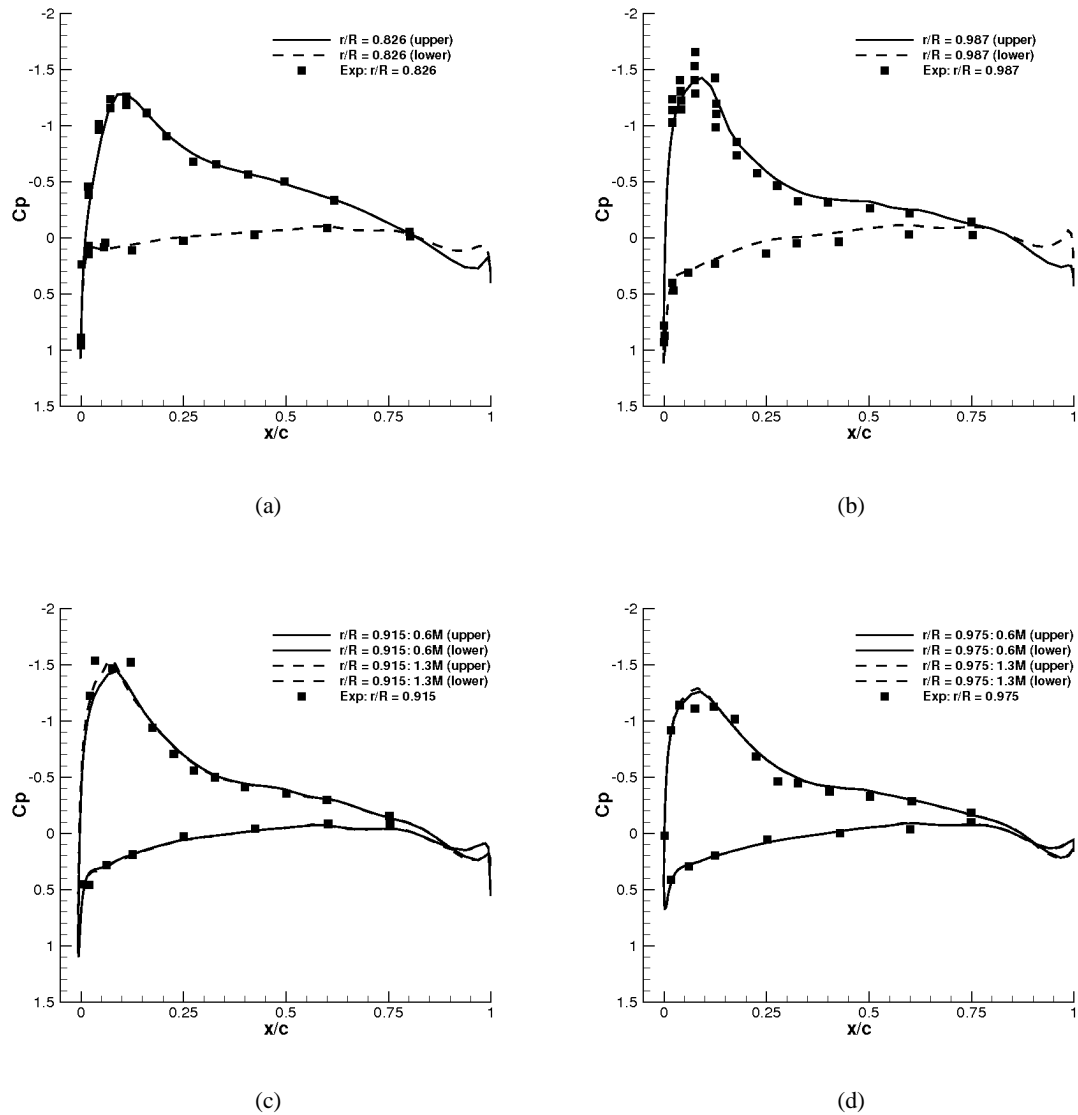
Figure 3.4: Comparison of Cp for ONERA. (a-b) 7A. r/R = 0.826 and 0.987. (c-d) 7AD1. r/R = 0.915 and 0.975 [106]. (M_T = 0.6612)

3.4 UH-60A Test Case

The UH-60A Black Hawk is one of the most common helicopters in modern use and provides an excellent example for CFD validation. The work by Lorber *et al.* [114] represents a comprehensive extraction of experimental data from hover tests of a scaled rotor using the UH-60A main rotor blade with a swept and tapered tip. The current validation considers the results for the swept tip (see Figure 3.5) with the tip Mach number of 0.626 at a preset blade collective angle and coning angle of 10.5^o and 2.31^o, respectively. Grids of 1, 2, and 3 million points are used to compare pressure coefficient values with experiment. All computations were run inviscid.
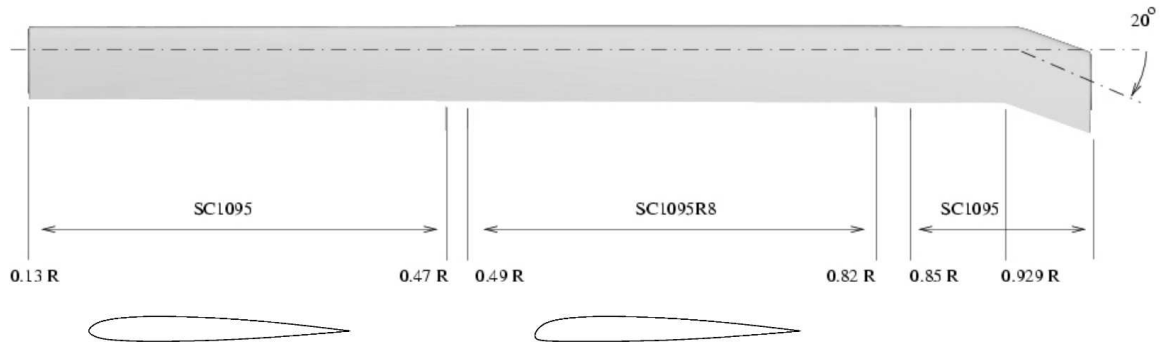
Figure 3.5: UH-60A Rotor Geometry.

The twist distribution is taken from Dindar *et al.* [115] and is presented in Figure 3.6(a). Figure 3.6(b)-(c) compares C_P values at blade stations, r/R = 0.775, 0.865, and 0.920 at the aforementioned test conditions. Excellent agreement with experiment for all the grids is evident for all locations.

3.5 HIMARCS I Test Case

A grid dependency study was conducted for the baseline HIMARCS I rotor and results can be found in Figure 3.7. Grid sizes of approximately 1.5 million, 2.65 million, and 4.8 million were compared for viscous solutions in hover. Convergence to a C_T of 0.00829 was achieved for all three grids and the respective results for C_Q and FM were evaluated. A grid independency trend can be clearly seen for grids with over 5 million points from both plots. The majority of grid sizes used in the current research focus around the 2-3 million point mark due to the high number of calculations. These grids employed for these calculations will be refered to as Blocking A. However, fine grids were also employed to assure solutions could be compared with confidence. These grids will be refered to as Blocking B.

Next, the effect of wake resolution on the computed blade loads was evaluated. This involved taking a fine grid that would provide grid independent solutions and reducing the number of points approaching and behind the blade by 10% and 20%. The grid used in this case was a modified grid compared to that used in Figure 3.7 to allow the addition of a blended flap with a total grid size of 5.25 million points. All three cases were run for the exact number of time steps with the same boundary and flow conditions. As can be seen from both plots, the reduction in points in the wake has had the effect of reducing the blade loads albeit by less than 1% in the most extreme case (see Figure 3.8(b)).

Finally, validation for the HIMARCS I test case is offered. Before the results are discussed, a few factors should be considered with respect to the experiment itself. Firstly, the experiment employed a model fuselage with a hub during testing, where the current work assumes an isolated rotor with a modelled shaft. Secondly, the trim settings employed in the experimental testing were not published. To overcome this, a reduced-order, rotorcraft aerodynamic code is employed to give rough predictions for the rotor trim, which was then built-in to the rotor blade geometry. Thirdly, the only data published for validating against was performance data (C_T, C_Q, FM). No pressure data or flowfield visualisations were offered, which hinders attempts at comprehensive validation. To confirm the validity of the code for such studies, the aforementioned test cases were presented. Finally, the actual domain of the wind tunnel appears quite restrictive for hover testing where the downwash may interact with the walls. However, tunnel wall effects were considered negligible and no corrections were implemented. With this in mind, the farfield domains used in the current work were similar to those in the experiment.

Figure 3.9 presents the validation results for the 3D CFD against experiment. Figure 3.9(a-b) compares C_Q versus C_T and C_T versus FM for the medium, inviscid and viscous grids used in the current work. The inviscid CFD gives reasonable predictions compared to experiment, but overpredicts at medium to high thrust settings which is to be expected since these calculations do not properly account for drag and cannot predict blade stall. The viscous CFD compares well with experiment and both methods capture the trends well. The slight dip in performance for the viscous solution could be attributed to the turbulence model underpredicting blade stall, a well-known issue regarding the k-ω model in aerospace applications [116, 117]. For the results using the finer grids (see Figure 3.9(c-d)), two separate boundary conditions were applied. The first set of results used the original farfield domains as in the experiment, with the second set of results having the farfield and outflow located at 4 times the blade span. The results using the experimental boundaries demonstrate the dip in performance at high thrusts as with the previous results. Extending the farfield boundaries, however, improves predictions and eliminates the element of blade stall. Investigation of the flowfield indiciates that the loss in performance evident with the narrow domain is because of the tip vortex striking the preceeding blade due to strong upwash caused by the farfield wall being too close; the blade vortex interaction causing local blade stall. Extending the domain reduces the strength of the upwash and the vortex passes beneath the blade, as expected. It is interesting to note, though, that both sets of results fall within experimental errors. The difference between the inviscid and viscous results is due to viscosity and the omission of viscous drag with the inviscid method, and not the choice of turbulence model which is coupled with the RANS solver and includes viscous effects.

Nonetheless, in the current study we are interested only in the relative differences in predictions between various configurations, with satisfactory validation of the solver achieved for all test cases.

(a)

(b)

(c)

(d)
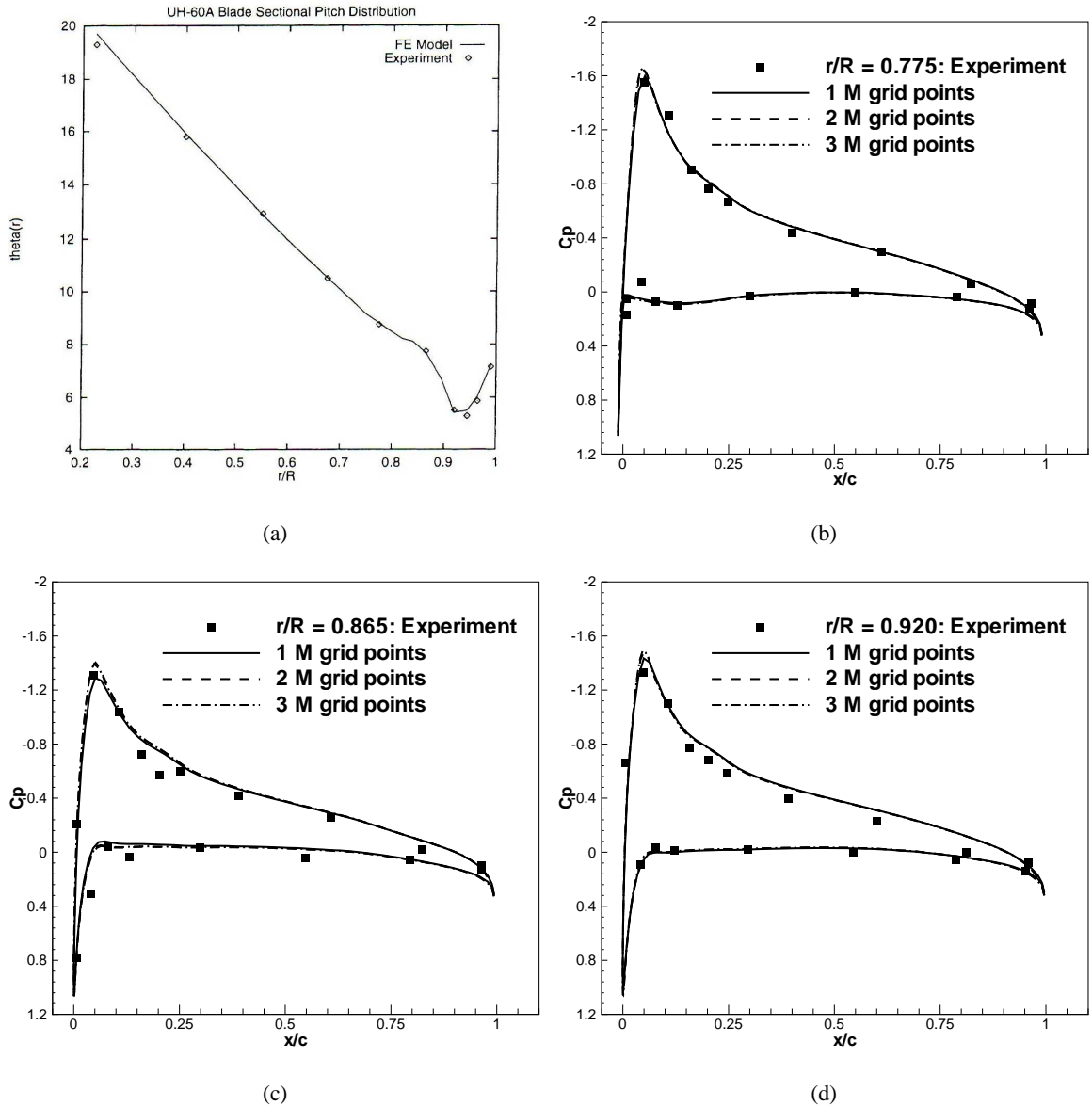
Figure 3.6: Comparison of Cp for UH-60A. (a) Twist distribution. (b) r/R = 0.775. (c) r/R = 0.865. (d) r/R = 0.920. ($M_T = 0.626$, $\theta_0 = 10.5^o$, $\beta_0 = 2.31^o$)

(a)   (b)
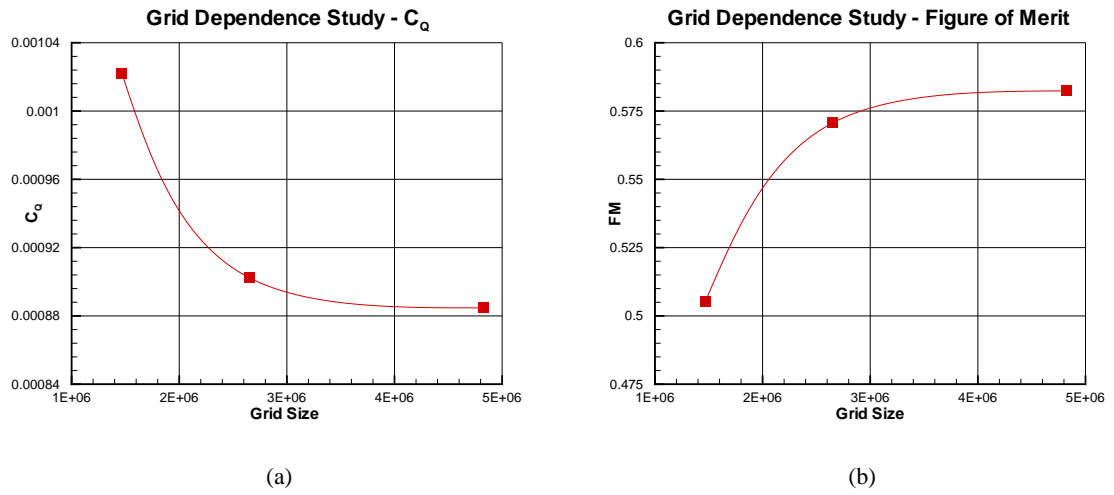
Figure 3.7: Grid dependency study for HIMARCS I rotor. (a) C_Q vs. Grid Size. (b) FM vs. Grid Size. ($M_T = 0.627$, Re = 168,000, k-ω turbulence model)

(a)   (b)
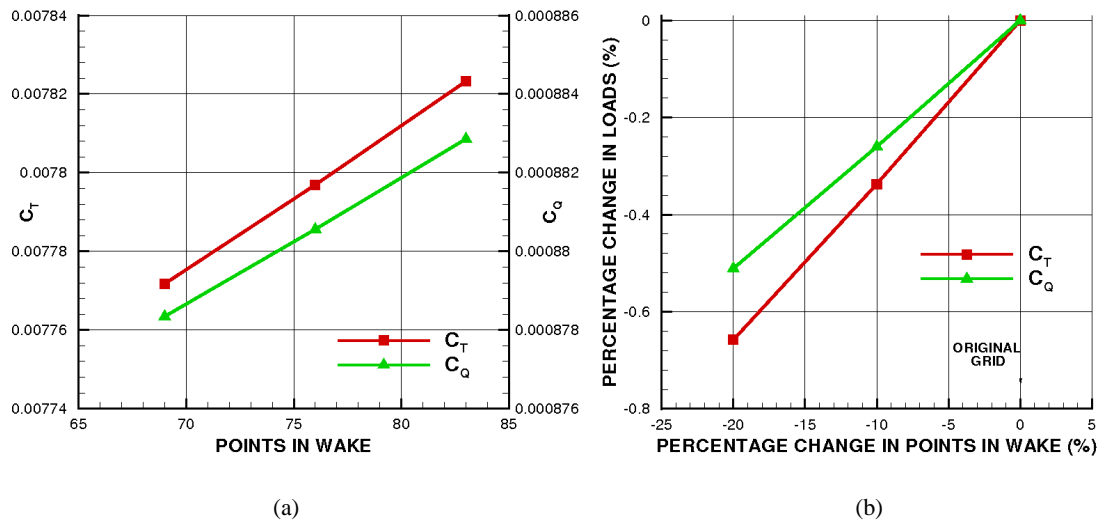
Figure 3.8: Wake resolution study. (a) Blade loads vs. wake resolution. (b) Percentage change in loads. ($M_T = 0.627$, Re = 168,000, k-ω turbulence model)

68
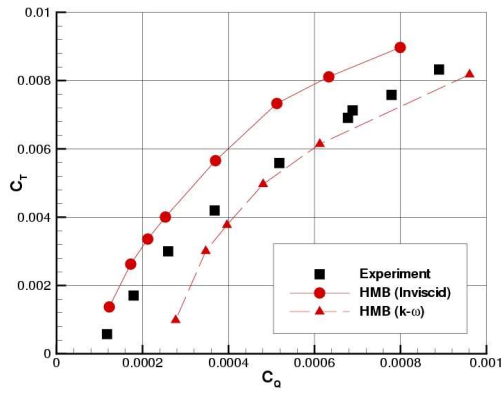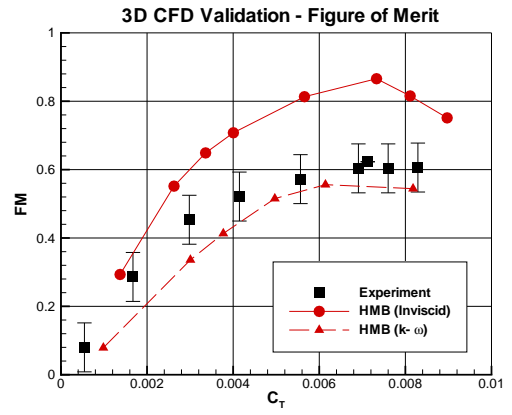
(a)   (b)
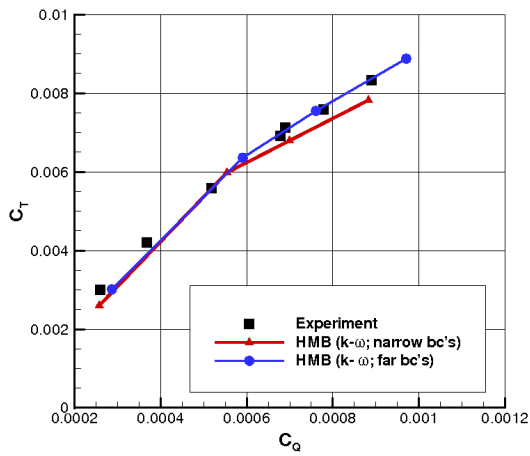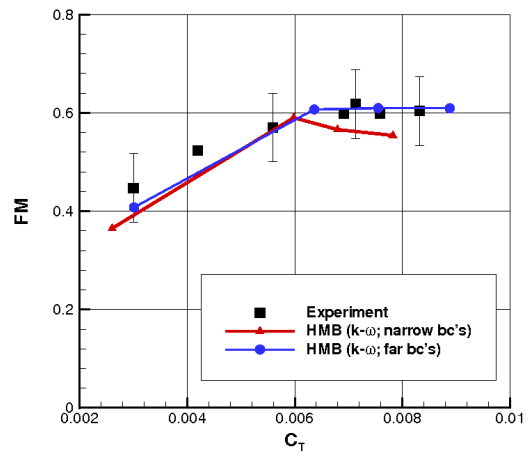
(c)   (d)

Figure 3.9: HIMARCS I hover performance validation. Blocking A: (a) C_T vs. C_Q. (b) FM vs. C_T. Blocking B: (c) C_T vs. C_Q. (d) FM vs. C_T. ($M_T = 0.627$, Re = 168,000, k-ω turbulence model)
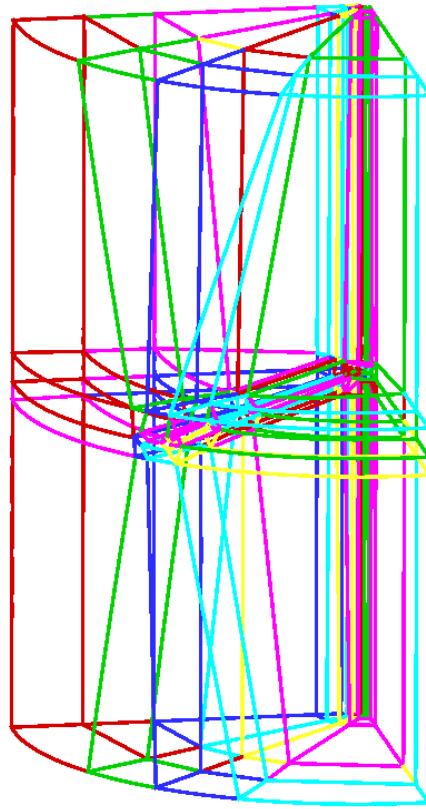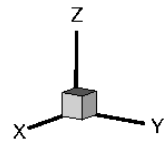
(a)
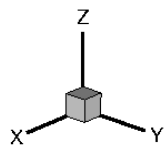
(b)

Figure 3.10: Farfield boundary distances. (a) Narrow domain. (b) Large domain.

Chapter 4

2D Hover Results

4.1   Introduction

This work focuses on the computational study of flapped rotor blades in hover for improved performance. As described before, two different computational methods are combined to facilitate this process, namely a reduced-order, rotor aeromechanical code and CFD. This section constitutes the design analysis conducted with the reduced-order model. The use of a small, time-efficient model allows for the assessment of a large spectrum of design conditions, although it lacks the fine detail achievable by CFD. The geometric and aerodynamic parameters that tune these models to specific cases have to be obtained external to the code; it has no way to assess blade aerodynamic properties purely from geometric data. This data was generated via 2D CFD computations of blade section geometric data. These sections were taken from the HIMARCS I rotor blade [16] experiment, which forms the foundation of the research presented here. The HIMARCS I experiment focused on reducing the required levels of blade twist and recuperating the loss in hover performance by deploying a slotted flap or slat, with varied levels of success. When transferring to forward flight, the high-lift device would be returned to its neutral position and improved forward flight performance would be obtained with reduced compressibility effects, and greater thrust at the advancing blade tip due to the lower, negative local blade pitch angle at the tip.

In their report, Noonan *et al.* [16] gave the sections and planform design of the HIMARCS I rotor, both for the clean case and for the fixed, 3° slotted flap placed at the tip. The HIMARCS I is a rectangular blade that consists of two blade sections - the RC(4)-10 inboard [96] and the RC(6)-08 outboard [97]. The outboard RC(6)-08 section was removable, which allowed for quick interchange between the various flow control devices. See Table 4.1 for a summary of the blade geometry com-

Rotor radius, R	56.224 inches	Flap type	Slotted
Blade chord, c	4.454 inches	Flap span	15% R
Rotor solidity	0.101	Flap location	92.5% R
Flap chord	32%c	Tip Mach No.	0.627

Span	Twist	Section Detail
0%-12.2%R	1° to 0°	Shaft axis to Root cut-out
12.2%-22.4%R	0° to -1°	Root cut-out to RC(4)-10
22.4%-80%R	-1° to -5.4^o	RC(4)-10
80%-85%R	-5.4^o to -5.8^o	Transition
85%-100%R	-5.8^o to -7°	RC(6)-08
85%-100%R	-5.8^o to -7°	3° slotted flap

* = from root to tip

Table 4.1: HIMARCS I rotor data.

piled from data presented in Ref. [16].

In this chapter, an analysis is conducted into the aerodynamics of a modelled HIMARCS I rotor blade with a slotted flap. The process by which the aerodynamic data required for this analysis was computed is described, including a summary of the influence each parameter has on the code's predictions. This includes the extraction of the constants from 2D CFD data and the setup of the CFD calculations. CFD had to be used since no experiments were available for the sectional aerodynamics of the single flapped rotor in the literature. The predictions using this data were indirectly validated since the final 3D model was close to the hover experimental values. In addition, the HMB solver is well-validated for such flows [109, 7, 108, 106]. The code is then used to perform an extensive parametric study of various flap configurations. After consideration of the results, optimum flap designs and their respective trim settings are selected for verification using the high fidelity, 3D CFD, which will be reported in the next chapter. A concise listing of this procedure can be found in table below:

1. Obtain 2D aerodynamic data via CFD.

2. Conduct parametric study using ROM of various flap configurations.

3. Evaluate results and select optimum ("best fit") designs.

4. Verification of results using inviscid and viscous 3D hover CFD.

5. Effect of the aerodynamics of both methods on hover trim state.

4.2 Design Method

The analysis of flapped rotors in hover requires the rapid assessment of many flap configurations and comparisons with clean blades over a wide range of thrust settings. The CPU demands of 3D CFD, which includes the time required to generate the necessary surface boundaries and to produce high-quality, block-structured grids, is too expensive to conduct such a venture alone, and will remain so until we see even greater advances in computing power. However, simpler models such as the blade element method as used in the current work lend themselves well to such studies.

4.2.1 Combined ROM-CFD

Although it lacks the entire package as offered by CFD, with the provision of 2D aerodynamics, these models allow for a time efficient analysis of various flight conditions at very low computational cost. Table 4.3 highlights the various CPU times required by the methods used in this study for calculating the performance of a rotor in hover. The blade element method is capable of evaluating over 7000 design conditions in under 3 hours on a single 2.4Ghz Pentium 4 processor with 1GB RAM. Calculations to obtain 2D aerodynamic data at a single Mach number for a single blade section for input into the model can take up to 8 hours alone. Although both methods are more time efficient than 3D CFD, a single hover computation offers much more detail in both blade loadings and flowfield visualisations.

Method	Grid Points	Processors[*]	Design Conditions	Wall Clock Hours
Blade Element Method	-	1	≈ 7700	≈ 2.5
2D URANS CFD	85,000	1	40	≈ 8
3D Inviscid CFD	2.2M	8	1	≈ 22
3D RANS CFD	2.7M	8	1	≈ 36
3D RANS CFD	5.25M	24	1	≈ 36

[*] 2.4-3Ghz Pentium 4 with 1GB DDR RAM.

Table 4.3: Grid size and CPU requirements for various methods.

Consequently, blade element computations were performed for a range of flap configurations over a range of thrust and trim settings. The flap parameters selected for investigation were (1) flap deflection angle, (2) flap location, (3) flap chordwise length, and (4) flap span-wise length. The blade element method splits the blade boundary into 44 sections and, with the exception of the most inboard element, the whole length of the blade was considered in the design process. Certain

constraints had to be applied on the possible flap configurations for the design to be viable. Firstly, the length of the flap had to be restricted due to potential problems with blade elasticity. The blade chord was limited in size to that used in the original experiment, since a flap too large would offer problems with structural stability. The original work in the HIMARCS I experiment considered a clean rotor and one with a slotted flap with fixed chord and deflection angle at the blade tip. To take into account variations in flap chord, slotted flap configurations geometrically-equivalent to the designs employed in the HIMARCS I paper were considered. Flap chord sizing was accomplished by extracting the geometric data of the original design and scaling it by a factor of 33% and 66% of the original flap geometry. The new geometry was then super-positioned on both clean sections with an approximation to the slot geometry accounted for in the same way. To reduce the number of 2D URANS calculations, the variations in flap chord lengths of 22.33%c and 11.67%c were considered by running CFD caclulations at M = 0.5 and Re = $3x10^6$, which is the middle region of the test matrix used for the other 2D calculations, and a ratio between the extracted coefficients between the original 32%c slotted flap and the new results was implemented. Variations in flap deflection angle could not be treated in the same way due to the need to properly model the influence of adverse pressure gradients at high flap deflection angles and boundar layer mixing. In this case, the geometry for the flap was rotated about its c/4 point by the necessary amount and 2D CFD calculations were conducted. Since no specification for the pivot point for the flap was given in the original report by Noonan *et al.*, it was estimated as a quarter of the distance from the most advance point and the trailing-edge of the flap. Although the flap itself is slightly cambered and this point may or may not reflect the actual c/4 point, with the lack of any further detail within the original report [16] this assumption is considered satisfactory for the purposes of this study.

4.2.2 Hover Trim

Each test configuration is considered at various thrust coefficients from C_T = 0.0005 to 0.00829. At each thrust setting, the blade element method uses a trimmer based on the Newton-Raphson method. At the first time step, the model approximates the trim settings based on an estimated helicopter weight. The helicopter thrust is then recalculated via the updated trim settings and the process continues until convergence to the designated thrust coefficient is achieved. In the model, the tolerance that the trimmer must match is in the order of 1%, which can be deemed satisfactory for what is already an approximate method. As detailed in Figure 4.1(a), the model requires 8 retrimming steps to converge to a solution, which equates to a few seconds in real time. On average, these retrimming steps number from 5-10, dependent on the accuracy of the initial approximation to

the helicopter weight. When compared to the computational time required by a single, inviscid 3D hover calculation in Figure 4.1(b), the time efficiency of the method for the purpose it was designed for is clear to see, although the trimmer in this case may require more intermediate steps before re-trimming occurs. The precision of the predicted trim settings using the blade element method and 3D inviscid hover CFD will be compared using 3D viscous CFD, to see the effect of the accuracy in the aerodynamics of both methods.

(a)   (b)
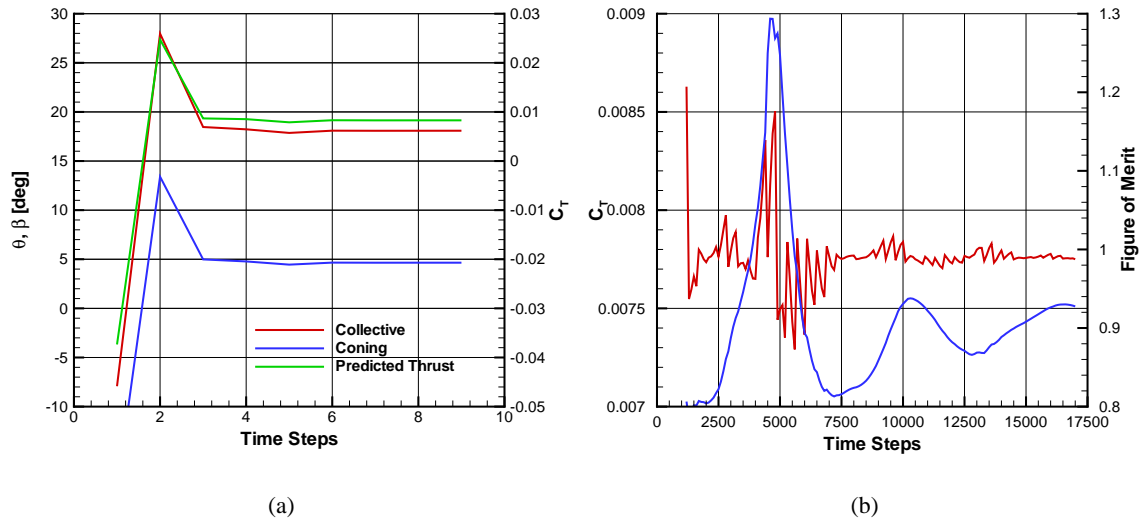
Figure 4.1: Computational cost of blade element trimming methods.

4.2.3 Grid Generation

The CFD solver used here, HMB, requires high quality, block structured grids for its computations. In the process of generating the sectional data required by the blade element method, 2D computational grids were created. Several grid topologies had to be considered and these are summarised in Table 4.4. The baseline HIMARCS I rotor is made out of two sections, the RC(4)-10 [96] and the RC(6)-08 [97]. Also, both had to be considered with flaps of varied chord and deflection angle. All meshes were created using ICEM CFD Hexa package, which allows for block-structured grid generation of complex planforms. This is accomplished by placing blocks around the wall and farfield boundaries where fluid is present, and applying gemoetric laws to the block edges to obtain desired distribution of grid points. As presented in Figure 4.2, all clean sections in this work use C-type grids, which allow for optimum mesh quality near or around the leading edge and the wake of the aerofoil. Sections with slotted flaps, however, require more elaborate multiblock topologies with more than double the number of blocks required for a clean section. In the current work, a C-C grid is employed which allows for high quality cells at the leading-edges of both the main aerofoil

and the flap. This means we have blocks situated between the main element and flap so that flow through the slot is captured.

Geometry	Grid Topology	Blocks	Grid Size	Points on Surface	Points on Flap	First Cell Distance
RC(6)-08	C grid	6	83,000	360	-	10^{-5}c
RC(4)-10	C grid	6	83,000	360	-	10^{-5}c
3° Slotted Flap (O)	C-C grid	14	81,200	320	220	10^{-5}c
6° Slotted Flap (O)	C-C grid	14	81,200	320	220	10^{-5}c
10° Slotted Flap (O)	C-C grid	14	81,200	320	220	10^{-5}c
3° Slotted Flap (I)	C-C grid	14	81,200	320	220	10^{-5}c
6° Slotted Flap (I)	C-C grid	14	81,200	320	220	10^{-5}c
10° Slotted Flap (I)	C-C grid	14	81,200	320	220	10^{-5}c
O - Outboard, I - Inboard						

Table 4.4: 2D multiblock grid details used for viscous CFD calculations.

All the 2D grids in the current work utilise first wall spacings and cell clustering that is deemed necessary for an aerofoil section operating in turbulent flow with boundary layer transition. Normal to the surface, a first wall spacing of 10^{-5}c is applied to ensure at least 10 grid points are resident in the boundary layer, with the exception being at the trailing-edge where a spacing of 10^{-4}c is deemed sufficient to ensure the pressure is resolved properly. The distribution of points in the streamwise direction varies. At the leading edge, cells begin at 10^{-3}c to ensure the geometry is matched adequately. This is especially important since the behavior of the boundary layer over the remaining portion of the aerofoil is sensitive to the leading-edge curvature. The distribution of points from the leading-edge to the point of maximum camber is sufficient to ensure adequate matching of the original geometry.

Using the previous criteria, grid sizes were aimed at around 80,000 to 90,000, that from previous experience were shown to offer grid independency in the calculated integrated loads. With respect to points on the surface, clean sections had a total of 360 grid points with the flapped sections having 320 and 220 grid points for the main and flapped elements, respectively. For comparison, the distribution of points for both sets of grids were kept as similar as possible.

4.3   2D Aerodynamic Data

Using the aforementioned grids, 2D CFD calculations were conducted to generate the necessary aerodynamic parameters required for the blade element method. These parameters allow the method to model any rotor blade that is formed by the geometric sections. In the current work, 2D URANS CFD was used to provide the necessary data via quasi-steady ramping calculations. Runs were made from Mach numbers of 0.3 to 0.9 in steps of 0.1 at a fixed Re = $3x10^6$. Linear interpolation was used to obtain the Mach numbers at every intermediate step. Table 4.5 lists all 2D computations completed for the generation of the aerodynamic look-up table.

Computational Parameters					
Case	*Re*	*M*	α^+	$(x/c)_r$	*Motion*
RC(4)-10	$3x10^6$	0.3-0.8	0.4	0.25	-5-35° Ramping
RC(4)-10 + 3°, 32%c flap	$3x10^6$	0.3-0.8	0.35	0.25	-5-35° Ramping
RC(4)-10 + 6°, 32%c flap	$3x10^6$	0.3-0.8	0.35	0.25	-5-35° Ramping
RC(4)-10 + 10°, 32%c flap	$3x10^6$	0.3-0.8	0.35	0.25	-5-35° Ramping
RC(4)-10 + 3°-10°, 21.33%c flap	$3x10^6$	0.5	0.35	0.25	-5-35° Ramping
RC(4)-10 + 3°-10°, 10.67%c flap	$3x10^6$	0.5	0.35	0.25	-5-35° Ramping
RC(6)-08	3×10^6	0.3-0.9	0.4	0.25	-5-35° Ramping
RC(6)-08 + 3°, 32%c flap	$3x10^6$	0.3-0.8	0.35	0.25	-5-35° Ramping
RC(6)-08 + 6°, 32%c flap	$3x10^6$	0.3-0.8	0.35	0.25	-5-35° Ramping
RC(6)-08 + 10°, 32%c flap	$3x10^6$	0.3-0.8	0.35	0.25	-5-35° Ramping
RC(6)-08 + 3-10°, 21.33%c flap	$3x10^6$	0.5	0.35	0.25	-5-35° Ramping
RC(6)-08 + 3-10°, 10.67%c flap	$3x10^6$	0.5	0.35	0.25	-5-35° Ramping

Table 4.5: Test conditions to generate the aerodynamic data for the hover study

The ramping calculations were setup so as to ensure adequate capture of the zero-lift angle, the stall angle, and the moment break. The grids were pitched about their quarter-chord from angles of attack of -5° to 35°. Although the aerofoils generally stalled earlier than this maximum value, the extra time steps allowed for resolution of the loading during separated flow. Time steps corresponding to increments in angle of attack of 0.35^o were used to again ensure proper resolution of the integrated load curves, from which the aerodynamic parameters are extracted. There parameters are presented in the following tables. They are listed for the RC(6)-08 outboard section in Table 4.6 and in Table 4.7 for the RC(4)-10 inboard section. Plots of the data sets can be found in Appendix A. Where it was impossible to extract the relevant coefficients from the data set due to oscillations in curve data, appropriate values based on a standard rectangular blade were implemented. However, it should be noted that this was never required for the major parameters in this work, namely the lift-curve slope, the zero-lift angle, the stall angle, and the zero lift drag coefficient.
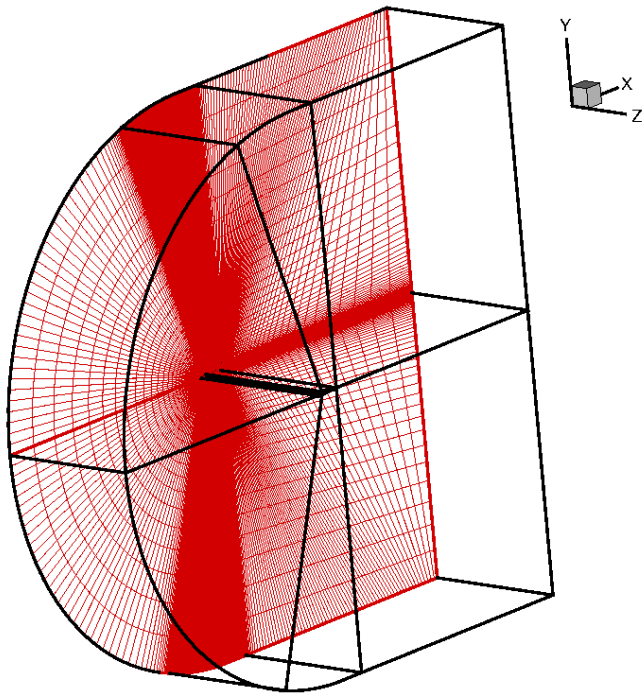
(a)
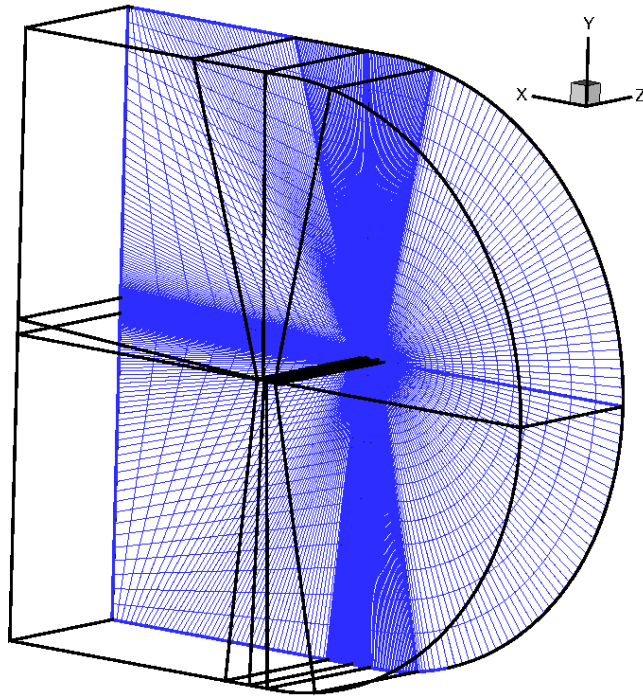
(b)

Figure 4.2: 2D multiblock topology. (a) Clean section. (b) Section with slotted flap.

Examining the aerodynamic coefficients, it is apparent that there is a slight inconsistency in the values for the stall angles. There exists a large change in the stall angle from the clean section to the 3° flapped section, but a smaller jump from the 3° section to the 10° section. This is down to the method stated by Beddoes [65] for extracting the static stall parameter, which was designed with clean aerofoils in mind. To confirm the validity of the original data, Figure 4.3 presents the lift- and moment-curves for the RC(4)-10 section with variable flap chord lengths. This demonstrates the increase in maximum lift tending to a peak value with increased flap size. The issue with the Beddoes method is with the parameter $F = 0.7$, at which point blade stall is said to occur. However, since this was a slotted flap aerofoil, this criteria was implemented on the main element only, which is considerably shorter than the clean aerofoil. Hence, it occurs that the Beddoes criteria [44, 65, 71, 118] finds that the flapped aerofoils stall earlier than normal. Infact, in most results it was apparent that the flap's boundary layer remained fully attached. Fortunately, this has little bearing on the computed results due to the stronger influence of the zero-lift angle, lift-curve slope, and the zero-lift drag coefficient on the predictive capability of the model in hover.
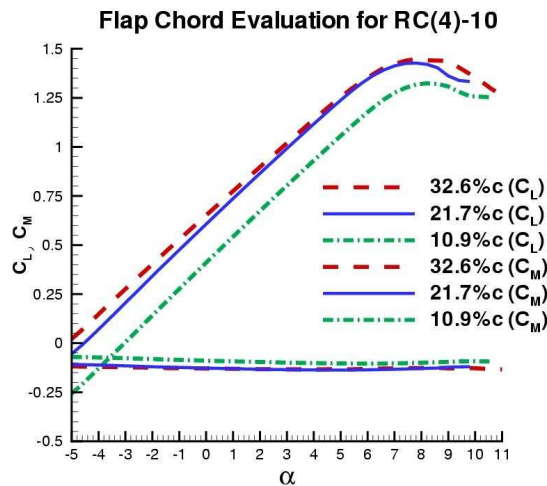
Figure 4.3: CFD computed sectional lift and moment coefficient data for the RC(4)-10 with a 10.69%, 21.33%, and 32% chord slotted flap at 10° flap deflection from current method. (M = 0.5 and Re = $3x10^6$)

4.4 Parametric Study

A parametric study has been conducted to investigate the potential for improving helicopter rotor blade performance by implementing trailing-edge flaps on the rotors. As described in Chapter 1, the concept for performance enhancement with flaps is that of achieving the same levels of thrust

Mach	C_{L_α}	α_0	α_1	S1	S2	k_0	k_1	k_2	m	C_{M_0}	C_{D_0}
0.3	0.1074	-0.8795	16.9440	1.9772	2.1390	0.0089	-0.1879	0.1890	0.1749	-0.0234	0.0029
0.4	0.1109	-0.6371	14.8147	1.4302	3.3410	0.0192	-0.1939	0.3435	0.1141	-0.0191	0.0032
0.5	0.1185	-0.5994	12.4041	1.2020	2.3699	0.0129	-0.2114	0.3727	0.0401	-0.0087	0.0028
0.6	0.1243	-0.8057	10.6684	0.8916	9.6668	0.0211	-0.2246	0.3790	0.1324	-0.0120	0.0029
0.7	0.1440	-0.7214	8.9793	0.6274	2.4638	0.0295	-0.2505	0.3867	0.5051	-0.0150	0.0035
0.8	0.1853	-0.6028	4.5831	1.0112	15.0756	-0.0819	-0.1566	0.0298	0.3225	-0.0244	0.0042

RC(6)-08

Mach	C_{L_α}	α_0	α_1	S1	S2	k_0	k_1	k_2	m	C_{M_0}	C_{D_0}
0.3	0.0987	-2.3491	14.0437	2.0000	2.0000	-0.0192	-0.1623	0.0000	0.1500	-0.0625	0.0059
0.4	0.0918	-1.7598	12.2920	2.0000	2.0000	-0.0827	-0.1154	0.0000	0.1500	-0.0433	0.0048
0.5	0.0920	-1.7853	9.84562	2.0000	2.0000	-0.0728	-0.1405	0.0000	0.1500	-0.0401	0.0048
0.6	0.1065	-1.7066	8.80473	2.0000	2.0000	-0.0793	-0.1533	0.0000	0.1500	-0.0416	0.0044
0.7	0.1116	-1.6760	7.40411	2.0000	2.0000	-0.0874	-0.1471	0.0000	0.1500	-0.0504	0.0044
0.8	0.2357	-1.2604	7.27676	2.0000	2.0000	-0.1481	-0.0941	0.0000	0.1500	-0.0585	0.0065

RC(6)-08 with 3° slotted flap

Mach	C_{L_α}	α_0	α_1	S1	S2	k_0	k_1	k_2	m	C_{M_0}	C_{D_0}
0.3	0.1153	-5.9198	13.7049	0.2627	0.1538	-0.0307	-0.1778	0.8325	0.0198	-0.1130	0.0033
0.4	0.1216	-5.6062	11.5061	0.2193	0.7933	-0.0202	0.0000	0.0000	0.1500	-0.1151	0.0072
0.5	0.1299	-5.3413	8.94631	0.1667	0.9507	-0.0310	0.0000	0.0000	0.1500	-0.1179	0.0091
0.6	0.1418	-5.0331	7.54988	0.1420	4.9036	-0.0301	0.0000	0.0000	0.1500	-0.1199	0.0109
0.7	0.1414	-4.6845	4.46866	0.0913	9.2888	-0.0773	0.0000	0.0000	0.1500	-0.1294	0.0156
0.8	0.2165	-4.0253	9.83200	0.9036	5.8651	-0.1044	0.0000	0.0000	0.1500	-0.1531	0.0205

RC(6)-08 with 10° slotted flap

Table 4.6: CFD generated aerodynamic parameters for the RC(6)-08 blade section with various flap arrangements. (Upper) RC(6)-08. (Middle) RC(6)-08 with 3° slotted flap. (Lower) RC(6)-08 with 10° slotted flap.

$Mach$	C_{L_α}	α_0	α_1	$S1$	$S2$	k_0	k_1	k_2	m	C_{M_0}	C_{D_0}
0.3	0.1074	-1.3249	22.4831	2.6075	2.8409	0.0107	-0.0725	0.2606	0.1509	-0.0264	0.0035
0.4	0.1118	-1.0869	18.2186	2.0191	11.9962	0.0200	-0.1083	0.0552	0.1005	-0.0217	0.0039
0.5	0.1395	-1.0685	13.6977	1.4525	1.1291	0.0158	-0.1418	0.3326	0.1086	-0.0130	0.0031
0.6	0.1235	-1.4495	10.9048	0.8996	11.4906	0.0303	-0.1794	0.3041	0.0456	-0.0208	0.0031
0.7	0.1295	-1.7383	7.8214	0.5448	4.3438	0.0340	-0.1905	0.3041	0.0456	-0.0347	0.0073
0.8	0.2169	-1.1430	3.0396	0.7891	16.4785	-0.0621	-0.1037	0.1102	0.3902	-0.0538	0.0217
					RC(4)-10						
0.3	0.1156	-1.7883	16.1145	0.3055	1.9265	-0.0241	0.0000	0.0000	0.1500	-0.0439	0.0040
0.4	0.1203	-1.8439	15.4263	0.2931	2.2985	-0.0264	0.0000	0.0000	0.1500	-0.0460	0.0034
0.5	0.1299	-1.8651	12.0345	0.2414	2.7154	-0.0347	0.0000	0.0000	0.1500	-0.0489	0.0032
0.6	0.1491	-1.6593	8.5313	0.1765	6.2348	-0.0404	0.0000	0.0000	0.1500	-0.0488	0.0046
0.7	0.1968	-1.6104	5.6825	0.1124	9.2263	-0.0731	0.0000	0.0000	0.1500	-0.0498	0.0097
0.8	0.2634	-1.5173	3.5900	0.3337	2.0689	-0.1035	0.0000	0.0000	0.1500	-0.0775	0.0243
					RC(4)-10 with 3° slotted flap						
0.3	0.1163	-5.6590	18.4516	0.3527	2.6919	-0.0112	-0.1376	0.3434	0.3509	-0.1140	0.0088
0.4	0.1209	-5.3849	14.6005	0.2910	3.2506	-0.0097	-0.1630	0.2373	0.3697	-0.1154	0.0115
0.5	0.1275	-5.1399	10.9180	0.2146	1.5201	-0.0118	0.0000	0.0000	0.1500	-0.1180	0.0119
0.6	0.1422	-4.8778	7.7901	0.1619	5.7921	-0.0177	0.0000	0.0000	0.1500	-0.1245	0.0143
0.7	0.1678	-4.3467	5.6128	0.1188	7.9802	-0.0578	0.0000	0.0000	0.1500	-0.1152	0.0256
0.8	0.1941	-4.4192	4.9056	0.5864	18.7677	-0.0760	0.0000	0.0000	0.1500	-0.1721	0.0498
					RC(4)-10 with 10° slotted flap						

Table 4.7: CFD generated aerodynamic parameters for the RC(4)-10 blade section with various flap arrangements. (Upper) RC(4)-10. (Middle) RC(4)-10 with 3° slotted flap. (Lower) RC(4)-10 with 10° slotted flap.

from a rotor, but at a reduced blade tip angle. Rotor blades have a dynamic head that is at a maximum at the blade tip, which is the zone where strong tip vortices are shed. This leads to increased induced drag, induced power, and therefore increased rotor torque. Blade twist helps weaken the tip vortices by offering higher local blade angles inboard of the rotor, hence the ability to achieve the same amount of thrust as a lower twist blade, but with a smaller blade tip angle. This reduces the loading outboard and hence the levels of induced drag. This study looks to evaluate a low twist rotor which, although with clear benefits in forward flight performance [15], has the disadvantage of large levels of induced drag due to the aforementioned physics. The location of slotted flaps both inboard and outboard of the HIMARCS I rotor to see if benefits in the rotor performance can be achieved are also considered. This research was conducted in two stages: (1) a manual variation of the flap parameters was attempted to gain an insight into expected results, and (2) a comprehensive, automated parametric study was completed.

Although the blade element method is efficient, its predictions are dependent on having access to external aerodynamic data, unlike CFD. To obtain this data, every flap configuration had to be tested in 2D using CFD, which allowed for an aerodynamic database to be compiled for test conditions described in Section 4.3. This database served as the lookup table for the blade element method and was validated as much as possible, as discussed previously. CFD was used since nothing else was available and the code is well-validated for such cases. Also, the theoretical/CFD method was approximate and was used here to see the effect of the flap with respect to the clean blade. The method was then relied upon for calculating the performance data and trim settings of the full rotor. The results were evaluated and optimum flap configurations that offer the lowest torque per equivalent thrust i.e. high FM over the widest range were selected and computed using 3D CFD.

Table 4.8 presents the variations applied to each parameter and the overall number of assessed designs considered. When considering the inboard location of the flap, a maximum flap span of up to 24%R was considered for flap centre locations from 28%R-68%R. To allow for closed blade tips, cut-off locations were introduced at 1%R. Such constraints were possible for the inboard section of the rotor since it constituted almost 58% of the actual rotor span. The flap was considered to have a null effect beyond these boundaries. Combined with three flap chord lengths and two flap angles, the total number of designs evaluated per C_T was 396. Similarly, for the outboard section, a maximum flap span of up to 10% was considered with the flap centre located at 90%R-96%R. Combined with the flap chord lengths and deflection angles, the number of designs considered totalled 120 per C_T. This is noticeably smaller than for the inboard section, but is understandable when one considers the

outboard section of the HIMARCS I rotor is only 15% of the actual rotor span [16]. Nonetheless, the parameter space being evaluated was considered sufficient for evaluating the current concept.

	Flap Location	Flap Span	Flap Chord	Flap Deflection	Number of Designs
Figure 4.4	23%R, 92.5%R	5%- 25%R	32%c	3°	6 at 15 C_T's
Figure 4.5	23%R- 92.5%R	5%	32%c	3°	6 at 15 C_T's
Figure 4.6	23%R, 92.5%R	15%	32%c	3°, 10°	4 at 15 C_T's
Preliminary test matrix.					
Inboard	28%- 68%R	4%- 24%R	11.67%c, 22.33%c, 32%c	3°, 10°	396 at 15 C_T's
Outboard	90%- 96%R	2%- 10%R	11.67%c, 22.33%c, 32%c	3°, 10°	120 at 15 C_T's
Parametric study test matrix.					

Table 4.8: Summary of the parameter space investigated. (Upper) Preliminary results. (Lower) Parametric study.

4.4.1   Preliminary Results

The following calculations were performed using the blade element method with the aerodynamic parameters detailed in Tables 4.6 and 4.7. A coarse test matrix was first considered due to the manual setup of the problems. Results are presented in terms of the thrust coefficient, C_T, versus the Figure of Merit, FM. The former represents the lifting force coefficient of the rotor disc and the latter is the ratio of idealised power required to actual power required.

Figures 4.4(a) and 4.4(b) compare the thrust coefficient, C_T, against FM for various flap sizes inboard and outboard. The inboard and outboard flaps are set at a fixed deflection angle of $\delta = 3^o$ and are located at 23%R and 92.5%R, respectively. Figure 4.4(a) shows a considerable improvement in performance for an inboard flap per increment in flap size. As with a highly twisted rotor, initial results suggest that an increase in inboard loading with a flap seems to benefit rotor performance in hover. Increasing the size of the flap outboard (see Figure 4.4(b)) is shown to have a detrimental effect in hover, with the performance loss increasing with the flap size. The aerodynamic data from Table 4.6 suggests this could be due to a poor lift-to-drag ratio that is predicted for the flapped RC(6)-08 at near transonic Mach numbers. However, the influence of increased outboard loading due to the lift enhancement device on the strength of the induced drag could also be a factor here.

Figures 4.5(a) and 4.5(b) compare C_T versus FM for various flap locations. The flaps are set at a fixed size of 5%R and deflection angle of $\delta = 3^o$. In Figure 4.5(a), the inboard flap is moved from the quarter chord to the 3/4-chord span. A loss in performance is predicted as it moves further outboard (see Table 4.7), since the drag increases dramatically for the inboard sections at the higher Mach numbers. Figure 4.5(b) shows a large increase in performance with an outboard flap at moderate thrust levels, but predicts a degradation in performance elsewhere as the flap is moved from the tip to the 3/4-chord. This would suggest the outboard flap would be beneficial with a closed blade tip where it possibly has a lesser effect on the induced drag. A good combination of lift-to-drag along the entire blade may also be attributed to this rise in performance.

Results for varying the flap deflection are shown in Figures 4.6(a) and 4.6(b) where again C_T is plotted against FM. Flap deflections of $\delta = 3^o$ and 10° were used for both inboard and outboard flaps. The flap size was kept fixed at 15%R and the location for the inboard and outboard configurations where at 23%R and 92.5%R, respectively. Figure 4.6(a) indicates that an increase in performance is obtainable from an inboard flap at medium-high thrust levels by deflecting the flap down. As will be presented later, this displays similar performance characteristics as a highly twisted rotor in hover. In Figure 4.6(b), increasing the flap deflection outboard decreases performance at low- and high thrust, but improves performance slightly at mid-thrust levels.

Finally, the effect of twist on rotor performance is evaluated including comparisons with the best results from the flap study. Figures 4.7(a) and 4.7(b) present C_T against FM for blade twists between -7° and -14°. Two flap configurations have been considered. For both cases, the flap was located at 23%R and had 10° of deflection. The flap length was, however, different with lengths of 15%R (case A) and 25%R (case B). Increasing the blade twist can be seen to decrease performance at low thrust levels and improve performance at higher thrust levels. This is more evident from Figure 4.7(a) where the C_T against FM is plotted. The performance increases at higher thrust levels follows the same trends as one would expect [15] from twisted blades. At lower thrust levels, the trend shows twisted blades having less effect. Generally, experimental data shows little performance difference between blades with different levels of twist at low thrust coefficients. Performance for the inboard flapped rotors can be seen to improve on the baseline HIMARCS I rotor in Figure 4.7(b). This is a promising result, but requires further attention for better consideration of optimum designs before any 3D CFD can be prepared.

4.4.2 Results - Detailed Study

The following section describes a comprehensive parametric study of numerous flap configurations for clarification of the results from the initial study. Various flap sizes, locations, chords, and deflection angles were evaluated for both the inboard and outboard locations of the HIMARCS I rotor. Details of the parameter space for the study can be found in Table 4.8. Flap sizes and locations are given in percentage of blade span. For each flap location, the flap span, chord, and deflection angles were varied which resulted in the evaluation of over 396 inboard and 120 outboard designs. This was repeated for a range of experimental C_T values (as previously), as well as intermittent values to smooth out the final curve.

Results are presented in Figures 4.8 to 4.13 in the form of carpet plots where improvements upon the baseline blade in hover can be identified. These are in the form of the x-y axis being attributed the flap span location and the flap span size, respectively, with the contours being of Figure of Merit. Plots are presented for all three evaluated flap chord sizes with 3° and 10° of flap deflection. As before, all calculations were performed at a rotor tip Mach number, $M_T = 0.627$. Selected results for thrust coefficients of 0.0007, 0.0028, and 0.00829 are presented, with all results available in Appendix B.

Figure 4.8 presents results for 3° of flap deflection angle at a low $C_T = 0.0007$. At low thrust, it is evident that for the inboard flap configuration, the larger flap gives better performance than a smaller flap with performance also improving when the flaps are moved midboard. The outboard flap, however, gives better performance the move inboard it is placed. As the flap deflection angle is increased, (see Figure 4.9), a large change in the optimum location occurs with both the inboard and outboard results deferring to as small a flap as possible. Essentially, it is clear that increasing flap deflection angle is unbeneficial in this case. This result is very interesting as it seems as though a lower flap deflection in this case offers a lower drag coefficient value than the larger flap, since both are operating at the same C_T.
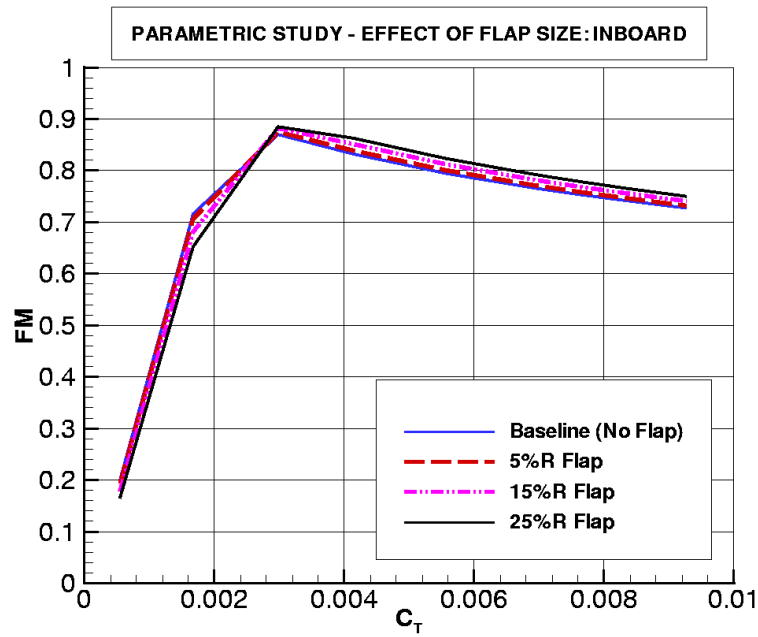
(a)
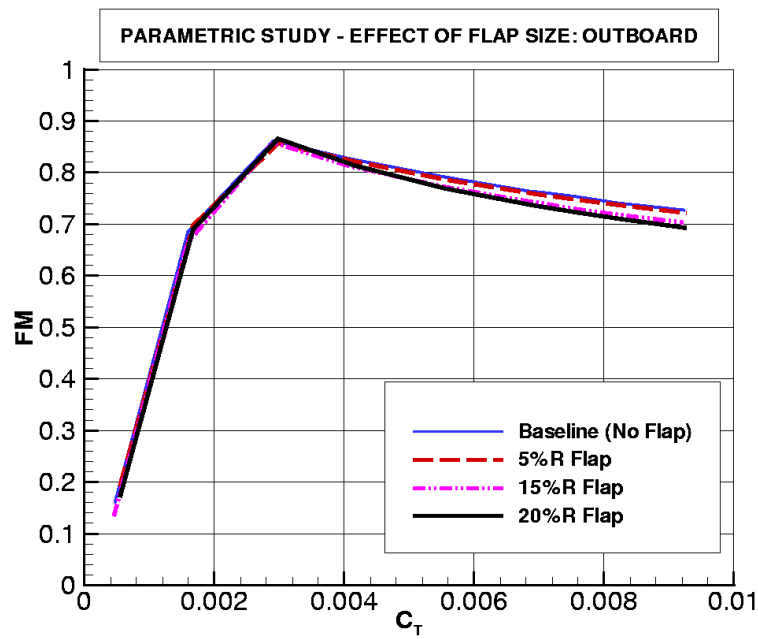
(b)

Figure 4.4: Effect of flap size in improving hover performance. The flap size is varied from 5%R to 25%R, with a fixed flap deflection angle, $\delta = 3^o$. (a) 23%R, inboard. (b) 92.5%R, outboard.
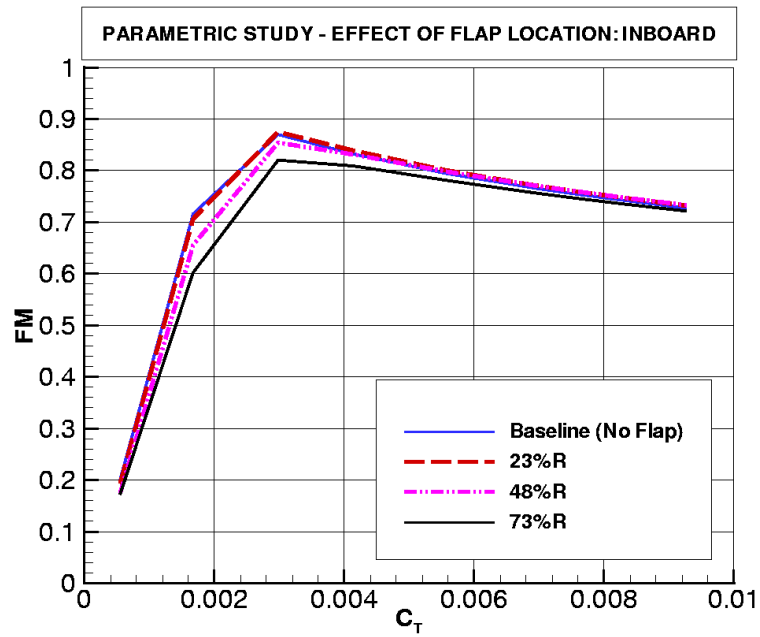
(a)
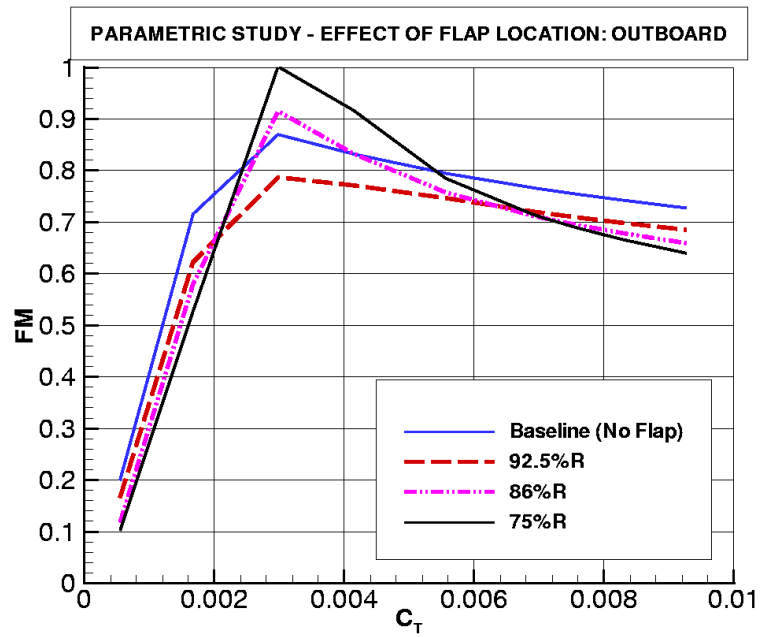
(b)

Figure 4.5: Effect of flap location in improving hover performance. The flap location is moved from 92.5%R to 23%R, with the flap deflection angle and flap size fixed at $\delta = 3^o$ and 5%R, respectively. (a) Inboard. (b) Outboard.

(a)

(b)
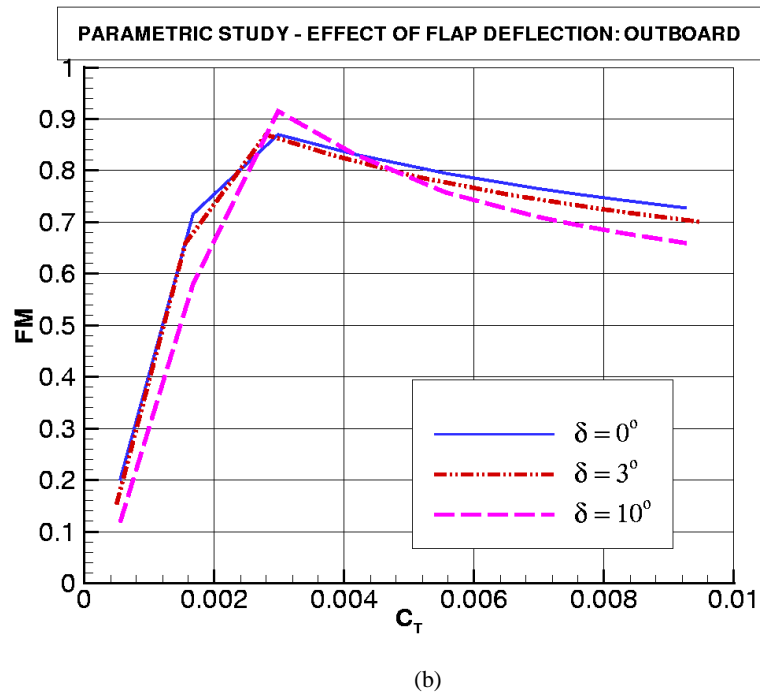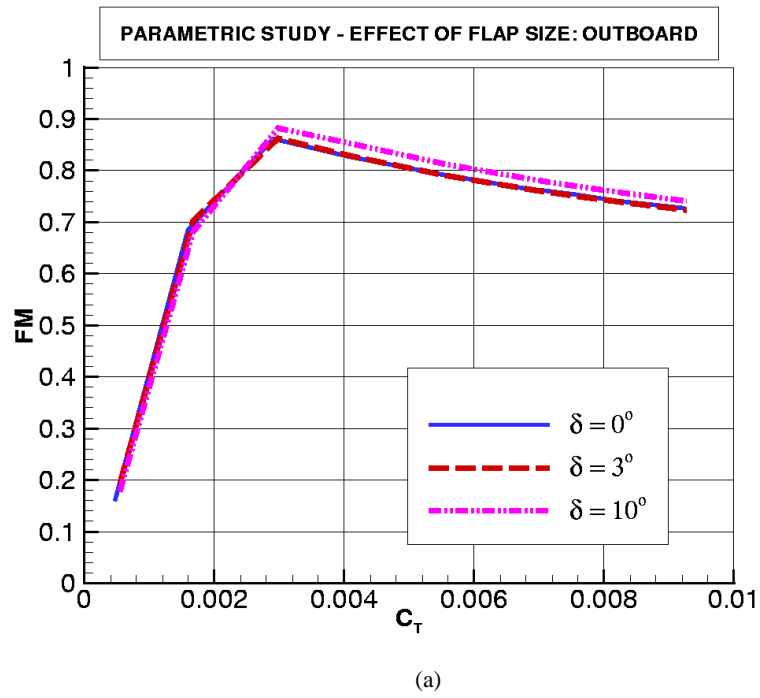
Figure 4.6: Effect of flap deflection angle in improving hover performance. The maximum flap deflection angle was 10°, and the flap size was fixed at 15%R at locations 92.5%R and 23%R. (a) 23%R, inboard. (b) 92.5%R, outboard.
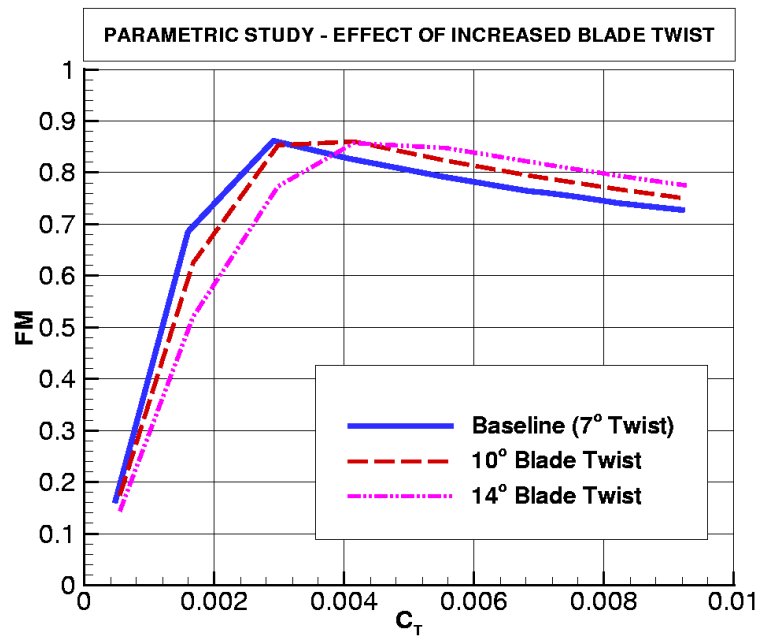
(a)
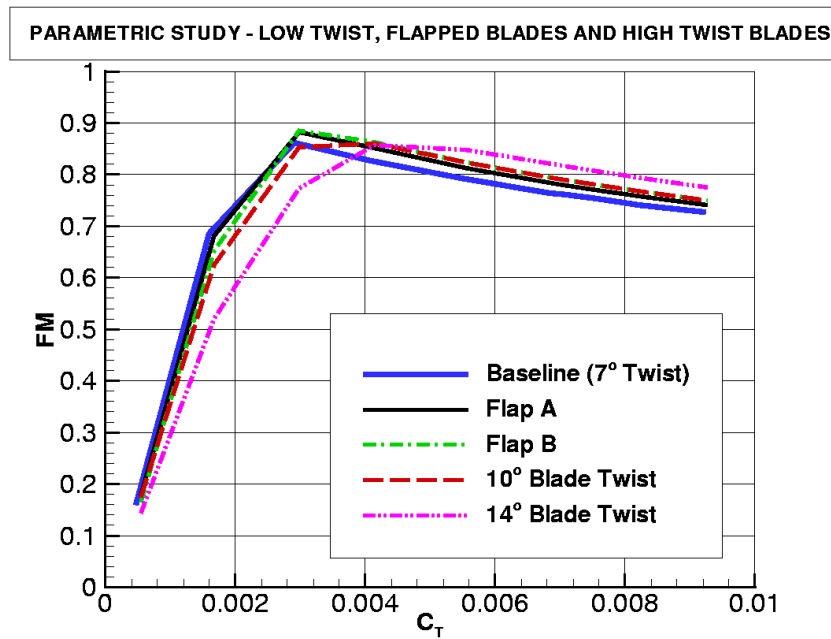
(b)

Figure 4.7: Flapped rotor performance enhancement. C_T vs. FM. (a) Twisted blade. (b) With flapped rotors.

Figure 4.10 presents results for the 3° flap deflection angle at a medium $C_T = 0.0028$. For the inboard flap, results again suggest that a flap with a large chord would be more beneficial, but with a flap span as small as possible located as far inboard as possible. For the outboard results, a small flap as far outboard as possible gives the best performance, which is still below that of the baseline rotor. The apparent discontinuity in the outboard flap results can be attributed to the coarse test

matrix conducted at each C_T due to the small area where the flap could be located, and is not considered an issue. So far, flap chord is tending to have a soft effect on the predicted improvements. As flap deflection angle is increased, however, as can be seen in Figure 4.11, we are aware of the first signs of the benefits possible with both an inboard and outboard flap. The optimum flap at this location would appear to be a large flap in size, both in rotor span and chord length, placed as far inboard as possible. Improvement in the baseline performance of 2.1% is possible with an inboard flap. For an outboard flap, more substantial improvements of up to 8.7% on the baseline rotor seem to be possible. A trend is evident in the results for all three flap chords and, although the larger flap chord offers the best performance, it is still clear that it has a soft effect.

Figure 4.12 presents results for the 3° flap deflection angle at a high $C_T = 0.00829$, which is also the maximum thrust value that is considered in this study. Results show that slight improvements are possible with a small inboard flap located close to the blade root. However, the outboard design underperforms compared to the baseline rotor. More interestingly, when the flap defection angle is increased again to $\delta = 10^o$ in Figure 4.13, the inboard flap gives a large performance increase of 4.7%, which if compared with the results in the previous section, is equivalent to a rotor with -13° of twist. The effect of the outboard flap agrees well with the trend for the original slotted flap design tested in the HIMARCS I experiment [16].

A summary of the optimum designs and the potential performance enhancement that they offer is presented in Tables 4.9 and 4.10 for the inboard and outboard flaps, respectively. As detailed earlier, optimum designs for both an inboard and outboard flap were to be selected and verified in the following chapter to confirm the validity of the design. From Table 4.9, the inboard flap gives a performance increase at very low thrust settings of 6%, with very little effect at medium thrust settings, and consistent improvements of more than 4% at high thrust settings. At the lower thrust settings, the smallest flap chord and deflection angle gives the best performance. This is also true of the flap span, with the flap location being closer to the blade root. At the higher thrust coefficients, the optimum flap span, chord, and deflection angle are consistent at 24%R, 32%c, and 10°, respectively. The optimum flap location shifts outboard as the blade loading increases. Table 4.10 lists the optimum outboard flap configurations at various C_T's. As with the inboard flap, at low thrust coefficients the smallest flap chord and deflection angle offer the optimum designs, although in this case it doesn't always offer an improvement. At medium thrust settings, the optimum configuration varies, but performance improvements of up to 9% are possible. Finally, at high thrust settings the optimum outboard flap designs give no improvements in performance again.

4.4.3 Optimum Blade Design

As seen previously, there were three or four designs that could have been implemented. Therefore, a decision was made to select a flap design that was located sufficiently inboard i.e. avoided the blade root and allowed for a closed blade tip, unlike the original HIMARCS I flapped rotor. The flaps selected were: (a) inboard, flap location: 36%R, flap span: 24%R, flap chord: 32%c, and flap deflection angle: 10°, and (b) outboard, flap location: 92%R, flap span: 8%R, flap chord: 32%c, flap deflection angle: 10°. The optimum inboard flap configuration should offer performance improvements of around 4% at high thrust settings. The optimum outboard flap should offer improvements of up to 9%.

4.5 Summary

The current chapter has considered a reduced order model based on the blade element method, combined with 2D CFD aerodynamics, to evaluate trailing-edge flaps for application on rotor blades to improve hover performance. Inboard and outboard slotted flaps were considered with varied flap span lengths, flap chord lengths, flap deflection angles, and flap spanwise locations. Results from the parametric study were evaluated with various possible options for obtaining the best performance at all blade loadings. Optimum designs for an inboard and outboard flap were selected and will be considered using 3D hover CFD in the following chapter.

(a)

(b)

(c)

(d)

(e)

(f)
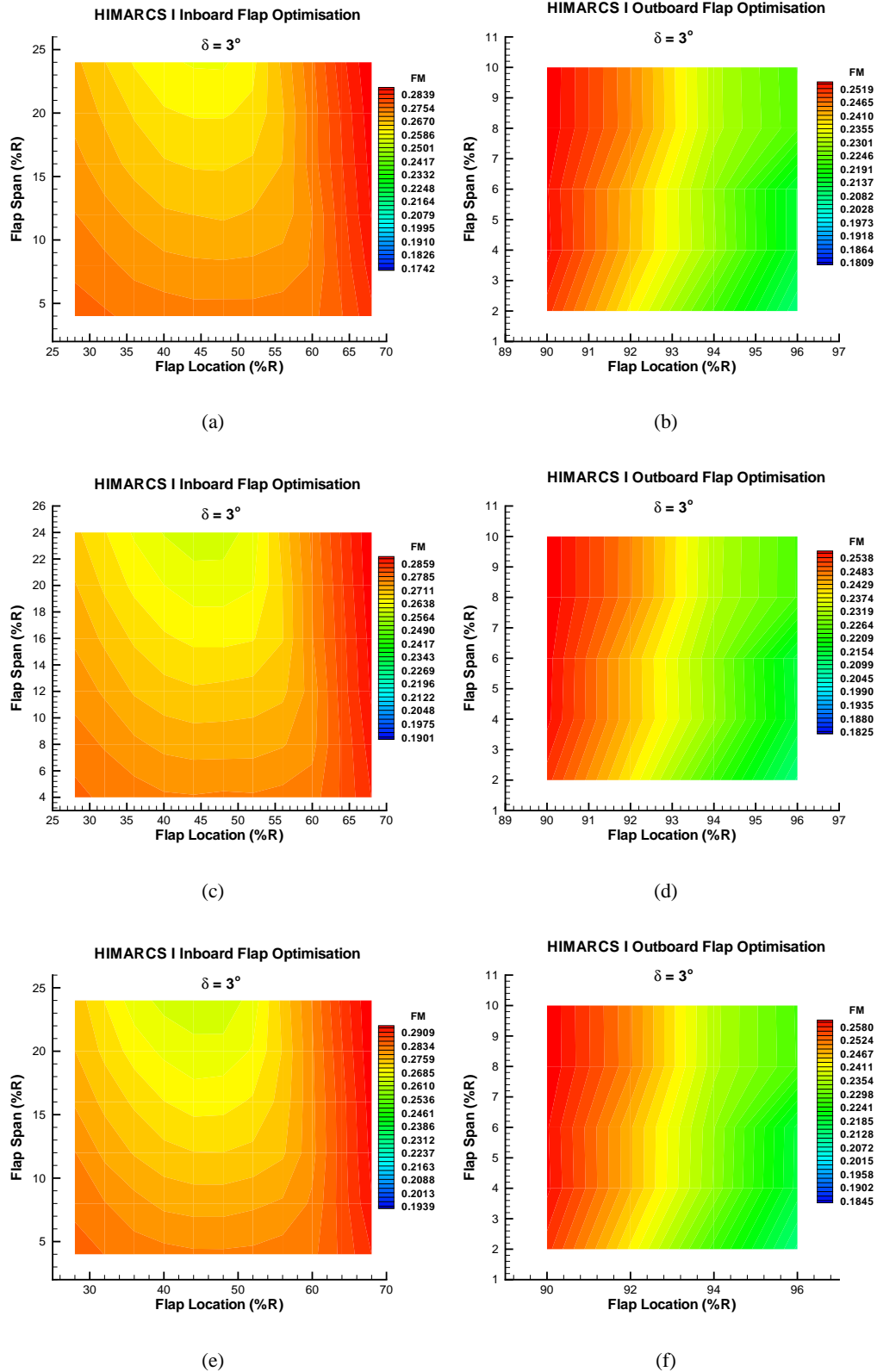
Figure 4.8: Carpet plot results from parametric study with $\delta = 3^o$ and $C_T = 0.0007$. 10.67%c: (a) Inboard. (b) Outboard. 21.33%c: (c) Inboard. (d) Outboard. 32%c: (e) Inboard. (f) Outboard. (Baseline FM = 0.3063, $M_T = 0.627$)

Figure 4.9: Carpet plot results from parametric study with $\delta = 10^o$ and $C_T = 0.0007$. 10.67%c: (a) Inboard. (b) Outboard. 21.33%c: (c) Inboard. (d) Outboard. 32%c: (e) Inboard. (f) Outboard. (Baseline FM = 0.3063, $M_T = 0.627$)
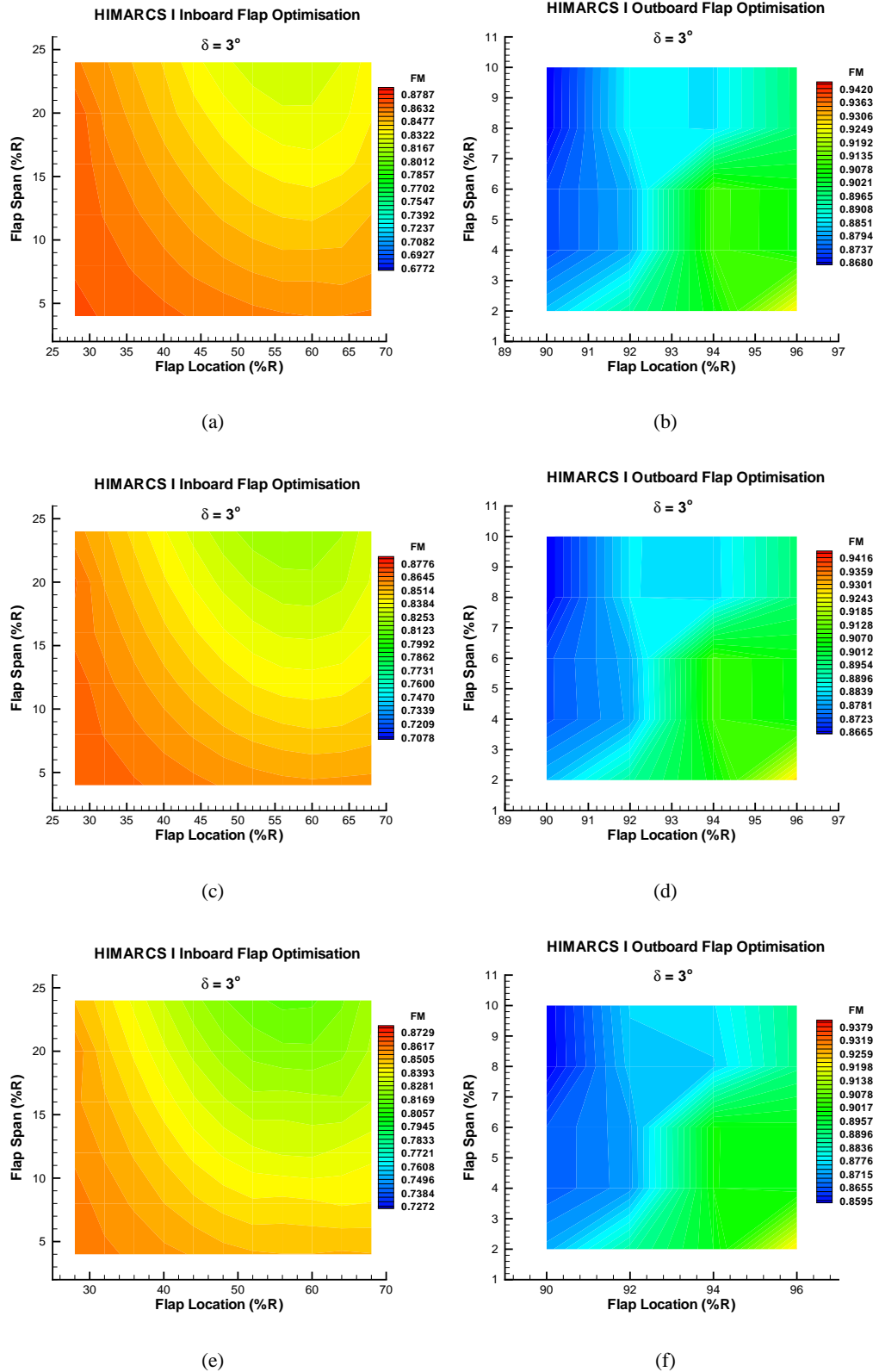
Figure 4.10: Carpet plot results from parametric study with $\delta = 3^o$ and $C_T = 0.0028$. 10.67%c: (a) Inboard. (b) Outboard. 21.33%c: (c) Inboard. (d) Outboard. 32%c: (e) Inboard. (f) Outboard. (Baseline FM = 0.8513, $M_T = 0.627$)

Figure 4.11: Carpet plot results from parametric study with $\delta = 10^o$ and $C_T = 0.0028$. 10.67%c: (a) Inboard. (b) Outboard. 21.33%c: (c) Inboard. (d) Outboard. 32%c: (e) Inboard. (f) Outboard. (Baseline FM = 0.8513, $M_T = 0.627$)

(a)

(b)

(c)

(d)

(e)

(f)
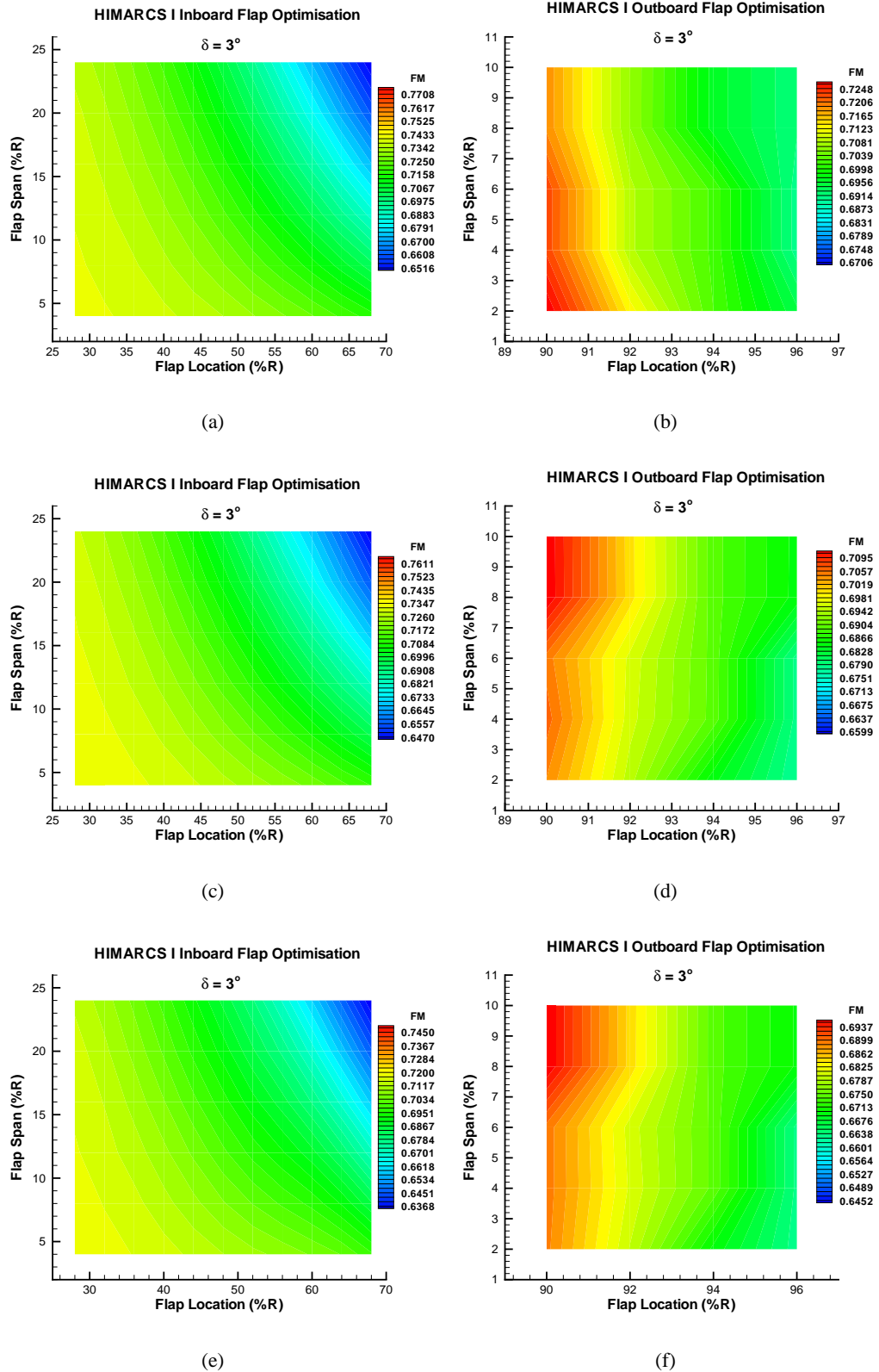
Figure 4.12: Carpet plot results from parametric study with $\delta = 3^o$ and $C_T = 0.00829$. 10.67%c: (a) Inboard. (b) Outboard. 21.33%: (c) Inboard. (d) Outboard. 32%c: (e) Inboard. (f) Outboard. (Baseline FM = 0.7247, $M_T = 0.627$)
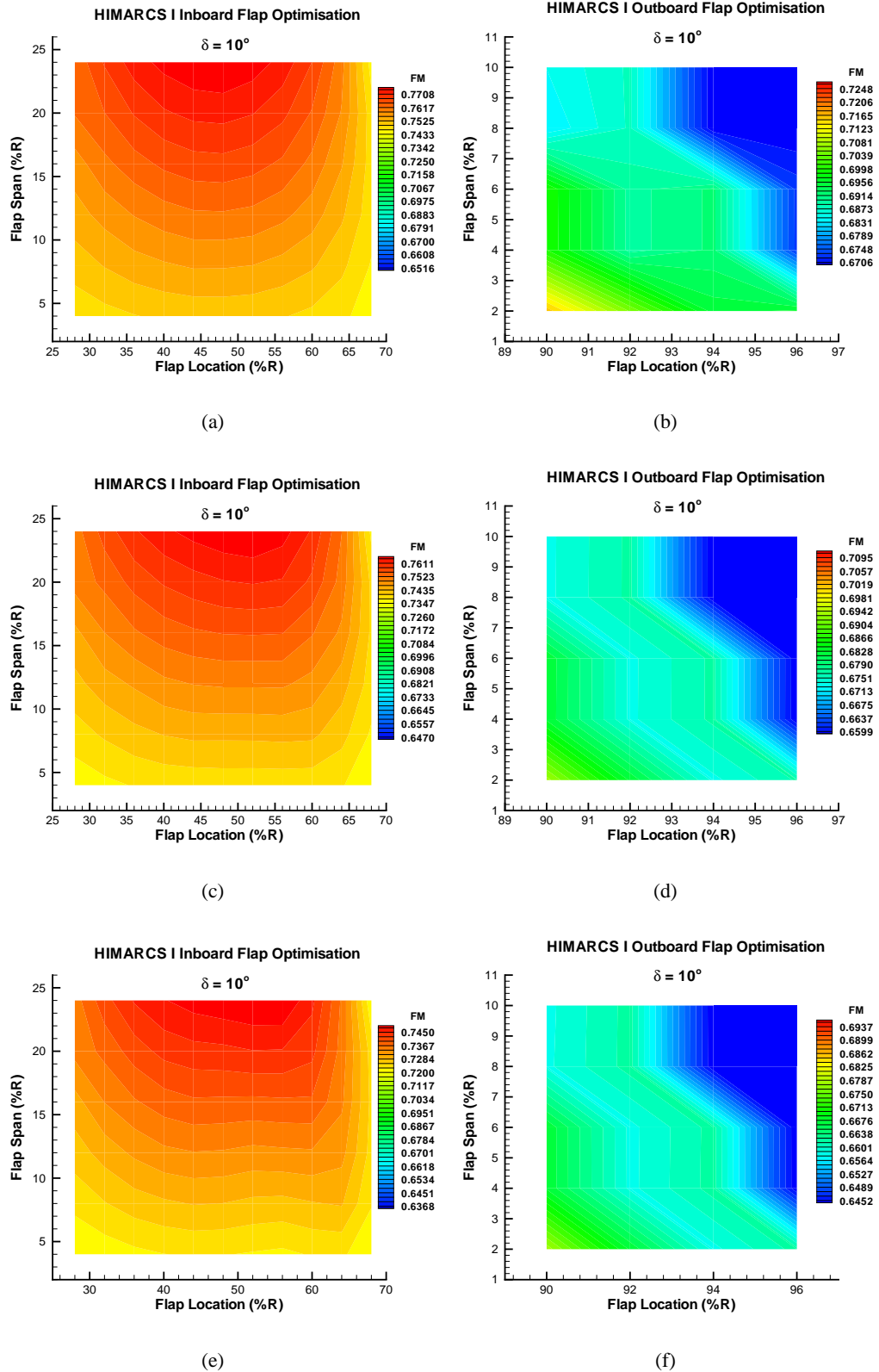
Figure 4.13: Carpet plot results from parametric study with $\delta = 10^o$ and $C_T = 0.00829$. 10.67%c: (a) Inboard. (b) Outboard. 21.33%c: (c) Inboard. (d) Outboard. 32%c: (e) Inboard. (f) Outboard. (Baseline FM = 0.7247, $M_T = 0.627$)

Inboard Flap Optimisation						
C_T	FM	Flap Size (%R)	Flap Location (%R)	Flap Angle (°)	Flap Chord (%R)	Change in Percent (%)
0.000545455	0.2128	24	68	3	10.67	6.5
0.0007	0.2958	"	"	"	"	5.8
0.0012	0.5495	4	32	"	"	1.3
0.0015942	0.7035	8	28	"	"	0.12
0.00167273	0.7262	4	"	"	"	0
0.0019	0.7793	"	"	"	"	0.26
0.0022	0.8348	"	"	10	"	0.8
0.0025	0.8672	19.6	"	"	21.33	0.69
0.0028	0.8890	"	"	"	32	2.1
0.00298182	0.8889	24	"	"	"	2.3
0.00414545	**0.8674**	**24**	**36**	**10**	**32**	**4.3**
0.00556364	0.8305	"	40	"	"	4.6
0.00690909	0.8017	"	44	"	"	4.7
0.00712727	0.7968	"	48	"	"	4.6
0.00829091	0.7770	"	48	"	"	4.7

Table 4.9: Optimum values of FM for various inboard flap spans, locations, chords, and deflection angles at a range of C_T's. Selected designs highlighted in bold.

Outboard Flap Optimisation						
C_T	FM	Flap Size (%R)	Flap Location (%R)	Flap Deflection (°)	Flap Chord (%R)	Change in Percent (%)
0.000545455	0.2011	2	90	3	10.67	0.65
0.0007	0.2618	8	"	"	"	-6.4
0.0012	0.5290	4	"	"	"	-2.45
0.0015942	0.7099	6	"	"	"	1
0.00167273	0.7367	8	92	"	"	1.4
0.0019	0.8042	4	94	"	"	3.5
0.0022	0.8743	6	"	"	"	5.6
0.0025	0.9224	10	92	10	"	7.1
0.0028	0.9458	10	"	"	32	8.7
0.00298182	**0.9481**	**8**	**92**	**10**	**32**	**9**
0.00414545	0.8582	6	94	"	"	3.2
0.00556364	0.7708	2	90	3	10.67	-3
0.00690909	0.7450	8	"	"	32	-2.7
0.00712727	0.7512	2	"	"	21.33	-1.4
0.00829091	0.7276	2	"	"	32	-1.9

Table 4.10: Optimum values of FM for various outboard flap spans, locations, chords, and deflection angles at a range of C_T's. Selected designs highlighted in bold.
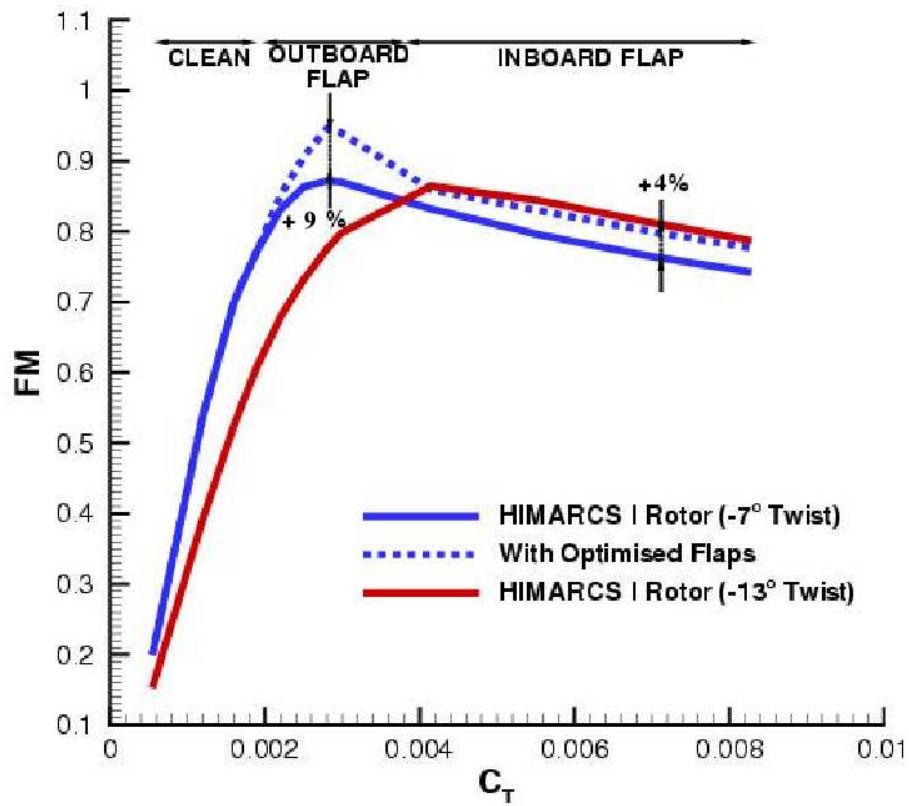
(a)
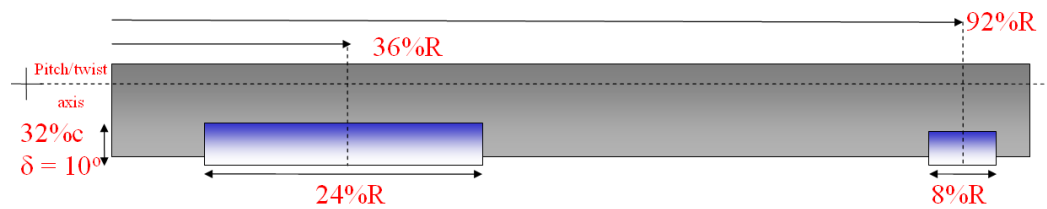
(b)

Figure 4.14: Results for optimum, or "best-fit", design for the range of thrust coefficients. (a) Plot showing deployment schedule for fixed flap in hover. (b) Schematic of HIMARCS I with optimised flaps.

Chapter 5

3D Hover Results

The present chapter details the results of the 3D Euler and RANS calculations performed for hovering rotor blades equipped with trailing edge flaps. Previously, a reduced order model was employed to quickly evaluate various design configurations for twisted and flapped rotor blades. However, further evidence is required to confirm the validity of the predictions. This verification will be provided by CFD calculations. These serve to highlight the effect of blade twist and verify the results of the parametric design study. Initially, the hover trimming obtained by the blade element method was combined with inviscid CFD, and results have been obtained for clean, twisted rotors Following this, inviscid and viscous CFD was used to examine the effect of blade twist on the performance of a rotor. The optimum, slotted flap designs were then considered and evaluated. Comparisons were then made between the computed viscous blade loadings using trim settings predicted with the blade element method, and the inviscid CFD trimmer. Finally, results were obtained for a blended flap rotor with the same configuration as the optimum inboard flap design, using the inviscid trimmer for initial predictions and then viscous CFD to fully verify the effectiveness of the design.

5.1   Grid Generation

The multiblock topologies used in this work vary with respect to the blade design being considered. Different topologies were required for clean and twisted blades, slotted flapped blades, and blended flap blades. Periodic boundaries are used where a quarter of the rotor disc plane is modelled, with the farfield boundaries set at roughly the same as that of the wind tunnel walls from the experiement [16].

All grids were generated using the ICEMCFD-Hexa software. Preparing 3D multiblock, block-structured grids even for a simple rotor presents a challenge, with a large amount of time and effort

spent on obtaining high quality meshes [119]. Firstly, it isn't possible to just extrude a 2D aerofoil to 3D, since important features such as blade twist, changes in planform, taper and flow physics would not be captured. Unlike modern unstructured methods, multiblock grids require the building of blocks around the specified geometry to define the computational domain where the blocks themselves define the fluid zones. Each block is defined by a vertex at each corner that defines connectivity with neighbouring blocks or geometry. Increasing the level of complexity of the geometry by adding another element to a rotor further complicates matters, since flow between the rotor and the flap or slat then has to be considered, which requires further modification of the block topology. The number and distribution of points along each edge of each block must then be specified explicitly. In doing so, the engineer has to be fully aware of the necessary cell sizes to capture the physics of the problem such as the boundary layer and tip vortex roll-up. Also, to facilitate good quality results, it is important to obtain good aspect ratios and cell quality. Finally, if limitations exist in computational time and memory requirements, then maximum grid sizes can further limit the size of the mesh. This provides an even greater problem as the allocation of points to different areas of the mesh has to be decided which, due to the structured nature of the grid, can be an drawn out procedure since the number of points on one edge must be carried to the farfield. This process improves with experience and knowledge of what is known to work for different geometries, but the major part of the applied effort can be considered for the most part to be trial and error.

The current work considers two different blocking topologies for rotors with slotted flaps. The first blocking scheme evolved from the original topology for a basic rotor to a highly complex one consisting of over 440 blocks. The topology allowed for a fine layer of blocks over the surface of the rotor and flap, but added to the complexity of the grid. This fine region of blocks proved the most difficult to transfer between rotors at different collective and coning angles, and major effort was placed in fine-tuning the mesh in this area. Another important problem when attempting to mesh a rotor blade with flaps is making sure that vortex roll-up at the flap-edges is captured properly, as well as at the extents of the rotor blade. To facilitate this, blocks were placed about the flap in such a way that their edges were located in the wake of the flap with a first cell size of 10^{-4}c. The high number of blocks also improved cell skewness due to increased flexibility in the distribution of points in the domain. This was especially important since the number of cells were limited to 2.6 million due to computational restraints.

The second set of results were obtained with blended flaps and utilised the built-in trimmer available in the HMB solver. The trimming method used a TFI approach for deforming the mesh, which

proved incompatible with the previous topology due to the fine layer of blocks beside the rotor sur-
face. Hence, a revised blocking scheme was implemented that also reduced the complexity of the
mesh, but retained the advantages of defined block edges at the extents of both the flap and the rotor
blade. It also allowed for adequate morphing of the original mesh by TFI with finer grids providing
excellent grid resolution.

Geometry	Grid Type	Blocks	1st Cell Distance Main:Tips	Grid Points Blade:Flap:Total
Inviscid				
Clean Blade	Coarse	106	10^{-4}c : 10^{-4}c	16k : 0 : 2.2M
Optimised Flaps	Coarse	446	10^{-3}c : 10^{-3}c	22k : 1.5k : 2.6M
Clean Blade (T)	Fine	144	10^{-4}c : 10^{-4}c	48k : 0 : 6.5M
Blended Flap (T)	Fine	144	10^{-4}c : 10^{-4}c	35k : 13k : 6.5M
Viscous				
Clean Blade	Coarse	106	10^{-5}c : 10^{-4}c	18k : 0 : 2.7M
Clean Blade (T)	Fine	178	10^{-5}c : 10^{-4}c	48k : 0 : 5.3M
Blended Flap (T)	Fine	178	10^{-5}c : 10^{-4}c	35k : 13k : 5.3M

Table 5.1: Details for 3D inviscid and viscous grids. Some grids were used with the CFD trimmer
only (T).

5.1.1   Rotor Blades without Flaps

The multiblock topologies used for clean and twisted blades were identical. Figure 5.1 presents the
surface mesh and block boundaries. These consist of an H-H topology with an embedded C-type
multiblock scheme and, as can be seen, the blade topology employed at the tip was similar to the
one used in Ref. [108]. The root cut-out was not modelled. The advantage of this topology is that
it allows flat and rounded tips, and it can be modified to account for the presence of integrated and
slotted flaps. Details of the grids for both inviscid and viscous cases can be found in Table 5.1. For
the inviscid grids, a wall spacing of 10^{-4}c was implemented normal to the upper sections, lower
sections, the tips, and the trailing edge. Roughly 16,000 points were present on the blade surface
with the total grid size approximately 2.2 million points. For the viscous grids, a wall spacing
of 10^{-5}c was used at the nose and leading-edge of the upper and lower surfaces. At the trailing-
edge and the tips 10^{-4}c was considered sufficient. The number of points on the blade surface was
increased to 18,000 and the total grid size increased to 2.7 million points.
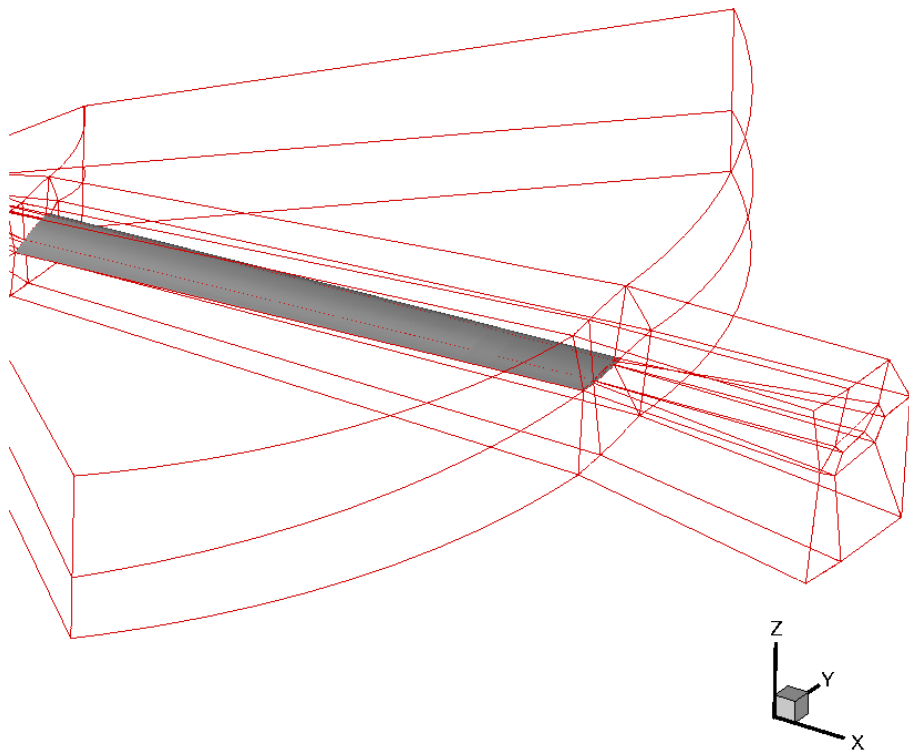
(a)
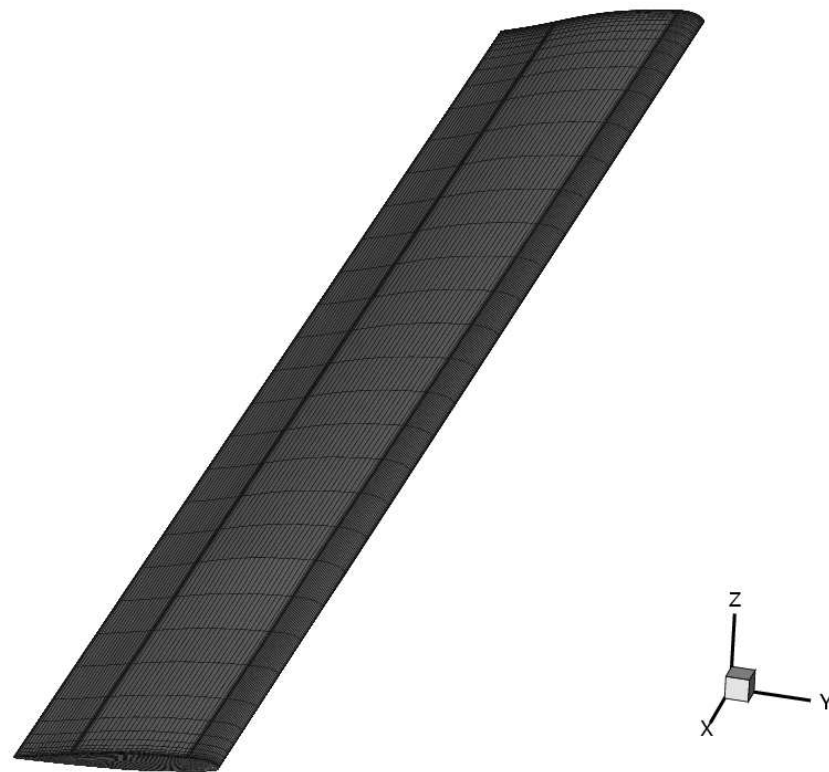
(b)

Figure 5.1: Baseline blade multiblock topology. (a) C-H blocking. (b) Surface mesh.

5.1.2   Rotor Blades with Slotted Flaps

The surface mesh and block boundaries near the inboard and outboard flaps are shown in Figures 5.2 and 5.3, respectively. The blocking scheme employed for the slotted flap geometry was much more complex and was essentially a C-grid within a C-grid within the overall H-H topology, highlighted by the increase in number of blocks from 106 to 446. This was necessary to allow for the inclusion of the slotted flap geometry including flap gap and flap edges. In the parametric study, no flap edges were considered. However, to allow for the inclusion of a topology around the flap, flap edges of 1%R were included either side of the flap. The inviscid grid used first wall spacings of 10^{-3} all around the rotor blade, including on the flap. The points on the surface of the rotor increased to 22,000 due to necessary refinement to obtain sufficient points on the flap surface for the inviscid calculation. This increased the overall size of the grid to 2.6 million points.

5.1.3   Rotor Blades with Blended Flaps

Rotor blades with blended trailing edge flaps were also considered. As shown in Figure 5.4, the blended flap is considered to have no flap gap as was the case with previous designs. The flap edges are closed and blended with the main blade geometry. Although the topology used for blended flaps was based on the original clean blade topology, an increased number of blocks was required to account for the blended region between the blade and the flap. The advantage of this topology is that the blocking for both the clean and flapped blades are identical, hence allowing for a direct comparison between the designs. Also, to ensure grid independent results, the mesh density particularly in the region around the blade was increased according to the outcome of the grid convergence study (see Chapter 3). In total, 144 blocks were required to model the inviscid blade and 178 blocks were required to model the viscous blade. The surface topology and mesh for both cases can be seen in Figures 5.4(a) and (c). The increase in blocks follows a greater requirement for even point distribution at the blending region on the viscous blade. The blended flap design was not tested using the BEM method in Chapter 4. In this case, the inviscid blade trimmer was used to estimate the trim settings for the viscous runs. The near wall spacings for both the inviscid and viscous grids remain the same as for the clean blade of the previous topology. Fine grids were considered for both the inviscid and viscous calculations. For inviscid runs, the grid sizes approached 6.5 million points with the majority concentrated near the blade tip, blade wake and around the blade/flap surface. For viscous calculations, grids of approximately 5.3 million points were used to reduce computational times. The number of points on the blade surface, at the tip and in the wake remained the same as with the inviscid grids, with the reduction in points occurring mainly around the shaft and the

105

(a)

(b)
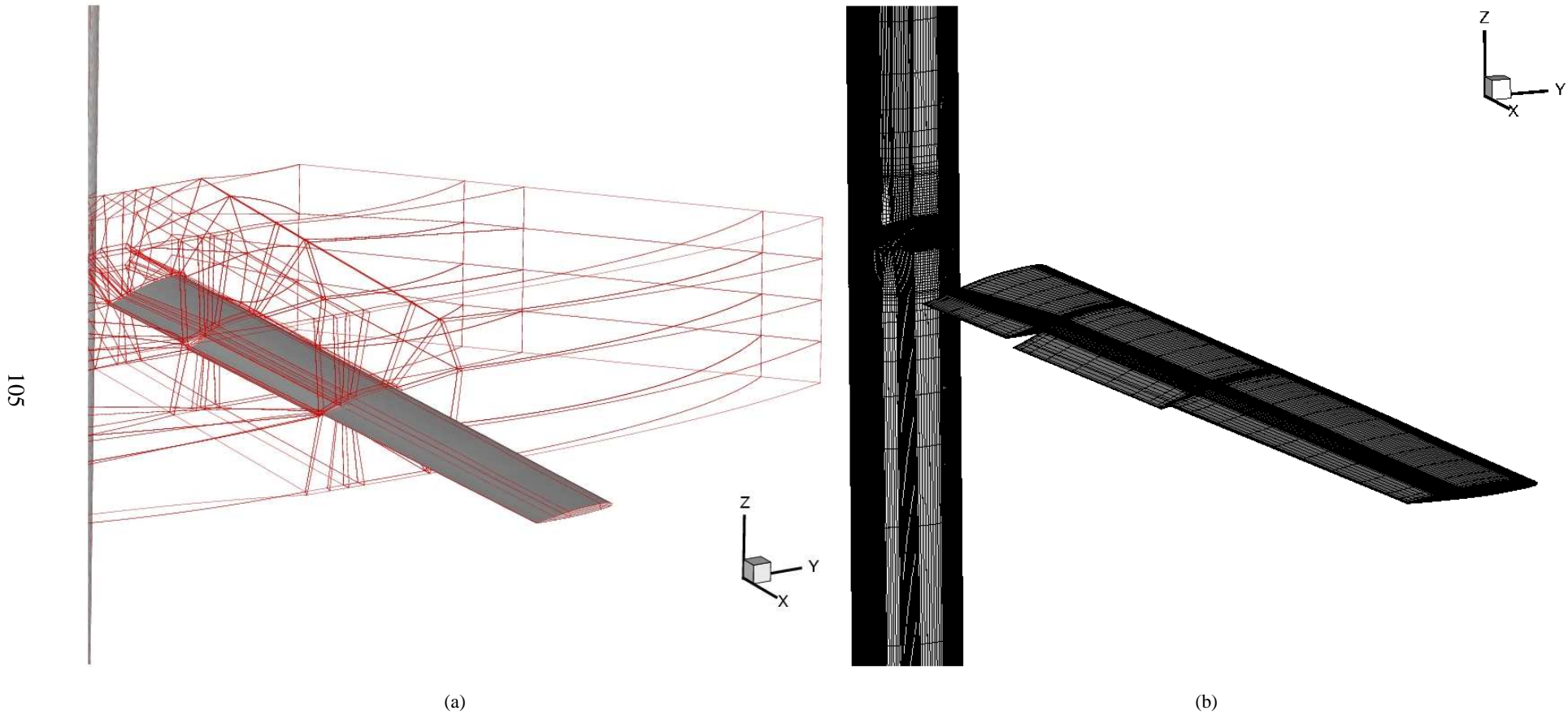
Figure 5.2: Inboard flappped blade multiblock topologies. (a) C-C-H blocking. (b) Surface mesh.

(a)

(b)
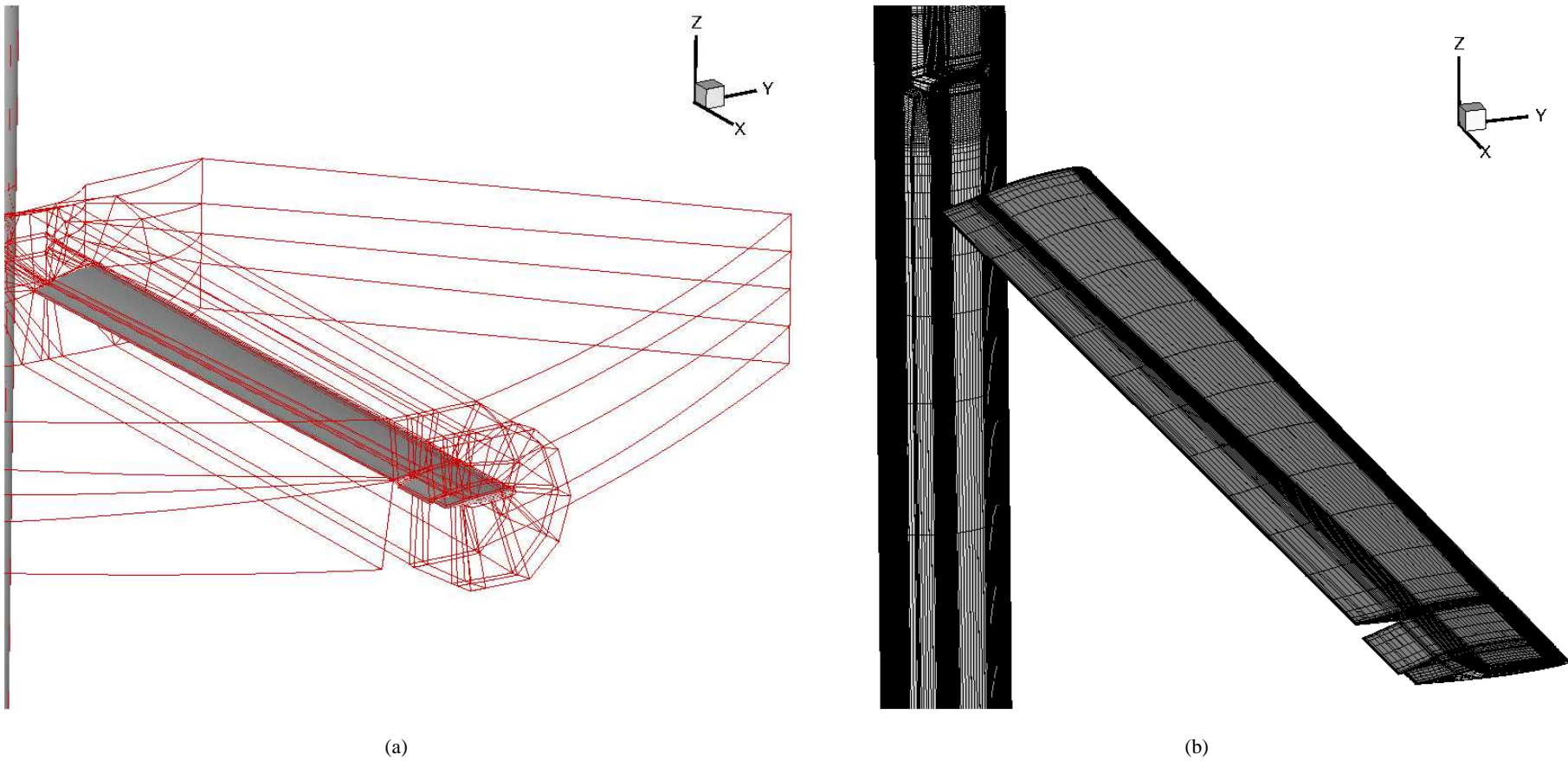
Figure 5.3: Outboard flappped blade multiblock topologies. (a) C-C-H blocking. (b) Surface mesh.

farfield boundaries. A closer look at the mesh around the blended flaps can be found in Figures
5.4(b) and (d).

(a)

(b)

(c)

(d)
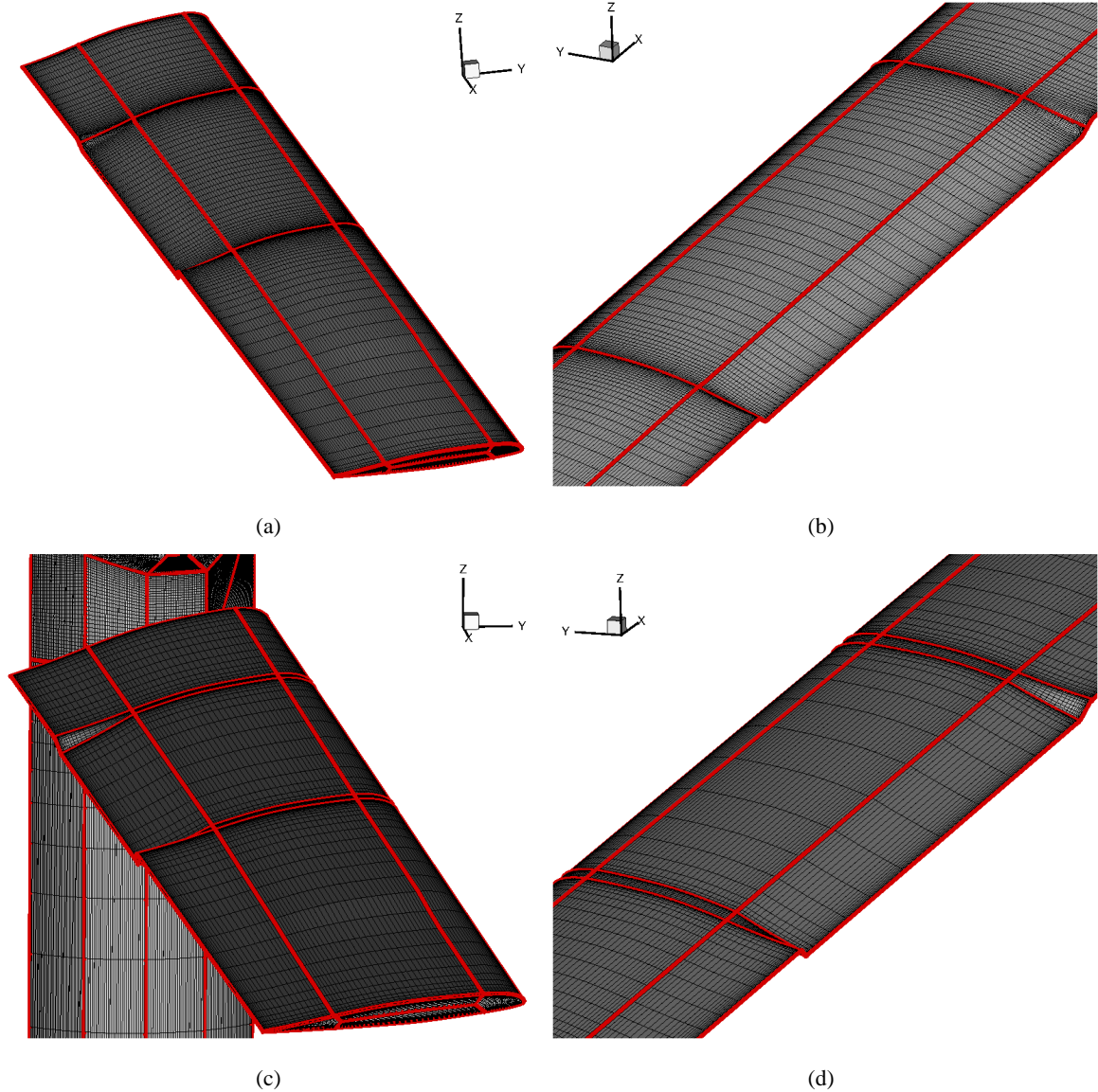
Figure 5.4: Blended flap multiblock topologies. Inviscid: (a) Surface mesh including block bound-
aries. (b) Mesh around the flap. Viscous: (c) Surface mesh including block boundaries. (d) Mesh
around the flap.

5.2 Effect of Blade Twist

Initially, the effect of twist on the performance of a hovering rotor was investigated. As described

previously in Chapter 1, the variation of the dynamic head along a rotor blade in hover gives rise to

an uneven load distribution along the blade. Increasing blade twist can help balance the loading by

allowing for greater generation of lift inboard and hence reducing the need for thrust production at

the blade tip. Consequently, the reduction in blade tip loading reduces induced power and improves hovering performance. Inviscid and viscous grids for blades with linear twist from -4° to -13° were considered to evaluate this effect. The grid topologies described in Section 5.1.1 were used here. Inviscid computations for a range of thrust coefficients between 0.002 and 0.01 were run and the obtained results were compared against the datum HIMARCS I blade which has -7° of linear twist [16]. The inviscid results for the C_T, C_Q, and FM are presented in Figures 5.5(a), (c), and (e). The dipping of the results at high thrust was due to upwash from the farfield boundaries lifting the shed tip vortex up and causing it to hit the blade, which resulted in a higher drag penalty. However, the results are inviscid and consequently only relative comparisons can be made. As can be seen, the highly twisted blade has an advantage at moderate to high thrust settings. At lower thrust values, where the location of the blade loading has a lesser effect, it can be seen that the differences between the -7° and -13° blades diminishes. This trend can also be confirmed when comparing the rotors with -7° and -4° of twist (see Figure 5.5(e)). To further establish this conclusion, viscous computations were performed for the highly twisted blade at high thrust coefficients (see Figures 5.5(b), (d), and (f). These have the advantage of including more accurate physics in the solution including blade stall and viscous drag. The viscous computations confirm the inviscid predictions at high thrust coefficients, with the computed trends agreeing well with those evidenced via experimental measurements in Ref. [15].

To confirm the effect that blade twist has on the hover performance, the chord wise Cp distribution from the viscous calculations was examined along the HIMARCS I baseline rotor and the same rotor with -13° of twist at roughly the same thrust coefficient, $C_T \approx 0.00829$. In Figure 5.6, slices are taken at r/R = 0.317, 0.395, 0.475, 0.554, 0.871, and 0.96. From Figures 5.6(a)-(e), the results are as is expected of the highly twisted rotor. The inboard loading is greater for the blade with -13° of twist up to r/R = 0.554 where the two blades have similar local angles of attack.

As one moves further outboard towards the tip (see Figures 5.6(e)-(f)), the blade loading for the low twist rotor supercedes that of the highly twisted rotor, as expected. Thus we have the effect of lower twist rotors having high blade loadings at the tip and therefore giving rise to a greater induced drag. Rotors with greater twist, however, increase the blade loading inboard and consequently reduce the effect of induced drag outboard. This is more clearly seen in Figure 5.7, where the spanwise and chordwise distribution of pressure is plotted. At the blade tip, the low twist rotor (see Figure 5.7(a)) has clearly a lower maximum pressure compared to the highly twisted blade (see Figure 5.7(b)). Inboard, however, the effect of high twist is evident through a slight increase in pres-

sure loads compared to the low twist rotor. The results obtained so far have established confidence in the CFD method and helped to quantify the effect of blade twist in improving hover performance. In addition, the obtained results set a standard for expected performance from the flapped rotor. From results predicted in Chapter 4, the flapped blade with just -7° of twist should meet or exceed the performance of the highly twisted (-13°) rotor.

5.3   Slotted Flap Rotors

Next, the optimum flap configurations suggested by the blade element theory (see Chapter 4) were implemented on CFD grids for the inboard and outboard configurations. The details of the grids are shown in Table 5.1. Every effort was made to maintain consistent grid density for the clean and flapped rotors. However, due to the complexity of the employed multiblock topology, the requirements to model the near flap region, as well as to resolve the flap loading, an increase in the number of points was necessary. CFD results, including the trim states, were obtained for the optimum blade designs for a whole range of thrust settings. These are plotted in Figures 5.8(a)-(e) along with the results for the clean rotors with -7° and -13° of twist.

In confirmation of the predictions of the blade element method, the optimum inboard flap is shown to match and exceed the performance of the highly twisted blade for high thrust settings, as can be seen in Figures 5.8(a), 5.8(c), and 5.8(e). Another encouraging result from Figures 5.8(c) and 5.8(e) is that the optimum inboard flap design equaled the performance of the -13° twisted blade, but with reduced collective and coning angles of between 0.5^o-1°. For more information on how the collective and coning angles are calculated, see Section 2.1.4. An inboard flap shows promise, especially as it would not have an effect on the design of the blade tip shape or root cut-out section, which would offer further performance enhancement potential. The outboard flap configuration under-performs compared to blade element predictions. However, it does demonstrate the same range of thrust coefficients for best performance as the BEM method predicted, as well as similar savings in blade trim angles as the inboard flap (see Figure 5.8(c) and 5.8(e)). It must also be noted that the size of the flap gaps at the flap edges in the CFD was not optimised and their effect on the rotor performance was not investigated.

Comparisons of Cp are presented in Figure 5.9 at a C_T of approximately 0.0085, where the inboard flap configuration matches the performance of the highly twisted rotor, both of which outperform the low twist rotor. Slices are taken from the two clean blades and the optimum inboard flap at r/R

= 0.317, 0.396, 0.475, 0.554, 0.871, and 0.95. The blade loading on the main section of the flapped rotor can be seen to be generally less than both the twisted blades for all locations.
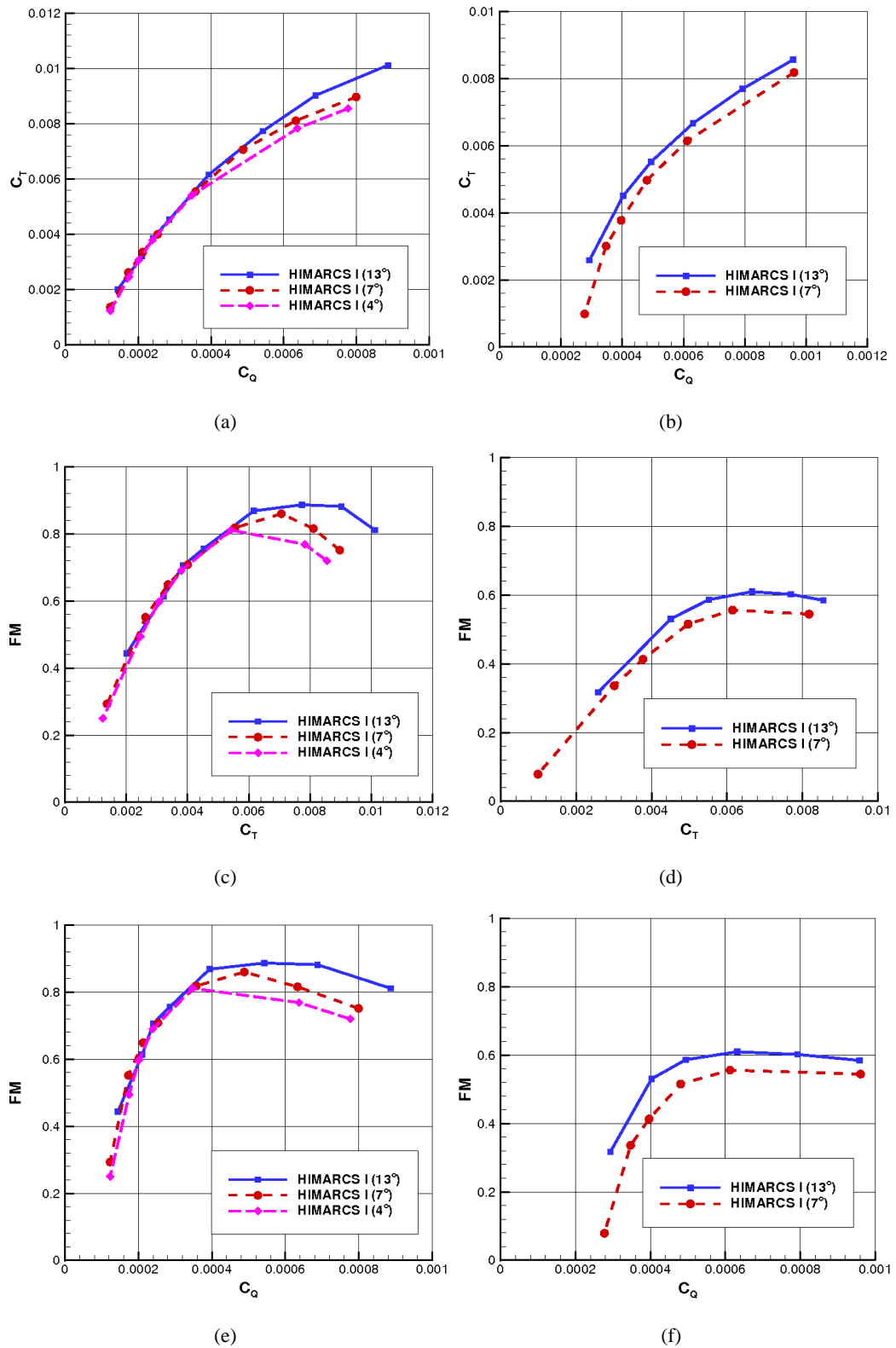
Figure 5.5: 3D CFD results showing the effect of blade twist. (a,c,e) Inviscid. (b,d,f) Viscous. (a)-(b) C_Q vs. C_T. (c)-(d) C_T vs. FM. (e)-(f) C_Q vs. FM.
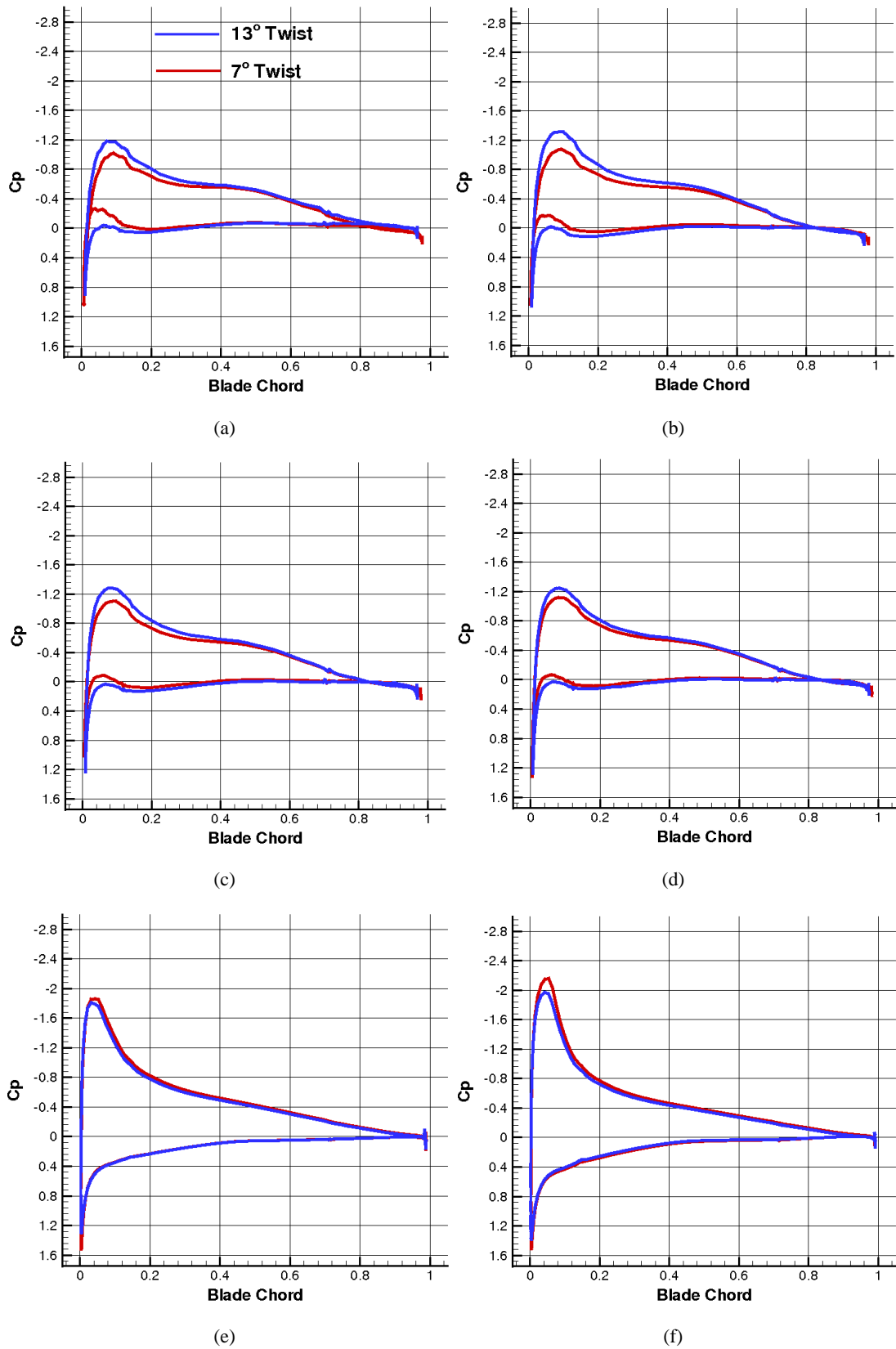
Figure 5.6: Chordwise Cp distribution for the HIMARCS I rotor with -7° and -13° of twist. r/R: (a) 0.317. (b) 0.396. (c) 0.475. (d) 0.554. (e) 0.871. (f) 0.95. ($C_T \approx 0.008$.)
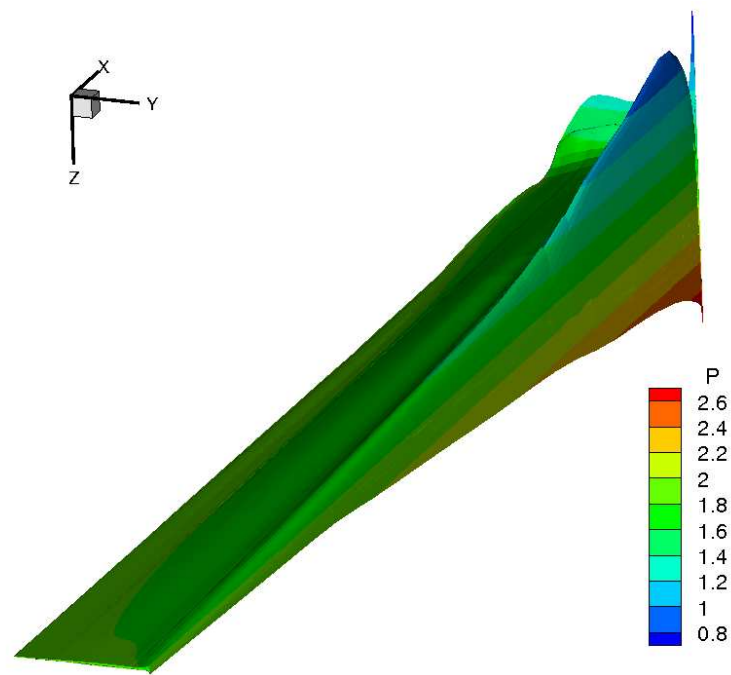
(a)
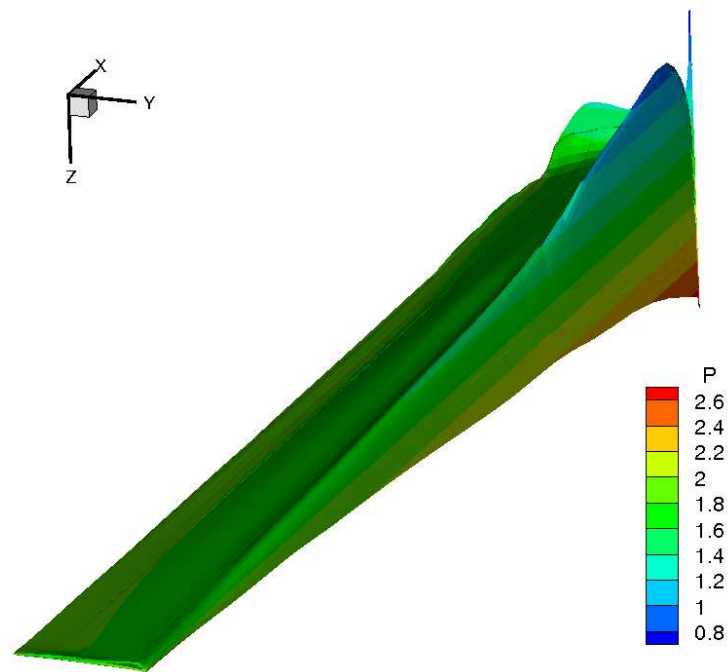
(b)

Figure 5.7: 3D pressure distribution for the HIMARCS I rotors with varied twist. (a) 7° twist. (b) 13° twist. ($C_T \approx 0.008$.)
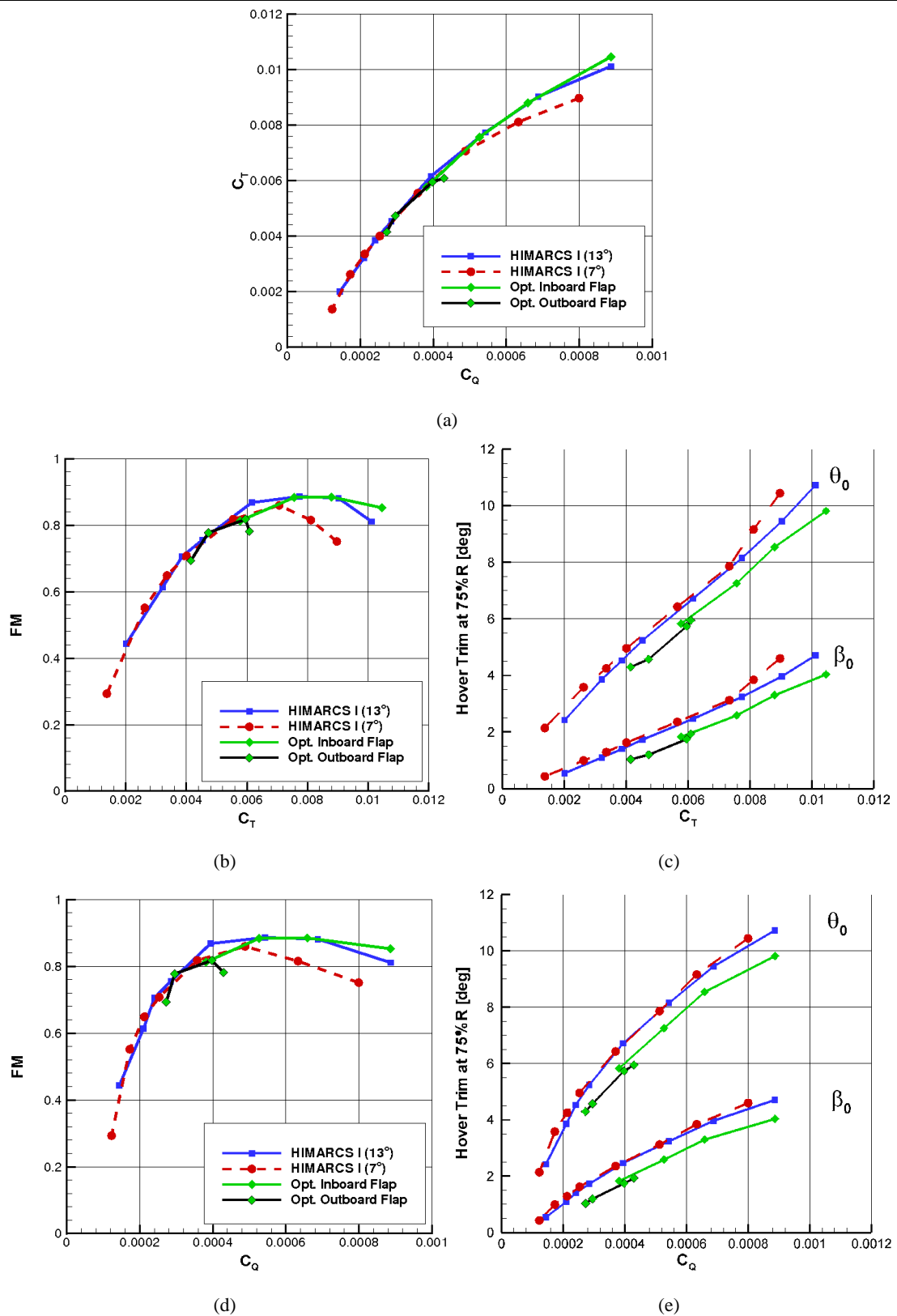
Figure 5.8: 3D CFD results with both inboard and outboard optimised flaps. (a) C_Q vs. C_T. (b) C_T vs. FM. (c) C_T vs. Trim. (d) C_Q vs. FM. (e) C_Q vs. Trim.

However, as can be seen at r/R = 0.395, 0.475, and 0.554, there is an increase in loading towards the trailing-edge of the section due to the presence of the slotted flap. This allows for the recovery of the

performance expected from the rotor with greater twist. As one approaches the tip of the blade, it is evident again that both the highly twisted and flapped rotors are less loaded at the specified C_T. Yet again, this is evidence to verify the effect of both twisted and inboard flapped blades in improving the performance of rotors whilst in hover.

Further comparisons of Cp are presented in Figure 5.10 for a C_T of approximately 0.004, where the clean rotors achieve near identical performance whilst the outboard flap configuration falls slightly below. Slices are taken from the two clean blades and the optimum outboard flap at r/R = 0.317, 0.396, 0.475, 0.554, 0.871, and 0.95. It is clear there is little difference in performance between the low twist rotor and the outboard flap rotor, with the highly twisted rotor again achieving higher inboard blade loadings for most cases. The optimum outboard flap configuration continues to closely match the performance of the clean rotor. At r/R = 0.95, the effect of the flap can be seen quite clearly. Further examination of the results identified the performance loss as being due to a combination of two factors. Firstly, with the outboard slotted flap being located further outboard, the strength of the downwash from the trailed Flap-Edge Vortices (FEV) is greater. The induced losses at the flap edges combined with the small flap size led to the CFD underpredicting the blade element method, which does not take induced power losses due to downwash around the flap into account. Secondly, the actual location of the suction peak on the flap's upper surface could be a factor. As can be seen in Figure 5.11, the maximum -Cp on the flap occurs directly below the main element and is therefore providing suction on its lower surface. This downforce on the lower surface of the main element's trailing-edge gives a reduction in lift, although the net increase due to the flap is still positive. Moving the expected suction peak location away from the main element's trailing-edge would be expected to result in greater increases in lift At such a low blade loading as presented in Figure 5.10, this interaction between the main element and the flap could be a serious performance-limiting factor.
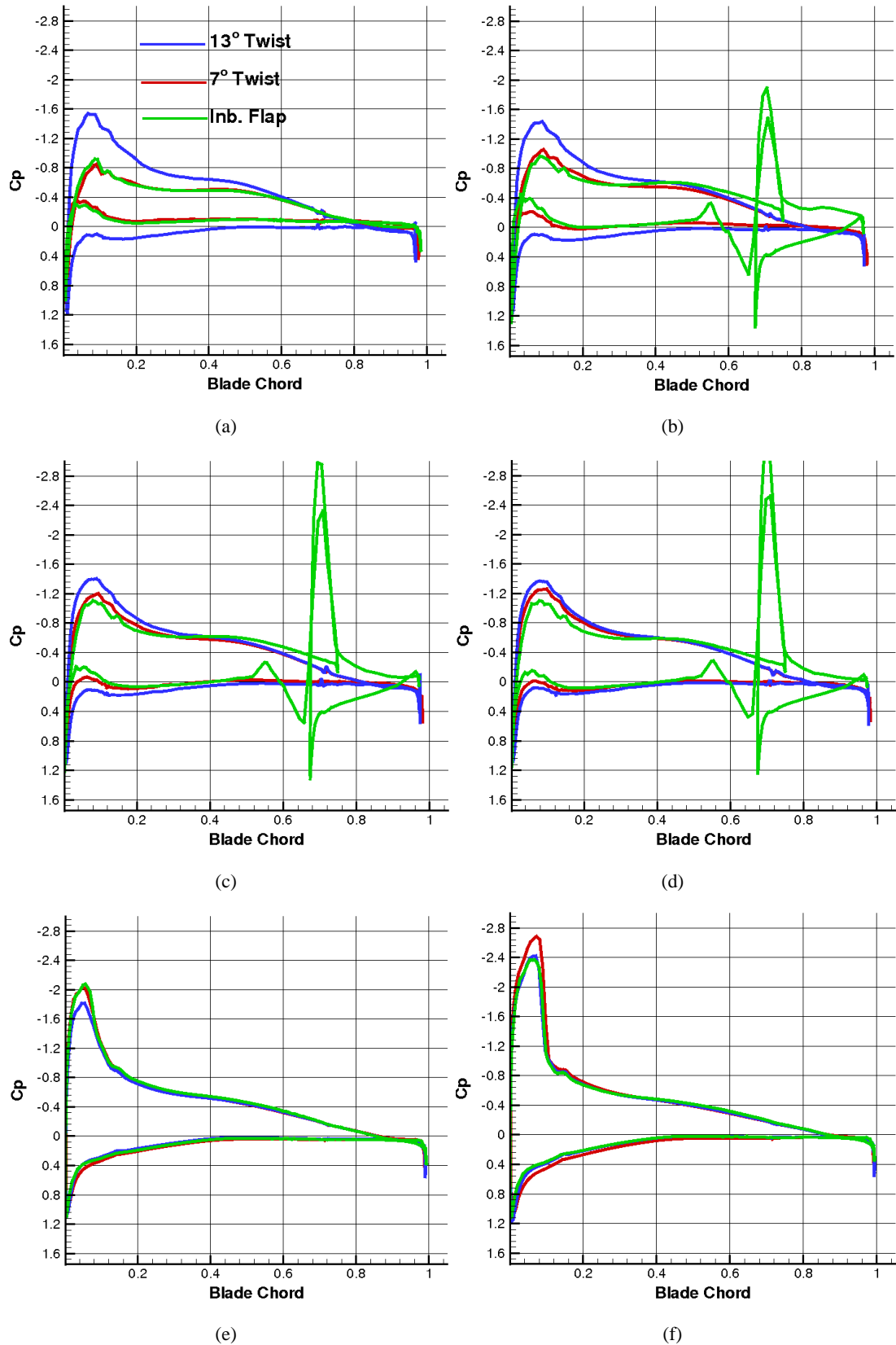
Figure 5.9: Chordwise Cp distribution for the HIMARCS I with -7° and -13° of twist, and the optimum inboard flap. r/R: (a) 0.317. (b) 0.396. (c) 0.475. (d) 0.554. (e) 0.871. (f) 0.95. ($C_T \approx$ 0.0087.)
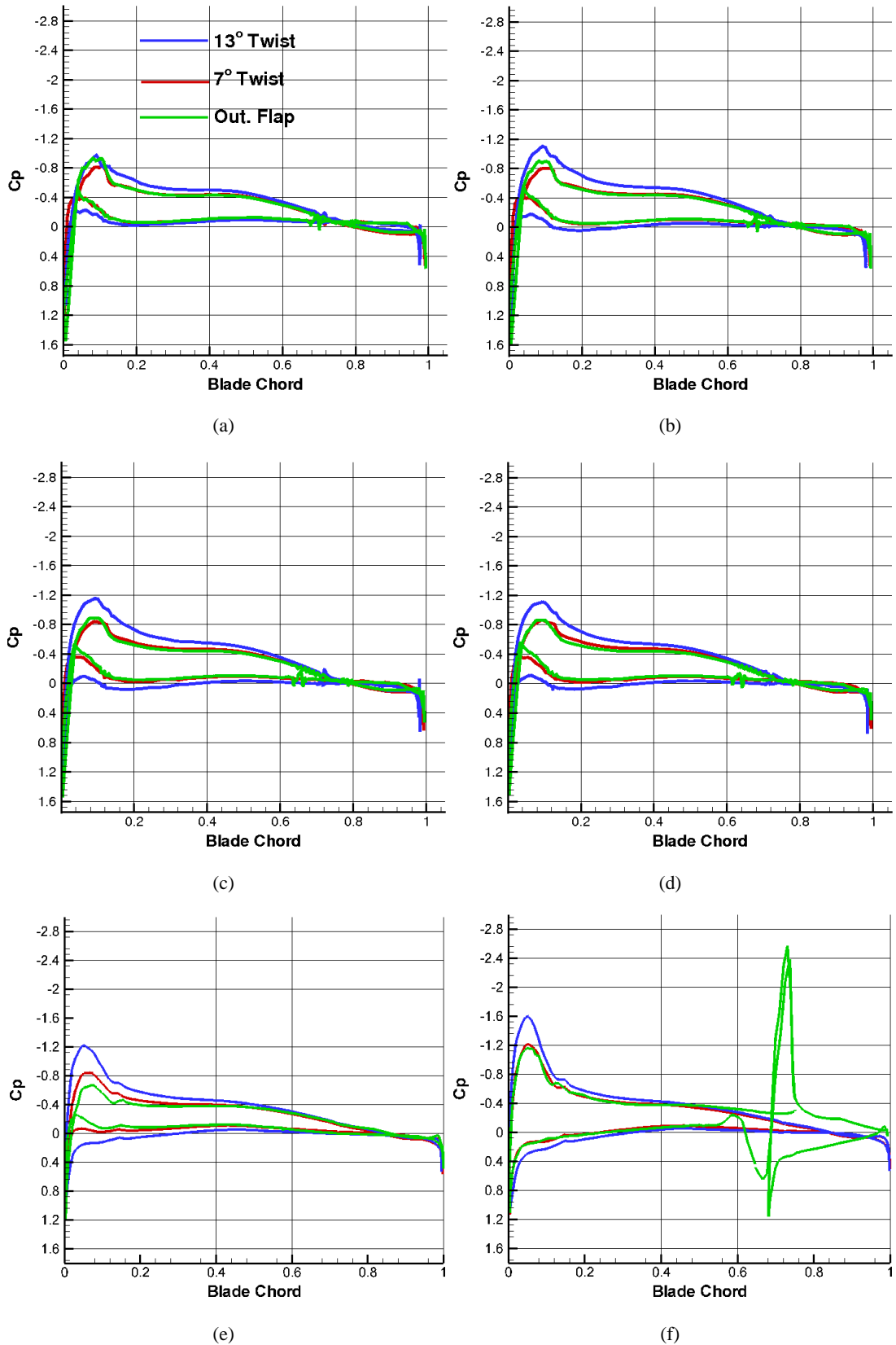
Figure 5.10: Chordwise Cp distribution for the HIMARCS I with -7° and -13° of twist, and the optimum outboard flap. r/R: (a) 0.317. (b) 0.396. (c) 0.475. (d) 0.554. (e) 0.871. (f) 0.95. ($C_T \approx$ 0.004.)
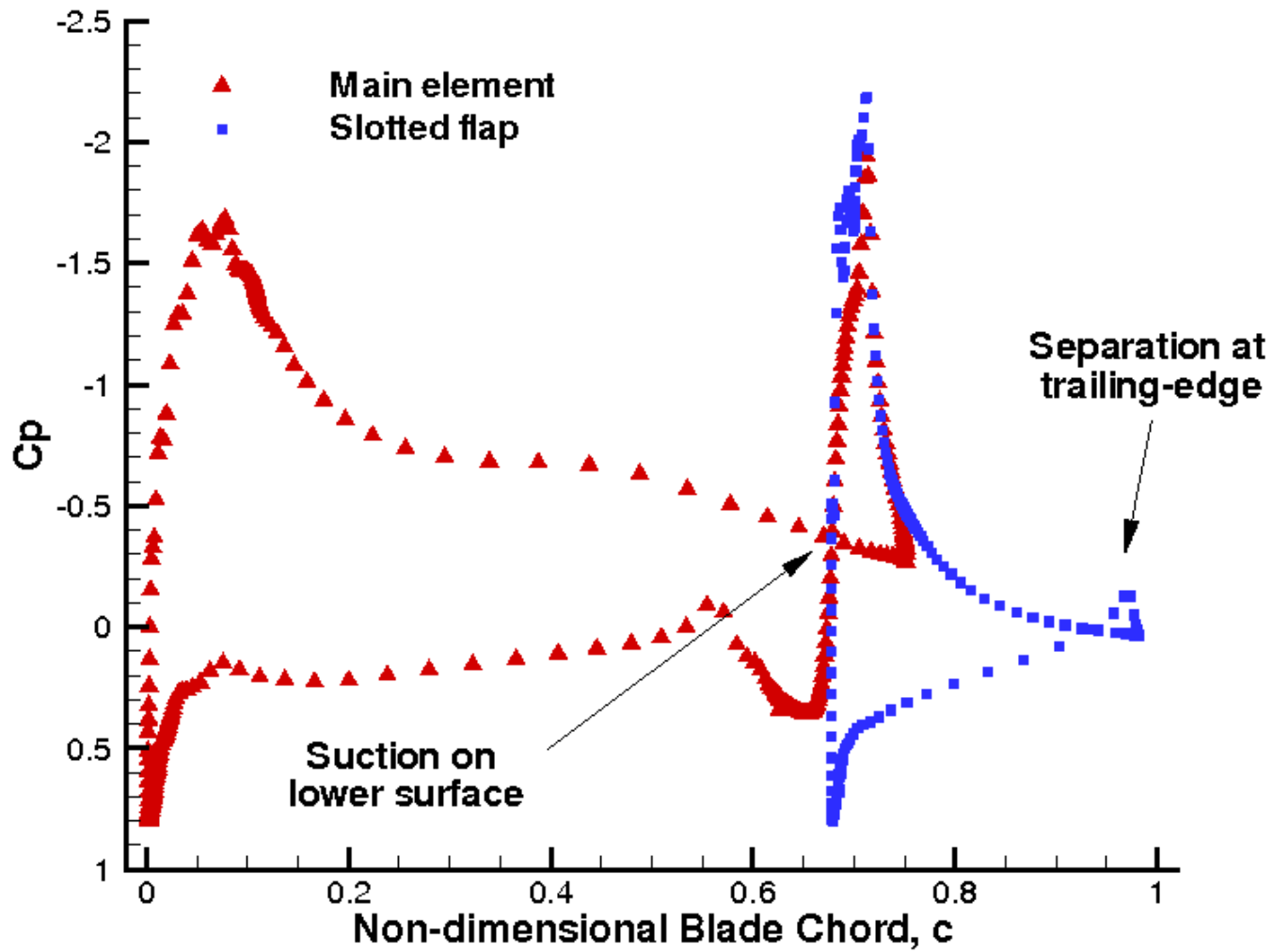
Figure 5.11: 2D Cp distribution over the RC(4)-10 section with a slotted flap. ($\alpha = 5^o$, $\delta = 10^o$, M = 0.5, Re = 5x10^6)

5.4   Hover Trimmer

So far, all the trim settings used to setup the rotor geometry in hover were calculated using the blade element method as described in the previous chapter. The main advantage of such a method is the short turnover times for adequate aerodynamic loads predictions. However, due to the lack of experimental trim settings in the original HIMARCS I report [16], it would be beneficial if comparisons of the accuracy of the BEM with a high fidelity method such as 3D RANS CFD could be made. Currently, the applied CFD solver has a built-in trim routine as described in Chapter 2, which is similar to that used in the BEM. Unlike the CFD method, whose predictive nature extends to the pressure on the surfaces and in the fluid around it, the BEM is entirely dependent on the input of external aerodynamic tables or polynomials, which in this case is supplied by 2D CFD-generated aerodynamic look-up tables.

It is of interest to investigate how both methods retrim the same rotor geometries, since essentially the only difference between them is the predicted aerodynamics. This was conducted using both the BEM and inviscid 3D with built-in trimmer to calculate the trim settings for a selection of high C_T's. These trim settings were used to setup the new blade geometries and 3D viscous calculations were carried out to evaluate the predicted aerodynamic performance of each test case.

5.4.1   Blade Element Method vs. Inviscid CFD

Figure 5.12 presents the predicted C_T, C_Q, FM and trim settings for the HIMARCS I rotors with -7° and -13° of twist. The graphs include viscous CFD results predicted from geometries setup using trim settings obtained from the BEM and inviscid CFD hover trimmer. As one can see in Figure 5.12(a), there is little difference in the predicted performance between the BEM and the inviscid trimmer. However, in general the CFD trim settings have predicted an increase in performance by as much as 2.5% more than the trim settings predicted by the BEM, which is more clear in Figures 5.12(b) and 5.12(d). If one examines the actual trim settings themselves, the predicted collective angle, θ_0, for the BEM compared to the CFD, each C_T is slightly greater by approximately 0.2^o and 0.6^o for the low twist and high twist rotors, respectively. For the predicted coning angles, β_0, we see similar differences of 0.8^o and 1.7^o for the low twist and high twist rotors, respectively. As expected, increasing the blade collective angle requires a higher coning angle for the rotor to produce the same amount of thrust. It is clear that better performance is predicted with a low θ_0-β_0 combination as predicted by the CFD trimmer. However, these CFD trimmer calculations are computationally expensive whereas the BEM trimmer offers turnover times 4-5 orders of magnitude faster with near

similar accuracy in viscous CFD predictions. However, one element of the inaccuracy in the BEM modelling could be the simple induced flow model used (the prescribed wake), which could be the cause for the higher predicted trim angles. Nonetheless, the differences overall are small.

5.4.2   Blended Flap Results

The initial optimum blade designs considered were based on slotted flap configurations since a similar device was tested on the HIMARCS I rotor during the experiments by Noonan *et al.* [16]. The fixed entity of the design means that power requirements would be limited and savings in blade twist would offer faster forward flying speeds. However, in reality the application of such a device on a rotor requires further investigation. Factors to the detriment of the slotted flap design include the need for flap edge gaps and strong nose-down pitching moments. The first causes an increase in drag and the second could potentially induce negative blade torsion that, inboard at least, would be detrimental to a hovering rotor's performance, whilst also increasing maintenance costs due to fatigue. The HIMARCS I slotted flap design minimised this effect by having the suction peak located directly below the main element, as described in Figure 5.11. With mprovements in PZT actuators and work being conducted by NASA on the ATR [12, 13], the application of the blended flap seems much more feasible for application to a full-scale helicopter rotor. The blended inboard flap was thus modelled by retaining the same flap spanwise length, chord length, and deflection angle as the optimum slotted flap design. No flap gap is implemented between the main element and the flap or at the edges of the flap length. Calculations were first run using the inviscid CFD trimmer and then computed using the viscous 3D hover CFD to evaluate the concept. The inviscid blocking scheme is clearly presented in Figure 5.4(b) and the viscous blocking in Figure 5.4(d).

Figure 5.13 presents the inviscid CFD trimmer results for C_T, C_Q, FM, and the predicted trim settings for the HIMARCS I rotor with -7°, -10°, and -13° of twist and the blended inboard flap configuration. It is already clear that the blended inboard flap offers up to 4% improved performance over the rotor with -7° of twist at trim settings of at least 1° less in collective and coning angle. However, it fails to match the performance of the rotor with -13° of twist, which is most likely due to the lack of flap gap and the flap stalling earlier than previously. Also, plain flaps aren't as effective as lift generators. Results do seem to show that it offers approximately the same levels of performance of a rotor with -10° of twist. This would equate to a saving of 3° in blade twist at approximately 1° less in collective and coning. The viscous computations are presented in Figure 5.14 and confirm the results from the inviscid computations. The low twist rotor with blended

inboard flap is shown to be comparable to a rotor with -10° of twist.

(a)

(b)

(c)

(d)

(e)
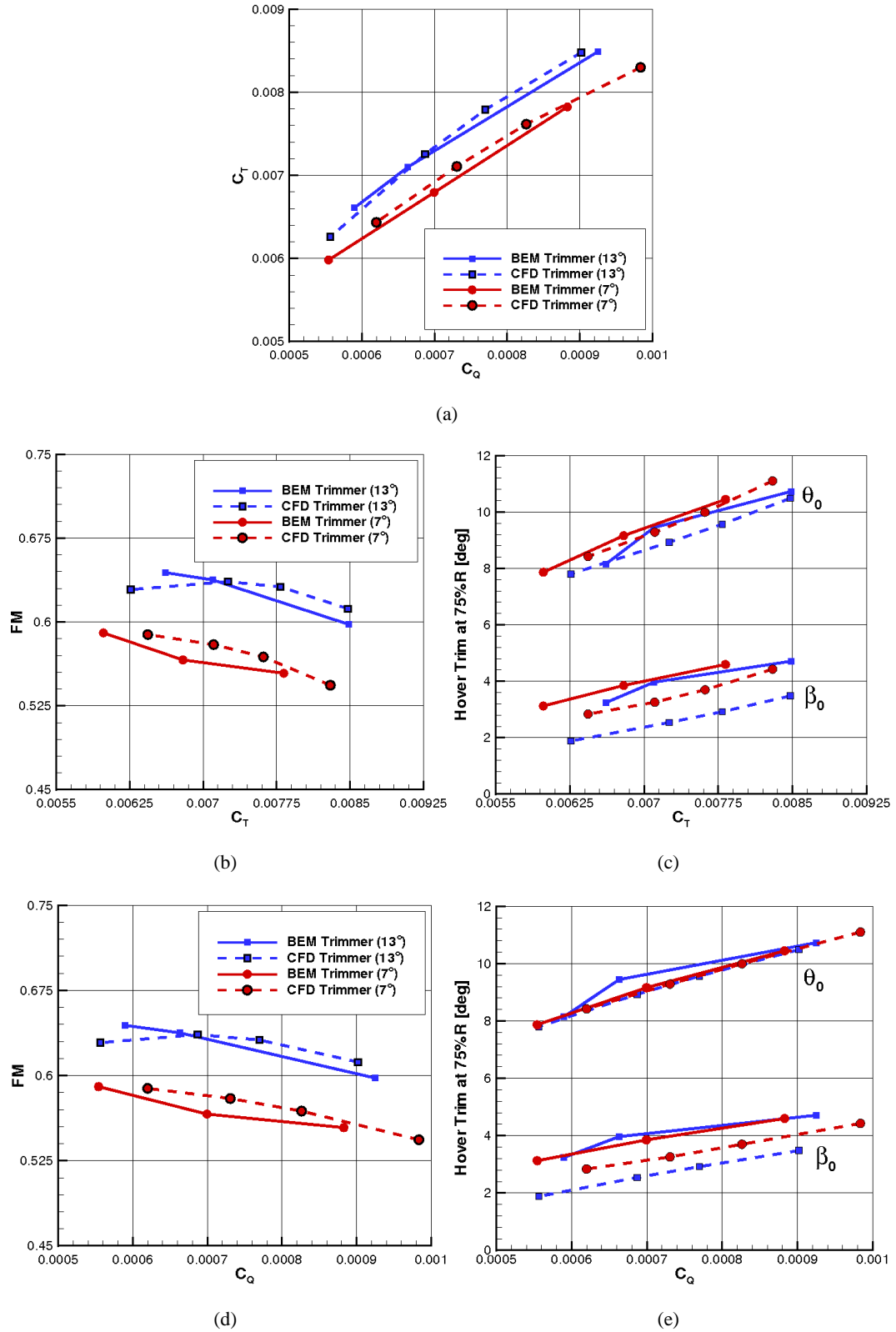
Figure 5.12: Rotor performance with predicted trim settings from BEM and inviscid CFD. (a) C_Q vs. C_T. (b) C_T vs. FM. (c) C_T vs. Trim. (d) C_Q vs. FM. (e) C_Q vs. Trim.

(a)

(b)   (c)

(d)   (e)
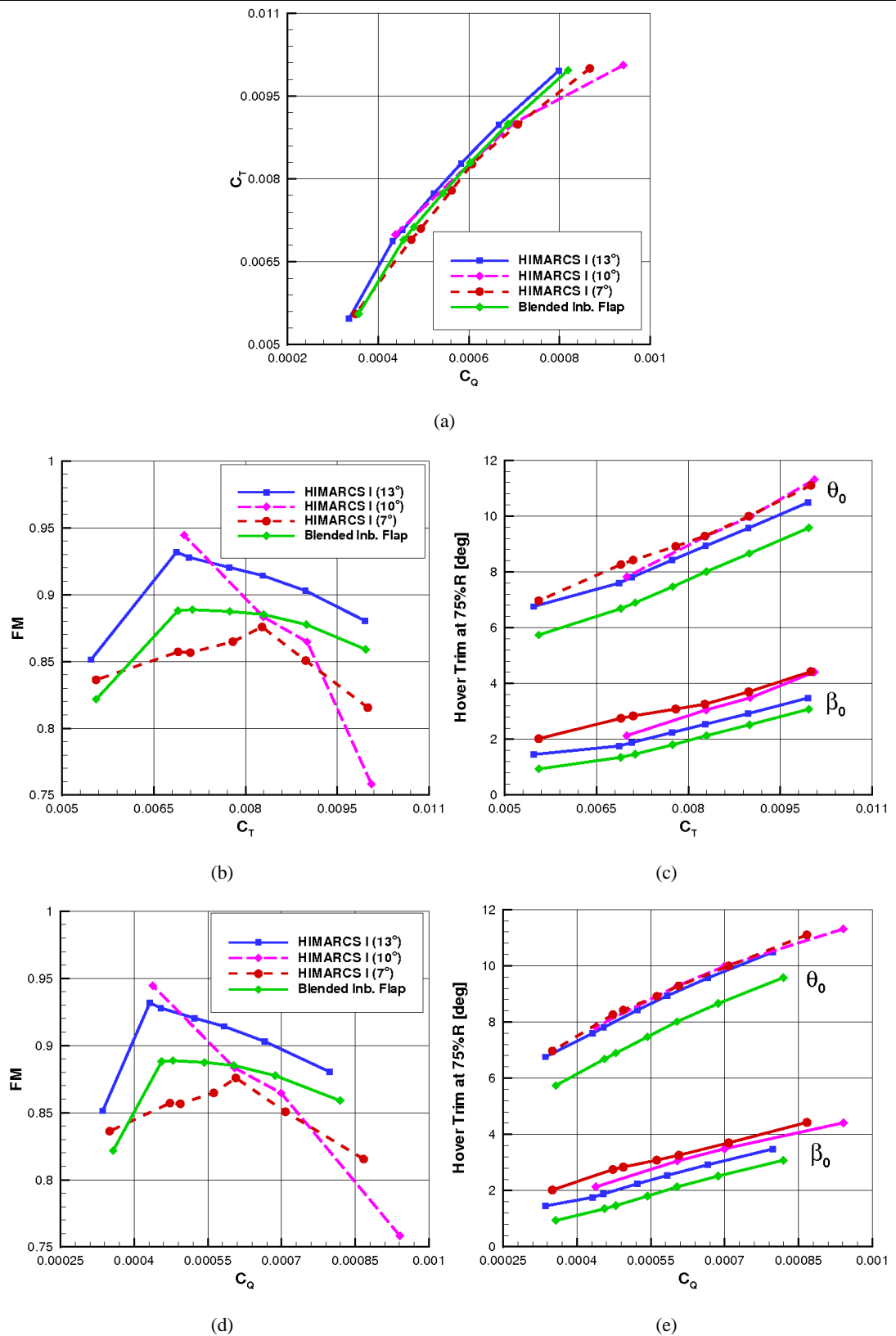
Figure 5.13: Inviscid 3D CFD results for the HIMARCS I with blade twist and blended inboard flap. (a) C_Q vs. C_T. (b) C_T vs. FM. (c) C_T vs. Trim. (d) C_Q vs. FM. (e) C_Q vs. Trim.

(a)

(b)

(c)

(d)

(e)
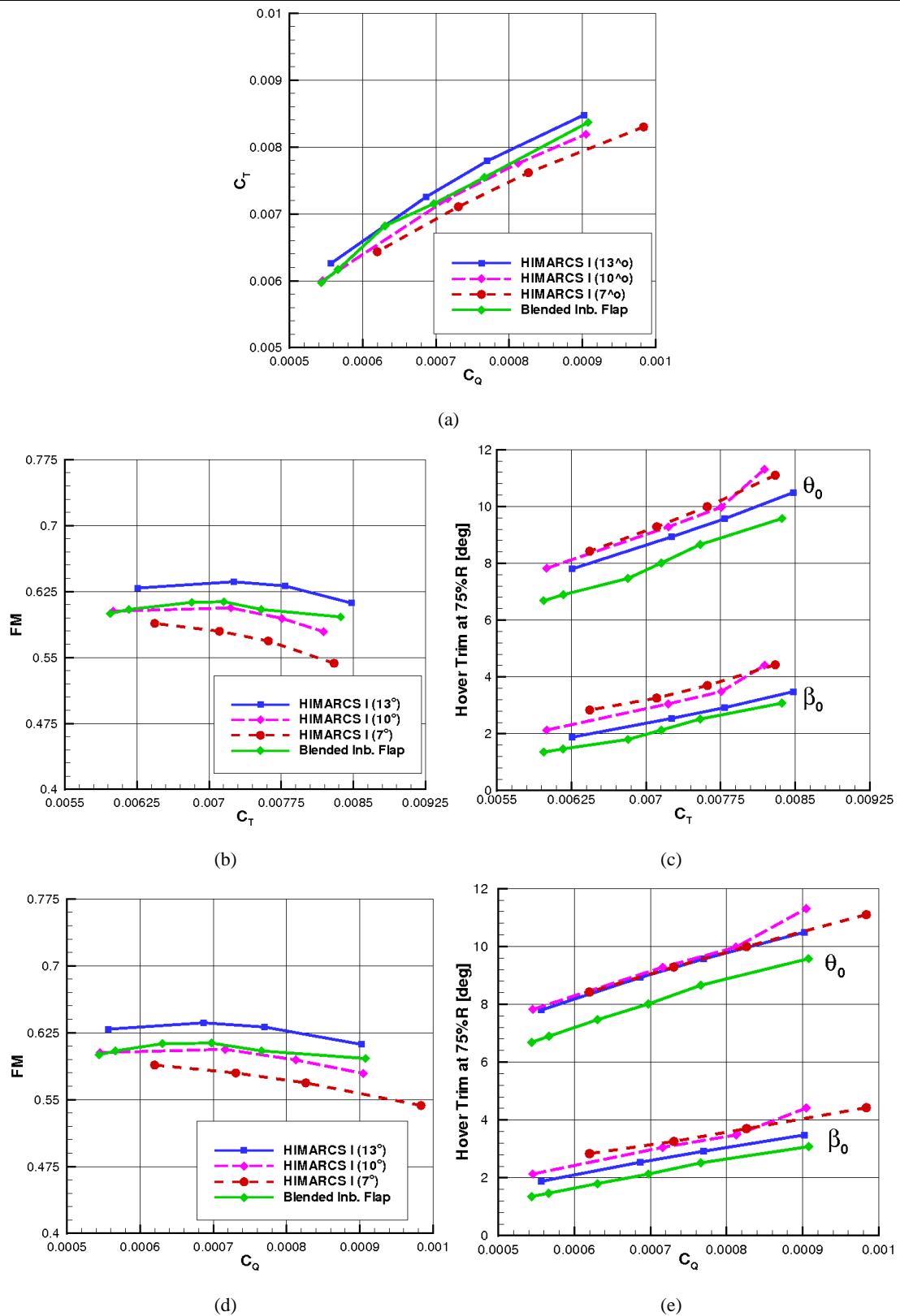
Figure 5.14: Viscous 3D CFD results for the HIMARCS I with blade twist and blended inboard flap. (a) C_Q vs. C_T. (b) C_T vs. FM. (c) C_T vs. Trim. (d) C_Q vs. FM. (e) C_Q vs. Trim.

The chordwise Cp distribution is presented in Figure 5.15 as before, with slices taken at r/R = 0.317, 0.396, 0.475, 0.554, 0.871, and 0.95. As was the case for the slotted flap results, the flapped rotor

has less blade loading than the highly twisted rotor away from the flap, most importantly at the tip of the rotor. However, in the flap region there is increased loading at the trailing edge due to the induced local suction where the increase in effective camber due to flap deflection accelerates the flow on the upper surface. There is the added benefit that all suction produced by the flap deflection offers pure lift performance, with no detrimental effects associated with interactions with the main element as witnessed with the HIMARCS I slotted flap design [16].

Figures 5.16 and 5.17 present iso-surfaces of λ_2 coloured by the turbulent Reynolds number for the HIMARCS I rotor with 10° of twist and the HIMARCS I rotor with blended inboard flap and 7° of twist, respectively. Although these solutions were obtained using a periodic boundary condition, for clarity the periodic solution for the single blade was copied around the azimuth. This allows for a much clearer representation of the flowfield. Figure 5.16 details the shedding of the tip vortex, the root vortex, and a thin layer of vorticity leaving the trailing-edge of the rotor. The higher levels of turbulence at the tip compared to the inboard region is highlighted by the levels of Re_T. The root vortex passes below the blade and is captured for a half revolution and has a very laminar flow. Further revolutions could be captured with higher values of λ_2, but is accompanied by a lack in clarity of solution as smaller elements of low pressure in the domain are captured. Further outboard, the change in the levels of turbulence around the tip vortex as it rotates and passes into the wake; the higher values indicating the passage of the shed vortex itself. Figure 5.17 presents the blended inboard flap configuration. Here the tip vortex is visualised, with the spanwise sheet of vorticity from the blade's trailing-edge, the flap edge vortices, and the root vortex. Similar aspects are captured with regards to the vortices at the tip and root of the blade, as previously. However, due to the presence of the inboard flap and the increased circulation there, there is also greater shed vorticity passing into the wake. This proves interesting since the blended flap has no flap edges from which vortices are shed; they originate from the blending region. This is clearly depicted in Figure 5.18, where perpendicular slices have been taken at both regions of blending between the flap and the blade. The levels of turbulence here are clearly evident as the vortices are shed and pass under the blade again.

5.5   Summary

In this chapter the effect of implementing trailing-edge flaps on a modern rotor blade was studied using 3D Computational Fluid Dynamics. Following a validation of the method in Chapter 3 and a blade element study in Chapter 4, multiblock grids were generated for both twisted and flapped

rotors and evaluated using inviscid CFD. Results confirmed the beneficial effect of applying a slot-ted inboard flap as a twist recovery mechanism on a low-twist rotor in hover. The effect of the aerodynamic modelling in Chapter 4 was also investigated by comparing inviscid and viscous 3D performance predictions using trim settings obtained from the blade element trimmer and the built-in CFD trimmer. To evidence both the potential of the inboard flap design and the use of a CFD trimmer in predicting hover performance, a blended inboard flap of the same configuration as the slotted design was evaluated. Again it was shown that the inboard flap configuration increased the blade loading inboard with a reduction in blade loading outboard to obtain similar performance as a rotor with 10° of twist.
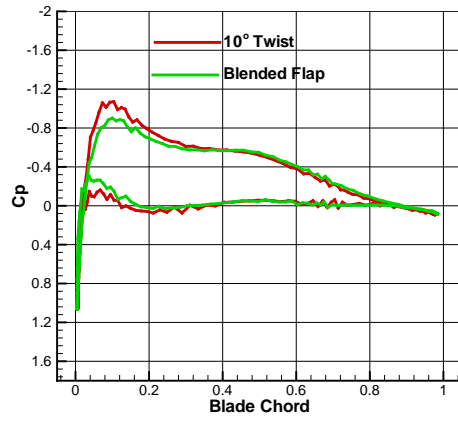
(a)
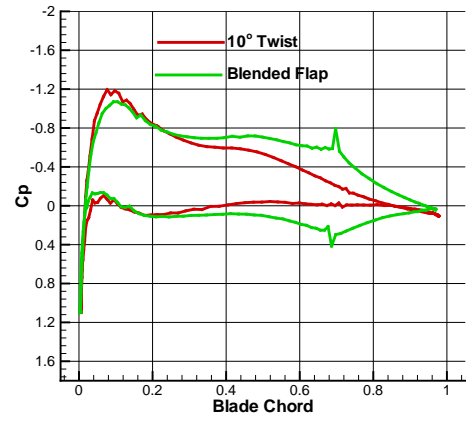
(b)
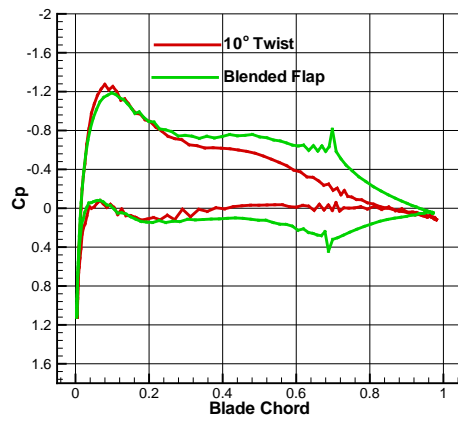
(c)
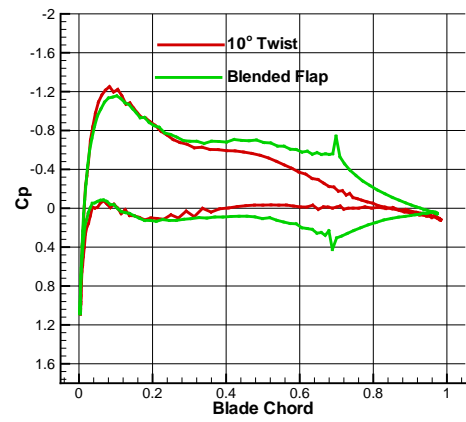
(d)
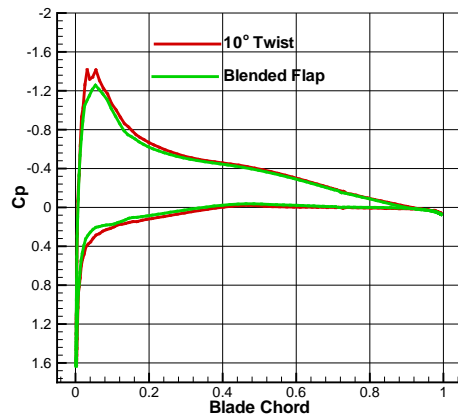
(e)
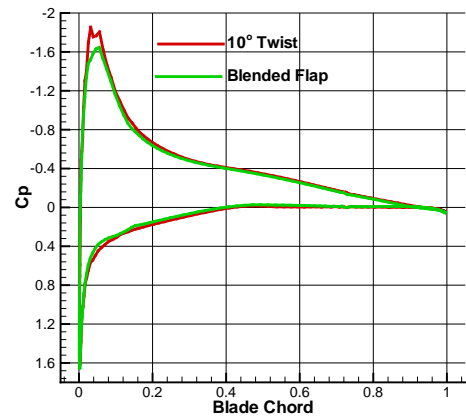
(f)

Figure 5.15: Chordwise Cp distribution for the HIMARCS I rotor with -10° of twist and blended inboard flap. r/R: (a) 0.317. (b) 0.396. (c) 0.475. (d) 0.554. (e) 0.871. (f) 0.95. ($C_T \approx 0.00829$.)

(a)
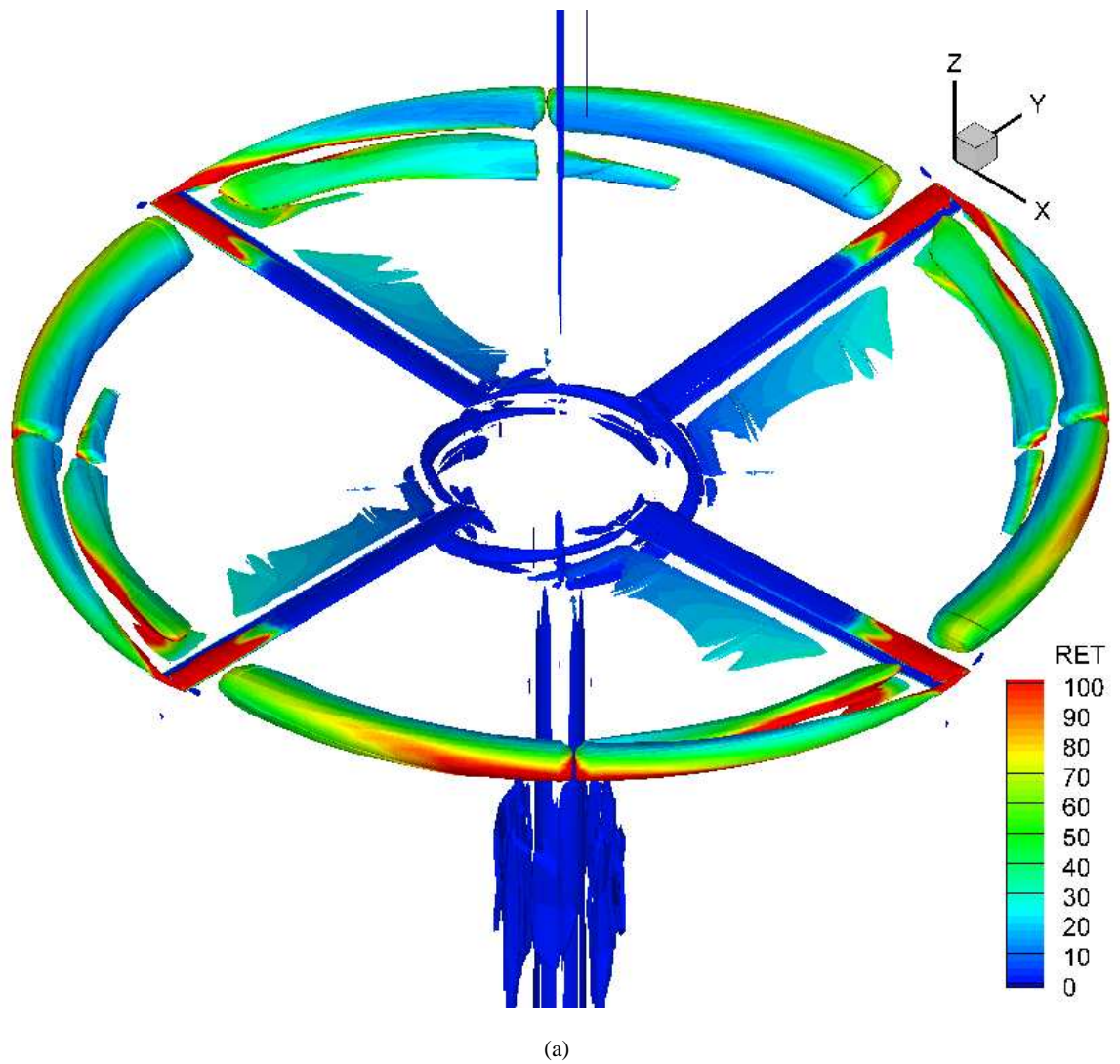
Figure 5.16: Iso-surfaces of λ_2 coloured by the turbulent viscosity ratio for the HIMARCS I with -10° of twist. (λ_2 = -0.0125.)

(a)
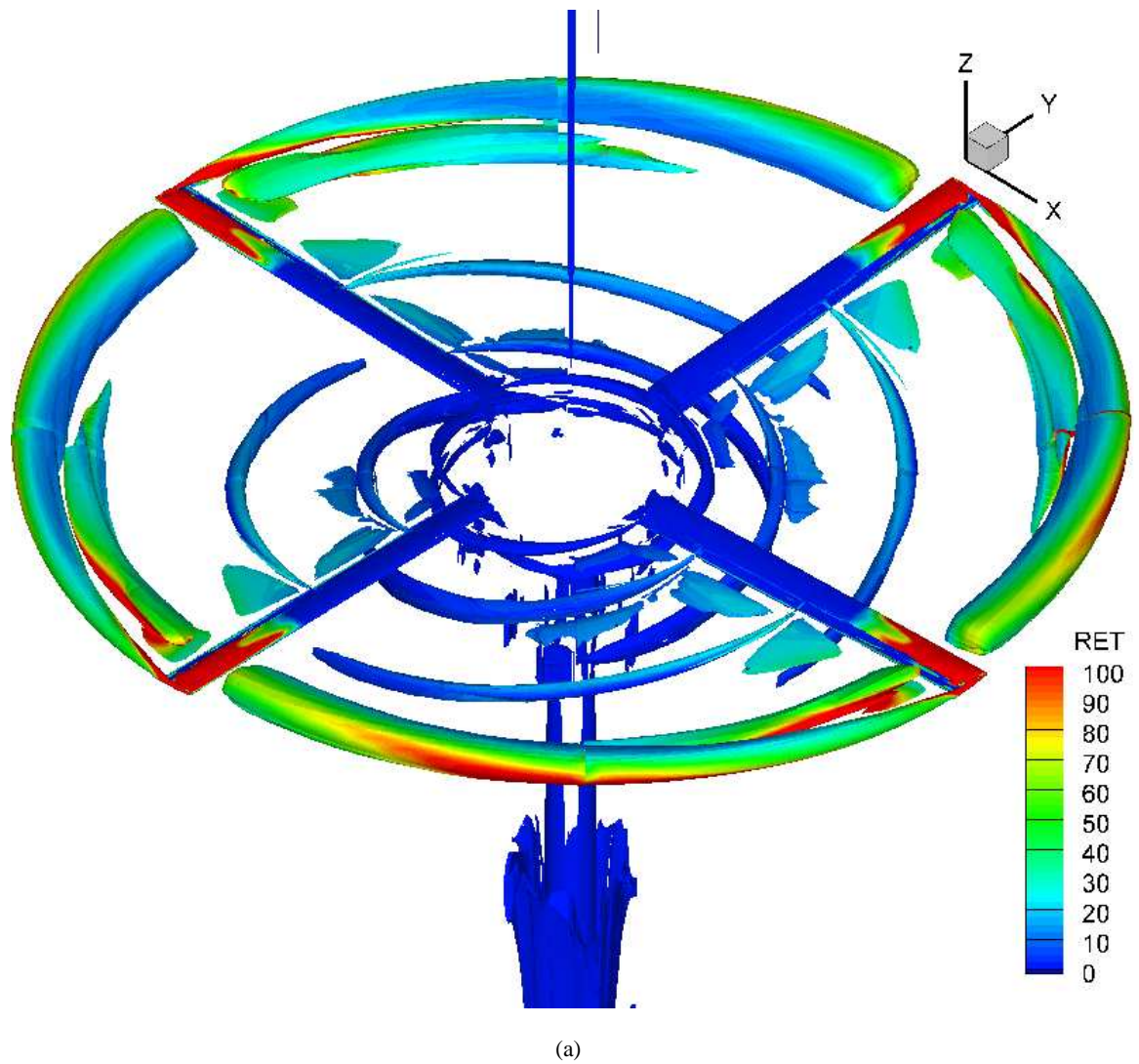
Figure 5.17: Iso-surfaces of λ_2 coloured by the turbulent viscosity ratio for the blended optimum inboard flap configuration. ($\lambda_2 = -0.0125$.)
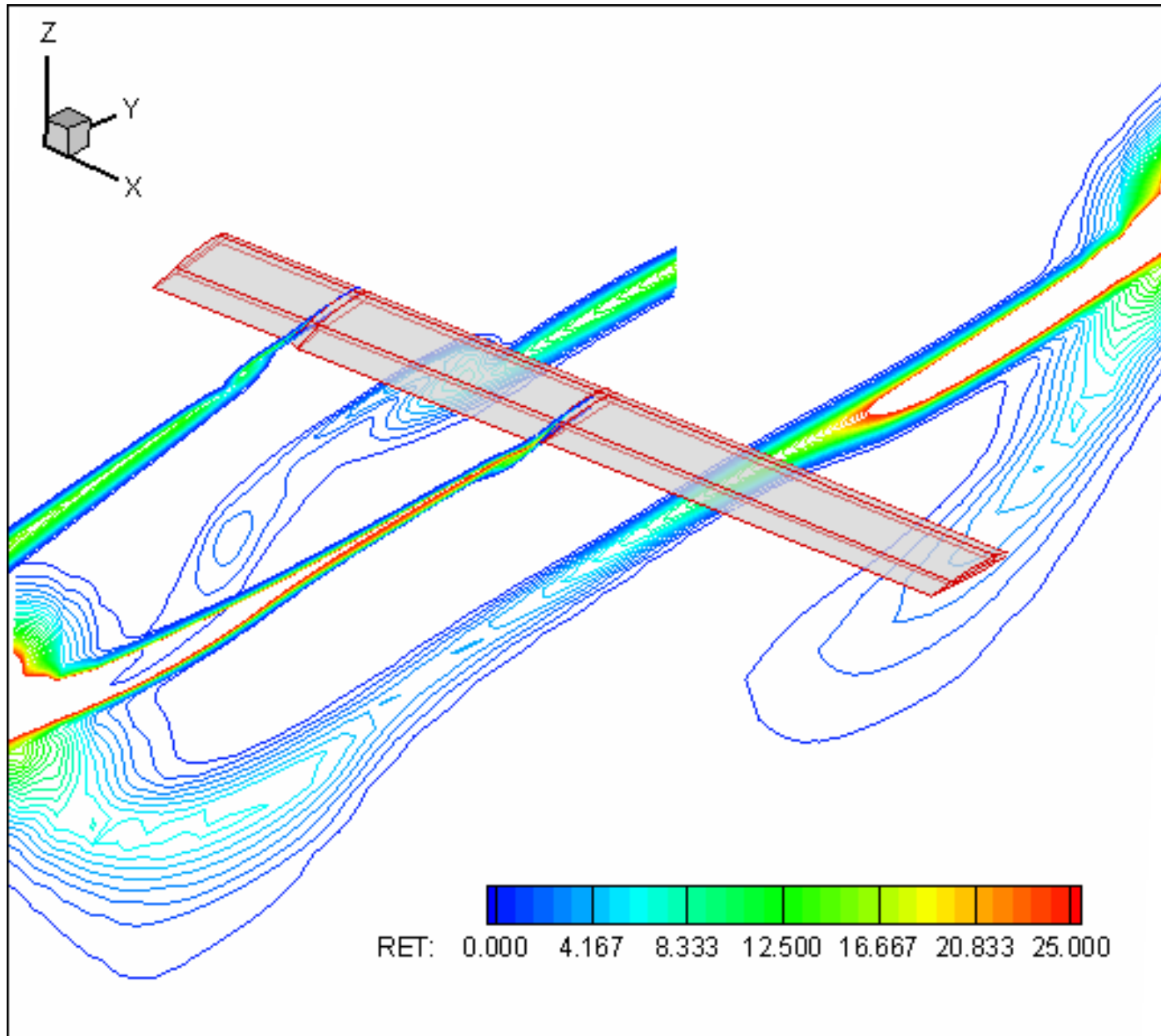
(a)

Figure 5.18: Slices along the x-axis of the turbulent viscosity ratio detailing the flap edge vortices shed from the blended inboard flap.

Chapter 6

Conclusions and Open Problems

This thesis considered the analysis and design of a hovering, low-twist rotor equipped with trailing-edge flaps using blade element methods and computational fluid dynamics. A low twist rotor provides benefits in forward flight where high levels of twist tend to propagate compressibility effects at the blade tip on the advancing side, whereas a high twist rotor can improve rotor performance in hover. The current work aimed to investigate this issue by providing a low twist rotor for improved forward flight performance and equipping it with trailing-edge flaps that, when in hover, could be deflected to recover performance lost due to lack of built-in blade twist. Here now follows the conclusions of this research and suggestions for future work.

6.1   Conclusions

The BEM employed was shown to be capable of rapidly evaluating several design configurations for a slotted flap placed both inboard and outboard on a modern rotor blade. As well as providing a parametric study to identify optimum configurations, the trim settings for each design were obtained. This allowed for the verification of the model's results using 3D CFD. Slotted flaps were evaluated at a range of thrust coefficients from 0.0005 to 0.00829. Results from the BEM model indicated that an inboard flap would be more beneficial at high thrust, whereas an outboard flap could offer benefits at medium thrust settings. Therefore, two optimum flap configurations (inboard and outboard) were selected for further study. An inboard flap was located at 36%R, with a flap span of 24%R, chord of 32%c, and deflection angle of 10°. The inboard flap demonstrated the potential to improve rotor performance by 3%-4.5% at high thrust, which is equivalent to a gain of 6° in rotor twist. An outboard flap was located at 92%R, with a flap span of 8%R, chord of 32%c, and deflection angle of 10°. The optimum outboard flap also showed potential to improve performance by up to 10% compared to the baseline rotor at medium thrust coefficients. Both configurations reduced

the collective and coning angles compared to the baseline rotor by approximately 0.5^o-1°.

The next stage was to verify the blade element methods results by using 3D inviscid and viscous CFD. Results for a study on the effect of twist indicated that greater levels of twist provide benefits at higher thrust coefficients, by redistributing the loading along the blade. Due to rotating-blade motion and the varying dynamic head, the tip of the blade sees a higher effective inflow velocity than the root and contributes more to the lifting performance of a rotor. High tip loading has the effect of increasing rotor downwash and the induced drag results in high power requirements. As blade twist is increased, the effective loading at the blade tip is reduced whilst the inboard region is loaded.

Next, the effect of the optimum slotted flap configurations were considered against the twisted blades. The inboard slotted flap on a low twist rotor was shown to provide the same levels of performance as a rotor with 6° more twist with saving in trim angles of 0.5^o to 1° at high thrust settings. Again, the loading on the blade was investigated. It was indicated by the results that, by deflecting an inboard flap in hover, an increase in inboard blade loading was created with the flap having a similar effect as an increase in blade twist. Consequently, the inboard loading also reduces the requirement for blade tip loading and reduces blade trim angles. This has the effect of reducing the strength of the shed wake outboard and hence the induced power. The outboard slotted flap design, however, did not perform to expectations and failed to offer performance improvements over the baseline rotor. It was concluded that this was due to a combination of strong outboard flap edge vortices generating substantial downwash and a small flap size, hence reducing the overall effectiveness of the flap. The outboard location of the flap would also have the effect of increasing outboard blade loading and increasing induced drag. Interestingly, the optimum outboard configuration was able to achieve similar savings in trim angles as the optimum inboard flap, which is itself a benefit.

The fidelity of the blade element method used in this work was then considered. This was conducted by comparing the predicted trim settings from the model with predictions obtained from inviscid CFD with a built-in trimmer, and evaluating their respective predictions for hover performance using viscous 3D CFD. At the same thrust coefficient, the blade element method predicted collective and coning angles of around 0.5^o-1° greater than the CFD trimmer. In the viscous calculations, these results translated into an improvement in performance of around 0.5% using the CFD-predicted trim settings, indicating that a combination of low trim angles for the same thrust coefficient is more beneficial with regards to hover performance. The blade element method, however, demonstrated its efficiency since it was significantly faster than CFD. This confirms the use

of simple mathematical models for design studies is feasible provided input data is available from wind tunnel or CFD computations, although greater accuracy can be obtained by using 3D CFD with corresponding increases in computational time.

To give further evidence of the capability of inboard flaps in improving the performance of a low twist rotor, the CFD trimmer was then exploited to evaluate a blended inboard flap configuration of the same dimensions as the slotted inboard flap considered earlier. The blended flap had no flap gaps and was completely embedded within the rotor geometry; a more likely implementation of the concept on any advanced rotor blade design. This design confirmed previous blade element and CFD predictions by recovering up to 3° of twist with savings of approximately 1° in trim settings. This provided final confirmation of the effectiveness of the inboard flap configuration for twist recovery in hover.

6.2   Open Problems

There are a few areas where further work could be conducted.

1) The first to be considered is the effect of turbulence modelling on the predicted blade loads and shed wake vorticity. For the present work, the turbulence model remained constant since we were only concerned with the relative differences between various design configurations. Also, it was shown that with a fine grid the Wilcox k-ω model was more than adequate at matching experimental data. However, it is known that this model overpredicts off-wall turbulence and accelerates vortex breakdown in other areas such as delta wing vortical flows. Therefore, a potential extension to this work would be to look at the effect that turbulence modelling has on both the validation and the shed vortices. Turbulence models that could be considered include the Spalart-Allmaras one-equation model that was designed specifically for aerospace applications, or the Mentor SST model that combines the strengths of the k-ω model at the wall and the k-ε model away from the wall. Detached Eddy Simulation may also be one to consider in future research.

2) With respect to the shed wake, the proposition of an inboard or outboard flap offers two potential issues that have to be investigated. Firstly, an inboard flap on a a 4-bladed helicopter will produce 8 inboard vortices that can interact with the fuselage and potentially increase cabin vibrations. For operations such as sea and rescue where there is the likelihood of flap deployment in hover, this added element to the downwash could cause problems for any individual(s) attempting

to leave or enter the cabin whilst in flight. Similarly, any unsteady loading on the fuselage due to the tip vortex may be exacerbated by the implementation of an outboard flap that offers two strong flap edge vortices and possibly an even stronger tip vortex. Their effect could be the subject of future investigations.

3) The introduction of other flow control devices such as leading-edge flaps or slats could further enhance performance in hover and, at least for a blended leading-edge flap, would prove as simple to implement as a blended trailing-edge flap. There is also room for the addition of passive tip devices or surface blowing to further delay trailing-edge separation and allow the rotor to achieve higher thrust coefficients.

4) Considerations for the inboard flap's deployment in forward flight could also be made. A well-known issue surrounding helicopter forward flight performance under heavy load is dynamic stall on the retreating blade, contrasted by the formation of shocks at the rotor tip on the advancing blade. As in hover, the inboard flap could be actuated in forward flight, redistributing the blade loading along the blade. The increase in lift on the retreating side by deflection of the inboard flap could reduce blade stall effects and limit the shedding of the dynamic stall vortex with reductions in vortex drag and permitting heavier payloads. On the advancing side, with careful optimisation of the flap deflection angle, the flap could be deflected upwards hence inducing a nose-up pitching moment to achieve a zero incidence at the blade tip, thus reducing wave drag and increasing the top speed of the helicopter. Improving on both issues would also lead to reductions in blade and hub vibrations and control loads.

References

[1] Leishman, J.G. *Principles of Helicopter Aerodynamics*. Cambridge University Press, 2002.

[2] Friedmann, P.P., and Shanthakumaran, P. Optimum Design of Rotor Blades for Vibration Reduction in Forward Flight. *Journal of the American Helicopter Society*, 29:70–80, October 1984.

[3] Hassan, A.A., and Charles, B.D. Airfoil Design for Helicopter Rotor Blades-A Three-Dimensional Approach. *Journal of Aircraft*, 34:197–205, March-April 1997.

[4] Ganguli, R., and Chopra, I. Aeroelastic Optimization of an Advanced Geometry Helicopter Rotor. *Journal of the American Helicopter Society*, 41:18–28, January 1996.

[5] Caradonna, F.X. and Tung. C. A Review of Current Finite Difference Rotor Flow Methods. In *American Helicopter Society 42nd Annual Forum*, June 1986.

[6] US Army. Army Science and Technology Master Plan. Technical report, US Government, 1998. www.fas.org/man/dod-101/army/docs/astmp98/sec4d.htm.

[7] Beedy, J., Barakos, G.N., Badcock, K.J., and Richards, B.E. Using CFD to Improve the WHL Rotor Load Aerodynamic Model. In *30th European Rotorcraft Forum*, September 2004.

[8] Datta, A., Sitaraman, J., Chopra, I., and Baeder, J.D. CFD/CSD Prediction of Rotor Vibratory Loads in High-Speed Flight. *Journal of Aircraft*, 43:1698–1709, November-December 2006.

[9] Gad-el-Hak, M. Flow Control - The Future. *Journal of Aircraft*, 38:402–418, May-June 2001.

[10] Lemnios, A.Z., and Howes, H.E. Wind Tunnel Investigation of the Controllable Twist Rotor Performance and Dynamic Behaviour. Technical report, Eustis Directorate, June 1997. USAAMRDL-TR-77-10.

[11] Wei, F.S., and Weisbrich, A.L. Multicyclic Controllable Twist Rotor Data Analysis. Technical report, NASA, January 1979. NASA-CR-152251.

[12] Sekula, M.K., Wilbur, M.L., and Yeager, W.T. Aerodynamic Design Study of an Advanced Active Twist Rotor. In *American Helicopter Society's 4th Decennial Specialist's Conference on Aeromechanics*, January 2004.

[13] Shin, S., Cesnik, C.E.S., and Hall, S.R. Closed-loop Control Test of the NASA/ARMY/MIT Active Twist Rotor for Vibration Reduction. In *American Helicopter Society 59th Annual Forum*, May 2003.

[14] Le Pape, A., and Beaumier, P. Numerical Optimization of Helicopter Rotor Aerodynamic Performance in Hover. *Aerospace Science and Technology*, 9:191–201, March 2005.

[15] Keys, C., Tarzanin, F., and McHugh, F. Effect of Twist on Helicopter Performance and Vibratory Loads. In *13th European Rotorcraft Forum*, September 1987.

[16] Noonan, K.W., Yeagar, W.T., Singleton, J.D., Wilbur, M.L., and Mirick, P.H. Wind Tunnel Evaluation of a Helicopter Main-Rotor Blade with Slotted Airfoils at the Tips. Technical report, NASA Langley Research Centre, Decemeber 2001. NASA-TP-2001-211260.

[17] Wachspress, D.A., and Quackenbush, T.R. BVI Noise Mitigation Via Steady Flap Deflection - An Analysis-Led Test Program. In *American Helicopter Society 4th Decenial Specialist's Conference on Aeromechanics*, January 2004.

[18] Roth, D., Enenkl, B., and Dieterich, O. Active Rotor Control by Flaps for Vibration Reduction - Full Scale Demonstrator and First Flight Test Results. In *32nd European Rotorcraft Forum*, September 2006.

[19] Pescara, R.P. Screw Propeller of Helicopter Flying Machines. U.S. Patent 1,449,129, filed July 17, 1920, issued March 20, 1923.

[20] D'Ascanio, C. Helicopter. U.S. Patent 1,960,141, filed February 5, 1930, issued May 22, 1934.

[21] Kaman, C.H. Aircraft of Rotary Wing Type. U.S. Patent 2,455,866, filed August 19, 1946, issued December 7, 1948.

[22] Dawson, S., Marcolini, M., Booth, E., Straub, F., Hassan, A., Tadghighi, H., and Kelly, H. Wind Tunnel Test of an Active Flap Rotor: BVI Noise and Vibration Reduction. In *American Helicopter Society 51st Annual Forum*, May 1995.

[23] Koratkar, N.A., and Chopra, I. Wind Tunnel Testing of a Smart Rotor Model with Trailing-Edge Flaps. *Journal of the American Helicopter Society*, 47:263–272, October 2002.

[24] Shen, J., and Chopra, I. Swashplateless Helicopter Rotor with Trailing-Edge Flaps. *Journal of Aircraft*, 41:208–214, March-April 2004.

[25] Straub, F.K., Ngo, H.T., Anand, V., and Domzalski, D.B. Development of a Piezoelectric Actuator for Trailing Edge Flap Control of Full-scale Rotor Blades. *Journal of Smart Materials and Structures*, 10:25–34, 2001.

[26] Enenkl, B., Kloppel, V., Preibler, D., and Janker, P. Full Scale Rotor with Piezoelectric Actuated Blade Flaps. In *28th European Rotorcraft Forum*, September 2002.

[27] Ardelean, E.V., McEver, M.A., Cole, D.G., and Clark, R.L. Active Flutter Control with V-Stack Piezoelectric Flap Actuator. *Journal of Aircraft*, 43:407–418, March-April 2006.

[28] Smith, A.M.O. High-Lift Aerodynamics. *Journal of Aircraft*, 12:501–530, June 1975.

[29] Wright, O. and Jacobs, J.W. Split Flap. US patent number 1,504,663. Accepted August 12, 1924.

[30] Liebeck, R.H. Design of Subsonic Airfoils for High Lift. *Journal of Aircraft*, 15:547–561, September 1978.

[31] Theodorsen, T. General Theory of Aerodynamic Instability and the Mechanism of Flutter. Technical report, NACA, 1935. NACA Report No. 496.

[32] Kussner, H.G., and Schwartz, L. The Oscillating Wing with Aerodynamically Balanced Elevator. Technical report, NACA, December 1940. NACA-TM-991.

[33] Lowry, J.G. and Polhamus, E.C. A Method for Predicting Lift Increments due to Flap Deflection at Low Angles of Attack in Incompressible Flow. Technical report, NACA, January 1957. NACA-TN-3911.

[34] Vepa, R. Finite State Modelling of Aeroelastic Systems. Technical report, NACA, February 1977. NACA-CR-2779.

[35] Millot, T.A., and Friedmann, P.P. Vibration Reduction in Hingeless Rotors Using an Actively Controlled Partial Span Trailing Edge Flap Located on the Blade. Technical report, NASA, June 1994. NASA-CR-4611.

[36] Narkiewicz, J.P., Ling, A., and Done, G.T.S. Unsteady Aerodynamic Loads on an Aerofoil with a Deflecting Tab. *The Aeronautical Journal*, 99:282–292, August/September 1995.

[37] Hariharan, N., and Leishman, J.G. Unsteady Aerodynamics of a Flapped Airfoil in Subsonic Flow by Indicial Concepts. *Journal of Aircraft*, 33:855–868, September-October 1996.

[38] Myrtle, T.F., and Friedmann, P.P. New Comprehensive Time Domain Unsteady Aerodynamics for Flapped Aifoils and its Application to Rotor Vibration Reduction Using Active Control. In *American Helicopter Society's 53rd Annual Forum*, May 1997.

[39] Hassan, A. Predicted Aerodynamic Characteristics of a NACA 0015 Airfoil Having a 25% Integral-Type Trailing-Edge Flap. Technical report, NASA, May 1999. NASA-CR-209328.

[40] Chan, W., and Brocklehurst, A. Performance Enhancement Evaluation of an Actuated Trailing Edge Flap. *The Aeronautical Journal*, 105:391–399, July 2001. Paper No. 2591.

[41] Leishman, J.G. Unsteady Lift of a Flapped Airfoil by Indicial Concepts. *Journal of Aircraft*, 31:288–297, March-April 1994.

[42] Johnson, W. *Helicopter Theory*. Dover Publications, Inc., 1st edition, 1994.

[43] Hariharan, N. Unsteady aerodynamics of a flapped airfoil in subsonic flow using indicial concepts. Technical report, PhD Thesis, Alfred Gessow Rotorcraft Centre, University of Maryland, 1995.

[44] Beddoes, T.S. Two and Three Dimensional Indicial Methods for Rotor Dynamic Airloads. In *AHS/National Specialist's Meeting on Rotorcraft Dynamics*, November 1989.

[45] Milgram, J., Chopra, I., and Straub, F.K. Rotors with Trailing-Edge Flaps: Analysis and Comparison with Experimental Data. *Journal of the American Helicopter Society*, 43:319–332, October 1998.

[46] Milgram, J. H. A comprehensive aeroelastic analysis of helicopter main rotors with trailing edge flaps for vibration reduction. Technical report, PhD Thesis, Alfred Gessow Rotorcraft Centre, University of Maryland, 1997.

[47] Charles, B., Tadghighi, H., and Hassan, A. Higher Harmonic Actuation of Trailing-Edge Flaps for Rotor BVI Noise Control. In *American Helicopter Society 52nd Annual Forum*, June 1996.

[48] Baeder, J.D., and Sim, B.W-C. Blade-Vortex Interaction Reduction by Active Trailing-Edge Flaps. In *American Helicopter Society 54th Annual Forum*, May 1998.

[49] Myrtle, T.F., and Friedmann, P.P. Vibration Reduction in Rotorcraft Using the Actively Controlled Trailing Edge Flap and Issues Related to Practical Implementation. In *American Helicopter Society 54th Annual Forum*, May 1998. Paper 00128.

[50] Straub, F.K., and Charles, B.D. Aeroelastic Analysis of Rotors with Trailing-Edge Flaps Using Comprehensive Codes. *Journal of the American Helicopter Society*, 46:192–199, July 2001.

[51] Depailler, G., and Friedmann, P.P. Alleviation of Dynamic Stall Induced Vibrations Using Actively Controlled Flaps. In *American Helicopter Society's 58th Annual Forum*, June 2002.

[52] Celi, R. Stabilization of Helicopter Blades with Severed Pitch Links Using Trailing Edge Flaps. *Journal of Guidance, Control, and Dynamics*, 26:585–600, July-August 2003.

[53] Shen, J., Chopra, I., and Johnson, W. Performance of Swashplateless Ultralight Helicopter Rotor with Trailing-Edge Flaps for Primary Flight Control. In *American Helicopter Society 59th Annual Forum*, May 2003.

[54] Zhang, J., Smith, E.C., and Wang, K.W. Active-Passive Hybird Optimization of Rotor Blades with Trailing Edge Flaps. *Journal of the American Helicopter Society*, 34:54–65, January 2004.

[55] Viswamurthy, S.R., and Ganguli, R. An Optimization Approach to Vibration Reduction in Helicopter Rotors with Multiple Active Trailing Edge Flaps. *Aerospace Science and Technology*, 8:185–194, February 2004.

[56] Gagliardi, A., Beedy, J., Steijl, R., Barakos, G., and Badcock, K.J. Analysis of Flapped Rotors using CFD and Indicial Methods. In *American Helicopter Society 61st Annual Forum*, June 2005.

[57] Maughmer, M., Lesieutre, G., and Kinzel, M. Miniature Trailing-Edge Effectors for Rotorcraft Performance Enhancement. In *American Helicopter Society 61st Annual Forum*, June 2005.

[58] Patt, D., Liu, L., and Friedmann, P.P. Rotorcraft Vibration Reduction and Noise Prediction Using a Unified Aeroelastic Response Simulation. *Journal of the American Helicopter Society*, 50:95–10, January 2005.

[59] Kim, J-S., Smith, E.C., and Wang, K.W. Helicopter Blade Loads Control via Multiple Trailing-Edge Flaps. In *American Helicopter Society 62nd Annual Forum*, May 2006.

[60] Dieterich, O., Enenkl, B., and Roth. D. Trailing Edge Flaps for Active Rotor Control - Aeroelastic Characteristics of the ADASYS Rotor System. In *American Helicopter Society 62nd Annual Forum*, May 2006.

[61] Liu, L., Friedmann, P.P., Kim, I., and Bernstein, D.S. Vibration Reduction and Performance Enhancement in Rotorcraft Using Active Flaps at High Advance Ratios. In *47th AIAA/ASME/ASCE/AHS/ASC Structures, Structural Dynamics, and Materials Conference*, May 2006. AIAA-2006-1862.

[62] Gagliardi, A., and Barakos, G. Improving Hover Performance of Low-Twist Rotors Using Trailing-Edge Flaps - A Computational Study. In *32nd European Rotorcraft Forum*, September 2006.

[63] Jones, M.P., and Newman, S.J. Vibration Reduction of a Lynx Aircraft Via Actively Controlled Trailing Edge Flaps. In *32nd European Rotorcraft Forum*, September 2006.

[64] Johnson, W. Rotorcraft Aerodynamic Models for a Comprehensive Analysis. In *American Helicopter Society 54th Annual Forum*, May 1998.

[65] Beddoes, T.S. Practical Computation of Unsteady Lift. *Vertica*, 8:55–71, 1984.

[66] Kitapliaglu, C., and Caradonna, F.X. Aerodynamics and Acoustics of Blade Vortex Inter-action Using An Independently Generated Vortex. In *American Helicopter Society Aerome-chanics Specialists Conference*, January 1994.

[67] Wenzinger, C.J., and Harris, T.A. Wind-tunnel Investigation of an N.A.C.A. 23012 Airfoil with Various Arrangements of Slotted Flaps. Technical report, NASA, 1950. Report No. 664.

[68] Shen, J., and Chopra, I. A Parametric Design Study for a Swashplateless Helicopter Rotor with Trailing-Edge Flaps. *Journal of the American Helicopter Society*, 34:43–53, January 2004.

[69] Shen, J., and Chopra, I. Swashplateless Helicopter Rotor with Trailing-Edge Flaps. *Journal of Aircraft*, 41:208–214, March-April 2004.

[70] Hariharan, N., and Leishman, J.G. Unsteady Aerodynamics of a Flapped Airfoil in Subsonic Flow by Indicial Concepts. Technical report, AIAA, April 1995. AIAA-95-1228-CP.

[71] Leishman, J.G., and Beddoes, T.S. A Semi-Empirical Model for Dynamic Stall. *Journal of the American Helicopter Society*, 34:3–17, July 1989.

[72] Leishman, J.G. Two-Dimensional Model for Airfoil Unsteady Drag Below Stall. *Journal of Aircraft*, 25:665–666, December 1988. Engineering Note.

[73] Standish, K.J., and van Dam, C.P. Computational Analysis of a Microtab-Based Aerody-namic Load Control System for Rotor Blades. *Journal of the American Helicopter Society*, 50:249–258, July 2005.

[74] Nelson, J.M., and Koratkar, N.A. Micro-Rotorcraft Performance Improvement Using Trailing-Edge Gurney Flaps. In *American Helicopter Society 60th Annual Forum*, June 2004.

[75] Basualdo, S. Load alleviation on wind turbines using variable airfoil geometry. Technical report, Masters Thesis, Technical University of Denmark, 2004.

[76] Joo, W., Lee, B-S., Yee, K., and Lee, D-H. Design Optimization of Passive Control Devices for Dynamic Stall Control. In *43rd AIAA Aerospace Sciences Meeting and Exhibit*, January 2005. AIAA-2005-1363.

[77] Yang, C., Aoyama, T., and Saito, S. Numerical Analysis of BVI Noise Reduction Using Active Flap Control. In *American Helicopter Society 61st Annual Forum*, June 2005.

[78] Kentfield, J.A.C. The Potential of Gurney Flaps for Improving the Aerodynamic Performance of Helicopter Rotors. 1993. AIAA-93-4883.

[79] Gai, S.L., and Palfrey, R. Influence of Trailing-Edge Flow Control on Airfoil Performance. *Journal of Aircraft*, 40:332–337, March 2003.

[80] Chandrasekhara, M.S., Martin, P.B., and Tung, C. Compressible Dynamic Stall Performance of a Variable Droop Leading Edge Airfoil with a Gurney Flap. In *42nd AIAA Aerospace Sciences Meeting and Exhibit*, January 2004. AIAA-2004-41.

[81] Hassan, A.A., Straub, F.K., and Noonan, K.W. Experimental/Numerical Evaluation of Inte-gral Trailing Edge Flaps for Helicopter Rotor Applications. *Journal of the American Heli-copter Society*, 50:3–17, January 2005.

[82] Gerontakos, R., and Lee, T. Dynamic Stall Flow Control via a Trailing-Edge Flap. *Journal of Aircraft*, 44:469–480, March 2006.

[83] Hassan, A.A., and Straub, F.K. Evaluation of a Flapped Airfoil Configuration for an Advanced Rotor. In *Aeromechanics Specialists Conference*, pages (7)40–60, October 1995.

[84] Hassan, A.A., Straub, F.K., and Noonan, K.W. Experimental/Numerical Evaluation of Integral Trailing Edge Flaps for Helicopter Rotor Applications. In *American Helicopter Society 56th Annual Forum*, May 2000.

[85] Straub, F.K., and Robinson, L.H. Dynamics of a Rotor with Nonharmonic Control. In *American Helicopter Society 49th Annual Forum*, May 1993.

[86] Dawson, S., Straub, F., Hassan, A., and Tadghighi, H. Blade-Mounted Flap Control for BVI Noise Reduction Proof-of-Concept Test. Technical report, NASA, July 1995. NASA-CR-195078.

[87] Settle, T.B., and Nixon, M.W. MAVSS Control of an Active Flaperon for Tiltrotor Vibration Reduction. In *American Helicopter Society 53rd Annual Forum*, April 29th - May 1st 1997.

[88] Nixon, M.W., Kvaternik, R.G., and Settle, T.B. Tiltrotor Vibration Reduction Through Higher Harmonic Control. In *American Helicopter Society 53rd Annual Forum*, April-May 1997.

[89] Fulton, M.V., and Ormiston, R.A. Small-Scale Rotor Experiments with On-Blade Elevons to Reduce Blade Vibratory Loads in Forward Flight. In *American Helicopter Society 54th Annual Forum*, May 1998.

[90] Ormiston, R.A., and Fulton, M.V. Aeroelastic and Dynamic Rotor Response with On-Blade Elevon Control. In *24th European Rotorcraft Forum*, September 1998.

[91] Koratkar, N.A., and Chopra, I. Analysis and Testing of Mach-Scaled Rotor with Trailing-Edge Flaps. *AIAA Journal*, 38:1113–1124, July 2000.

[92] Koratkar, N.A., and Chopra, I. Wind Tunnel Testing of a Mach-Scaled Rotor Model with Trailing-Edge Flaps. *Journal of Smart Materials and Structures*, 10:1–14, February 2001.

[93] Roth, D., Dietrich, O., Bebesel, M., Pongratz, R., Kube, R., and Munser, H. Individual Blade Control Demonstration: Recent Activities. In *28th European Rotorcraft Forum*, September 2001.

[94] Noboru, K., Kondo, N., Saito, S., Akasaka, T., and Tanabe, Y. An Experimental Study of On-Blade Active Tab for Helicopter Noise Reduction. In *30th European Rotorcraft Forum*, September 2004.

[95] Crozier, P., Leconte, P., Delrieux, Y., Gimonet, B., Le Pape, A., and Mercier des Rochettes, H. Wind-Tunnel Tests of a Helicopter Rotor with Active Flaps. In *32nd European Rotorcraft Forum*, September 2006.

[96] Noonan, K.W. Aerodynamic Characteristics of Two Rotorcraft Airfoils Designed for Application to the Inboard Region of a Main Rotor Blade. Technical report, NASA, 1990. NASA-TP-3009.

[97] Noonan, K.W. Aerodynamic Characteristics of a Rotorcraft Airfoil Designed for the Tip Region of a Main Rotor Blade. Technical report, NASA, 1991. NASA-TM-4264.

[98] Beedy, J. Using computational fluid dynamics to improve rotorcraft aerodynamic codes. Technical report, PhD Thesis, CFD Laboratory, University of Glasgow, 2007.

[99] Wagner, H. Uber die Entstehung des Dynamischen Auftriebes von Tragflugeln. *Zeitschrift fur Angewandte Mathematik und Mechanik*, 5:17–35, February 1925.

[100] Kuethe, A.M., and Chow, C-Y. *Foundations of Aerodynamics*. Wiley, 1998.

[101] Jones, R.T. The Unsteady Lift of a Finite Wing. Technical report, NACA, January 1939. No. 682.

[102] Leishman, J.G., and Beddoes, T.S. A Generalised Model for Airfoil Unsteady Aerodynamic Behaviour and Dynamic Stall Using the Indicial Methods. In *American Helicopter Society 42nd Annual Forum*, June 1986.

[103] Leishman, J.G. Validation of Approximate Indicial Aerodynamic Functions for Two-Dimensional Subsonic Flow. *Journal of Aircraft*, 25:914–922, October 1988.

[104] Seddon, J. *Basic Helicopter Aerodynamics*. BSP Professional Books, 1st edition, 1990.

[105] Wilcox, D.C. Reassessment of the Scale-Determining Equation for Advanced Turbulence Models. *AIAA Journal*, 26:1299–1310, November 1988.

[106] Steijl, R., Barakos, G., and Badcock, K. A Framework for CFD Analysis of Rotors in Hover and Forward Flight. *International Journal for Numerical Methods in Fluids*, 51:819–847, January 2006.

[107] Badcock, K.J., Richards, B.E., and Woodgate, M.A. Elements of Computational Fluid Dynamics on Block Structured Grids Using Implicit Solvers. *Progress in Aerospace Sciences*, 36:351–392, July-August 2000.

[108] Spentzos, A., Barakos, G.N., Badcock, K.J., Richards, B.E., Wernert, P., Schreck, S., and Raffel, M. Investigation of Three-Dimensional Dynamic Stall Using Computational Fluid Dynamics. *AIAA Journal*, 43:1023–1033, May 2005.

[109] Morvant, R., Barakos, G.N., Badcock, K., and Richards, B.E. Airfoil-Vortex Interaction Using the Compressible Vorticity Confinement Method. *AIAA Journal*, 43:63–75, January 2005.

[110] Osher, S., and Solomon, F. Upwind Difference Schemes for Hyperbolic Systems of Conservation Laws. *Mathematics of Computation*, 38:339–374, April 1982.

[111] Jeong, J. and Hussain, F. On the Identification of a Vortex. *Journal of Fluid Mechanics*, 285:69–94, 1995.

[112] Caradonna, F.X. and Tung, C. Experimental and Analytical Studies of a Model Helicopter Rotor in Hover. Technical report, NASA Langley Research Centre, September 1981. NASA-TM-81232.

[113] Van der Ven, H., and Boelens, O.J. A Framework for Aeroelastic Simulations of Trimmed Rotor Systems in Forward Flight. In *30th European Rotorcraft Forum*, September 2004.

[114] Lorber, P.F., Stauter, R.C., and Landgrebe, A.J. A Comprehensive Hover Test of the Airloads and Airflow of an Extensively Instrumented Model Helicopter Rotor. In *American Helicopter Society 45th Annual Forum*, May 1989.

[115] Dindar, M., Shephard, M., Flaherty, J., and Jansen, K. Adaptive CFD Analysis for Rotorcraft Aerodynamics. *Computer Methods in Applied Mechanics and Engineering*, 189:1055–1076, September 2000.

[116] Rogers, S.E., Menter, F., Durbin, P.A., and Mansour, N.N. A Comparison of Turbulence Models in Computing Multi-Element Airfoil Flows. January 1994. AIAA-94-0291.

[117] Rumsey, C.L., Gatski, T.B., Ying, S.X., and Bertelrud, A. Prediction of High-Lift Flows Using Turbulent Closure Models. In *15th Applied Aerodynamics Conference*, June 1997. AIAA-97-31809.

[118] Beddoes, T.S. A 3D Separation Model for Arbitrary Planforms. In *American Helicopter Society 47th Annual Forum*, May 1991.

[119] Baker, T.J. Mesh Generation: Art or Science? *Progress in Aerospace Sciences*, 41:29–63, January 2005.

Appendix A

2D Aerodynamic Input

The aerodynamic input for the ICARA model is generated via 2D CFD and consists of 19 aerodynamic parameters at 12 Mach numbers from 0.3 to 0.8. This data is used to complete a parametric study for optimum flap deployment in hover, which also presents the aerodynamic parameters in tablular format. In this appendix, these parameters are presented in graphical format for the RC(6)-08 and the RC(4)-10 sections with and without flaps. As described in the thesis, where certain data could not be extracted, standard values were used instead. This at times can lead to peculiar curve trends (for example, see Figure A.4), but in hover the parameters for which this was required have little effect on predicted performance.

A.1 HIMARCS I Rotor Blade

A.1.1 RC(6)-08 Sections
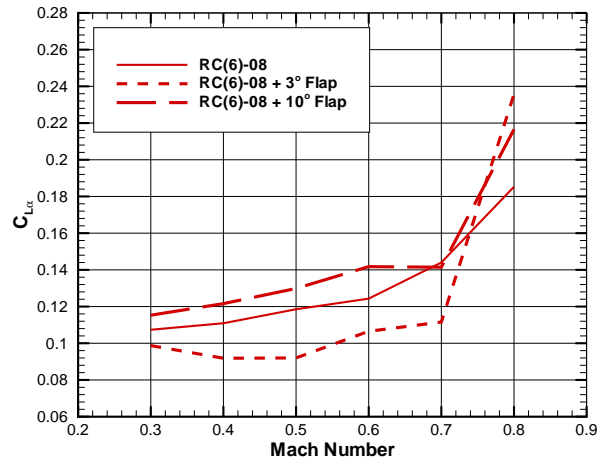
(a) C_{L_α}
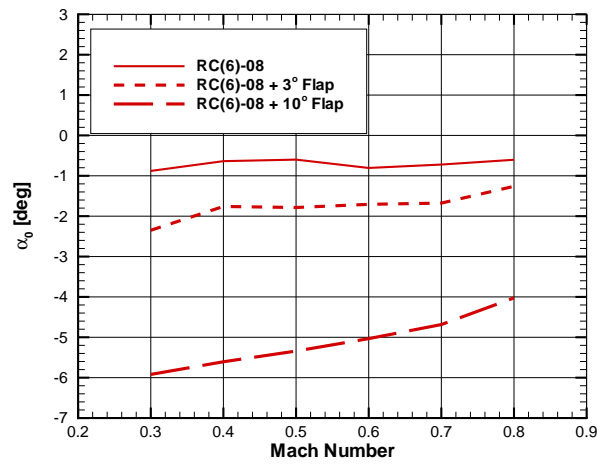
(b) α_0

Figure A.1: C_{L_α} and α_0 parameters for the RC(6)-08 clean and flapped sections from 2D CFD.

(a) α_1

(b) $S1$
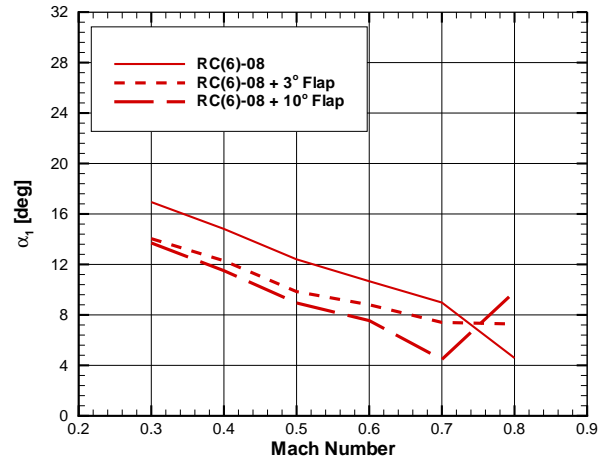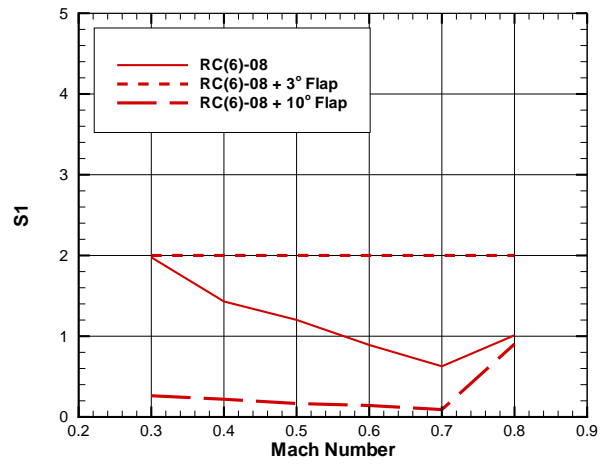
Figure A.2: α_1 and $S1$ parameters for the RC(6)-08 clean and flapped sections from 2D CFD.
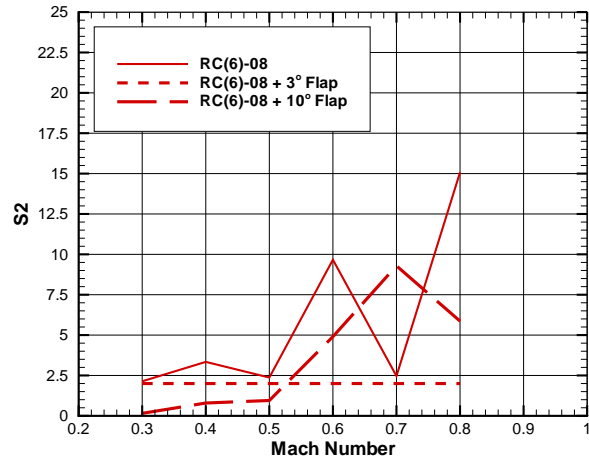
(a) *S2*
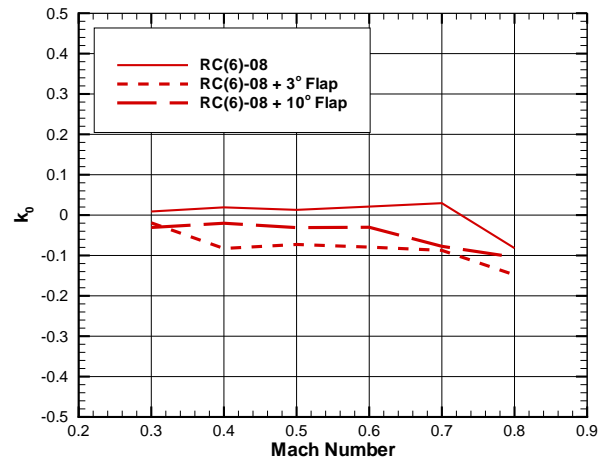
(b) k_0

Figure A.3: *S2* and k_0 parameters for the RC(6)-08 clean and flapped sections from 2D CFD.
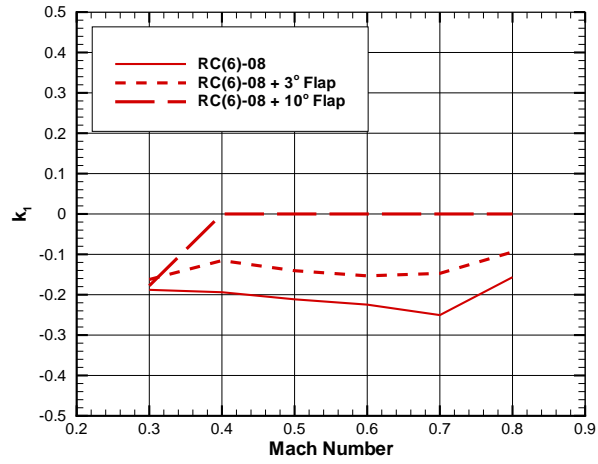
(a) k_1
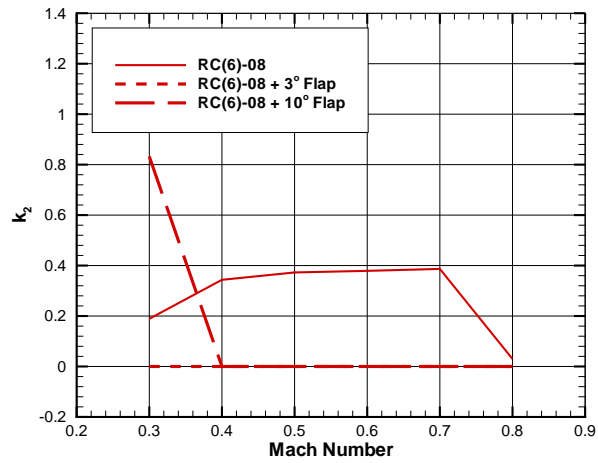
(b) k_2

Figure A.4: k_1 and k_2 parameters for the RC(6)-08 clean and flapped sections from 2D CFD.
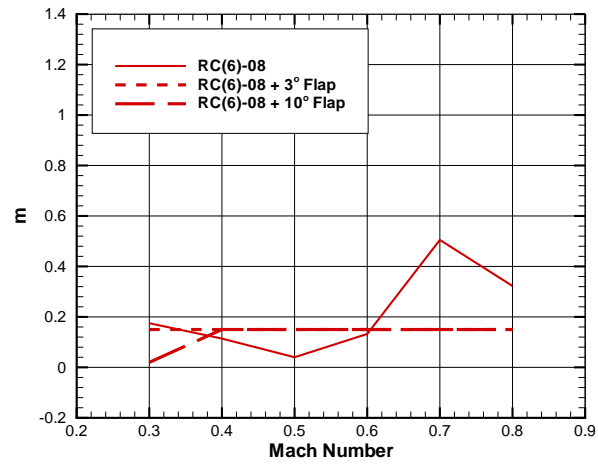
(a) *m*
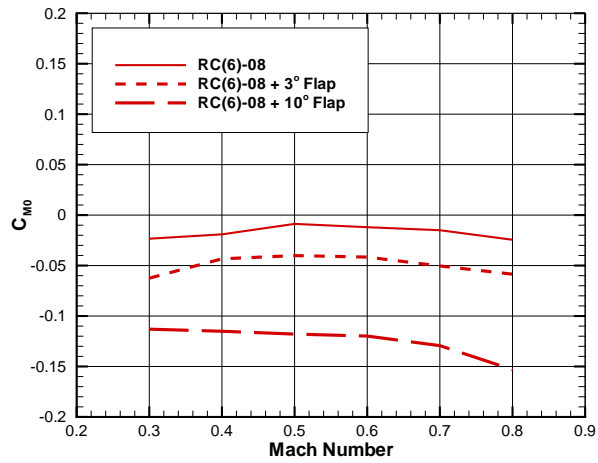
(b) C_{M_0}

Figure A.5: *m* and C_{M_0} parameters for the RC(6)-08 clean and flapped sections from 2D CFD.

146
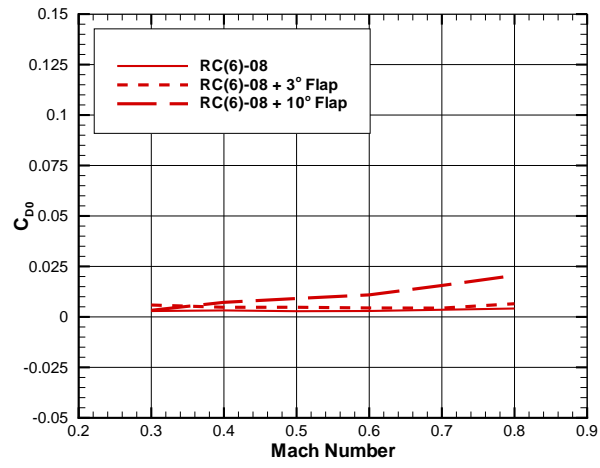
(a) C_{D_0}

Figure A.6: C_{D_0} parameters for the RC(6)-08 clean and flapped sections from 2D CFD.

A.1.2   RC(4)-10 Sections
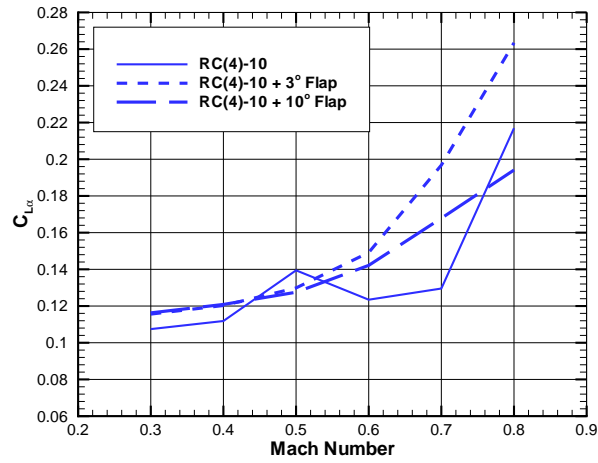
(a) C_{L_α}
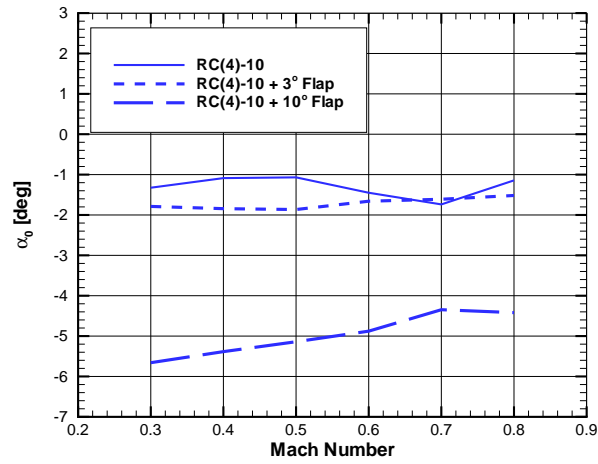
(b) α_0

Figure A.7: C_{L_α} and α_0 parameters for the RC(4)-10 clean and flapped sections from 2D CFD.

(a) α_1

(b) $S1$
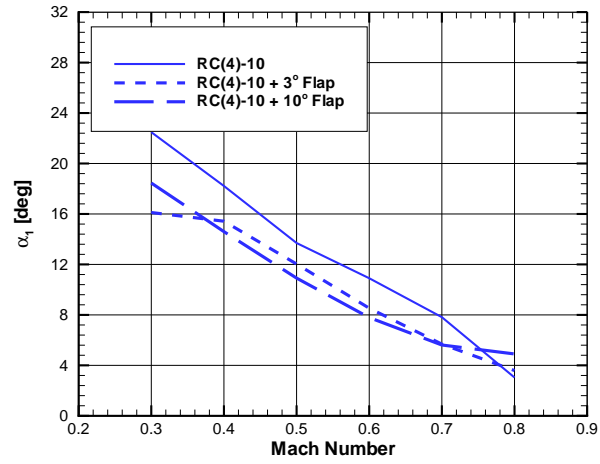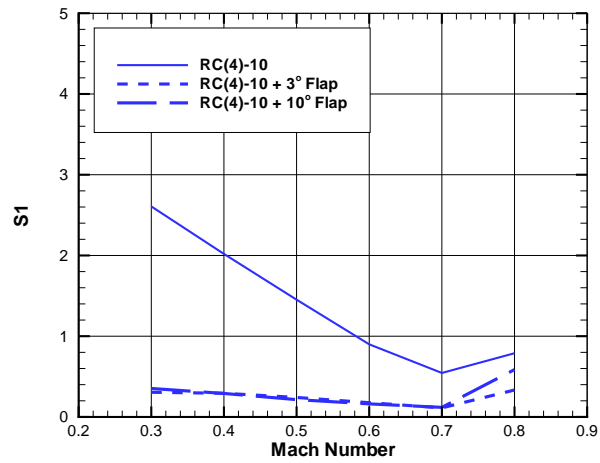
Figure A.8: α_1 and $S1$ parameters for the RC(4)-10 clean and flapped sections from 2D CFD.
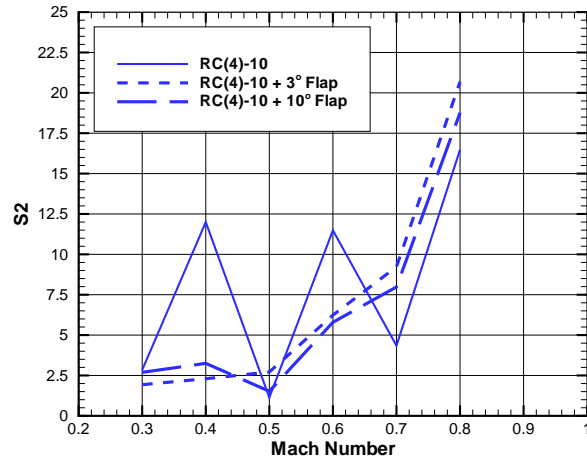
(a) *S2*
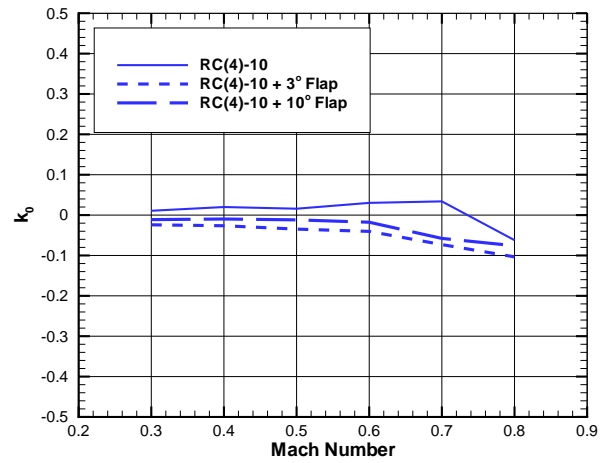
(b) k_0

Figure A.9: *S2* and k_0 parameters for the RC(4)-10 clean and flapped sections from 2D CFD.

150
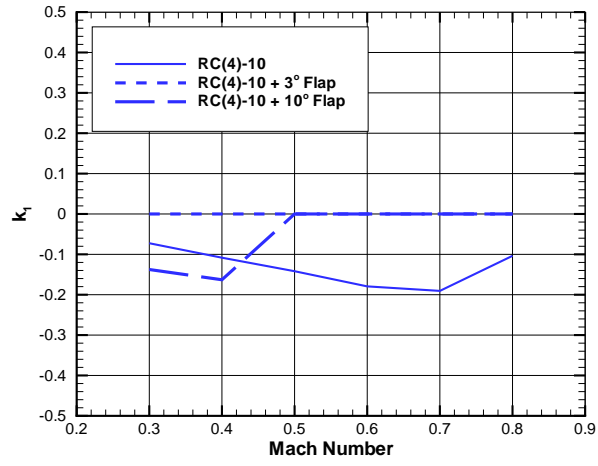
(a) k_1
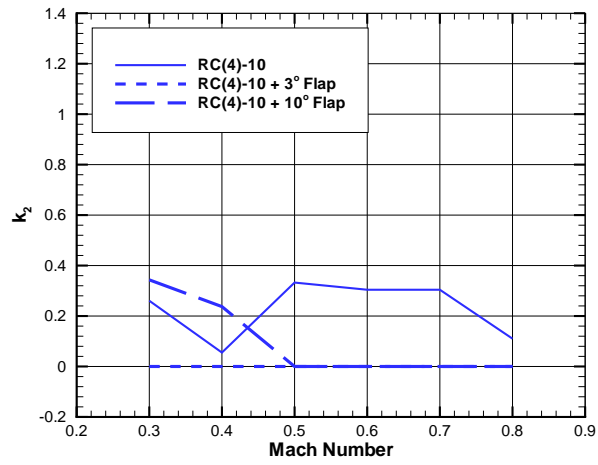
(b) k_2

Figure A.10: k_1 and k_2 parameters for the RC(4)-10 clean and flapped sections from 2D CFD.
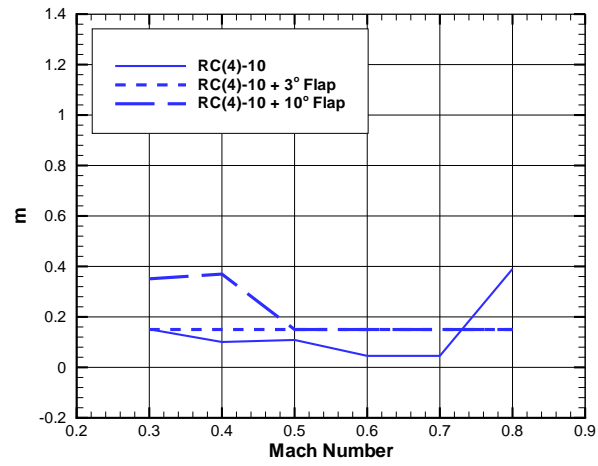
(a) *m*
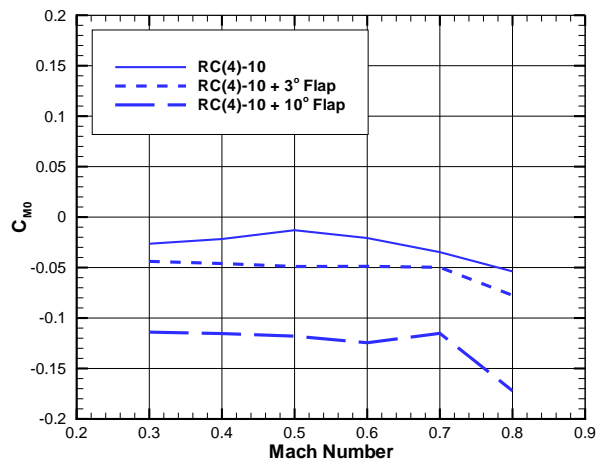
(b) C_{M_0}

Figure A.11: *m* and C_{M_0} parameters for the RC(4)-10 clean and flapped sections from 2D CFD.
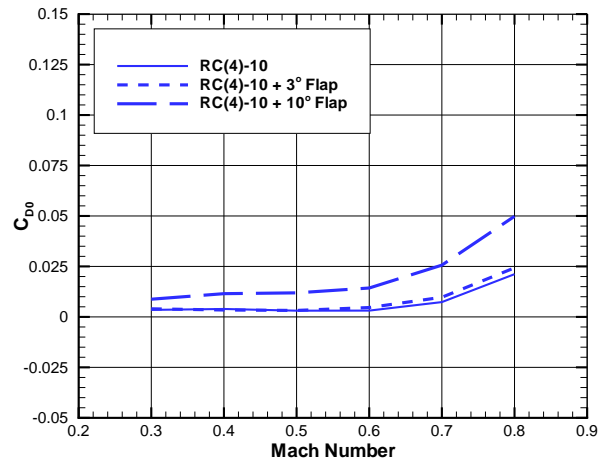
(a) C_{D_0}

Figure A.12: C_{D_0} parameters for the RC(4)-10 clean and flapped sections from 2D CFD.

Appendix B

Parametric Study Results

Contour plots from the parametric study conducted in Chapter 3. The data is presented for each flap chord length, 32%c, 21.33%c, and 10.67%c, at 15 different thrust coefficients with flap deflection angles of 3° and 10°. The flap location along the blade is represented by the x-axis in percentage of blade span. The flap span-wise size is represented by the y-axis.

An overlay of the grids used for both flap locations can be found in Figure B.1. Some of the staircase effects that can be seen in the results can be easily explained when one considers the density of grid points considered. For the inboard flap, a much greater spread of results was able to be considered due to the larger proportion of the blade that the inboard section made up of the HIMARCS I rotor [16]. The outboard section was more limited and hence the test matrix was not as fine. Plus, the study assumed a closed blade tip. Thus, if a specific flap configuration was of a span-wise length that included the blade tip, it was automatically shortened within the code to account for the closed tip condition. Due to this, some results show that two or three different flap configurations offer the same level of performance, essentially because the flap configuration has not changed. For an example of this, see Figure B.40.

(a) (b)
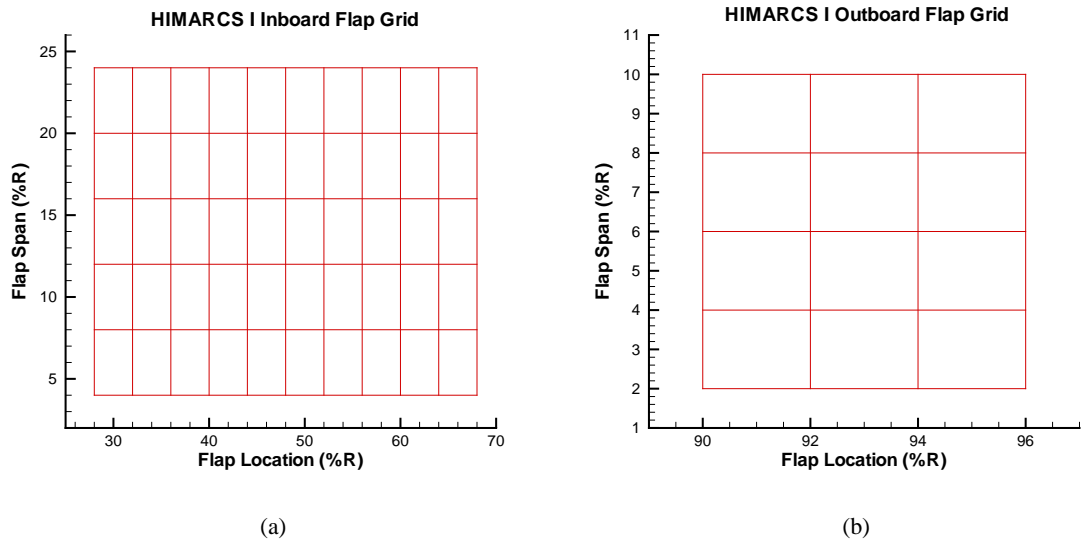
Figure B.1: Overlayed grids used in the following contour plots. (a) Inboard grid. (b) Outboard grid.

B.1 Flap Chord, 10.67%c

(a)   (b)

(c)   (d)
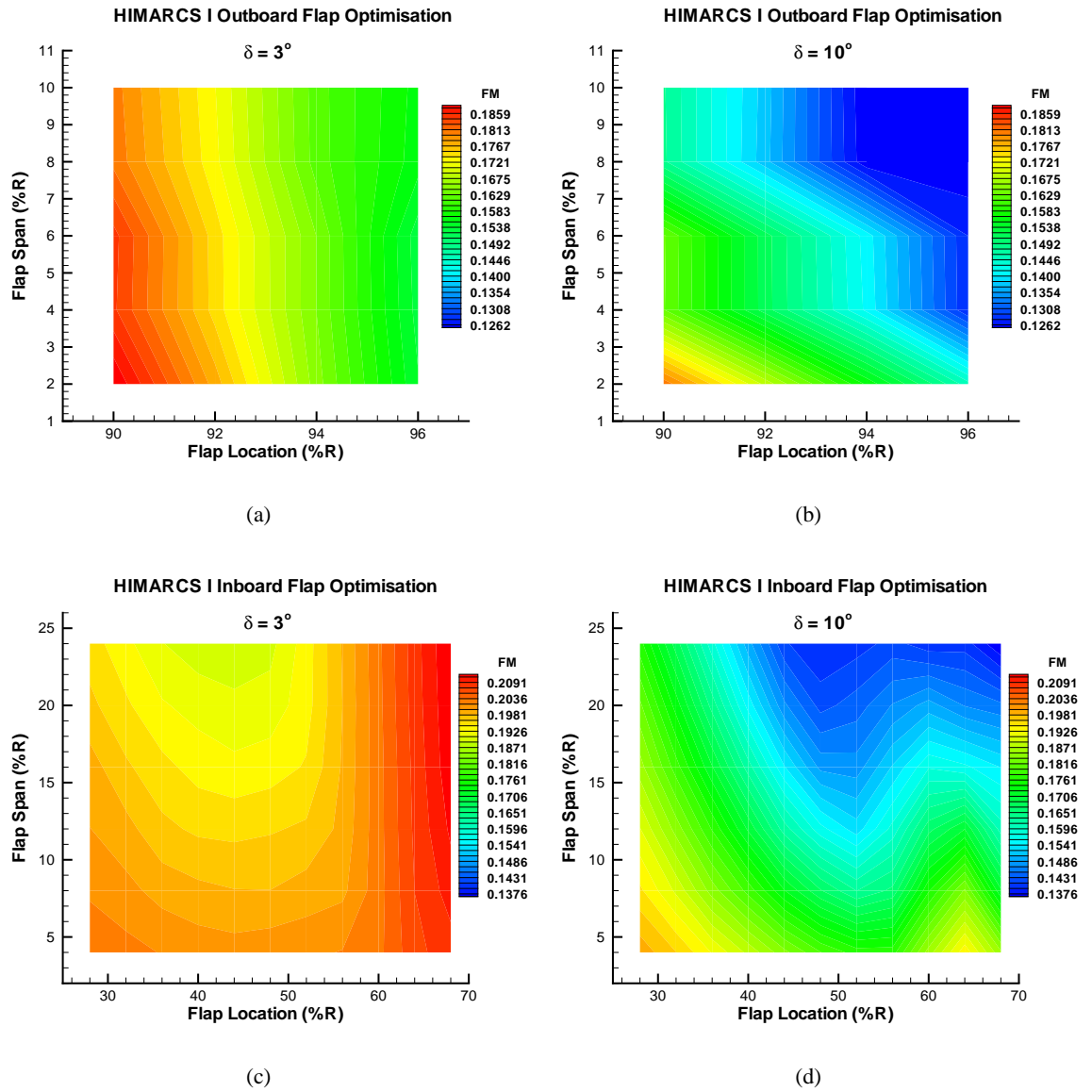
Figure B.2: Contours of Figure of Merit at $C_T = 0.000545455$ for flap chord of 10.67%c. (a) Outboard, 3°. (b) Outboard, 10°. (c) Inboard, 3°. (d) Inboard, 10°. FM (Baseline) = 0.19976322.

(a)

(b)

(c)

(d)
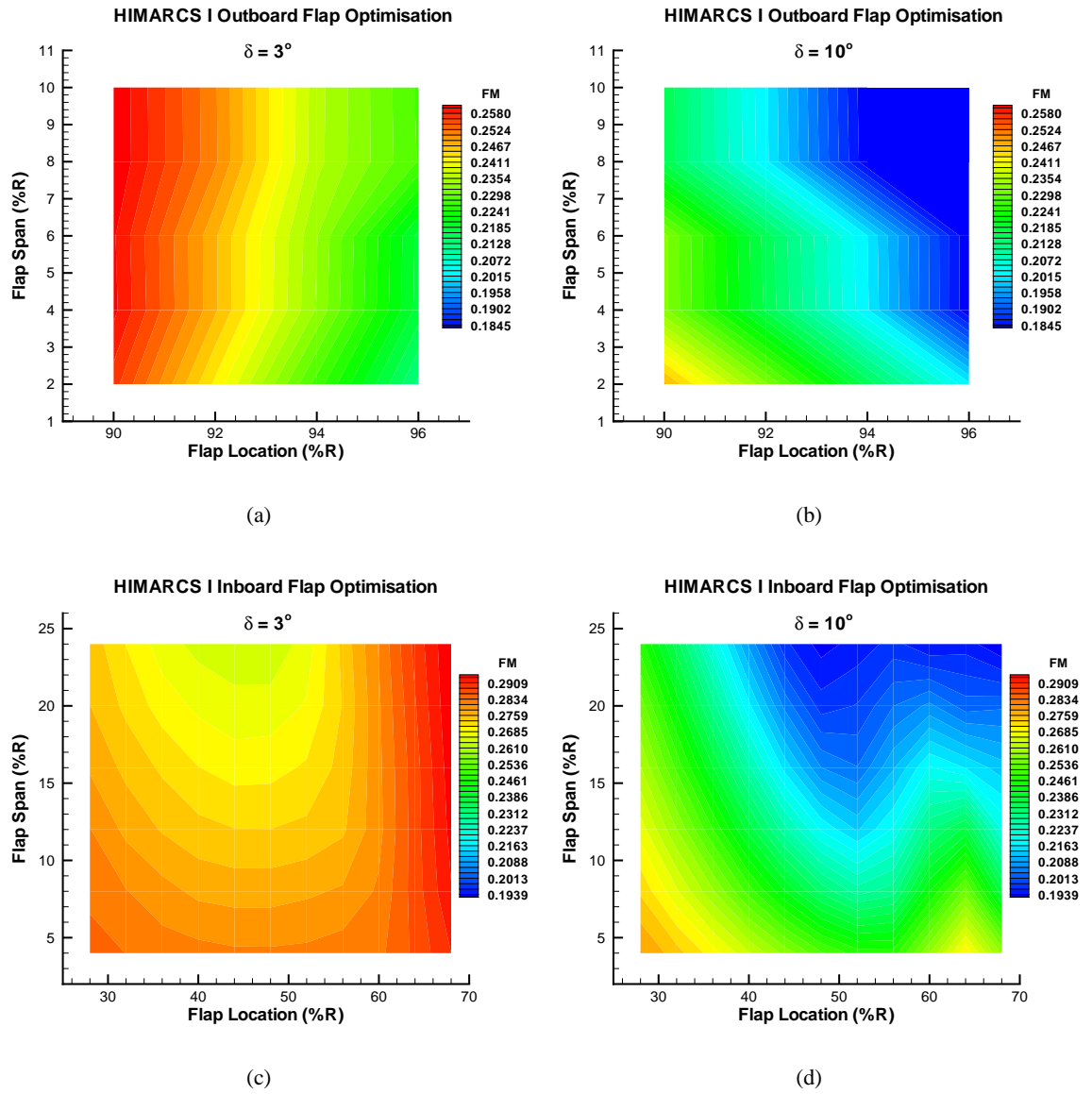
Figure B.3: Contours of Figure of Merit at $C_T = 0.0007$ for flap chord of 10.67%c. (a) Outboard, 3°. (b) Outboard, 10°. (c) Inboard, 3°. (d) Inboard, 10°. FM (Baseline) = 0.27974284.

(a)

(b)

(c)

(d)
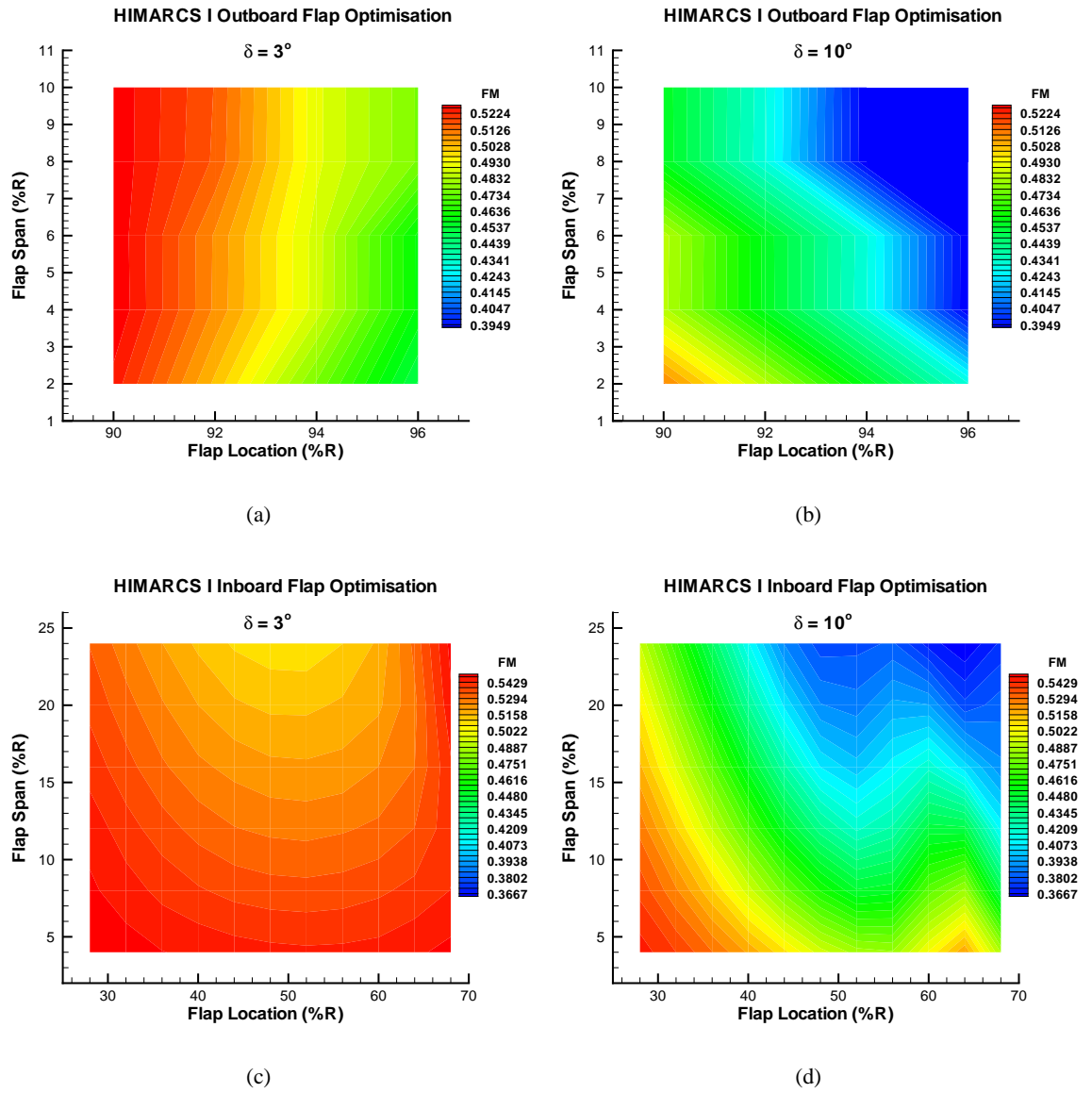
Figure B.4: Contours of Figure of Merit at $C_T = 0.0012$ for flap chord of 10.67%c. (a) Outboard, 3°. (b) Outboard, 10°. (c) Inboard, 3°. (d) Inboard, 10°. FM (Baseline) = 0.54232693.

(a)

(b)

(c)

(d)
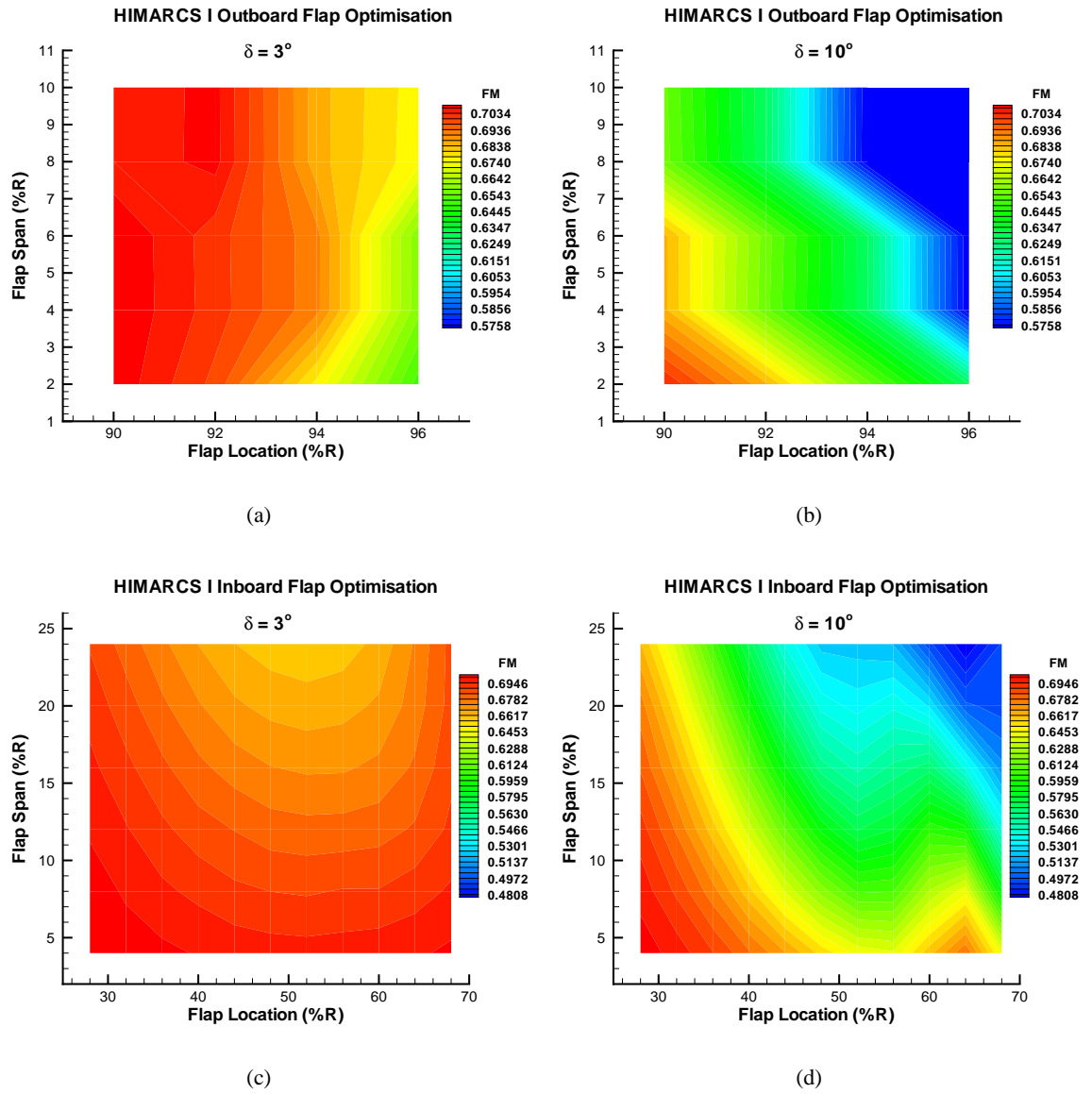
Figure B.5: Contours of Figure of Merit at $C_T = 0.0015942$ for flap chord of 10.67%c. (a) Outboard, 3°. (b) Outboard, 10°. (c) Inboard, 3°. (d) Inboard, 10°. FM (Baseline) = 0.70262504.

(a)

(b)

(c)

(d)
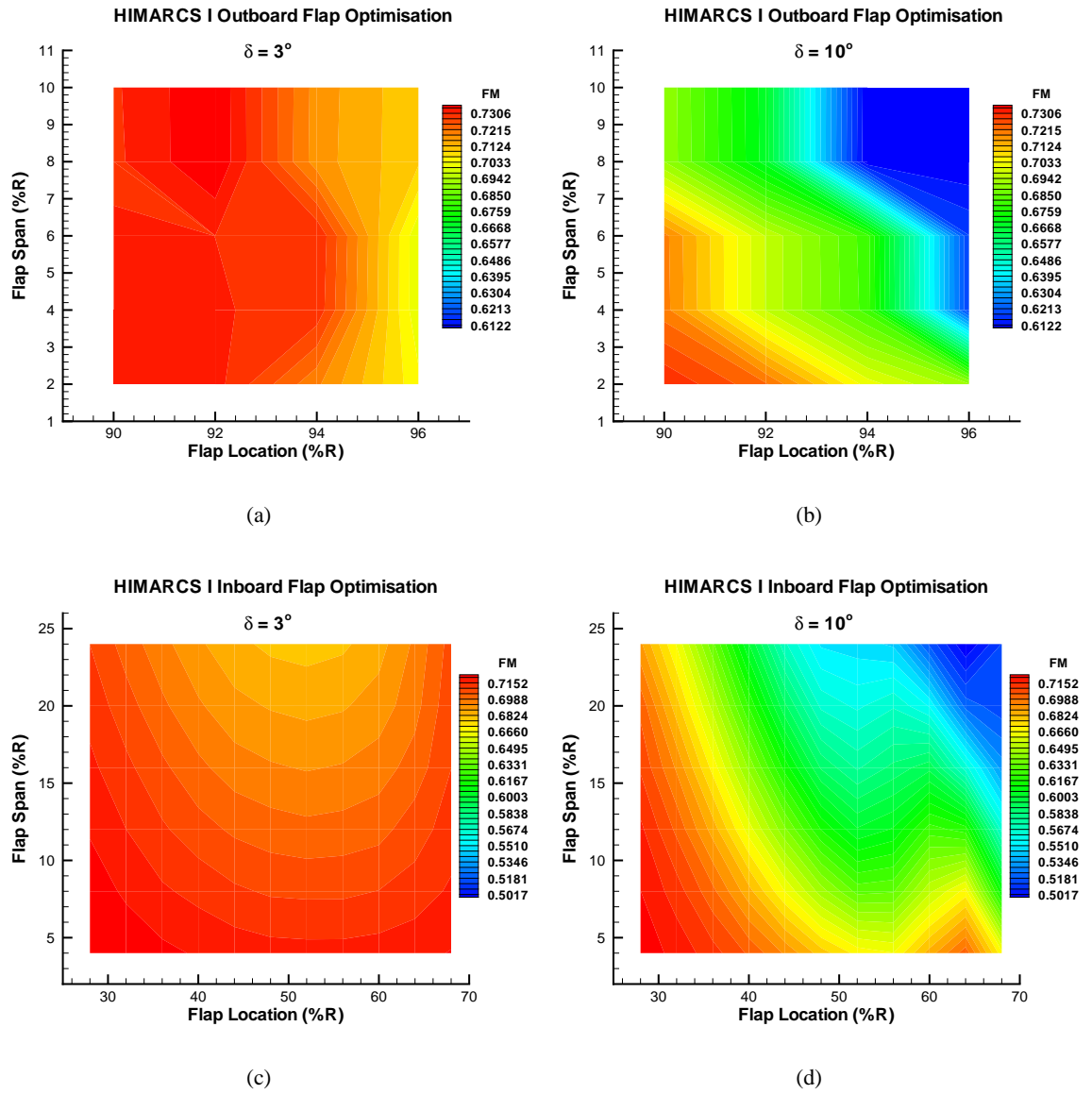
Figure B.6: Contours of Figure of Merit at C_T = 0.00167273 for flap chord of 10.67%c. (a) Outboard, 3°. (b) Outboard, 10°. (c) Inboard, 3°. (d) Inboard, 10°. FM (Baseline) = 0.72664547.

(a)

(b)

(c)

(d)
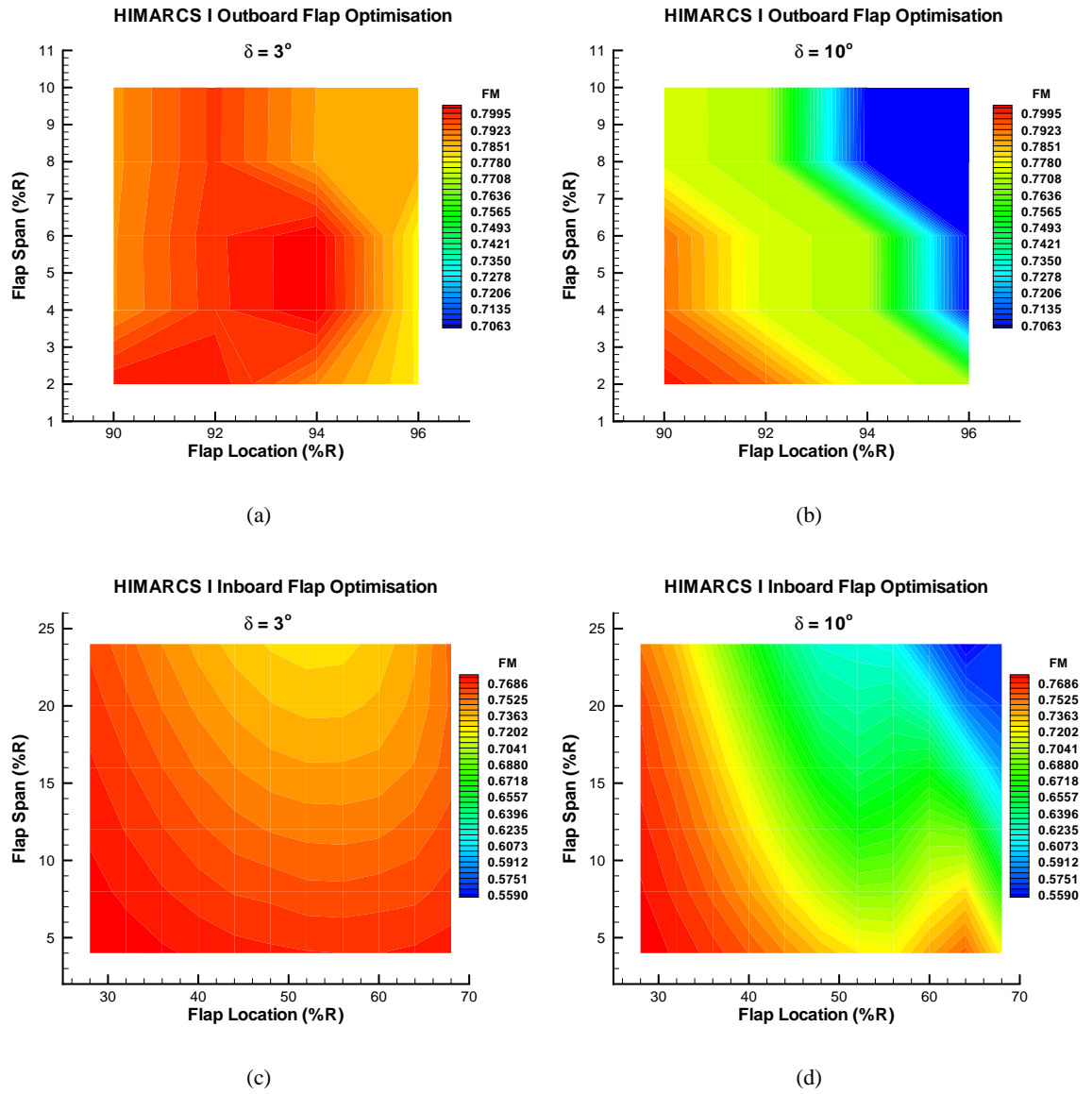
Figure B.7: Contours of Figure of Merit at $C_T = 0.0019$ for flap chord of 10.67%c. (a) Outboard, 3°. (b) Outboard, 10°. (c) Inboard, 3°. (d) Inboard, 10°. FM (Baseline) = 0.77728802.

(a)

(b)

(c)

(d)
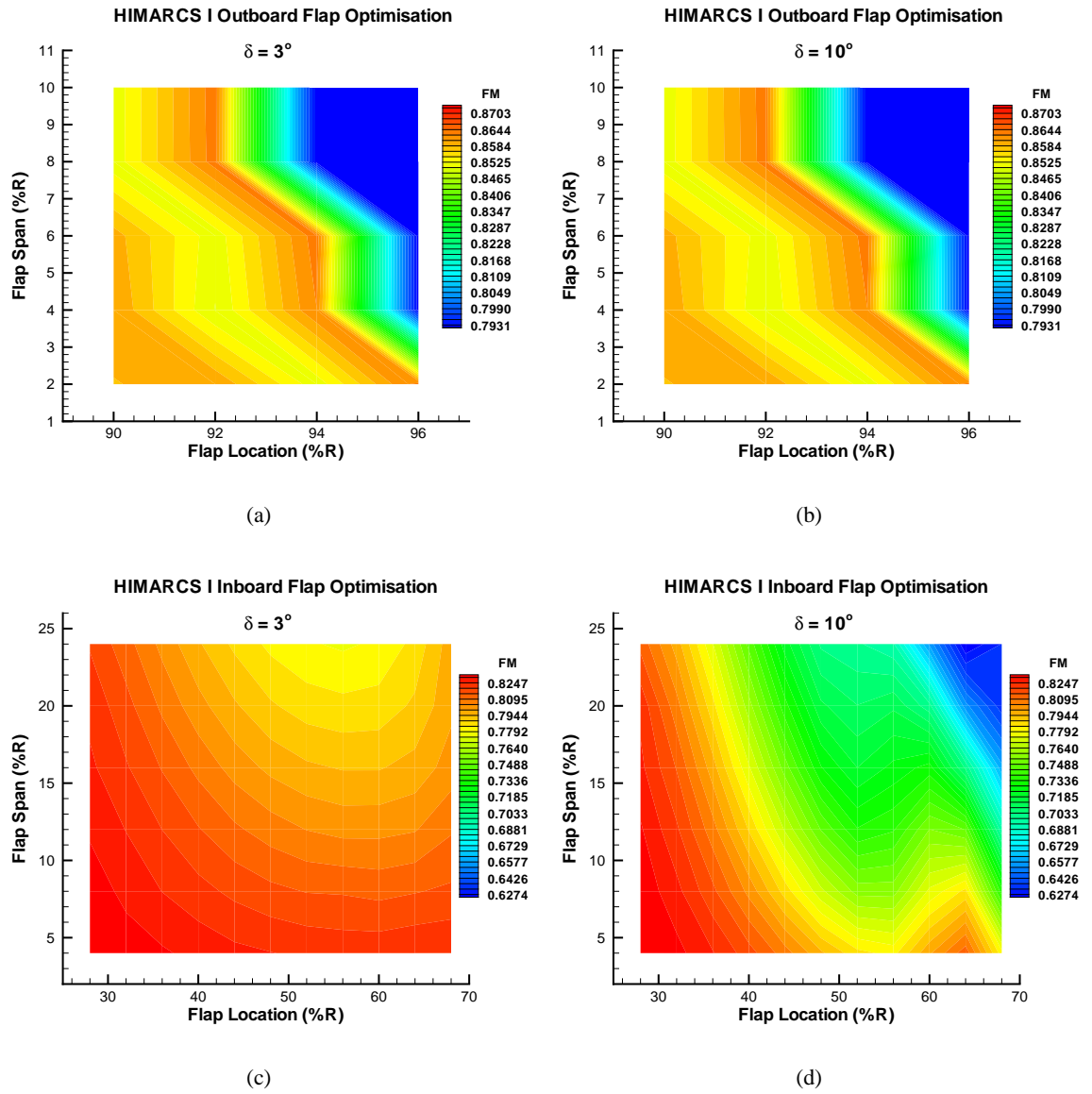
Figure B.8: Contours of Figure of Merit at $C_T = 0.0022$ for flap chord of 10.67%c. (a) Outboard, 3°. (b) Outboard, 10°. (c) Inboard, 3°. (d) Inboard, 10°. FM (Baseline) = 0.82768548.

(a)

(b)

(c)

(d)
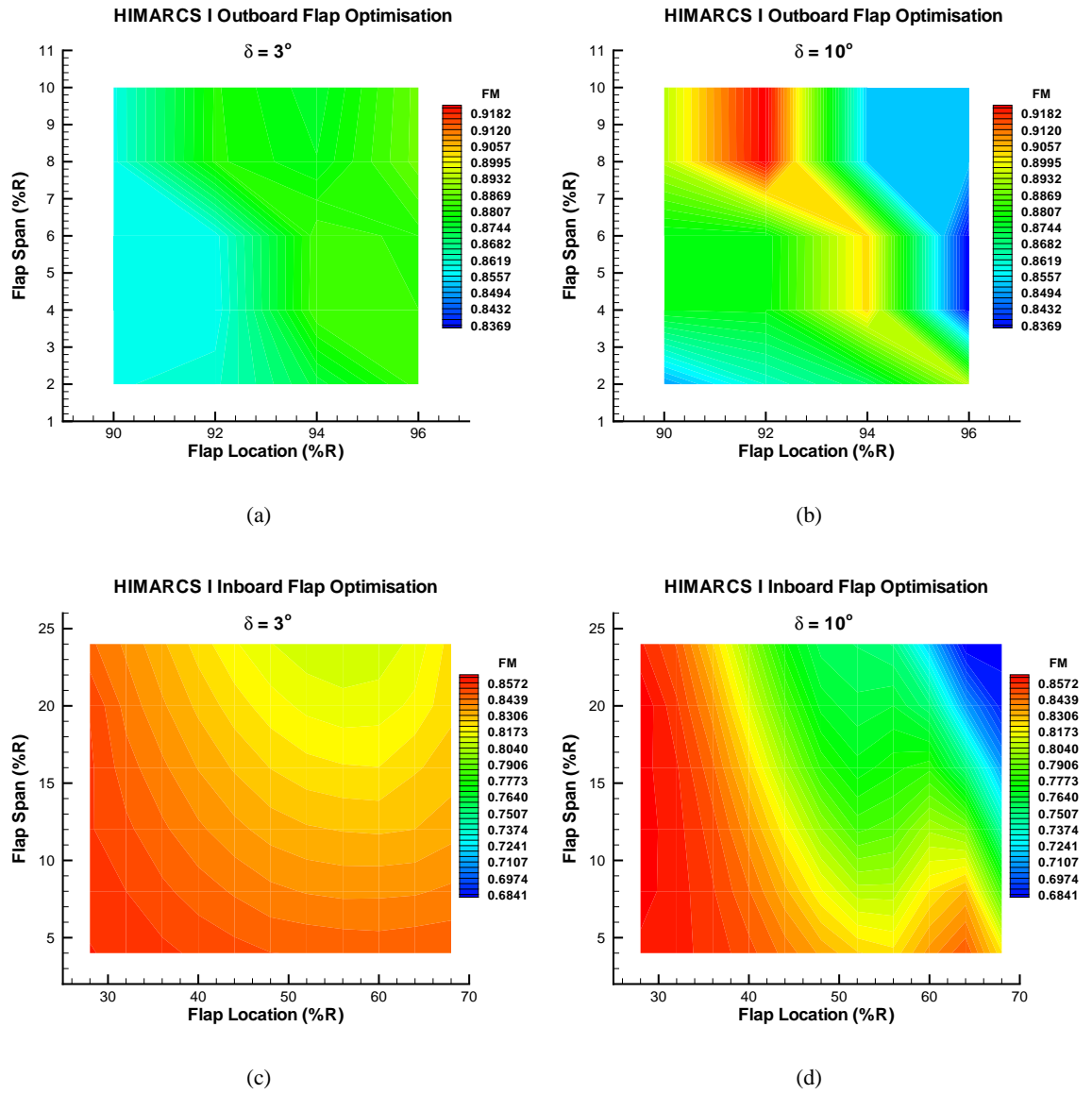
Figure B.9: Contours of Figure of Merit at $C_T = 0.0025$ for flap chord of 10.67%c. (a) Outboard, 3°. (b) Outboard, 10°. (c) Inboard, 3°. (d) Inboard, 10°. FM (Baseline) = 0.86130375.
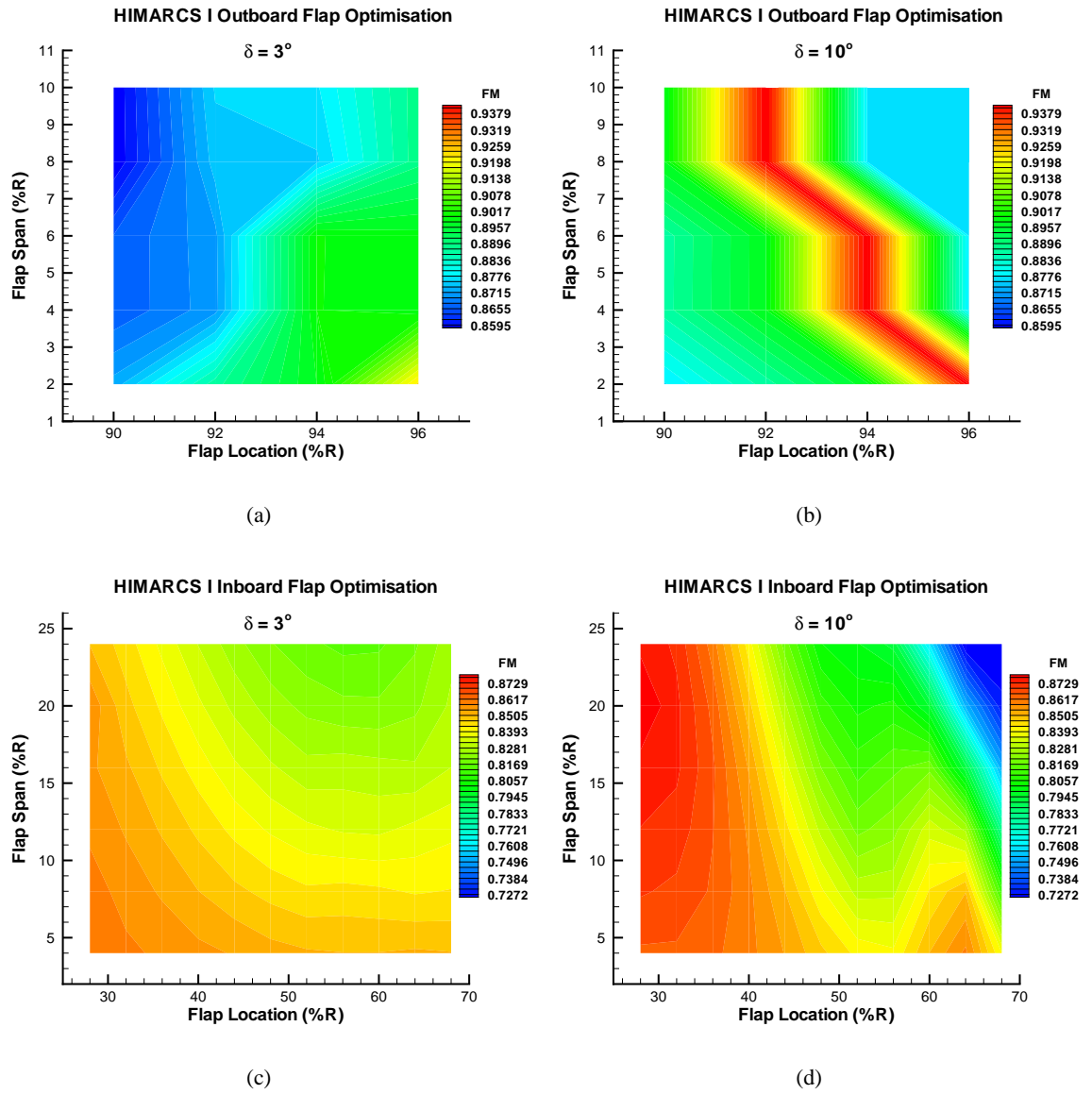
Figure B.10: Contours of Figure of Merit at $C_T = 0.0028$ for flap chord of 10.67%c. (a) Outboard, 3°. (b) Outboard, 10°. (c) Inboard, 3°. (d) Inboard, 10°. FM (Baseline) = 0.87034994.

(a)

(b)

(c)

(d)
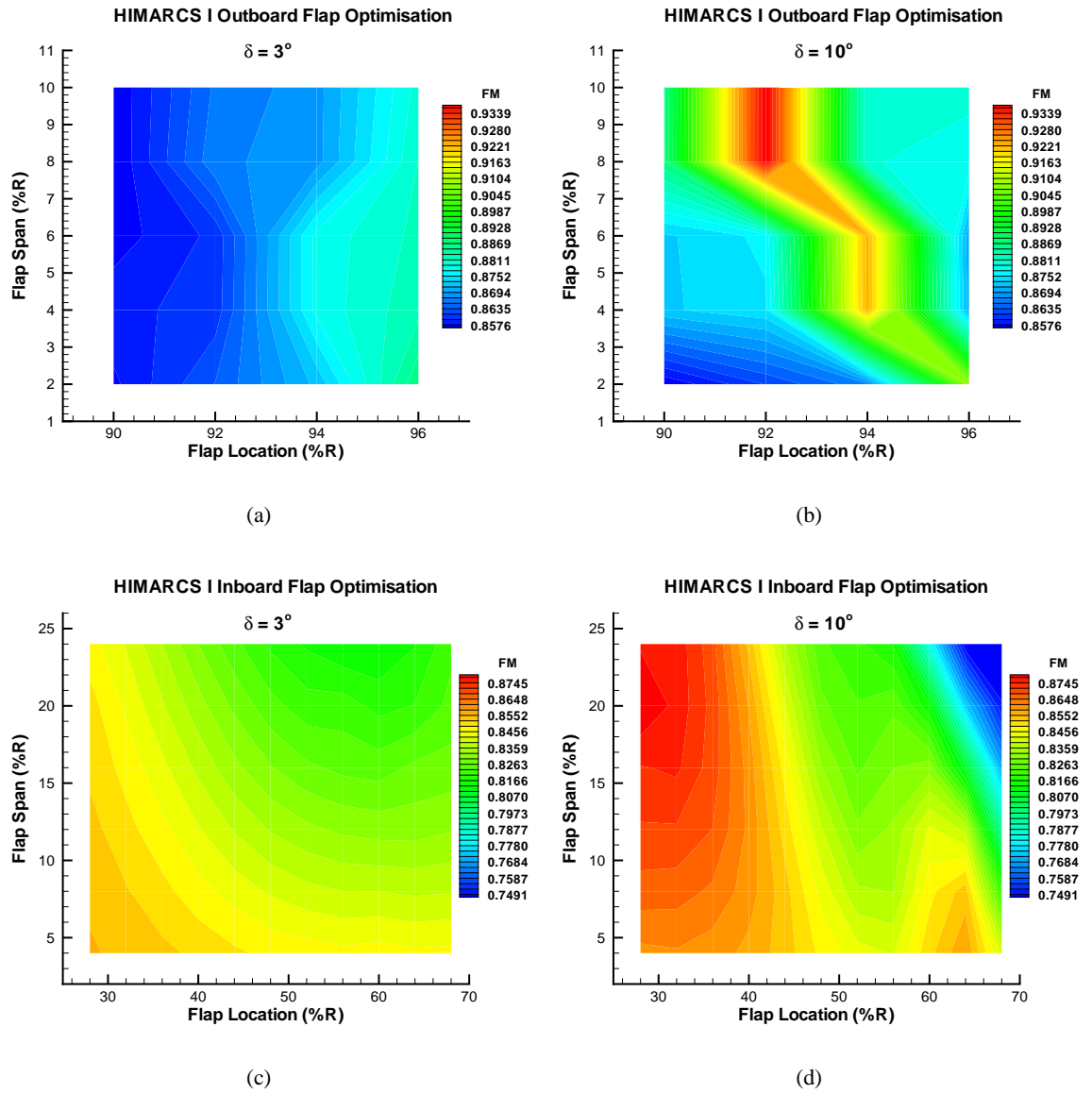
Figure B.11: Contours of Figure of Merit at C_T = 0.00298182 for flap chord of 10.67%c. (a) Outboard, 3°. (b) Outboard, 10°. (c) Inboard, 3°. (d) Inboard, 10°. FM (Baseline) = 0.86903244.

(a)

(b)

(c)

(d)
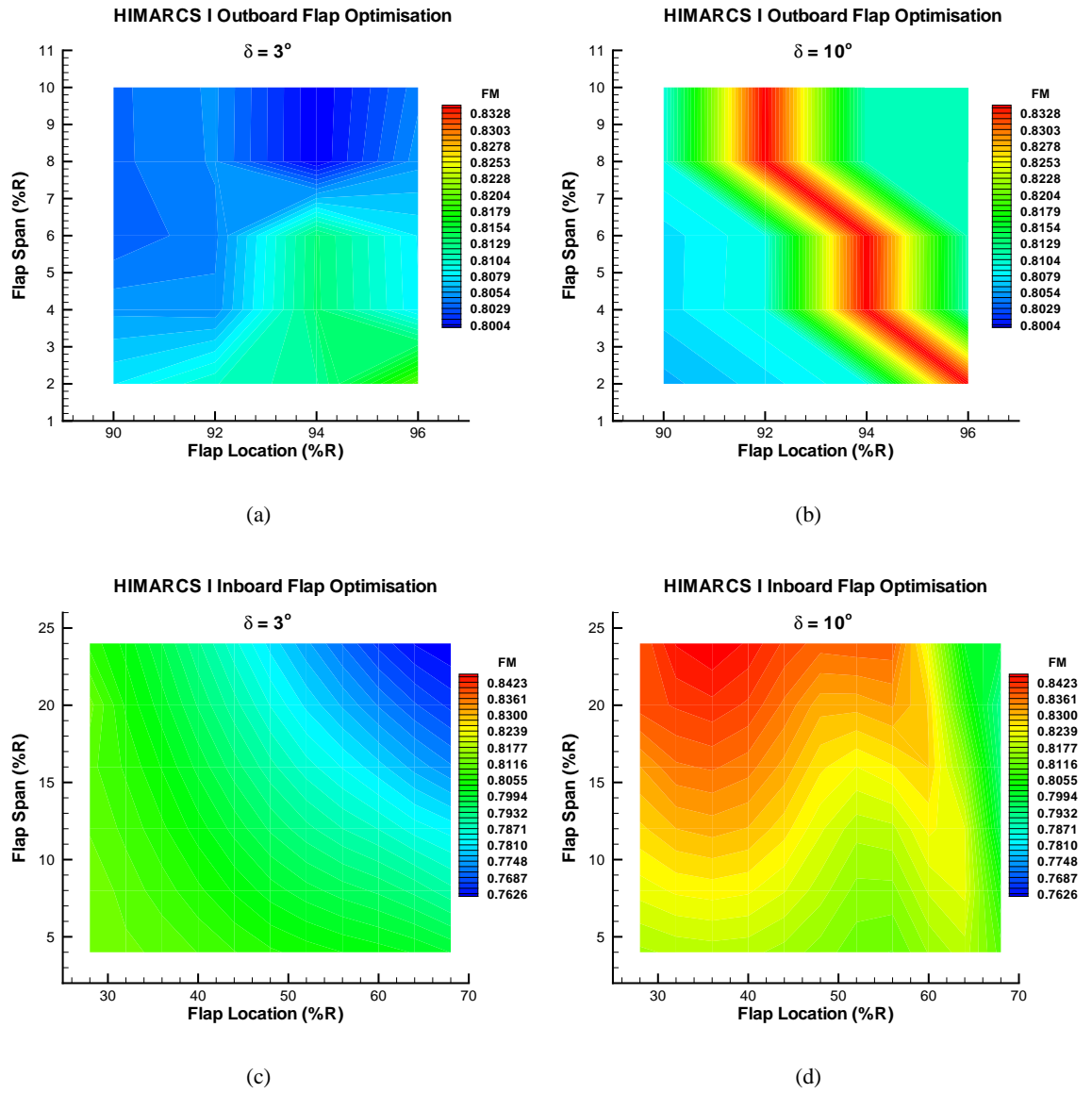
Figure B.12: Contours of Figure of Merit at $C_T = 0.00414545$ for flap chord of 10.67%c. (a) Outboard, 3°. (b) Outboard, 10°. (c) Inboard, 3°. (d) Inboard, 10°. FM (Baseline) = 0.83130002.

(a)

(b)

(c)

(d)
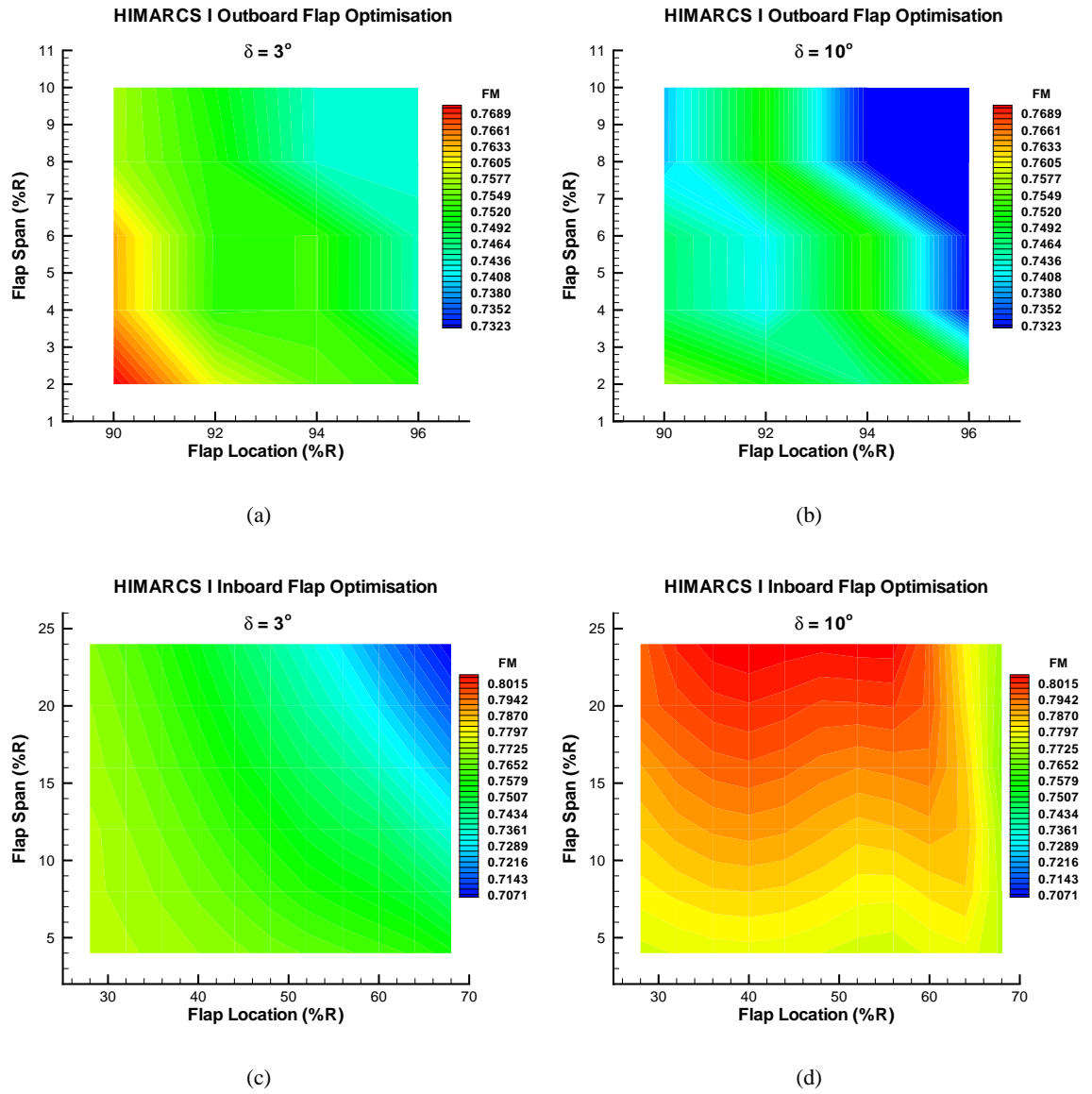
Figure B.13: Contours of Figure of Merit at $C_T = 0.00556364$ for flap chord of 10.67%c. (a) Outboard, 3°. (b) Outboard, 10°. (c) Inboard, 3°. (d) Inboard, 10°. FM (Baseline) = 0.79409397.
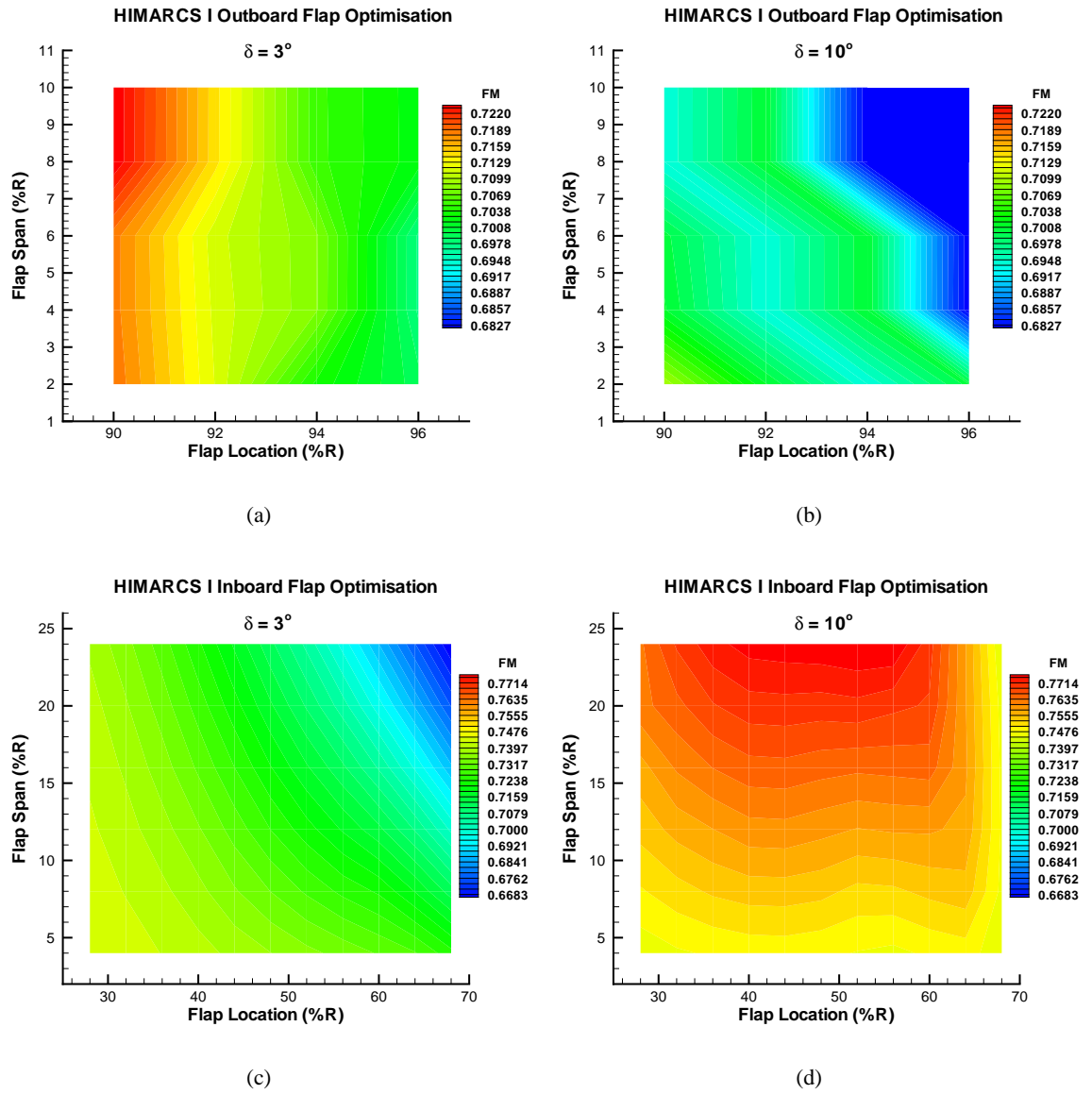
Figure B.14: Contours of Figure of Merit at C_T = 0.00690909 for flap chord of 10.67%c. (a) Outboard, 3°. (b) Outboard, 10°. (c) Inboard, 3°. (d) Inboard, 10°. FM (Baseline) = 0.76587558.

(a)

(b)

(c)

(d)
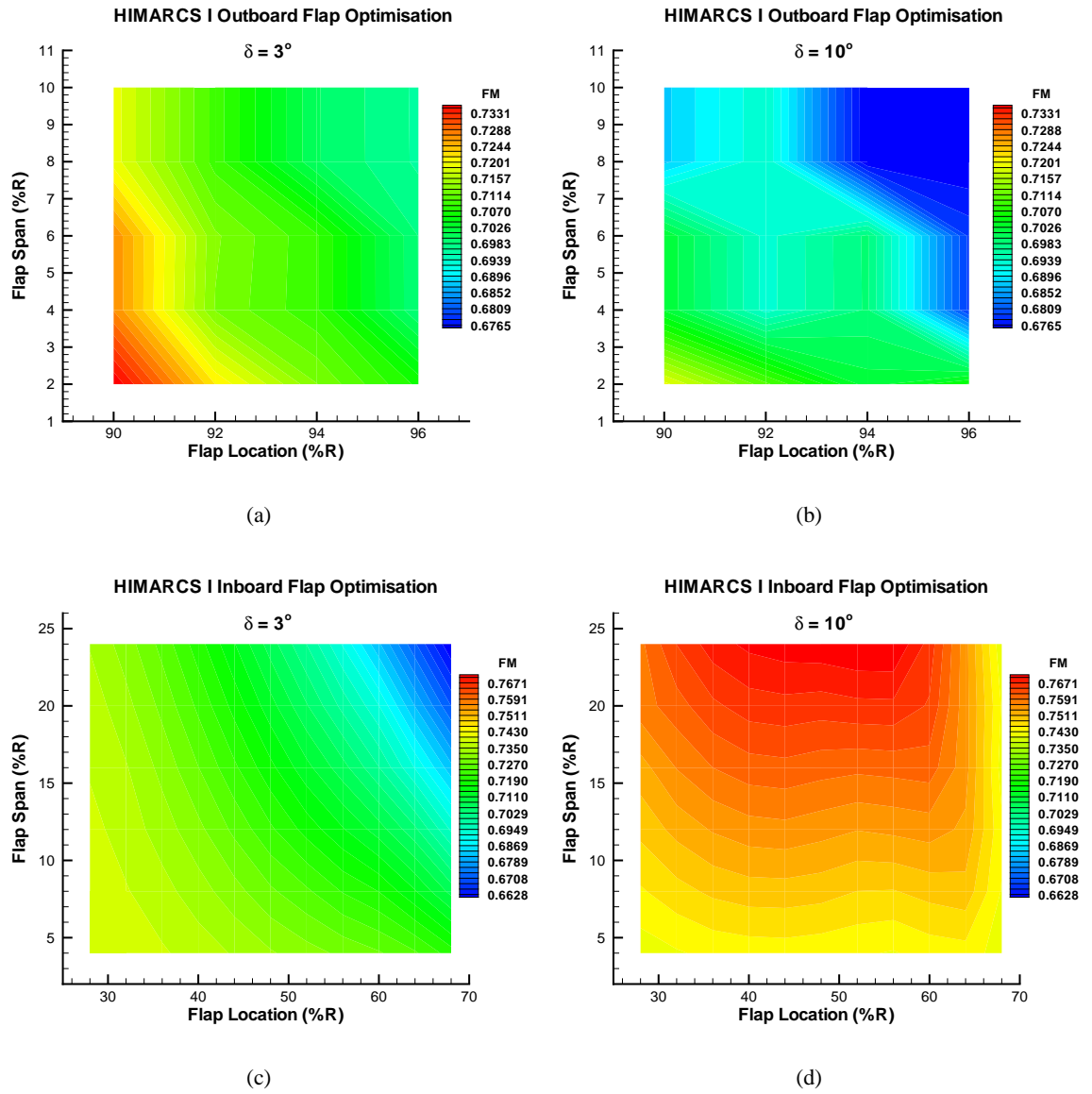
Figure B.15: Contours of Figure of Merit at $C_T = 0.00712727$ for flap chord of 10.67%c. (a) Outboard, 3°. (b) Outboard, 10°. (c) Inboard, 3°. (d) Inboard, 10°. FM (Baseline) = 0.76173294.

(a)

(b)

(c)

(d)
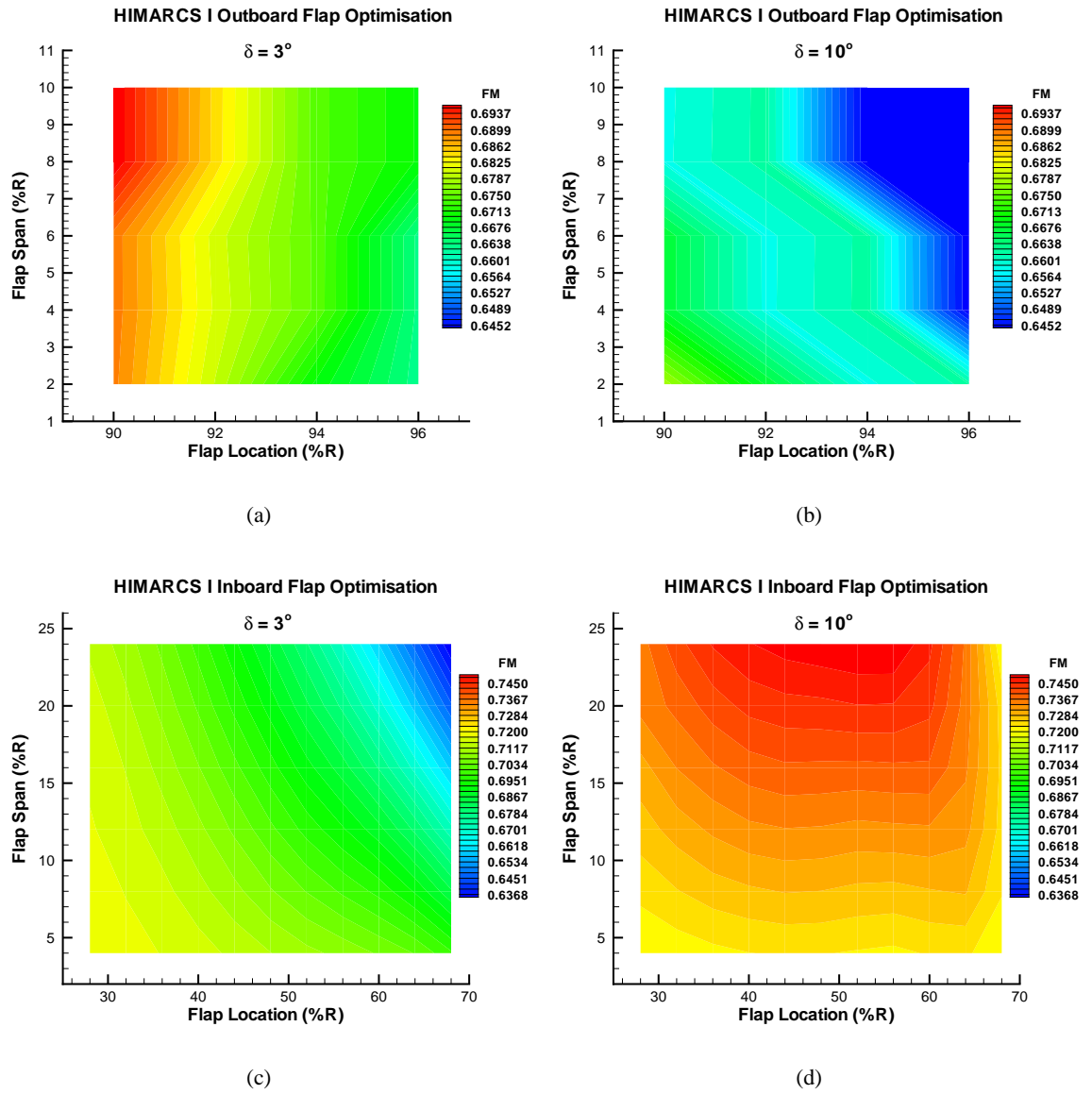
Figure B.16: Contours of Figure of Merit at $C_T = 0.00829091$ for flap chord of 10.67%c. (a) Outboard, 3°. (b) Outboard, 10°. (c) Inboard, 3°. (d) Inboard, 10°. FM (Baseline) = 0.74179268.

B.2 Flap Chord, 21.33%c
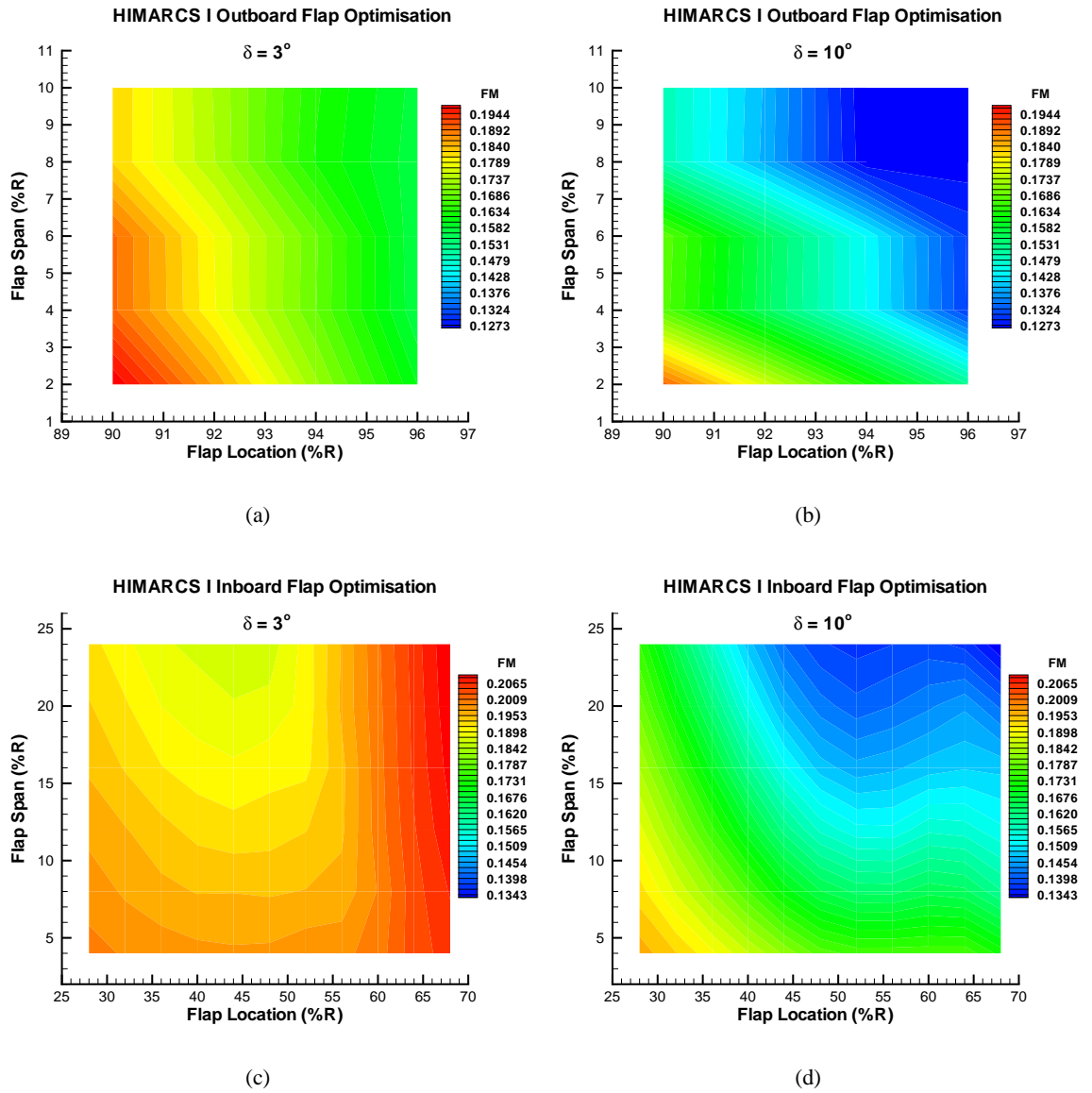
Figure B.17: Contours of Figure of Merit at $C_T = 0.000545455$ for flap chord of 21.33%c. (a) Outboard, 3°. (b) Outboard, 10°. (c) Inboard, 3°. (d) Inboard, 10°. FM (Baseline) = 0.19976322.
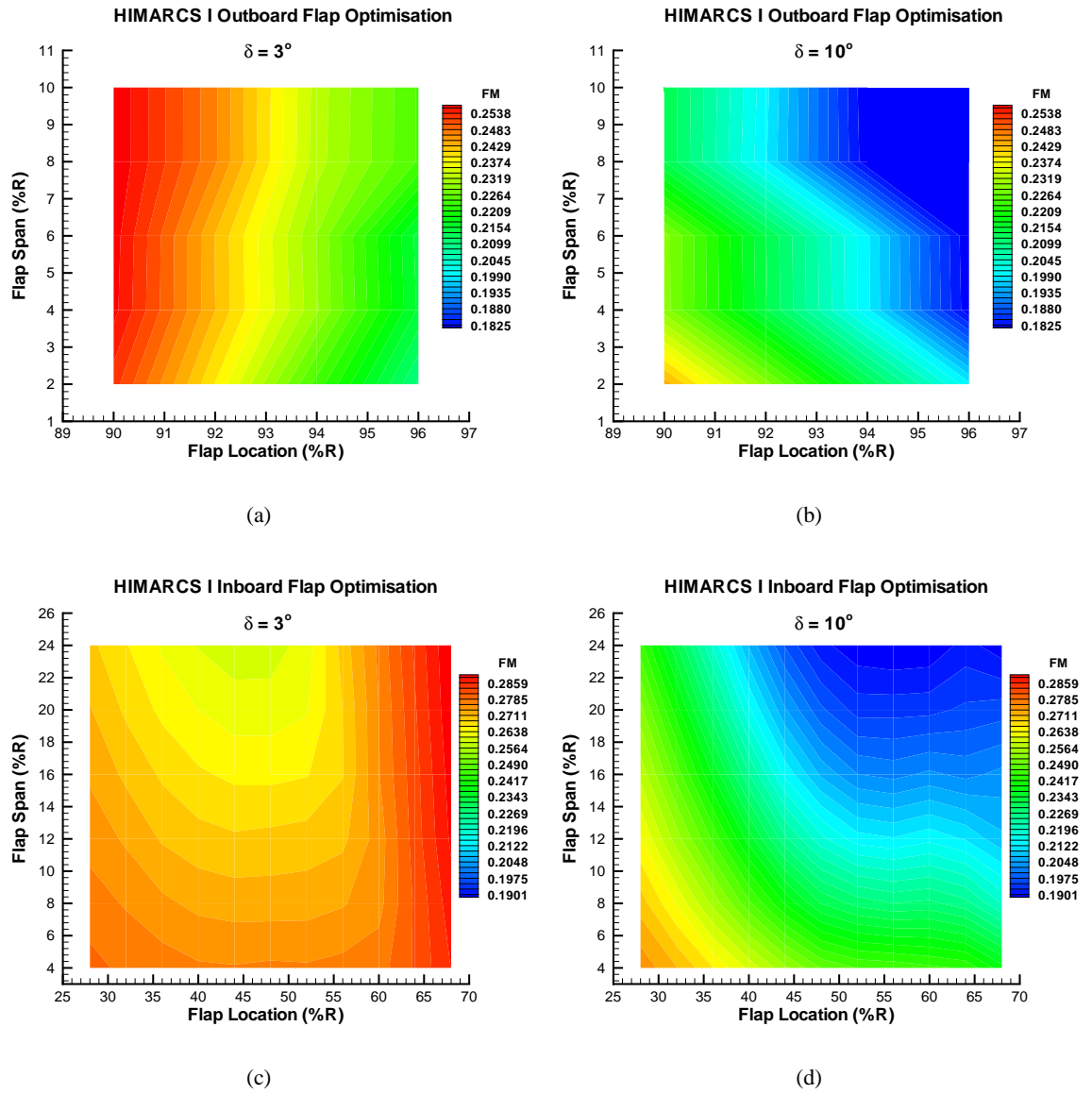
Figure B.18: Contours of Figure of Merit at $C_T = 0.0007$ for flap chord of 21.33%c. (a) Outboard, 3°. (b) Outboard, 10°. (c) Inboard, 3°. (d) Inboard, 10°. FM (Baseline) = 0.27974284.
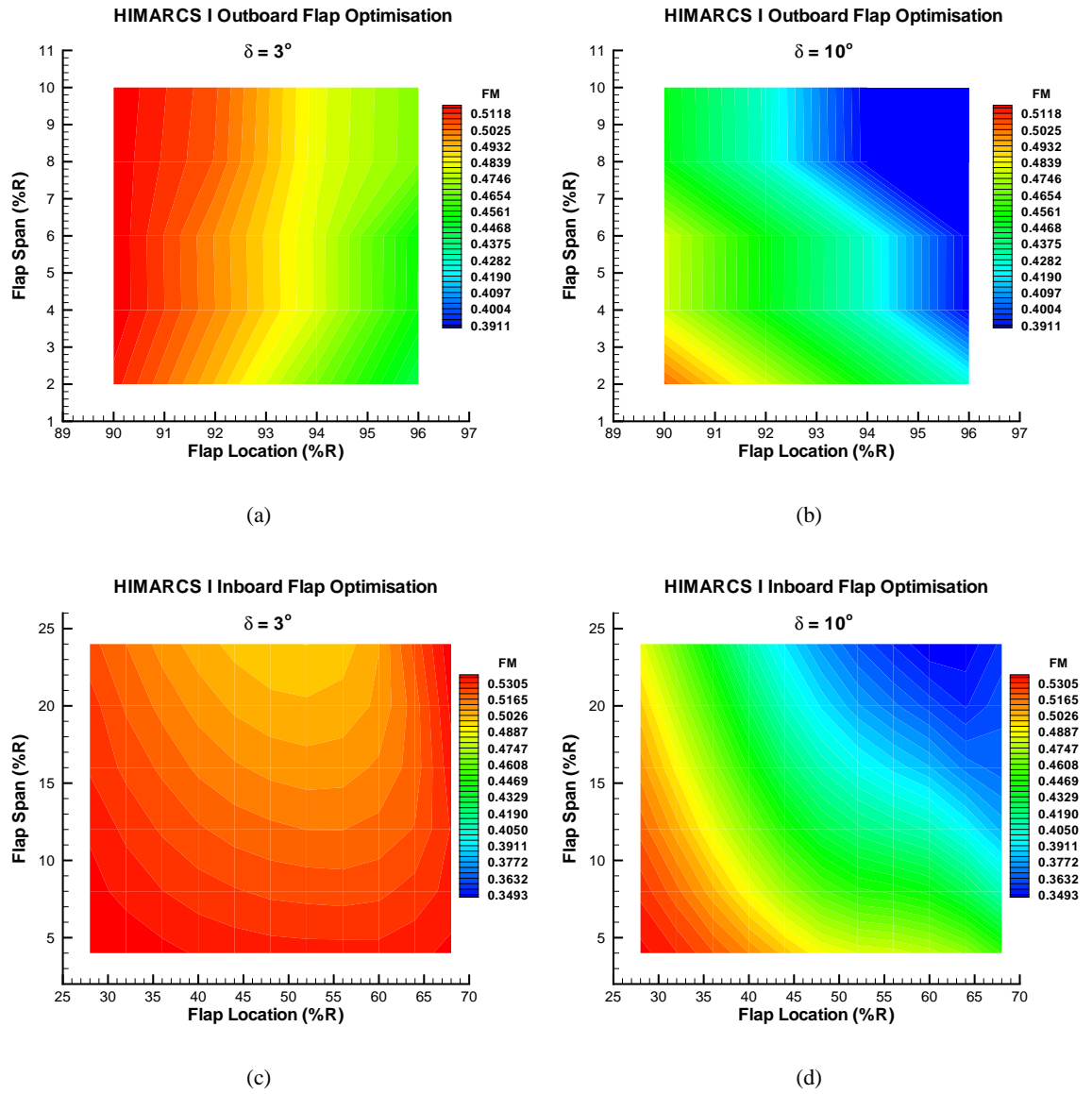
Figure B.19: Contours of Figure of Merit at $C_T = 0.0012$ for flap chord of 21.33%c. (a) Outboard, 3°. (b) Outboard, 10°. (c) Inboard, 3°. (d) Inboard, 10°. FM (Baseline) = 0.54232693.

(a)

(b)

(c)

(d)
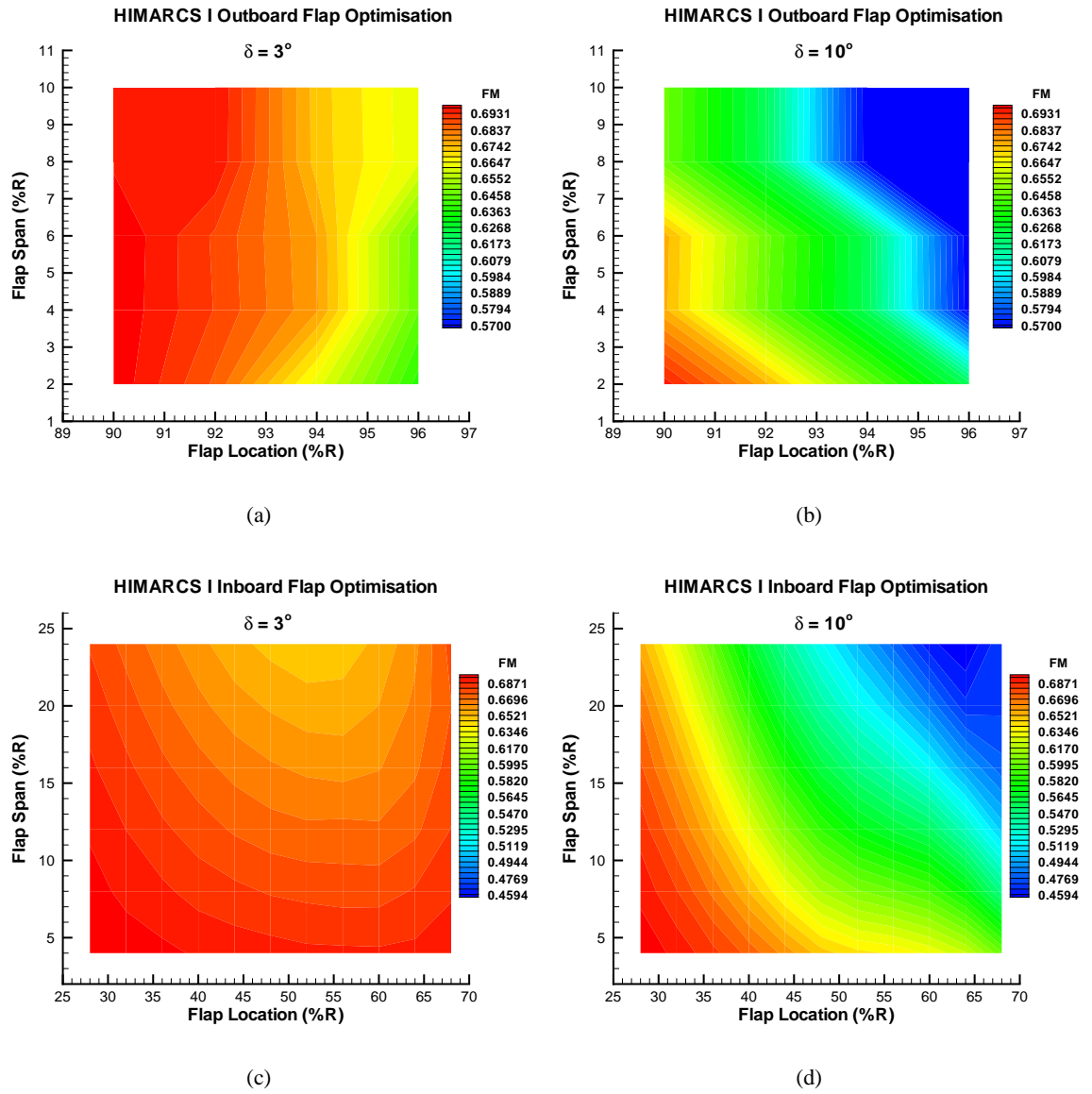
Figure B.20: Contours of Figure of Merit at $C_T = 0.0015942$ for flap chord of 21.33%c. (a) Outboard, 3°. (b) Outboard, 10°. (c) Inboard, 3°. (d) Inboard, 10°. FM (Baseline) = 0.70262504.
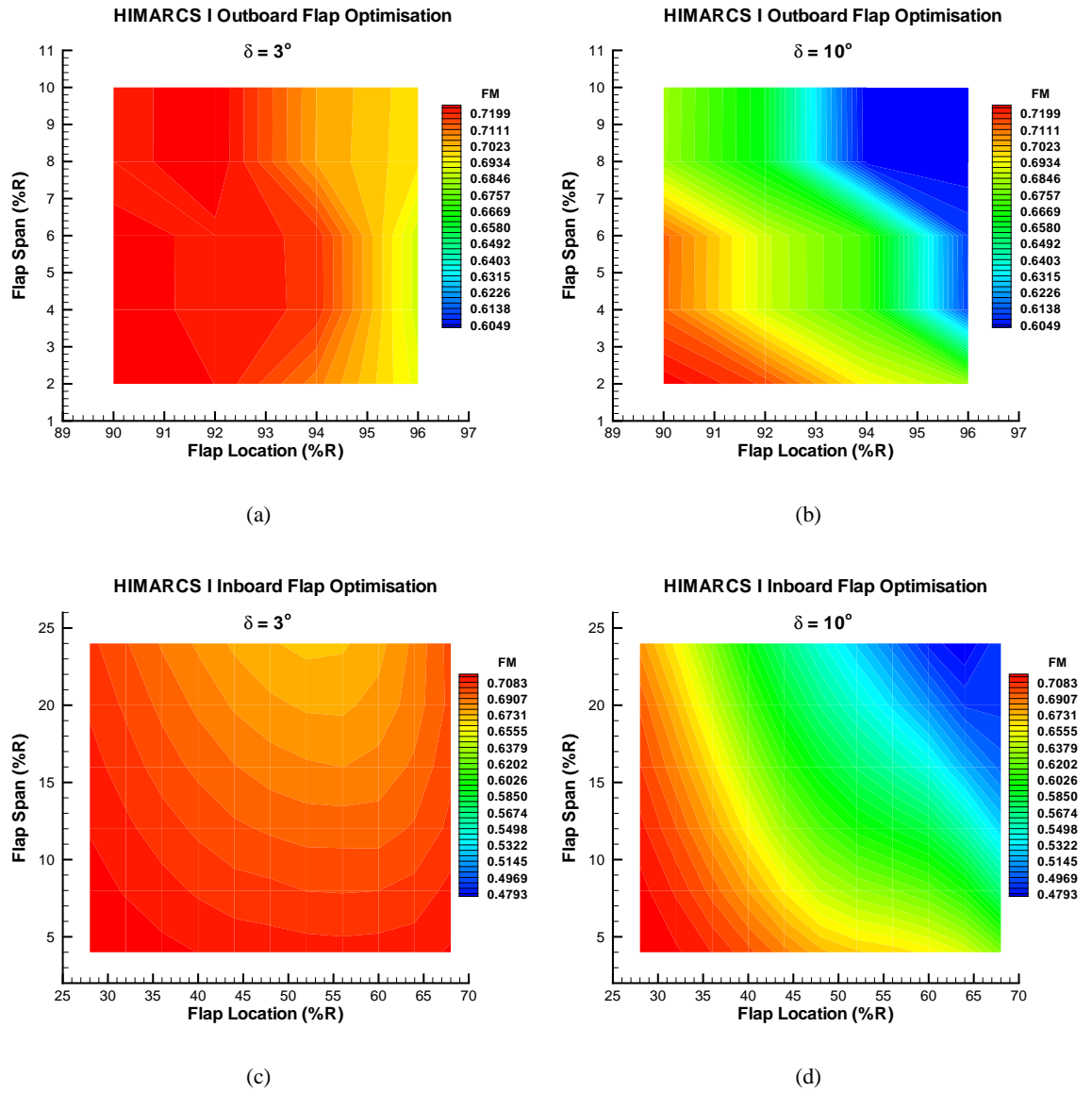
Figure B.21: Contours of Figure of Merit at C_T = 0.00167273 for flap chord of 21.33%c. (a) Outboard, 3°. (b) Outboard, 10°. (c) Inboard, 3°. (d) Inboard, 10°. FM (Baseline) = 0.72664547.

(a)

(b)

(c)

(d)
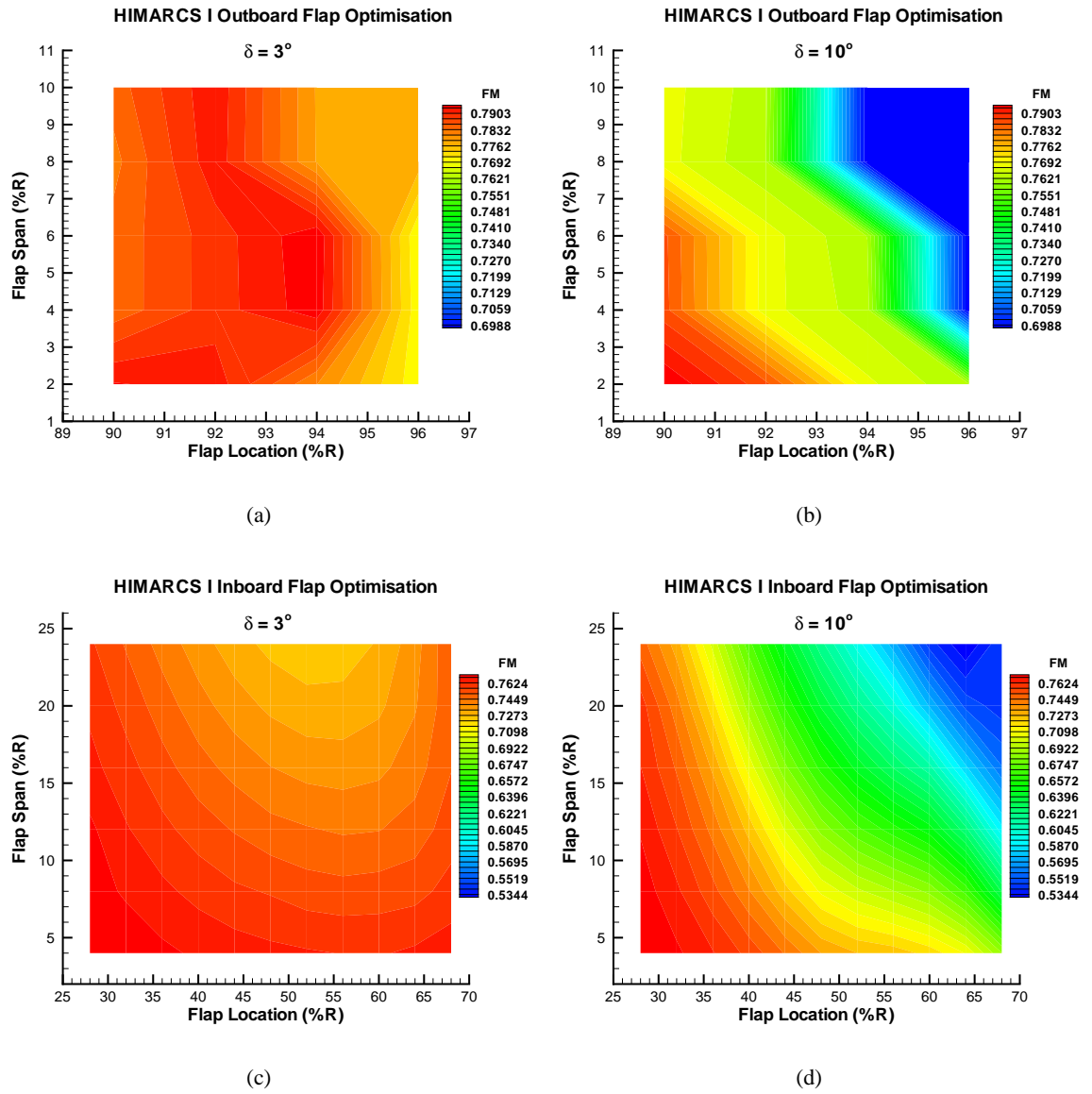
Figure B.22: Contours of Figure of Merit at $C_T = 0.0019$ for flap chord of 21.33%c. (a) Outboard, 3°. (b) Outboard, 10°. (c) Inboard, 3°. (d) Inboard, 10°. FM (Baseline) = 0.77728802.

(a)

(b)

(c)

(d)
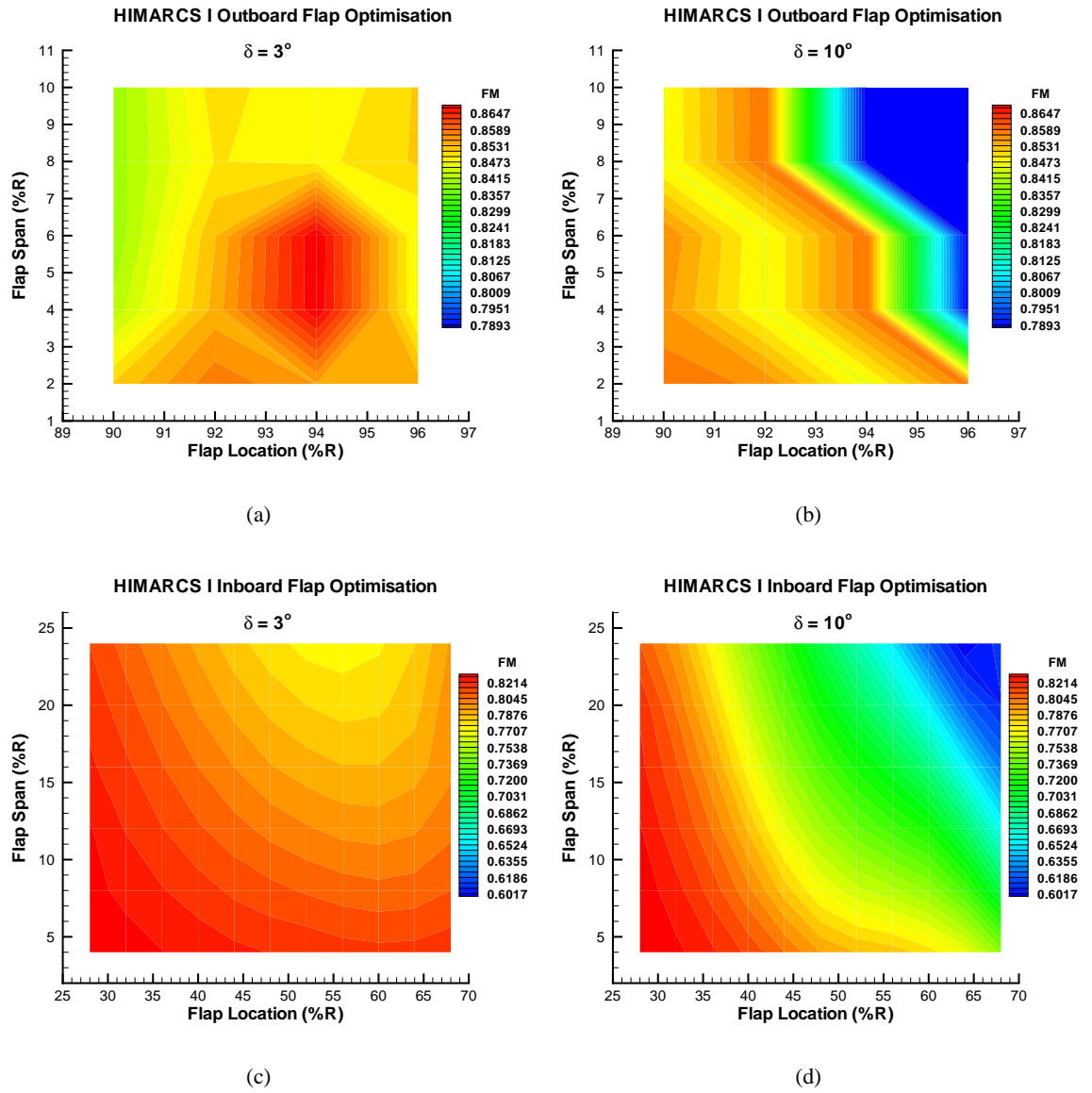
Figure B.23: Contours of Figure of Merit at $C_T = 0.0022$ for flap chord of 21.33%c. (a) Outboard, 3°. (b) Outboard, 10°. (c) Inboard, 3°. (d) Inboard, 10°. FM (Baseline) = 0.82768548.
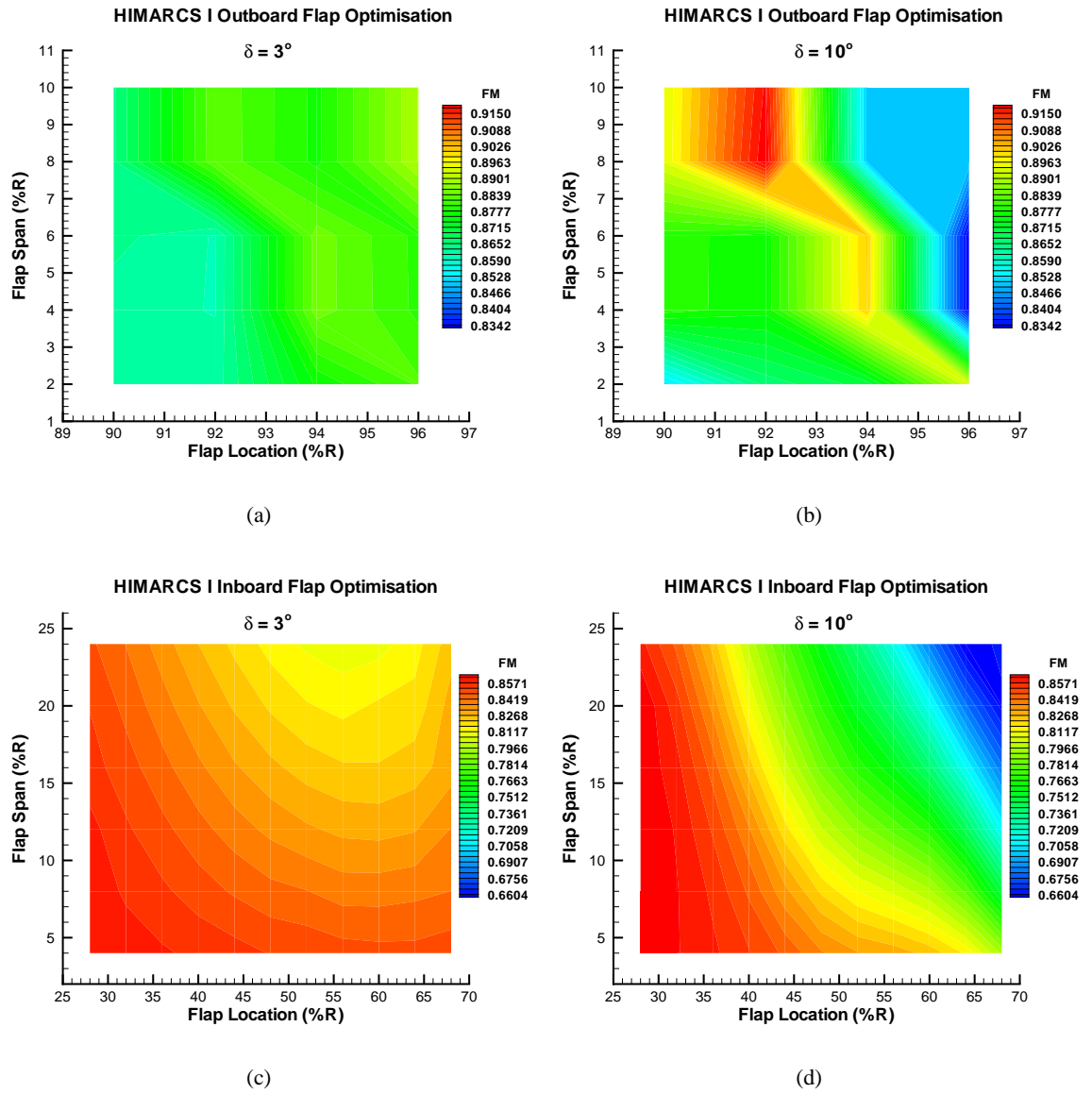
Figure B.24: Contours of Figure of Merit at $C_T = 0.0025$ for flap chord of 21.33%c. (a) Outboard, 3°. (b) Outboard, 10°. (c) Inboard, 3°. (d) Inboard, 10°. FM (Baseline) = 0.86130375.

(a)

(b)

(c)

(d)
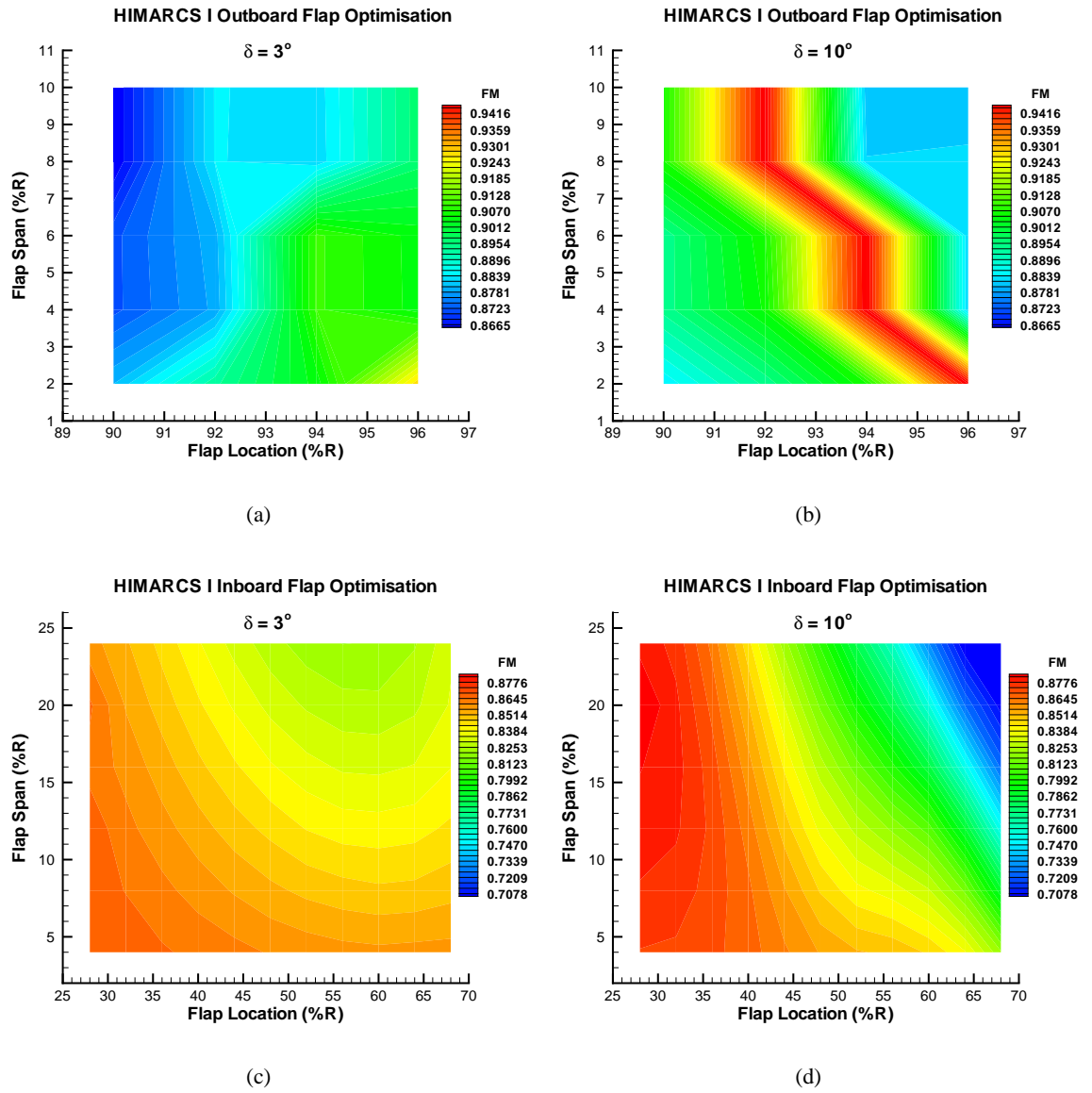
Figure B.25: Contours of Figure of Merit at $C_T = 0.0028$ for flap chord of 21.33%c. (a) Outboard, 3°. (b) Outboard, 10°. (c) Inboard, 3°. (d) Inboard, 10°. FM (Baseline) = 0.87034994.

(a)

(b)

(c)

(d)
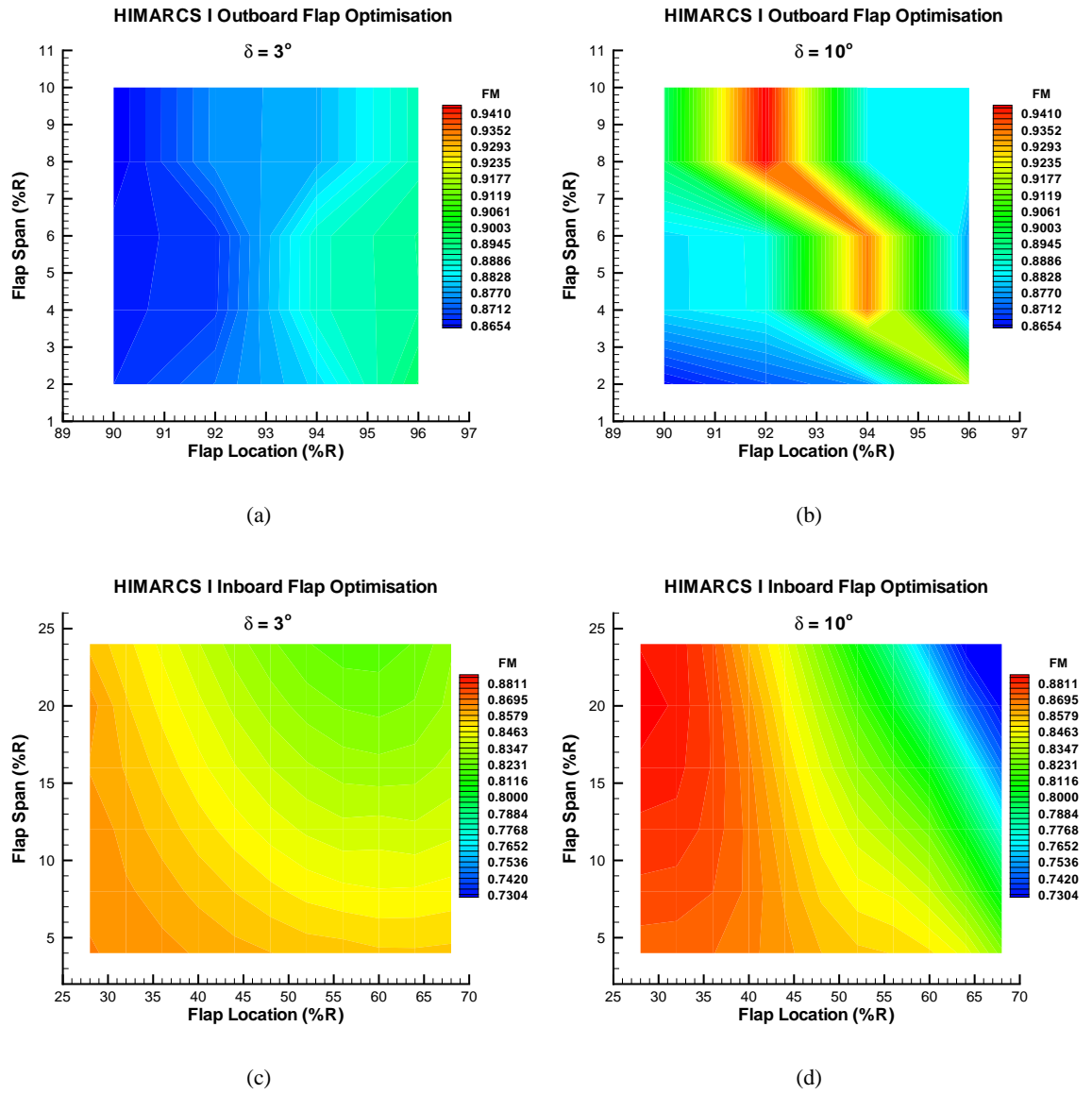
Figure B.26: Contours of Figure of Merit at $C_T = 0.00298182$ for flap chord of 21.33%c. (a) Outboard, 3°. (b) Outboard, 10°. (c) Inboard, 3°. (d) Inboard, 10°. FM (Baseline) = 0.86903244.
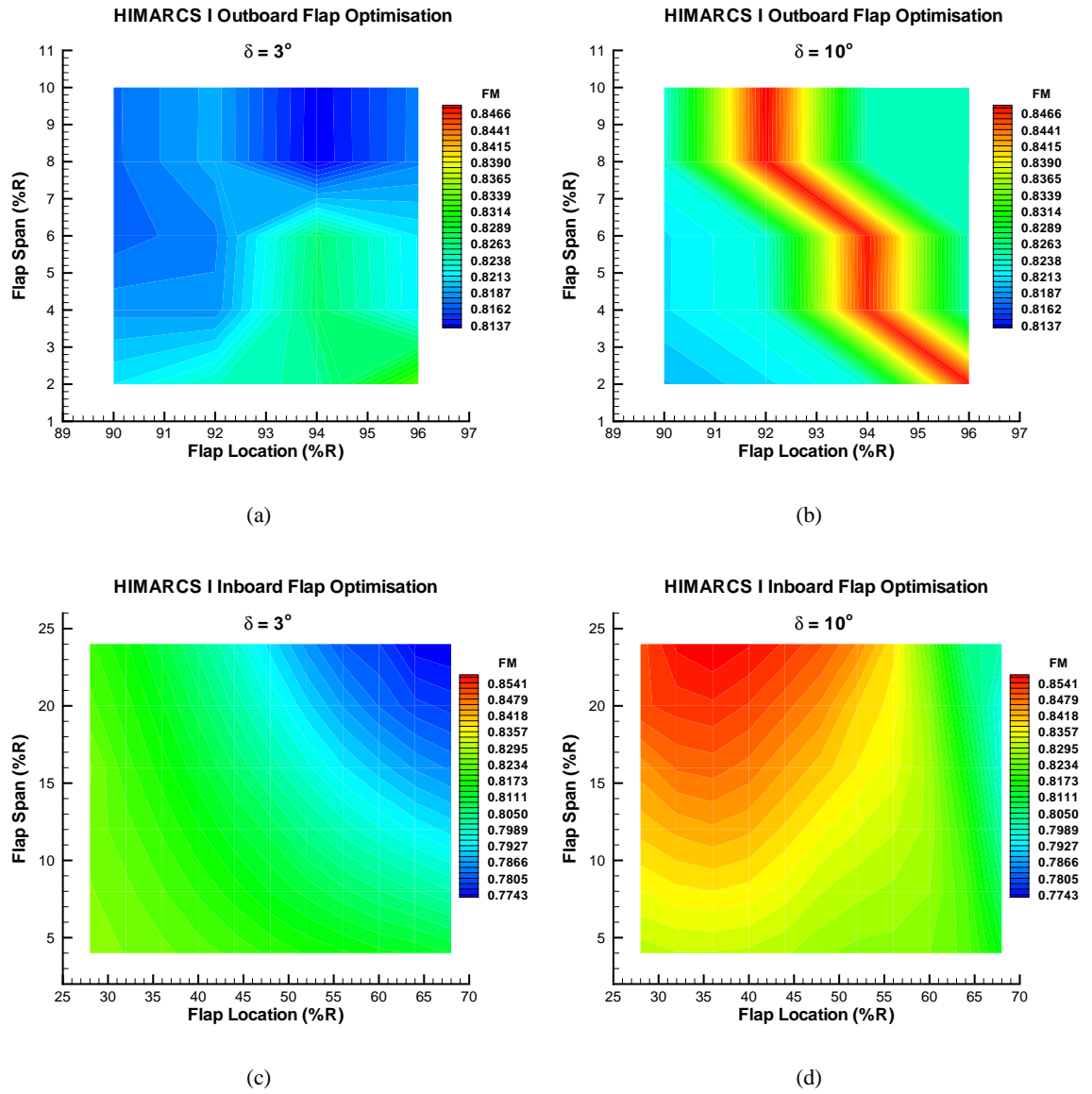
Figure B.27: Contours of Figure of Merit at $C_T = 0.00414545$ for flap chord of 21.33%c. (a) Outboard, 3°. (b) Outboard, 10°. (c) Inboard, 3°. (d) Inboard, 10°. FM (Baseline) = 0.83130002.

(a)

(b)

(c)

(d)
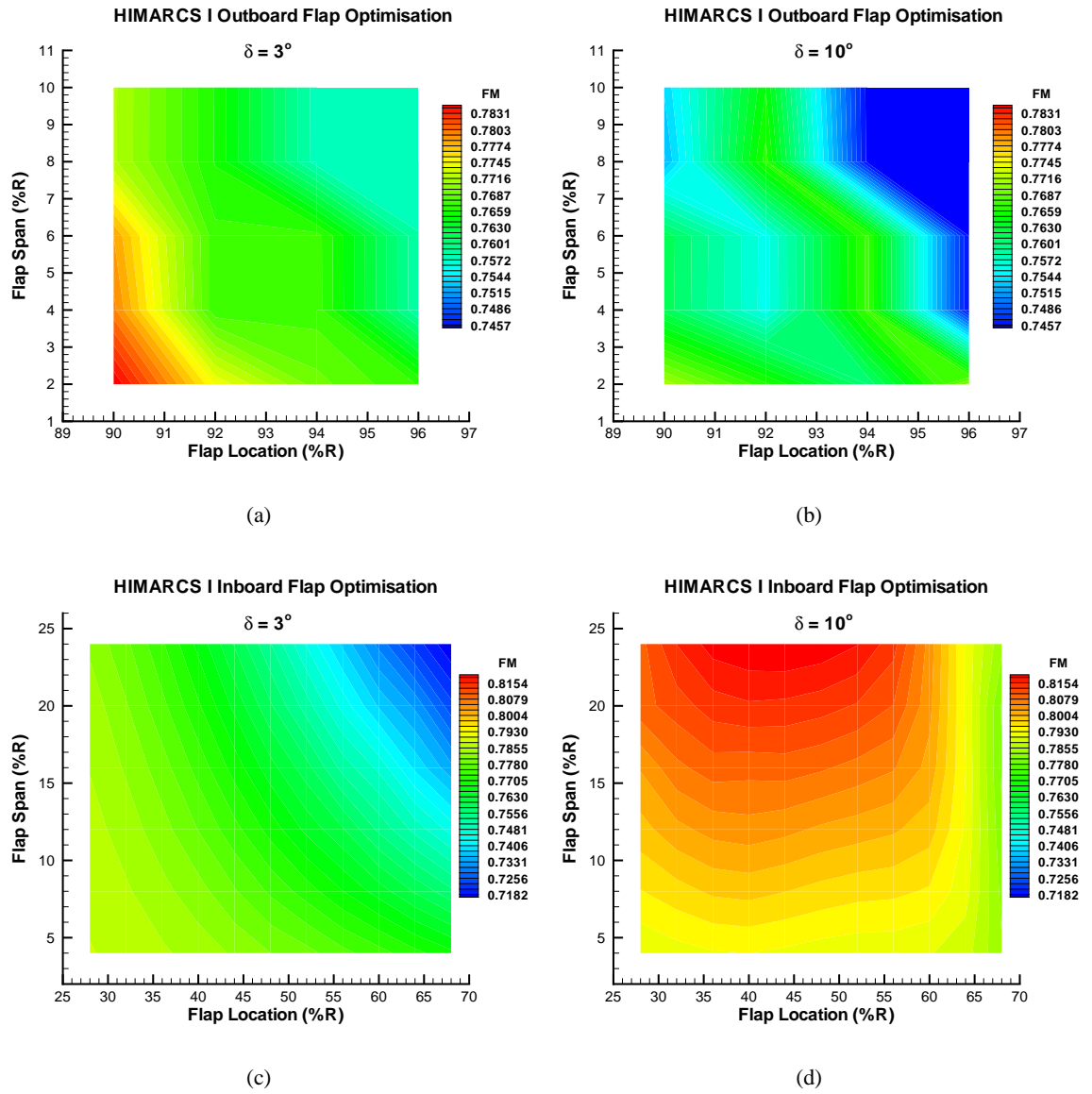
Figure B.28: Contours of Figure of Merit at $C_T = 0.00556364$ for flap chord of 21.33%c. (a) Outboard, 3°. (b) Outboard, 10°. (c) Inboard, 3°. (d) Inboard, 10°. FM (Baseline) = 0.79409397.
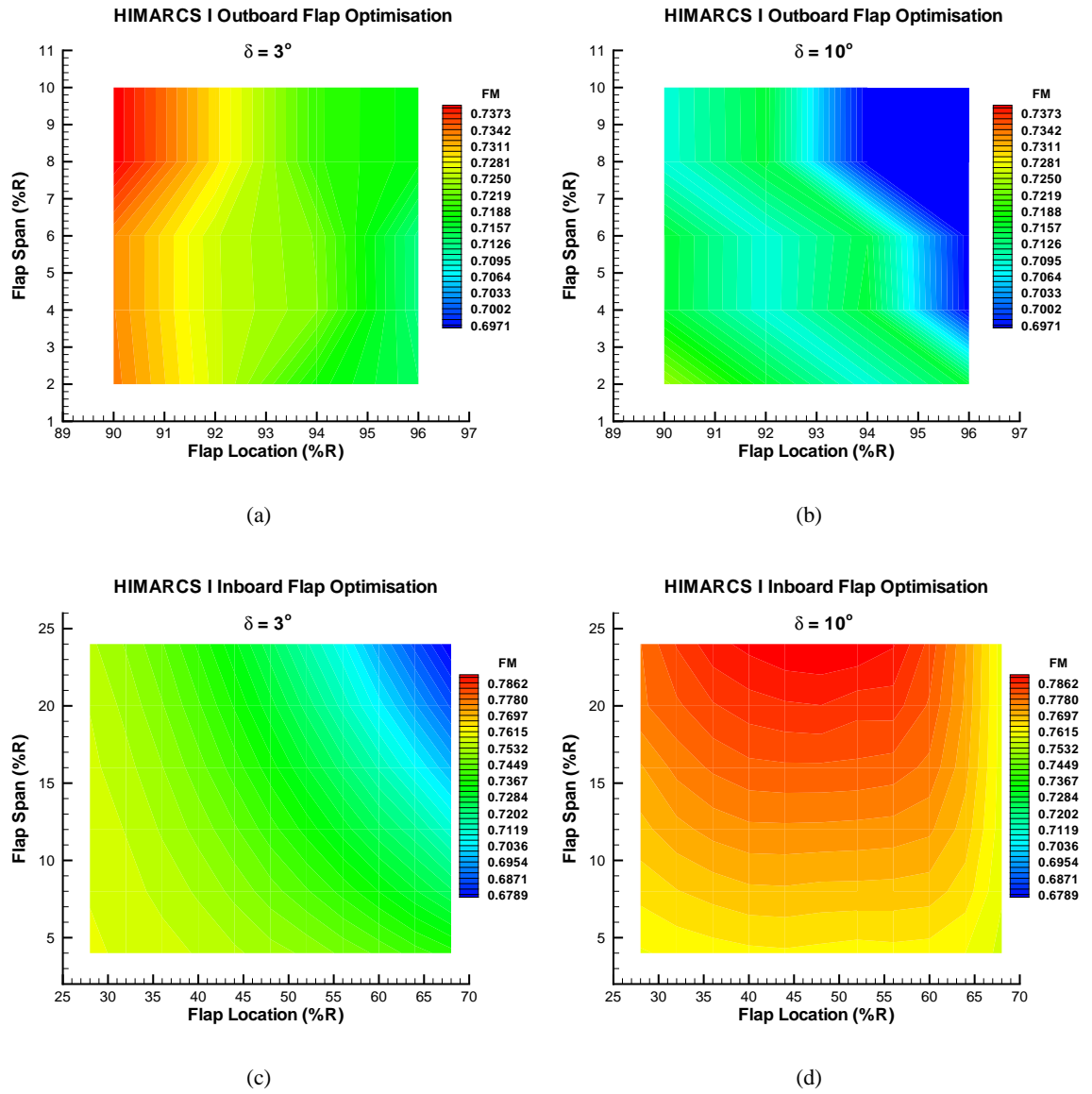
Figure B.29: Contours of Figure of Merit at $C_T = 0.00690909$ for flap chord of 21.33%c. (a) Outboard, 3°. (b) Outboard, 10°. (c) Inboard, 3°. (d) Inboard, 10°. FM (Baseline) = 0.76587558.
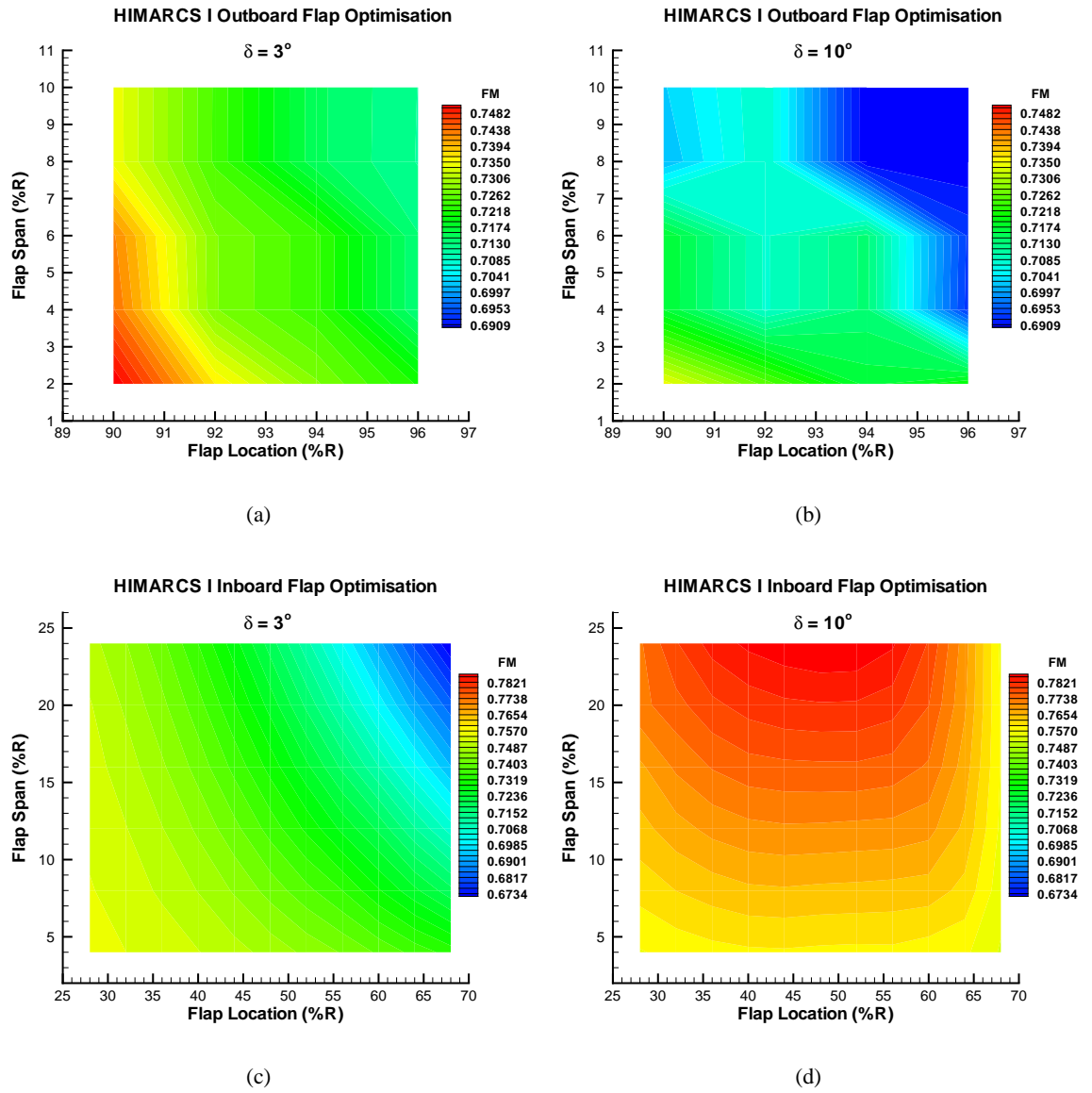
Figure B.30: Contours of Figure of Merit at $C_T = 0.00712727$ for flap chord of 21.33%c. (a) Outboard, 3°. (b) Outboard, 10°. (c) Inboard, 3°. (d) Inboard, 10°. FM (Baseline) = 0.76173294.
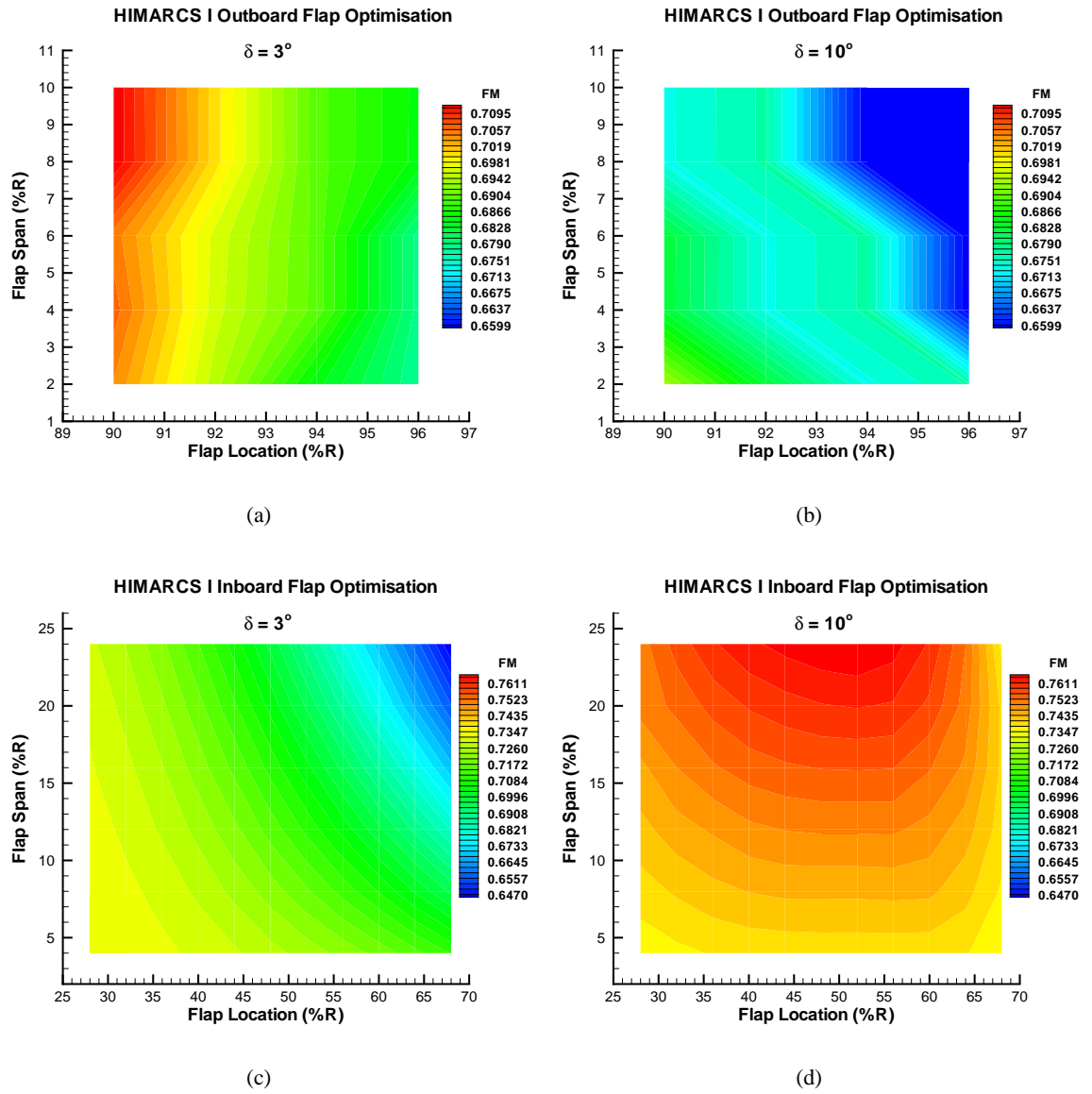
Figure B.31: Contours of Figure of Merit at $C_T = 0.00829091$ for flap chord of 21.33%c. (a) Outboard, 3°. (b) Outboard, 10°. (c) Inboard, 3°. (d) Inboard, 10°. FM (Baseline) = 0.74179268.

B.3 Flap Chord, 32%c
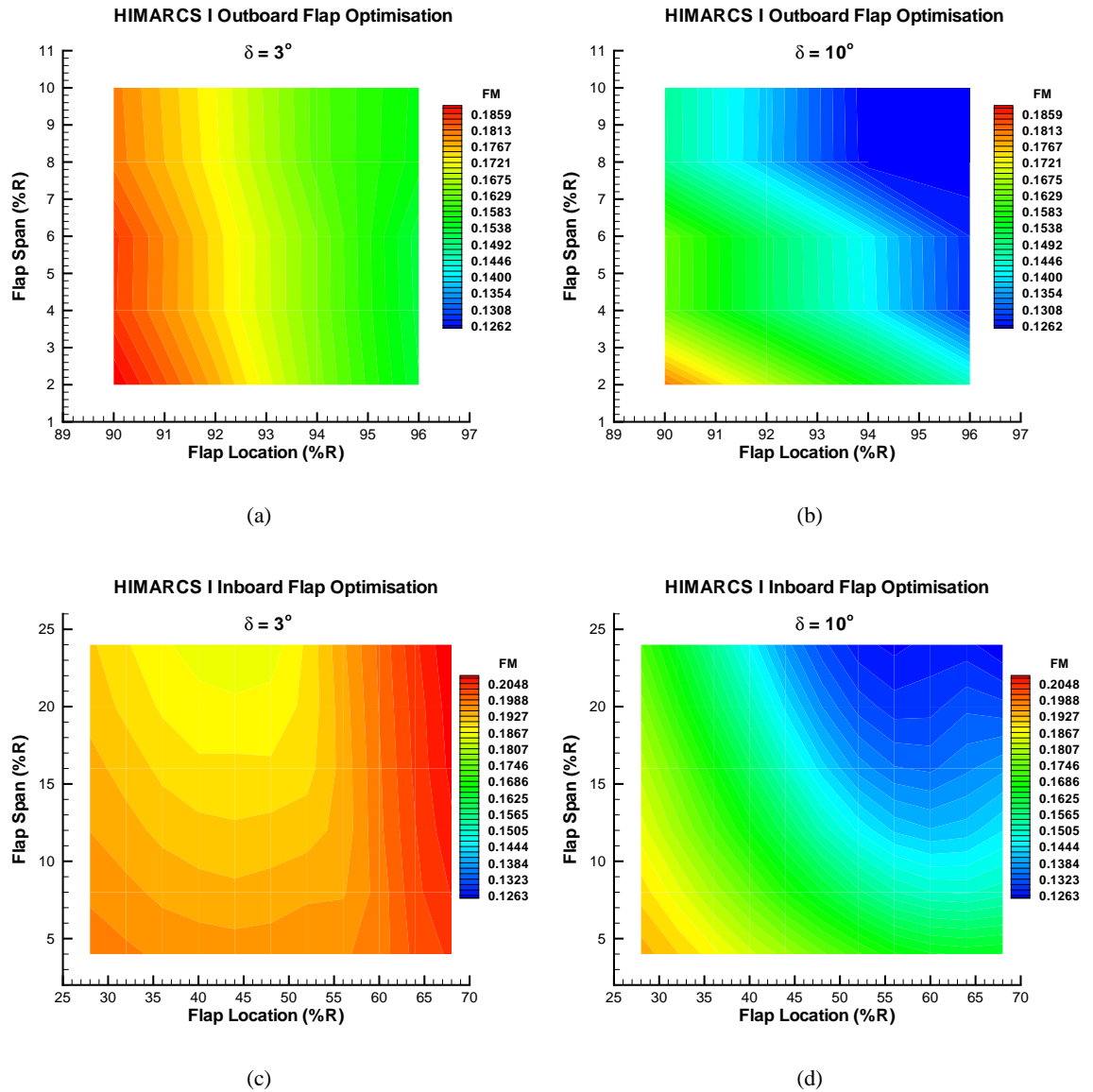
Figure B.32: Contours of Figure of Merit at $C_T = 0.000545455$ for flap chord of 32%c. (a) Outboard, 3°. (b) Outboard, 10°. (c) Inboard, 3°. (d) Inboard, 10°. FM (Baseline) = 0.19976322.

(a)

(b)

(c)

(d)
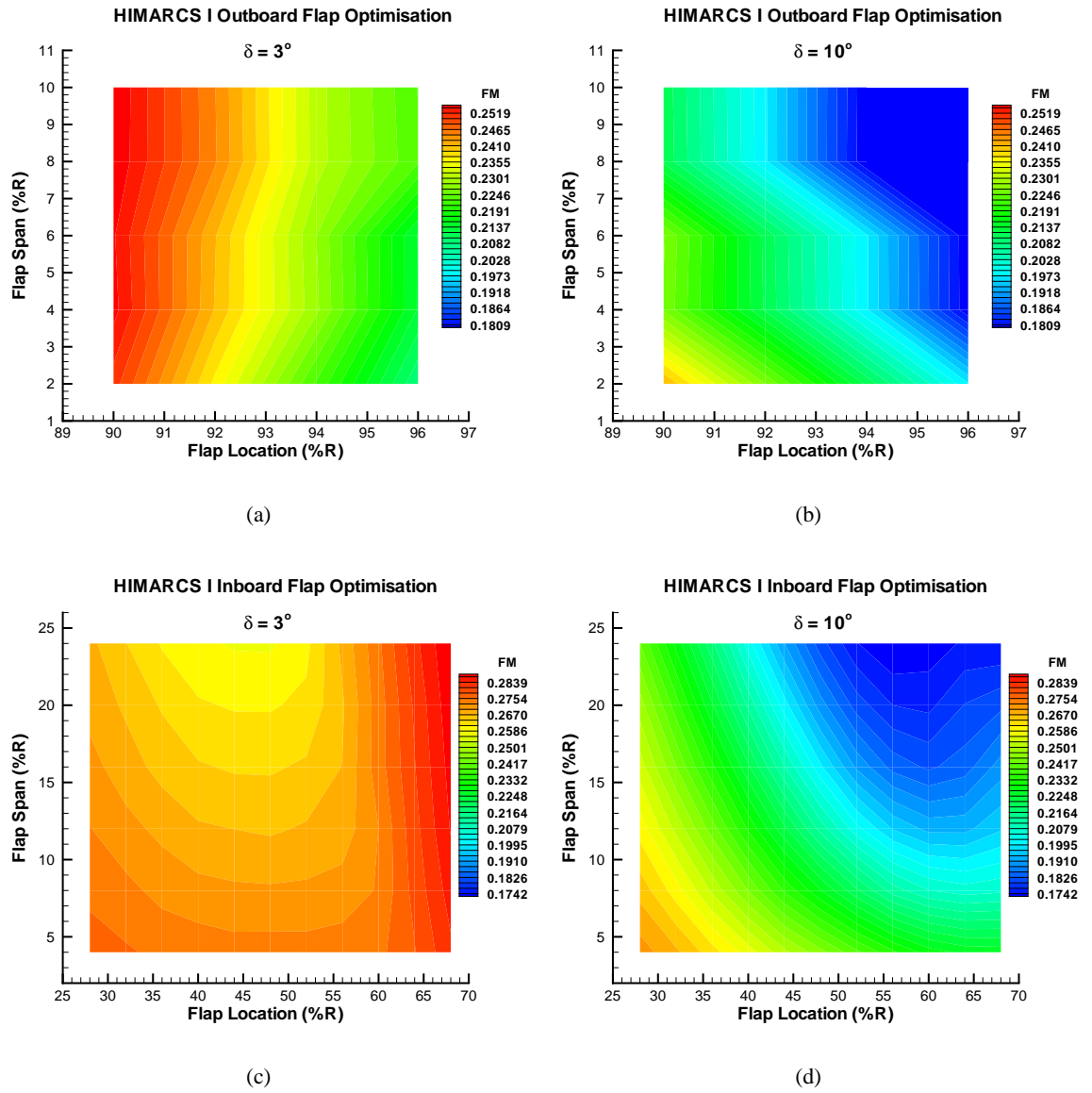
Figure B.33: Contours of Figure of Merit at $C_T = 0.0007$ for flap chord of 32%c. (a) Outboard, 3°. (b) Outboard, 10°. (c) Inboard, 3°. (d) Inboard, 10°. FM (Baseline) = 0.27974284.
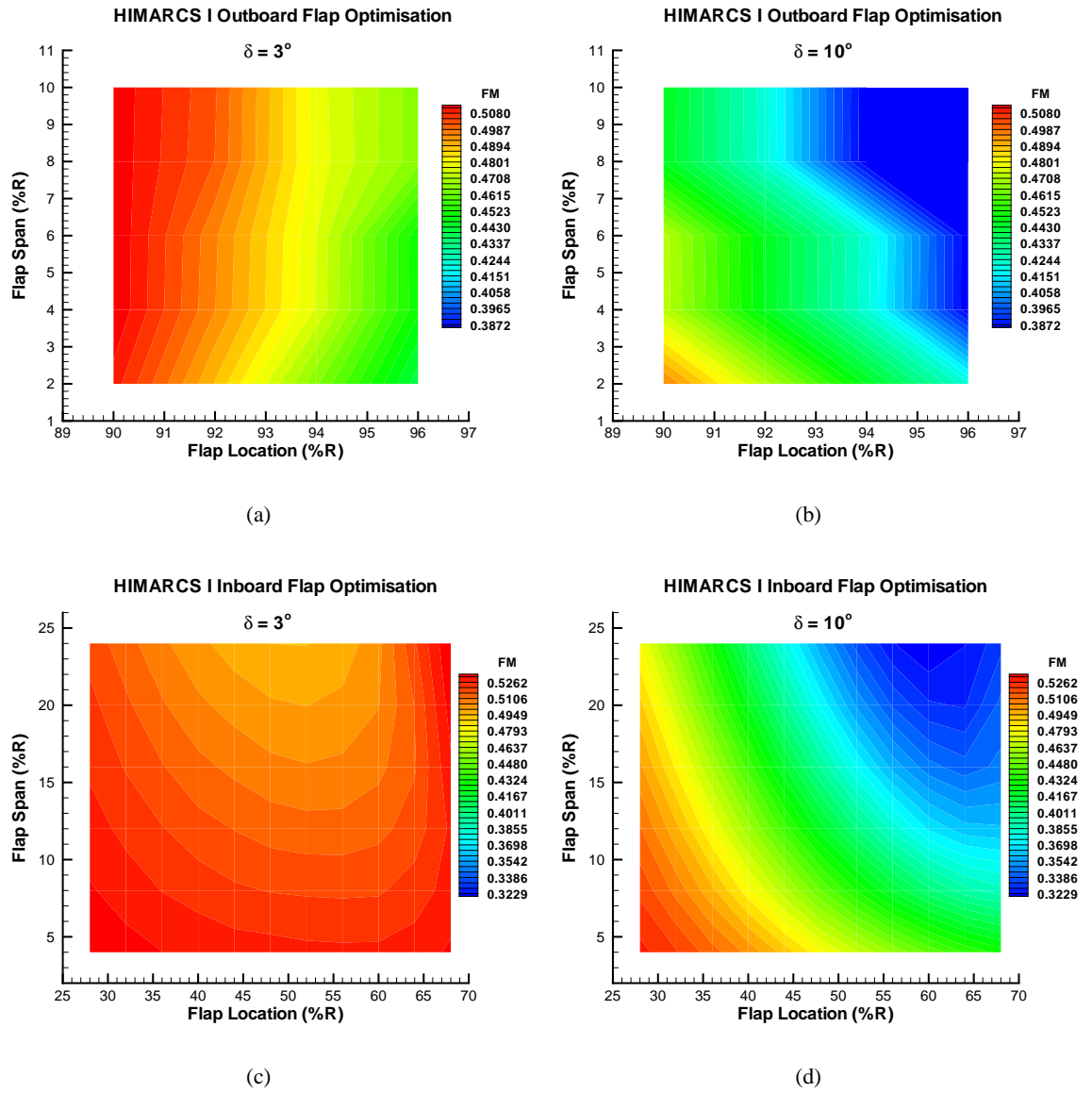
Figure B.34: Contours of Figure of Merit at $C_T = 0.0012$ for flap chord of 32%c. (a) Outboard, 3°. (b) Outboard, 10°. (c) Inboard, 3°. (d) Inboard, 10°. FM (Baseline) = 0.54232693.

(a)

(b)

(c)

(d)
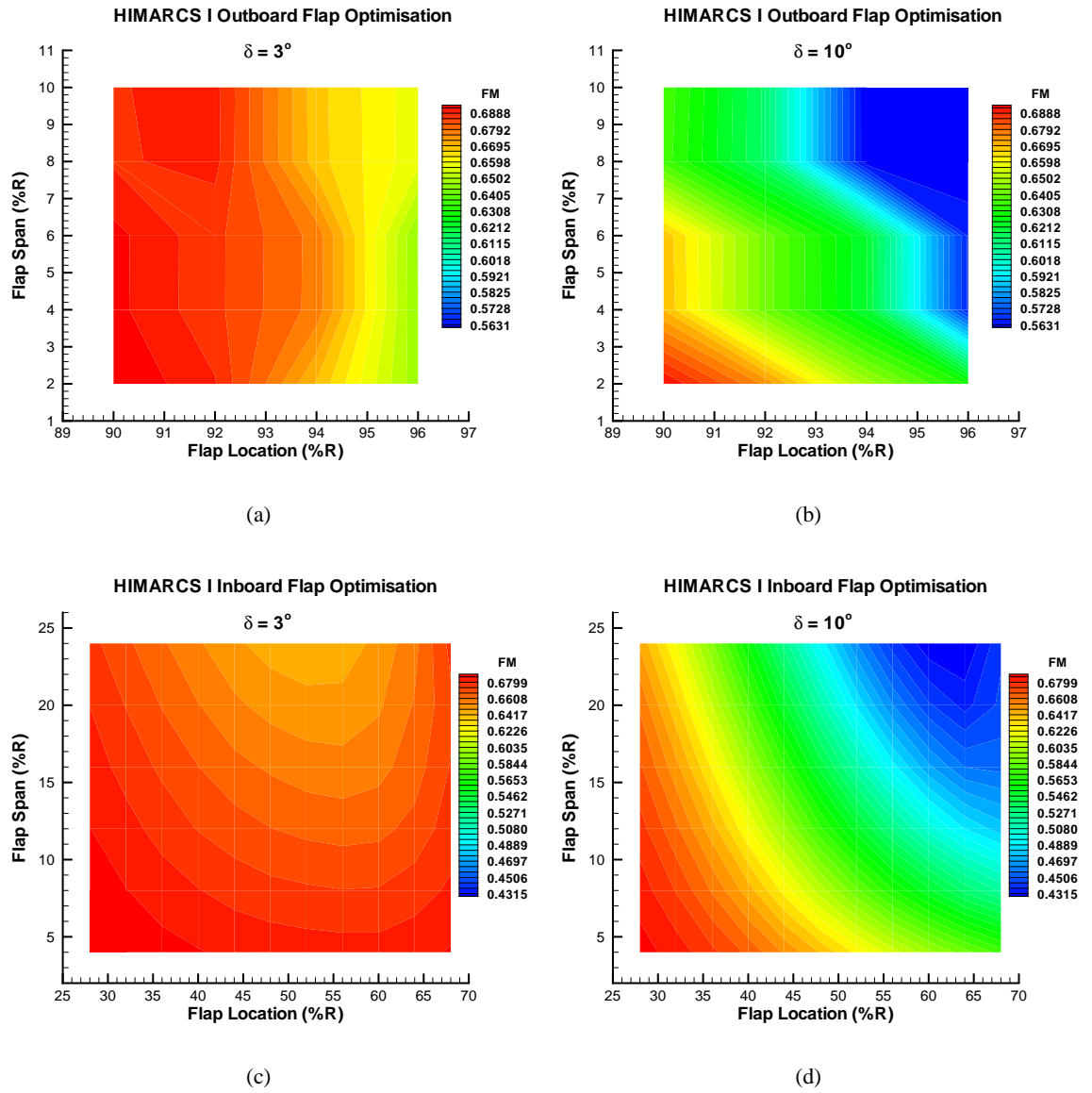
Figure B.35: Contours of Figure of Merit at $C_T = 0.0015942$ for flap chord of 32%c. (a) Outboard, 3°. (b) Outboard, 10°. (c) Inboard, 3°. (d) Inboard, 10°. FM (Baseline) = 0.70262504.

(a)

(b)

(c)

(d)
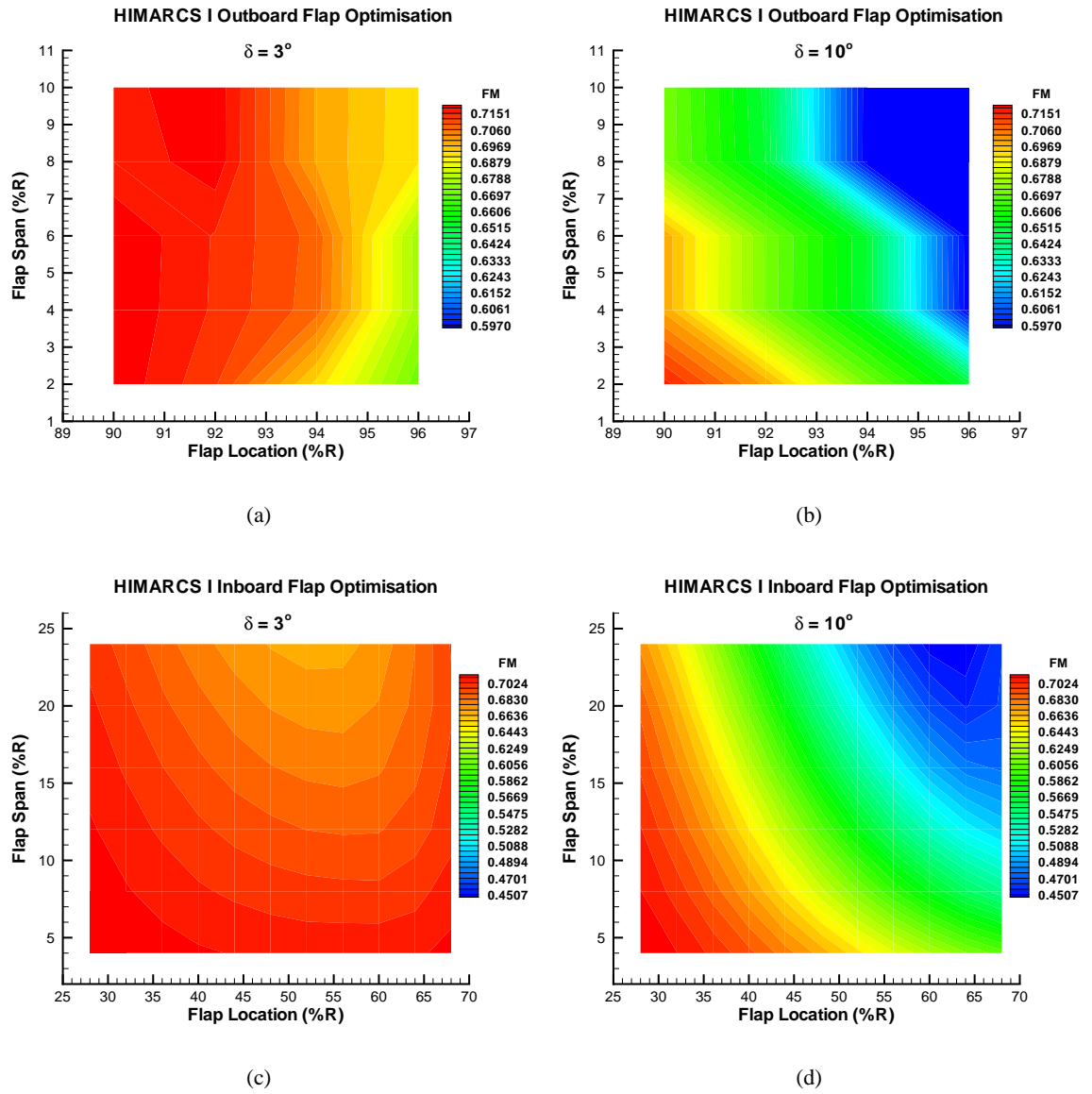
Figure B.36: Contours of Figure of Merit at $C_T = 0.00167273$ for flap chord of 32%c. (a) Outboard, 3°. (b) Outboard, 10°. (c) Inboard, 3°. (d) Inboard, 10°. FM (Baseline) = 0.72664547.

(a)

(b)

(c)

(d)
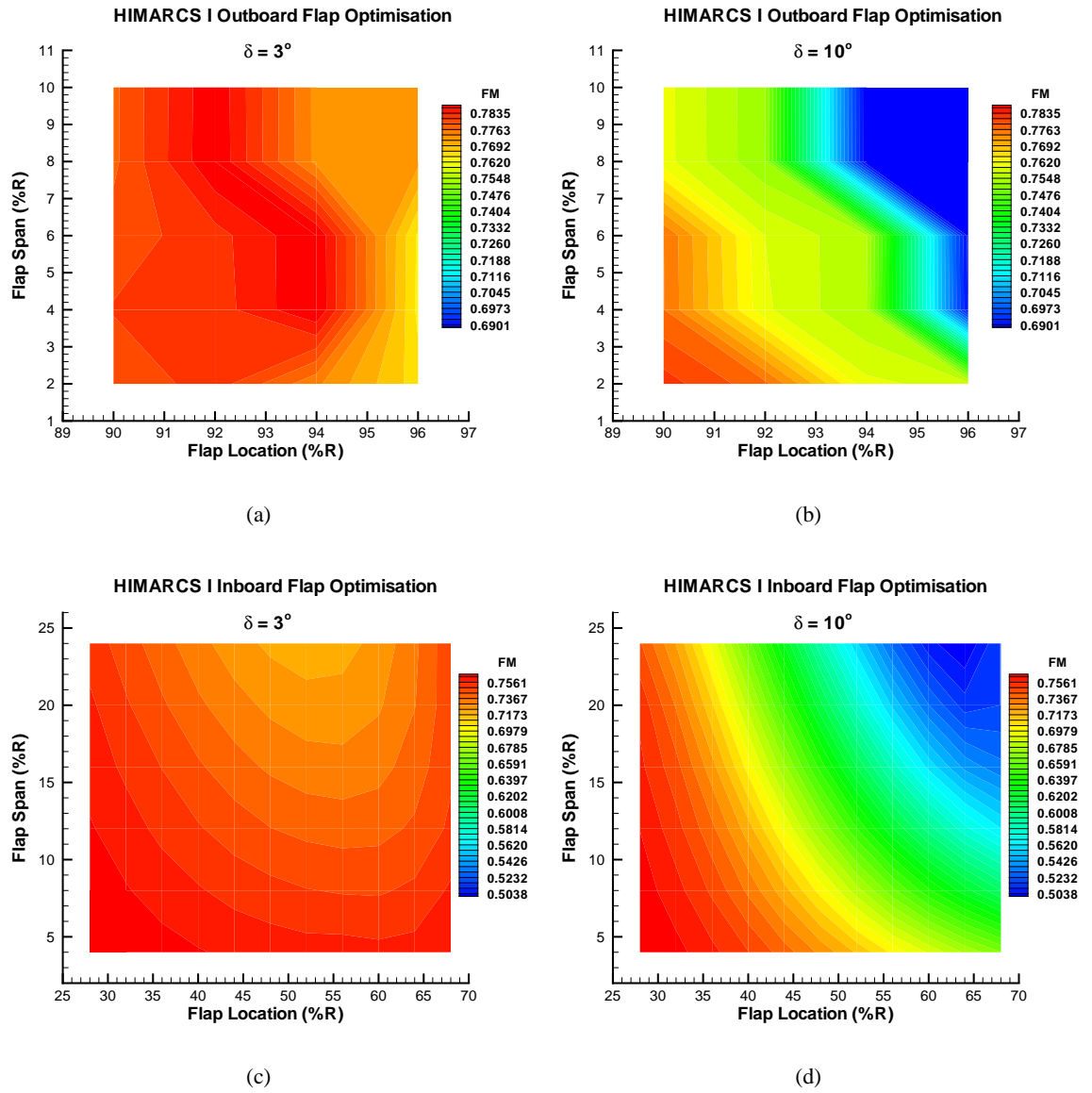
Figure B.37: Contours of Figure of Merit at $C_T = 0.0019$ for flap chord of 32%c. (a) Outboard, 3°. (b) Outboard, 10°. (c) Inboard, 3°. (d) Inboard, 10°. FM (Baseline) = 0.77728802.
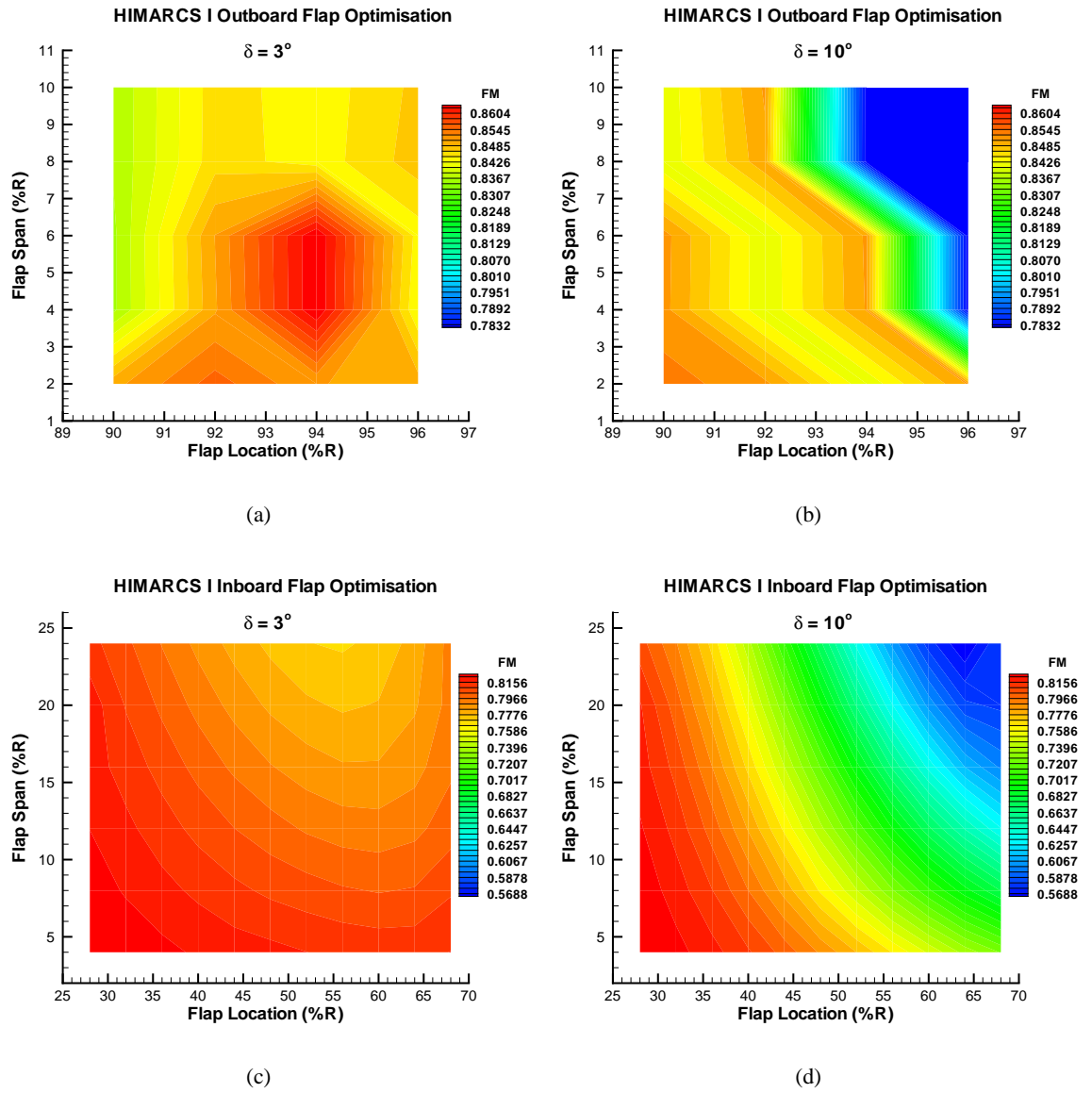
Figure B.38: Contours of Figure of Merit at $C_T = 0.0022$ for flap chord of 32%c. (a) Outboard, 3°. (b) Outboard, 10°. (c) Inboard, 3°. (d) Inboard, 10°. FM (Baseline) = 0.82768548.
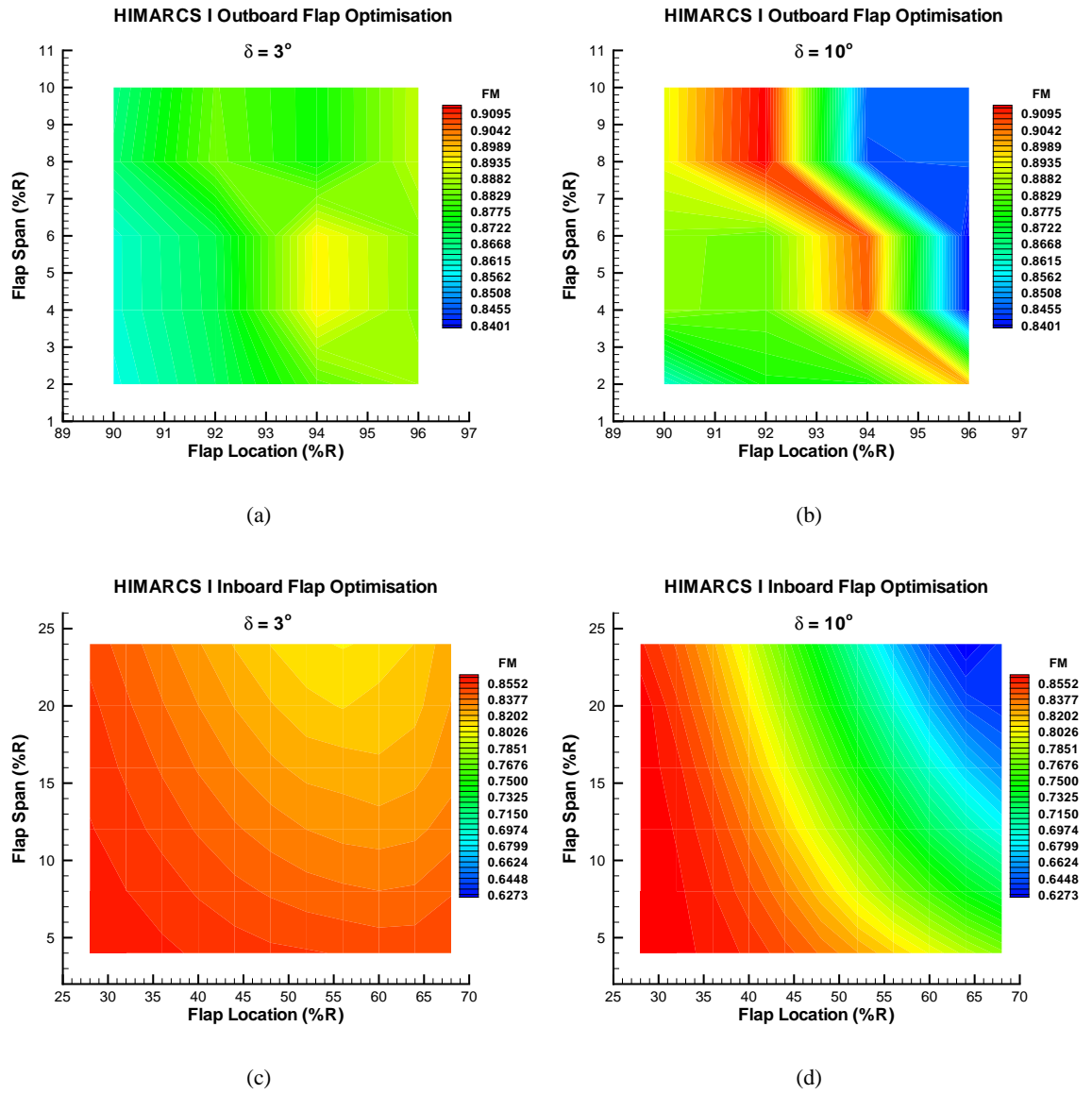
Figure B.39: Contours of Figure of Merit at $C_T = 0.0025$ for flap chord of 32%c. (a) Outboard, 3°. (b) Outboard, 10°. (c) Inboard, 3°. (d) Inboard, 10°. FM (Baseline) = 0.86130375.

(a)

(b)

(c)

(d)
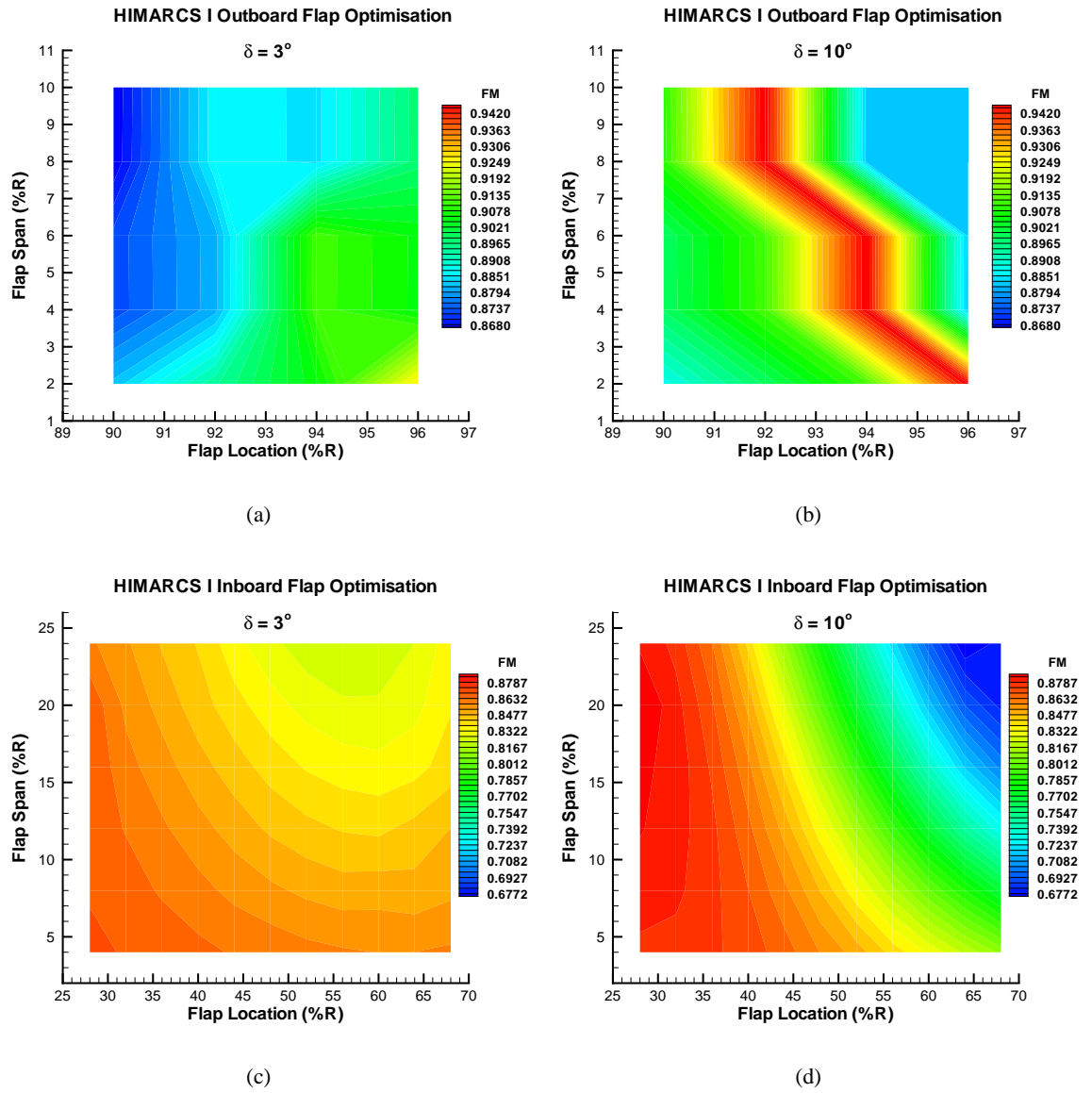
Figure B.40: Contours of Figure of Merit at $C_T = 0.0028$ for flap chord of 32%c. (a) Outboard, 3°. (b) Outboard, 10°. (c) Inboard, 3°. (d) Inboard, 10°. FM (Baseline) = 0.87034994.

(a)

(b)

(c)

(d)
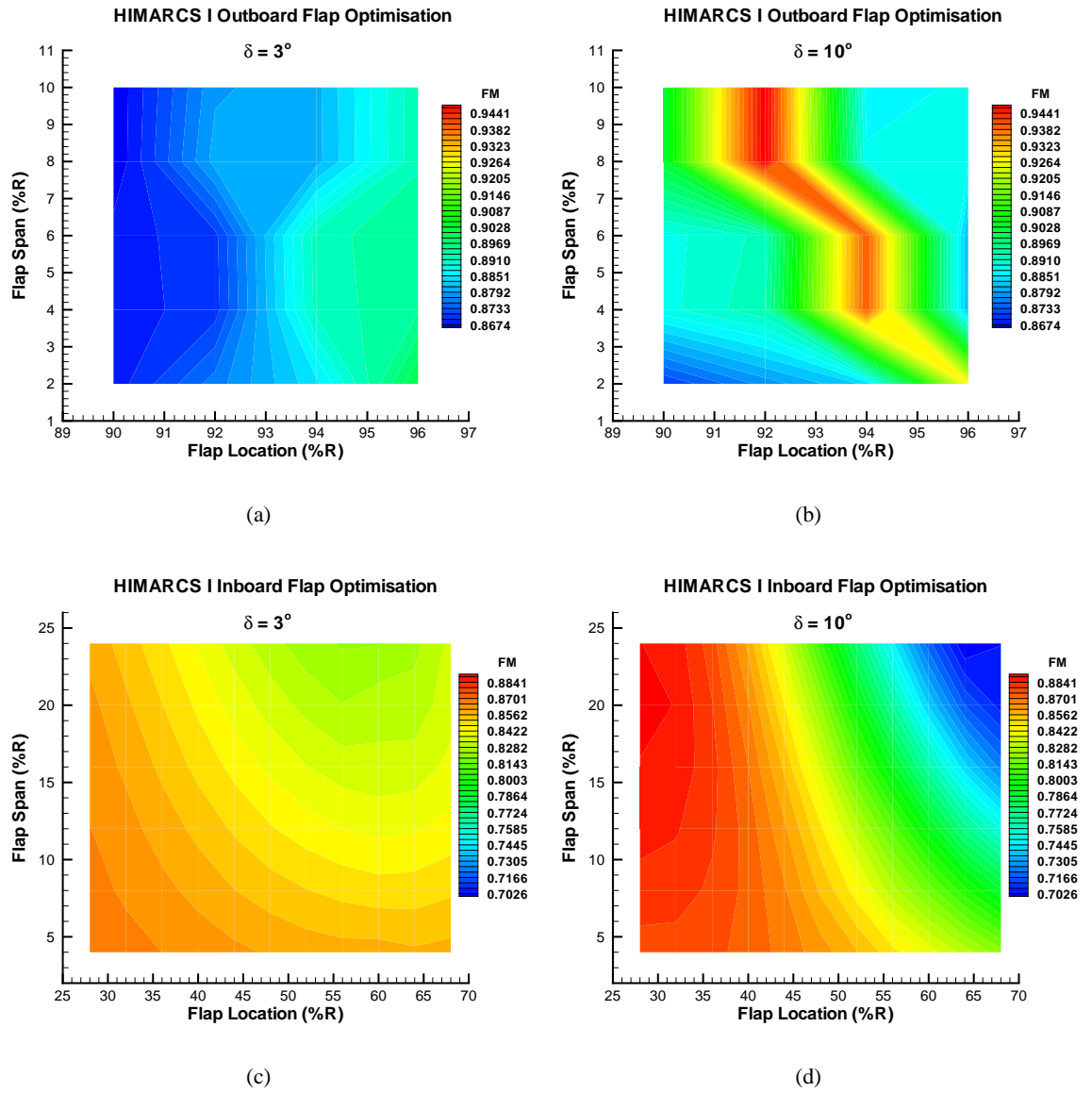
Figure B.41: Contours of Figure of Merit at $C_T = 0.00298182$ for flap chord of 32%c. (a) Outboard, 3°. (b) Outboard, 10°. (c) Inboard, 3°. (d) Inboard, 10°. FM (Baseline) = 0.86903244.
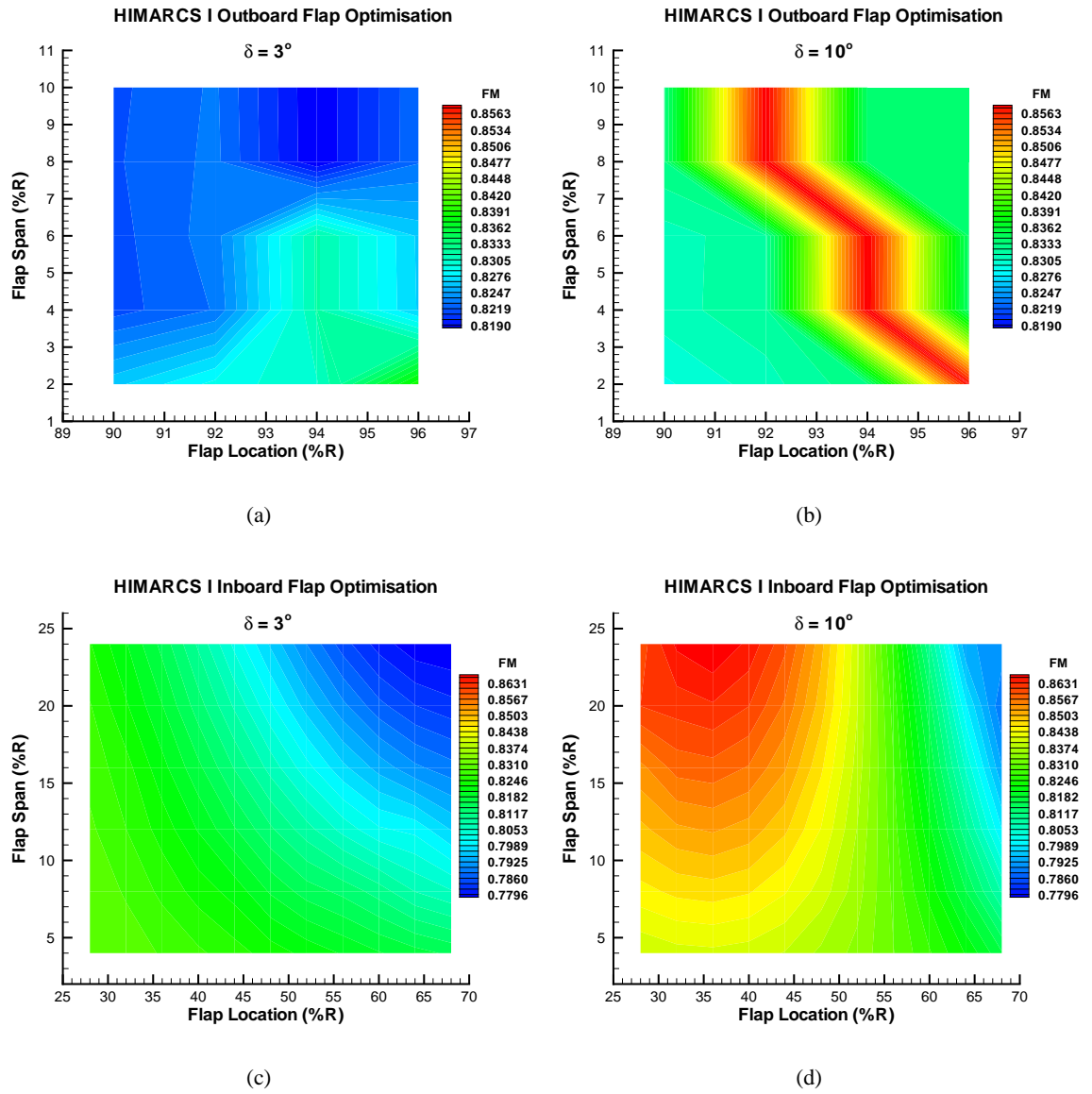
Figure B.42: Contours of Figure of Merit at $C_T = 0.00414545$ for flap chord of 32%c. (a) Outboard, 3°. (b) Outboard, 10°. (c) Inboard, 3°. (d) Inboard, 10°. FM (Baseline) = 0.83130002.

(a)

(b)

(c)

(d)
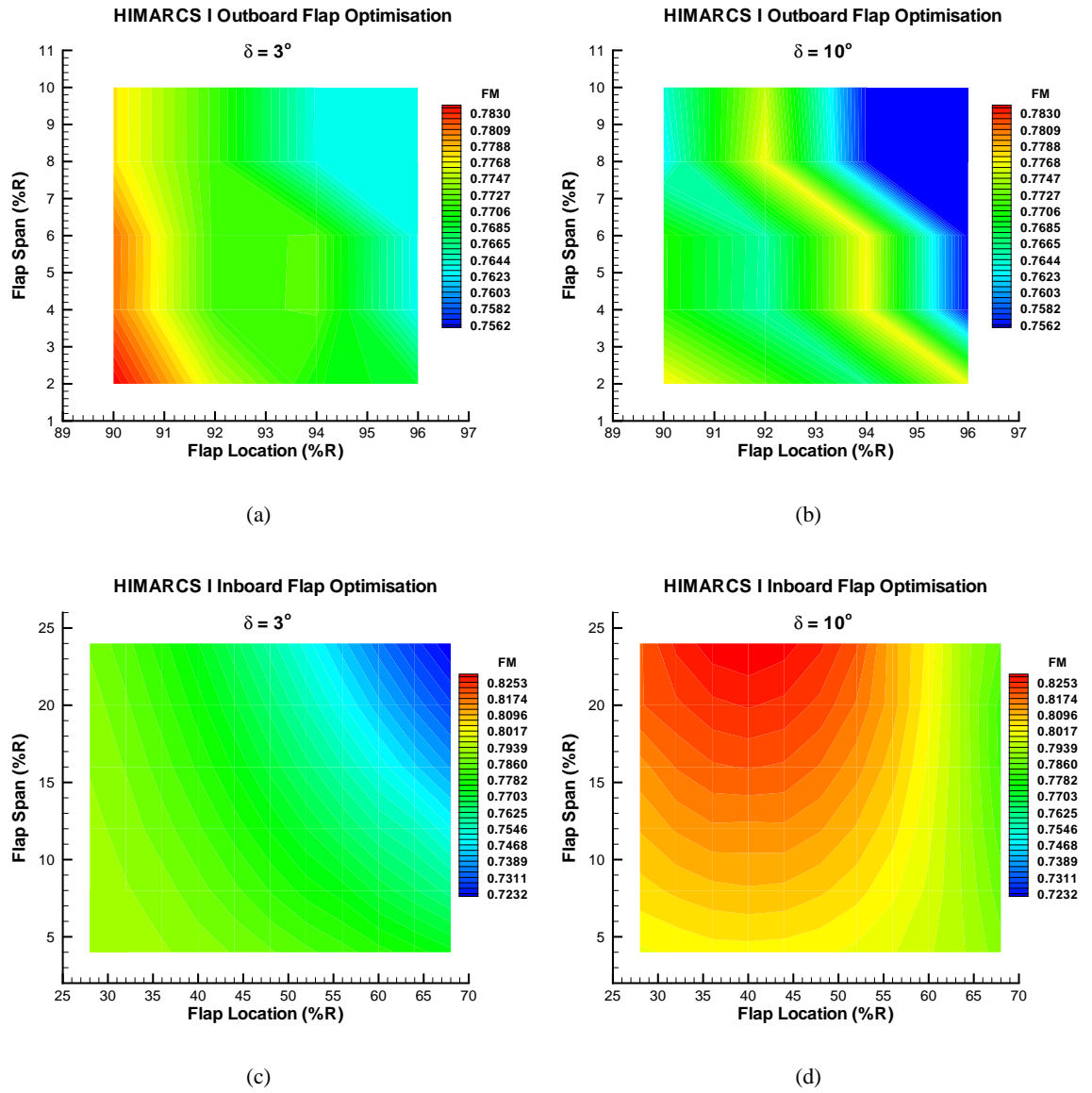
Figure B.43: Contours of Figure of Merit at $C_T = 0.00556364$ for flap chord of 32%c. (a) Outboard, 3°. (b) Outboard, 10°. (c) Inboard, 3°. (d) Inboard, 10°. FM (Baseline) = 0.79409397.
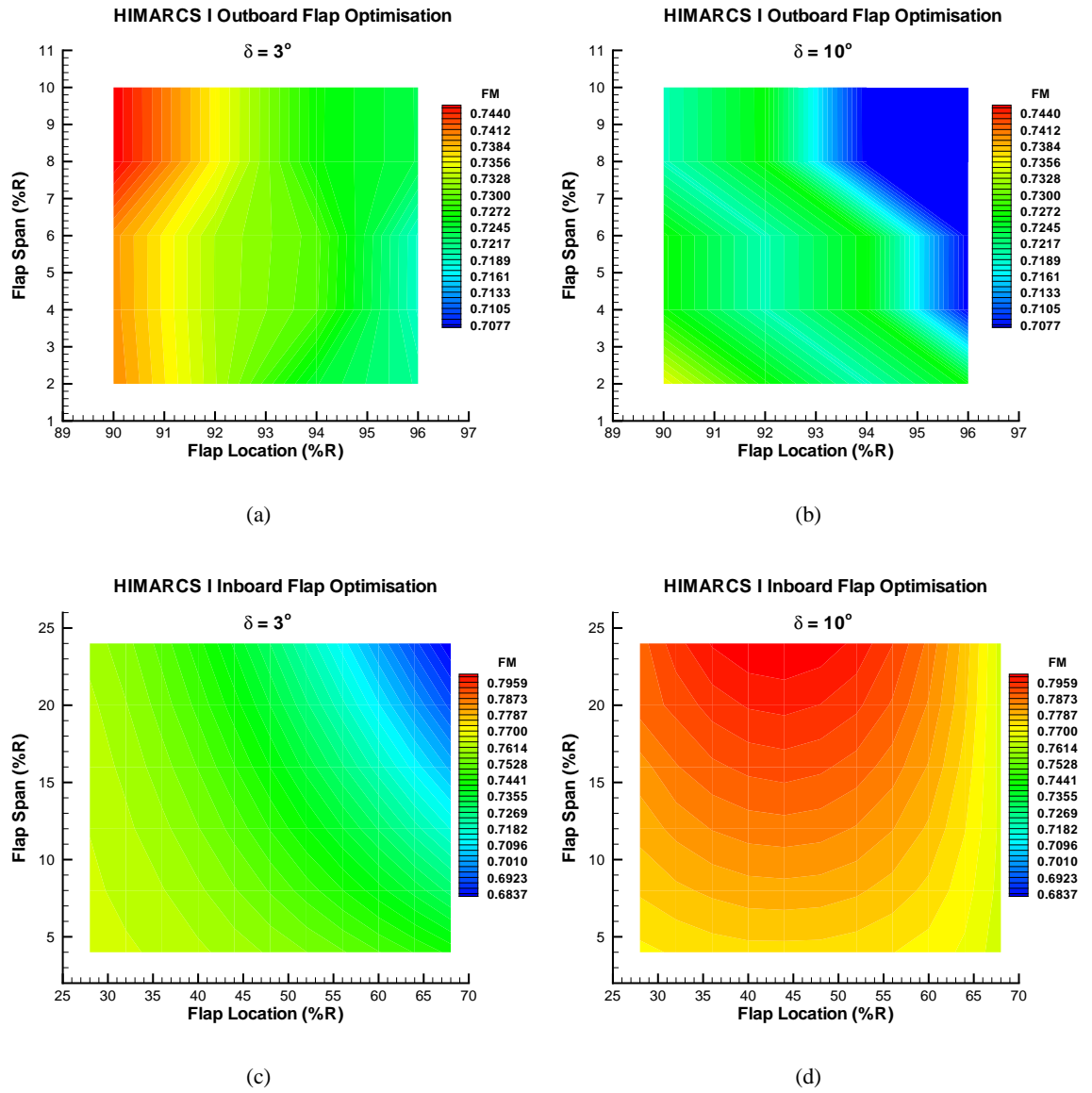
Figure B.44: Contours of Figure of Merit at $C_T = 0.00690909$ for flap chord of 32%c. (a) Outboard, 3°. (b) Outboard, 10°. (c) Inboard, 3°. (d) Inboard, 10°. FM (Baseline) = 0.76587558.

(a)

(b)

(c)

(d)
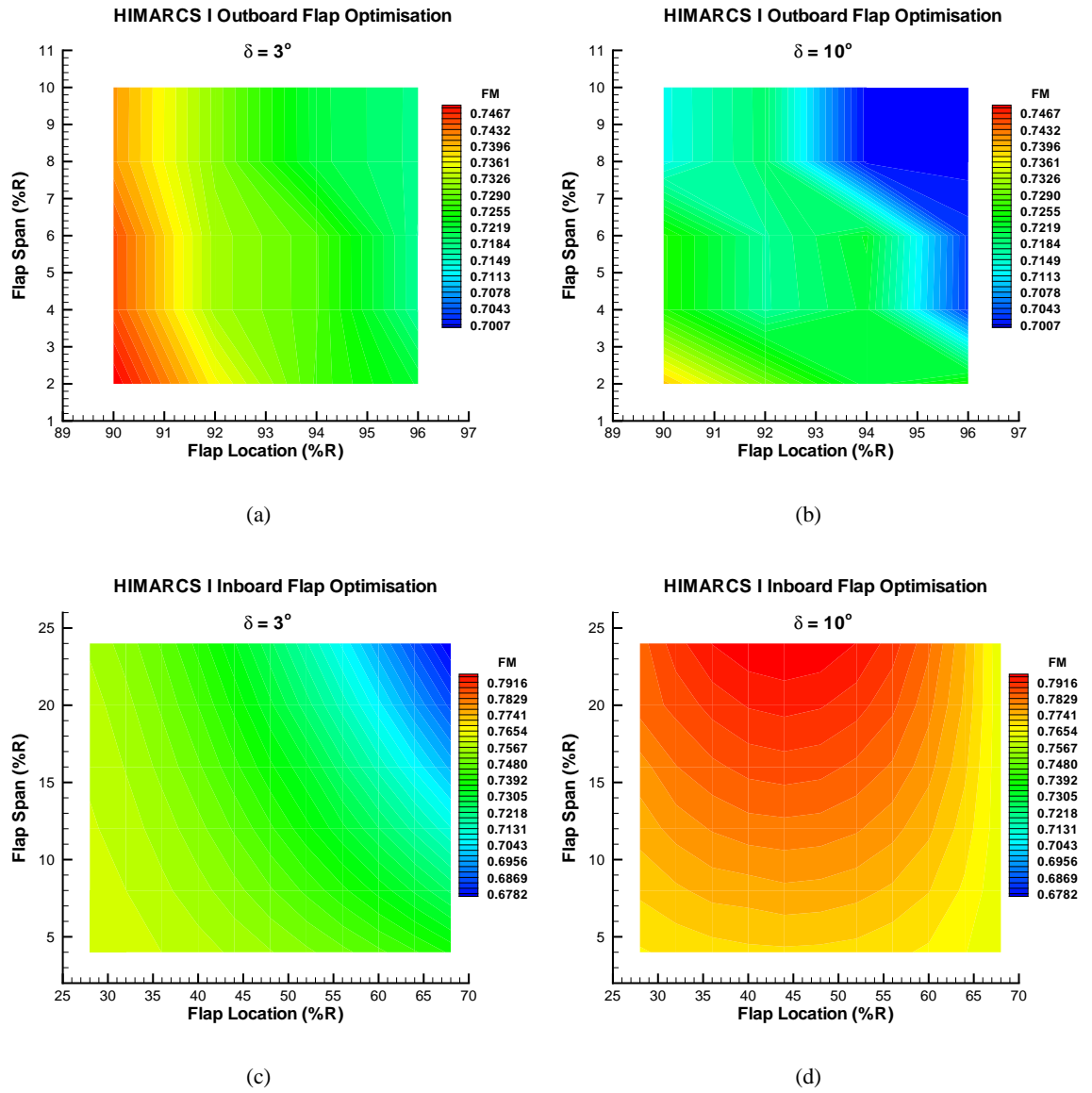
Figure B.45: Contours of Figure of Merit at $C_T = 0.00712727$ for flap chord of 32%c. (a) Outboard, 3°. (b) Outboard, 10°. (c) Inboard, 3°. (d) Inboard, 10°. FM (Baseline) = 0.76173294.

(a)

(b)

(c)

(d)
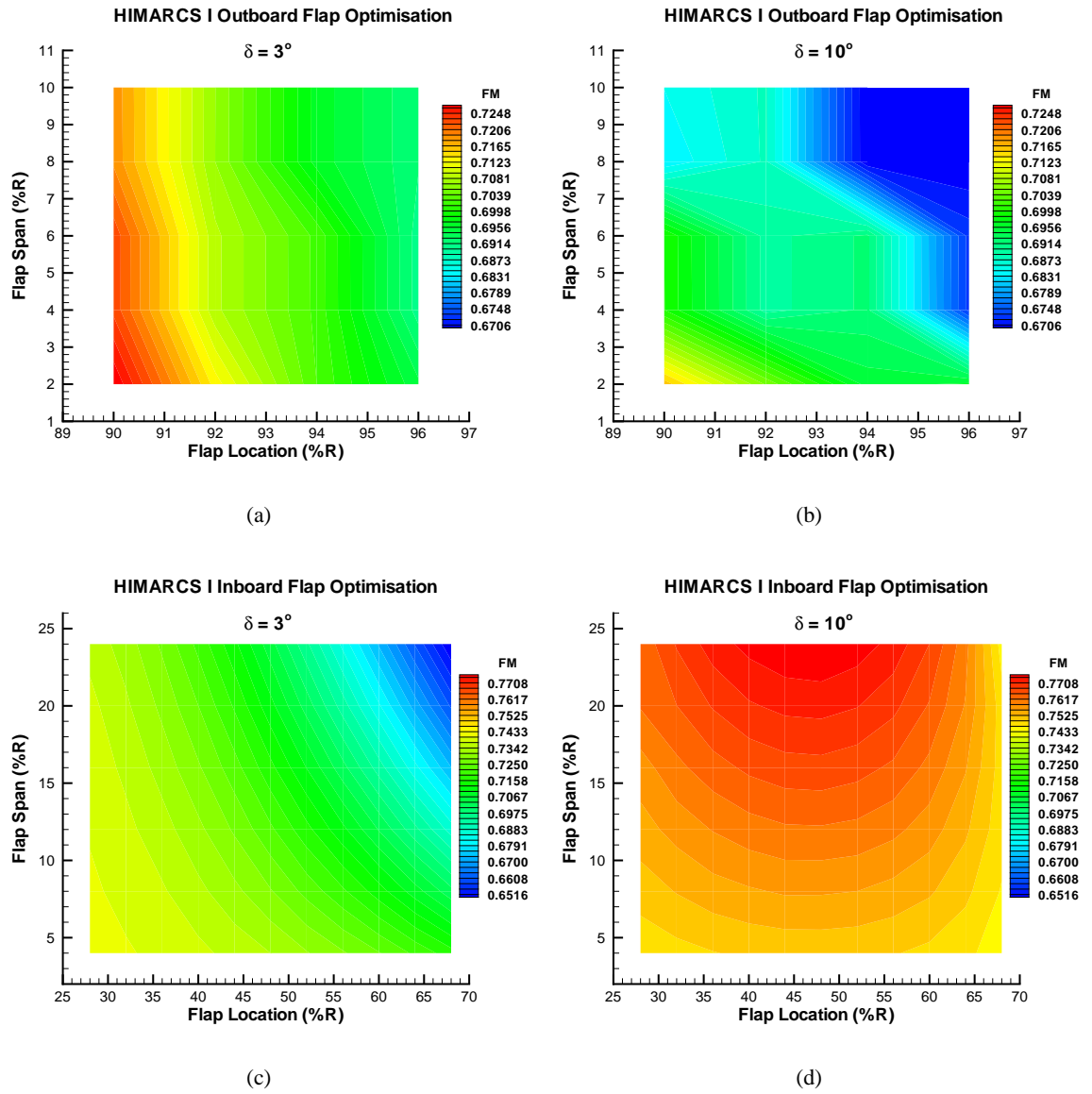
Figure B.46: Contours of Figure of Merit at $C_T = 0.00829091$ for flap chord of 32%c. (a) Outboard, 3°. (b) Outboard, 10°. (c) Inboard, 3°. (d) Inboard, 10°. FM (Baseline) = 0.74179268.